CP violation studies on the B0 -> DK*0 decays and hadronic trigger performance with the LHCb detector at CERN

Alexandra Martin Sanchez

HAL Id: tel-00852170
https://theses.hal.science/tel-00852170

Submitted on 20 Aug 2013

UNIVERSITÉ PARIS-SUD XI

École Doctorale : Particules, Noyaux et Cosmos - ED 517

Laboratoire de l'Accélérateur Linéaire - UMR 8607

Centre Scientifique d'Orsay, Bâtiment 200 - BP 34, 91898 Orsay CEDEX - France

Discipline : Physique des particules

THÈSE DE DOCTORAT

soutenue le 25 juin 2013

par

Alexandra MARTÍN SÁNCHEZ

Études de la violation de CP dans les désintégrations $\overline{B}^0 \to D\overline{K}^{*0}$ et des performances du système de déclenchement hadronique avec le détecteur LHCb au CERN

CP violation studies on the $\overline{B}^0 \to D\overline{K}^{*0}$ decays and hadronic trigger performance with the LHCb detector at CERN

Composition du jury :

M.	Jean-Pierre LEES	Rapporteur
M.	Fernando MARTÍNEZ VIDAL	Examinateur
M.	Jean ORLOFF	Examinateur
M.	Jonas RADEMACKER	Rapporteur
M.	Patrick ROBBE	Directeur de thèse
M.	Achille STOCCHI	Président

Résumé

Dans le Modèle Standard de la physique des particules, le mécanisme Cabibbo-Kobayashi-Maskawa (CKM) décrit le phénomène du mélange des quarks. De ses paramètres, l'angle γ est celui connu avec la moins grande précision. Les mesures directes donnent une incertitude d'environ 15°, importante comparée à celle sur la valeur extraite des ajustements globaux, de 3°. Pour vérifier la cohérence du Modèle Standard, γ doit être mesuré précisément. Cela est possible en utilisant des processus au niveau des arbres, où seules des contributions du Modèle Standard sont attendues, ou avec des processus impliquant des boucles, qui peuvent être sensibles à des effets au-delà. Des différences entre la mesure de γ avec des diagrammes en arbres et avec des boucles pourraient être donc une indication de nouvelle physique.

Cette thèse présente la première mesure des observables CP dans la désintégration $\overline{B}^0 \to D\overline{K}^{*0}$. Celle-ci est sensible à γ du fait de l'interférence entre l'amplitude des diagrammes $b \to u$ et $b \to c$, au niveau des arbres. L'asymétrie CP dans le mode $\overline{B}^0 \to [K^+K^-]_D\overline{K}^{*0}$ et le rapport des largeurs partielles avec $\overline{B}^0 \to [K^-\pi^+]_D\overline{K}^{*0}$ sont mesurés avec 1 fb^{-1} de données récoltées par l'expérience LHCb en 2011,

$$A_d^{KK} = -0,452\ ^{+0,228}_{-0,230} \pm 0,025 = A_{CP+},$$
$$R_d^{KK} =\ \ 1,360\ ^{+0,366}_{-0,319} \pm 0,075 = R_{CP+}.$$

L'asymétrie CP du mode supprimé $\overline{B}^0 \to [K^+\pi^-]_D\overline{K}^{*0}$ et le rapport des largeurs partielles avec le favorisé $\overline{B}^0 \to [K^-\pi^+]_D\overline{K}^{*0}$ sont mesurés avec 3 fb^{-1} de données récoltées en 2011 et 2012,

$$A_d^{sup} = -0,094\ ^{+0,303}_{-0,318} = A_{ADS},$$
$$R_d =\ \ 0,075\ ^{+0,023}_{-0,022} = R_{ADS}.$$

Par ailleurs, les études réalisées sur le système de déclenchement hadronique de l'expérience LHCb sont aussi présentées.

Abstract

In the Standard Model of particle physics, the Cabibbo-Kobayashi-Maskawa (CKM) mechanism describes the quark mixing effect. The CKM γ angle is one of the parameters of the Standard Model that are known less accurately. Direct measurements give an uncertainty of around $15°$, large with respect to the uncertainty on the value extracted from global fits, of $3°$. In order to test the Standard Model consistency, the γ angle needs to be measured precisely. This can be done using processes at the tree-level, where only Standard Model contributions are expected, or using processes involving loop diagrams, which can be sensitive to physics beyond the Standard Model. Differences in the γ measurement from tree and loop diagrams would be an indication of new physics.

This thesis presents the first measurement of the CP observables in the $\overline{B}^0 \to D\overline{K}^{*0}$ decay. Sensitivity to γ arises from the interference of the $b \to u$ mediated amplitude with the $b \to c$ one, at the tree-level. The CP asymmetry of the $\overline{B}^0 \to [K^+K^-]_D\overline{K}^{*0}$ mode and the partial width ratio of this channel with respect to $\overline{B}^0 \to [K^-\pi^+]_D\overline{K}^{*0}$ are measured using 1 fb^{-1} of data collected by the LHCb experiment in 2011,

$$A_d^{KK} = -0.452 \ ^{+0.228}_{-0.230} \pm 0.025 = A_{CP+},$$
$$R_d^{KK} = \quad 1.360 \ ^{+0.366}_{-0.319} \pm 0.075 = R_{CP+}.$$

The CP asymmetry of the suppressed $\overline{B}^0 \to [K^+\pi^-]_D\overline{K}^{*0}$ mode and the partial width ratio with respect to the favoured $\overline{B}^0 \to [K^-\pi^+]_D\overline{K}^{*0}$ are measured using the total 3 fb^{-1} of data collected in 2011 and 2012,

$$A_d^{sup} = -0.094 \ ^{+0.303}_{-0.318} = A_{ADS},$$
$$R_d = \quad 0.075 \ ^{+0.023}_{-0.022} = R_{ADS}.$$

In addition, the studies performed on the hardware hadronic trigger of the LHCb experiment are also presented.

Synthèse

La théorie décrivant actuellement la physique des particules est le Modèle Standard. Il a été introduit dans les années 70, et au fil des découvertes il s'est montré être singulièrement prédictif. Il contient 18 paramètres : 9 pour les masses des fermions, 4 correspondant au mélange des quarks, un pour la masse du boson de Higgs, une constante de couplage pour l'interaction forte et 3 paramètres de l'interaction électrofaible.

Le phénomène de mélange des quarks, ou le fait que les états propres de masse des quarks ne sont pas les mêmes que leurs états propres d'interaction, est introduit pour la première fois par Cabibbo à deux familles des quarks [22]. Cette rotation peut alors être paramétrée par un un angle θ_C. À trois familles de quarks, cela est representé par la matrice Cabibbo-Kobayashi-Maskawa (CKM) [22,27],

$$V_{CKM} = \begin{pmatrix} V_{ud} & V_{us} & V_{ub} \\ V_{cd} & V_{cs} & V_{cb} \\ V_{td} & V_{ts} & V_{tb} \end{pmatrix}. \tag{5}$$

Cette matrice peut être paramétrée par trois nombres réels et une phase complexe. La paramétrisation plus habituelle est celle de Wolfenstein [33],

$$V = \begin{pmatrix} 1 - \frac{\lambda^2}{2} & \lambda & A\lambda^3(\rho - i\eta) \\ -\lambda & 1 - \frac{\lambda^2}{2} & A\lambda^2 \\ A\lambda^3(1 - \rho - i\eta) & -A\lambda^2 & 1 \end{pmatrix} + \mathcal{O}(\lambda^4), \tag{6}$$

construite à partir du développement de chaque élément comme une série en fonction de puissances du facteur $\lambda \sim \sin\theta_C = 0,22$. Ce paramètre donne l'ordre de grandeur relatif des couplages d'interaction entre les différentes familles : les éléments de la diagonale sont d'ordre 1, pour des transitions dans une même famille ; les éléments concernant la première et la deuxième famille sont d'ordre λ, alors que pour des transitions entre la deuxième et la troisième ils sont d'ordre λ^2, et finalement d'ordre λ^3 entre la première et la troisième. Les couplages des interactions entre les quarks sont établis ainsi d'une façon naturelle.

La matrice CKM correspondant à un changement de base entre les états propres, elle doit être unitaire,

$$VV^\dagger = V^\dagger V = \mathbb{I}. \tag{7}$$

De cette condition, 9 relations entre les éléments de la matrice peuvent être extraites. Elles sont égales à 1 pour les termes de la diagonale du produit des matrices, et égales à 0 en dehors. Celles-ci peuvent être réprésentées comme un triangle dans le plan complexe (ρ, η), dont la surface caractérise la magnitude de la violation de la symétrie CP dans le secteur des quarks. En particulier, le triangle correspondant à la relation

$$V_{ud}V_{ub}^* + V_{cd}V_{cb}^* + V_{td}V_{tb}^* = 0 \tag{8}$$

a tous ses termes du même ordre λ^3. La Figure 1 représente le triangle qui en résulte après les changements de variable $\bar{\rho} = (1 - \lambda^2/2)\rho$, $\bar{\eta} = (1 - \lambda^2/2)\eta$ et en normalisant par rapport au terme $|V_{cd}V_{cb}^*|$. Il est connu comme le Triangle d'Unitarité.
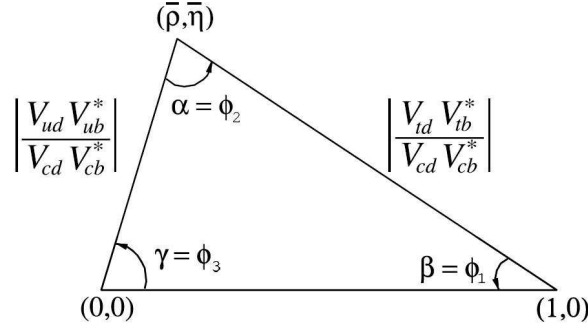
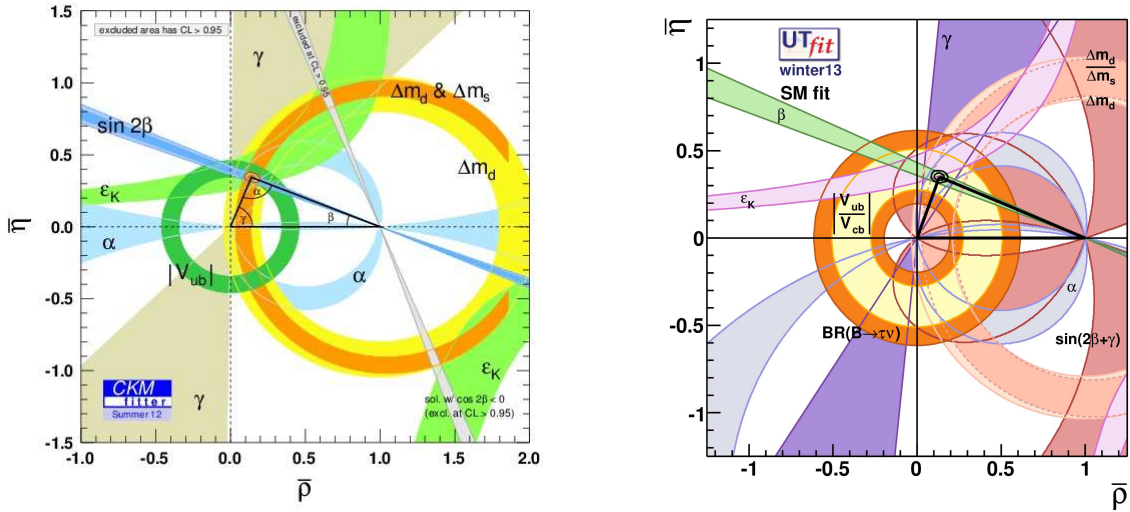Figure 1: *Le Triangle d'Unitarité de la théorie CKM.*

Figure 2: *Ajustement global du Triangle d'Unitarité de la théorie CKM (en noir, signalant l'apex du triangle), en utilisant toute les mesures expérimentales disponibles sur ses différents paramètres (zones colorées). Gauche : collaboration CKMfitter. Droite : collaboration UTFit.*

La physique du quark b intervient dans ce triangle, comme le montre l'Équation 8. En effet, le coté $\left|\frac{V_{ud}V_{ub}^*}{V_{cd}V_{cb}^*}\right|$ peut être mesuré à partir des désintégrations des mésons B, et $\left|\frac{V_{td}V_{tb}^*}{V_{cd}V_{cb}^*}\right|$ en étudiant les oscillations dans le système $B^0 - \overline{B}^0$. Les angles du triangle sont définis comme

$$\alpha = \mathrm{Arg}\left(-\frac{V_{td}V_{tb}^*}{V_{ud}V_{ub}^*}\right), \tag{9}$$

$$\beta = \mathrm{Arg}\left(-\frac{V_{cd}V_{cb}^*}{V_{td}V_{tb}^*}\right),$$

$$\gamma = \mathrm{Arg}\left(-\frac{V_{ud}V_{ub}^*}{V_{cd}V_{cb}^*}\right).$$

Ces angles peuvent être mesurés avec des désintégrations de mésons B qui ne conservent pas la symétrie CP. La physique du b joue alors un rôle principal pour contraindre la théorie CKM, et plus généralement le Modèle Standard.

L'état actuel des mesures sur le Triangle d'Unitarité est présenté dans la Figure 2. Les collaborations UTfit [35] et CKMfitter [36] utilisent ces mesures pour réaliser des ajustements globaux

et contraindre le triangle. La validité du Modèle Standard nécessite que toutes les mesures convergent en l'apex du triangle ; le cas contraire pourrait être une indication de l'existence de nouvelle physique au-delà du Modèle Standard.

On s'intéresse particulièrement à l'angle γ du Triangle d'Unitarité. La Figure 2 montre que cet angle est celui connu expérimentalement avec la moins grande précision. Les dernières mesures directes donnent [37–40]

$$
\begin{aligned}
\gamma^{\text{BaBar}} &= \left(69^{+17}_{-16}\right)^{\circ}, & (10) \\
\gamma^{\text{Belle}} &= \left(68^{+15}_{-14}\right)^{\circ}, & (11) \\
\gamma^{\text{LHCb}} &= \left(67 \pm 12\right)^{\circ}. & (12)
\end{aligned}
$$

Cependant, la valeur de γ obtenue à partir des ajustements globaux est

$$
\begin{aligned}
\gamma^{\text{UTfit}} &= (69,2 \pm 3,2)^{\circ}, & (13) \\
\gamma^{\text{CKMfitter}} &= \left(67,7^{+4,1}_{-4,3}\right)^{\circ}, & (14)
\end{aligned}
$$

dont l'incertitude est beaucoup plus petite. L'angle γ doit être mesuré expérimentalement avec une meilleure précision pour bien contraindre le Triangle d'Unitarité.

Des méthodes variées existent pour mesurer γ. On considère ici les méthodes avec des diagrammes en arbre (où des contributions au-delà du Modèle Standard, qui peuvent apparaître dans des boucles, ne sont pas attendues) indépendantes du temps. On utilise typiquement des désintégrations du type $B^{-,0} \to DK^{-,*0}$, où D est un méson D^0 ou un méson $\overline{D}^0$, et des états finaux accessibles à la fois par ces deux états intermédiaires. L'angle γ peut alors être mesuré grâce à l'interférence entre les amplitudes des diagrammes $b \to u$ et $b \to c$, par l'étude des observables reliées à la symétrie CP, en particulier l'asymétrie entre la désintégration du méson B et son anti-méson. Différents modes de désintégration sont possibles pour le méson D :

- Méthode GLW [45,46] : désintégrations vers un état propre de CP, comme $D \to K^+K^-$ ou $D \to \pi^+\pi^-$.

- Méthode ADS [47] : désintégrations vers un état spécifique de saveur, comme $D \to K^{\mp}\pi^{\pm}$.

- Méthode GGSZ [48] : désintégrations à trois corps, qui permettent une analyse du plot de Dalitz.

Les modes $B^- \to DK^-$ ont été étudiés par les usines à B et continuent à être exploités dans les expériences actuelles. Dans cette thèse, on utilise la désintégration $\overline{B}^0 \to D\overline{K}^{*0}$. La sensibilité à γ est plus grande dans ce mode, grâce au fait que les deux amplitudes qui interfèrent sont supprimées en couleur, alors que pour $B^- \to DK^-$ une est supprimée et l'autre favorisée ; cependant, les rapports de branchement sont plus petits ici qu'en $B^- \to DK^-$. Le méson K^{*0} se désintègre en $K^{*0} \to K^+\pi^-$, donc la saveur du méson B^0 au moment de sa désintégration peut être connue en identifiant le signe du K dans l'état final du K^{*0}. Les observables CP dans les méthodes GLW et ADS, construites à partir des largeurs partielles et sensibles à l'angle γ,

sont mesurées égales à

$$
\begin{aligned}
A_{CP+} &= \frac{\Gamma(\overline{B}^0 \to [K^+K^-]_D \overline{K}^{*0}) - \Gamma(B^0 \to [K^+K^-]_D K^{*0})}{\Gamma(\overline{B}^0 \to [K^+K^-]_D \overline{K}^{*0}) + \Gamma(B^0 \to [K^+K^-]_D K^{*0})} \\
&= \frac{2\kappa r_{B^0} \sin\delta_{B^0} \sin\gamma}{1 + r_{B^0}^2 + 2\kappa r_{B^0} \cos\delta_{B^0} \cos\gamma},
\end{aligned}
\tag{15}
$$

$$
\begin{aligned}
R_{CP+} &= \frac{\Gamma(\overline{B}^0 \to [K^+K^-]_D \overline{K}^{*0}) + \Gamma(B^0 \to [K^+K^-]_D K^{*0})}{\Gamma(\overline{B}^0 \to [K^-\pi^+]_D \overline{K}^{*0}) + \Gamma(B^0 \to [K^+\pi^-]_D K^{*0})} \\
&= \frac{1 + r_{B^0}^2 + 2\kappa r_{B^0} \cos\delta_{B^0} \cos\gamma}{1 + r_{B^0}^2 r_D^2 + 2\kappa r_{B^0} r_D \cos(\delta_{B^0} + \delta_D) \cos\gamma},
\end{aligned}
\tag{16}
$$

$$
\begin{aligned}
A_{ADS} &= \frac{\Gamma(\overline{B}^0 \to [K^+\pi^-]_D \overline{K}^{*0}) - \Gamma(B^0 \to [K^-\pi^+]_D K^{*0})}{\Gamma(\overline{B}^0 \to [K^+\pi^-]_D \overline{K}^{*0}) + \Gamma(B^0 \to [K^-\pi^+]_D K^{*0})} \\
&= \frac{2\kappa r_{B^0} r_D \sin(\delta_{B^0} - \delta_D) \sin\gamma}{r_{B^0}^2 + r_D^2 + 2\kappa r_{B^0} r_D \cos(\delta_{B^0} - \delta_D) \cos\gamma},
\end{aligned}
\tag{17}
$$

$$
\begin{aligned}
R_{ADS} &= \frac{\Gamma(\overline{B}^0 \to [K^+\pi^-]_D \overline{K}^{*0}) + \Gamma(B^0 \to [K^-\pi^+]_D K^{*0})}{\Gamma(\overline{B}^0 \to [K^-\pi^+]_D \overline{K}^{*0}) + \Gamma(B^0 \to [K^+\pi^-]_D K^{*0})} \\
&= \frac{r_{B^0}^2 + r_D^2 + 2\kappa r_{B^0} r_D \cos(\delta_{B^0} - \delta_D) \cos\gamma}{1 + r_{B^0}^2 r_D^2 + 2\kappa r_{B^0} r_D \cos(\delta_{B^0} + \delta_D) \cos\gamma}.
\end{aligned}
\tag{18}
$$

Dans ces équations, le facteur $r_{B^0} e^{i\delta_{B^0}}$ représente le rapport entre les amplitudes $b \to u$ et $b \to c$, $r_D e^{i\delta_D}$ est le rapport entre les amplitudes du mode doublement supprimé de Cabibbo $D^0 \to K^+\pi^-$ et du mode favorisé $D^0 \to K^-\pi^+$, et κ est un facteur de cohérence qui tient compte des contributions non résonantes $\overline{B}^0 \to DK^-\pi^+$. Ce facteur est estimé égal à $\kappa = 0,95 \pm 0,03$ pour une région de masse de ± 48 MeV/c^2 autour de la masse nominale du K^{*0} [57]. Les facteurs r_D et δ_D ont été mesurés par des expériences précédentes. Par contre, r_{B^0} et δ_{B^0} sont inconnus et doivent être extraits simultanément avec γ à partir de ces mesures.

L'expérience LHCb est spécialement conçue pour réaliser des mesures de précision dans le domaine des saveurs lourdes. Elle fait partie des expériences du grand collisionneur hadronique LHC au CERN (Genève, Suisse). Le LHC a fourni des collisions proton-proton à 7 TeV d'énergie dans le centre de masse en 2011 et 8 TeV en 2012. La section efficace de production de paires $b\bar{b}$ mesurée par LHCb en 2011 est $\sigma(pp \to b\bar{b}X) = (284 \pm 20 \pm 49)$ µb [70]. Avec une luminosité instantanée jusqu'à 400 (µb × s)$^{-1}$, LHCb a enregistré environ de 1 fb^{-1} en 2011 et 2,2 fb^{-1} en 2012.

Le détecteur LHCb [69] est présenté dans la Figure 3. Sa géométrie caractéristique, qui couvre une région en pseudorapidité $2 < \eta < 5$, est choisie pour tenir compte du fait que les paires $b\bar{b}$ sont produites majoritairement dans un cône étroit vers la direction avant ou arrière par rapport au point de collision. LHCb est donc un spectromètre à un bras, formé par un assemblage de sous-détecteurs, chacun avec une fonction précise. En particulier, pour les désintégrations purement hadroniques auxquelles nous nous intéressons ici, LHCb est bien équipé grâce au détecteur de vertex très précis (VELO), qui permet de distinguer les points de désintégration primaires des secondaires, et au détecteur Cherenkov, qui permet d'identifier les kaons et les pions. En plus, ce type de désintégrations est sélectionné efficacement par le système de déclenchement L0 hadronique.

Le système de déclenchement hadronique de LHCb a été étudié en détails pendant cette thèse, avec comme objectif de concevoir une méthode pour calculer son efficacité, donnée nécessaire dans les analyses de physique de l'expérience. Le premier niveau du système de déclenchement
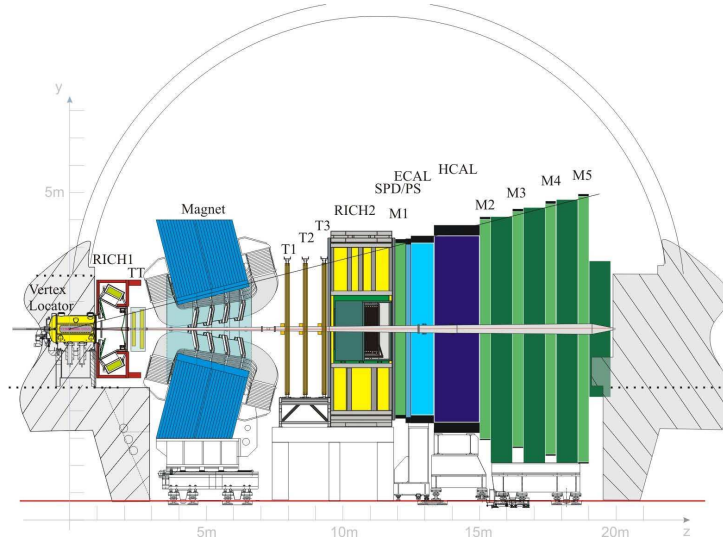
Figure 3: *Le détecteur LHCb. Les différents sous-détecteurs sont indiqués.*

L0 est implémenté dans de cartes d'électronique, et utilise les calorimètres et les chambres à muons pour identifier des hadrons, électrons, photons et muons qui portent un grande impulsion transverse. Ce système réduit le taux des collisions du LHC de 40 MHz à 1 MHz, dont 450 kHz correspondent au type hadronique. Un deuxième niveau de déclenchement, le HLT, utilise une ferme d'ordinateurs où des algorithmes spécifiques réduisent le taux à une valeur finale de 5 kHz.

L'efficacité du L0 hadronique est calculée pour des kaons et des pions en fonction de leur impulsion transverse, en utilisant des données d'étalonnage [80]. La méthode développée compare les objets du système de déclenchement, des amas de 2×2 cellules dans les calorimètres, avec le dépôt d'énergie correspondant à chaque particule, reconstruit comme un amas de 3×3 cellules. Le résultat est présenté, pour des données de 2012, dans la Figure 4. Les deux régions qui forment le calorimètre hadronique, dont l'extérieure a des cellules de taille double à celles de l'intérieure, sont traitées séparément. La Figure 4 montre aussi l'évolution dans le temps de l'efficacité intégrée pendant la même période.

L'étude des observables CP est réalisée avec 1 fb^{-1} de données de collisions proton-proton récoltées par LHCb en 2011. Le canal de désintégration $B^0 \to DK^{*0}$ avec $D \to K^+K^-$ est analysé. Les diagrammes de Feynman correspondants sont montrés dans la Figure 5 : comme expliqué précédemment, la sensibilité à l'angle γ provient de l'interférence entre les amplitudes des processus $b \to u$ et $b \to c$. Les événements du signal sont sélectionnés avec des coupures optimisées sur l'impulsion des particules dans l'état final, leur probabilité d'être des kaons et des pions, la qualité des vertex du B et du D, les paramètres d'impact et la masse invariante du D^0 et du K^{*0}, principalement. Les différents bruits de fond susceptibles d'introduire une contamination sont étudiés et supprimés par des coupures additionnelles, comme par exemple la contribution du mode $B^0 \to K^+K^-K^{*0}$, qui est réduit à un niveau négligeable avec une coupure sur la significance de la distance de vol du méson D. Le bruit de fond provenant de la contribution non-résonante du K^{*0}, c'est à dire du type $B^0 \to DK^+\pi^-$, est estimé à $(4,8 \pm 3,4)$ % du signal et considéré aussi négligeable.

Avec les critères de sélection appliqués, la distribution de masse invariante des candidats B est étudiée. Un ajustement avec la méthode du maximum de vraisemblance est réalisé pour déterminer le nombre d'événements de signal reconstruits dans l'échantillon. Les différents bruits de fond restants sont pris en compte dans l'ajustement par des fonctions de densité de probabilité adaptées : la contribution du mode de désintégration $B^0 \to D^*K^{*0}$, avec $D^* \to D\pi^0/\gamma$ quand le π^0 ou le γ ne sont pas reconstruits, s'accumule à basse masse ; la contribution du $B^0 \to D\rho^0$, avec
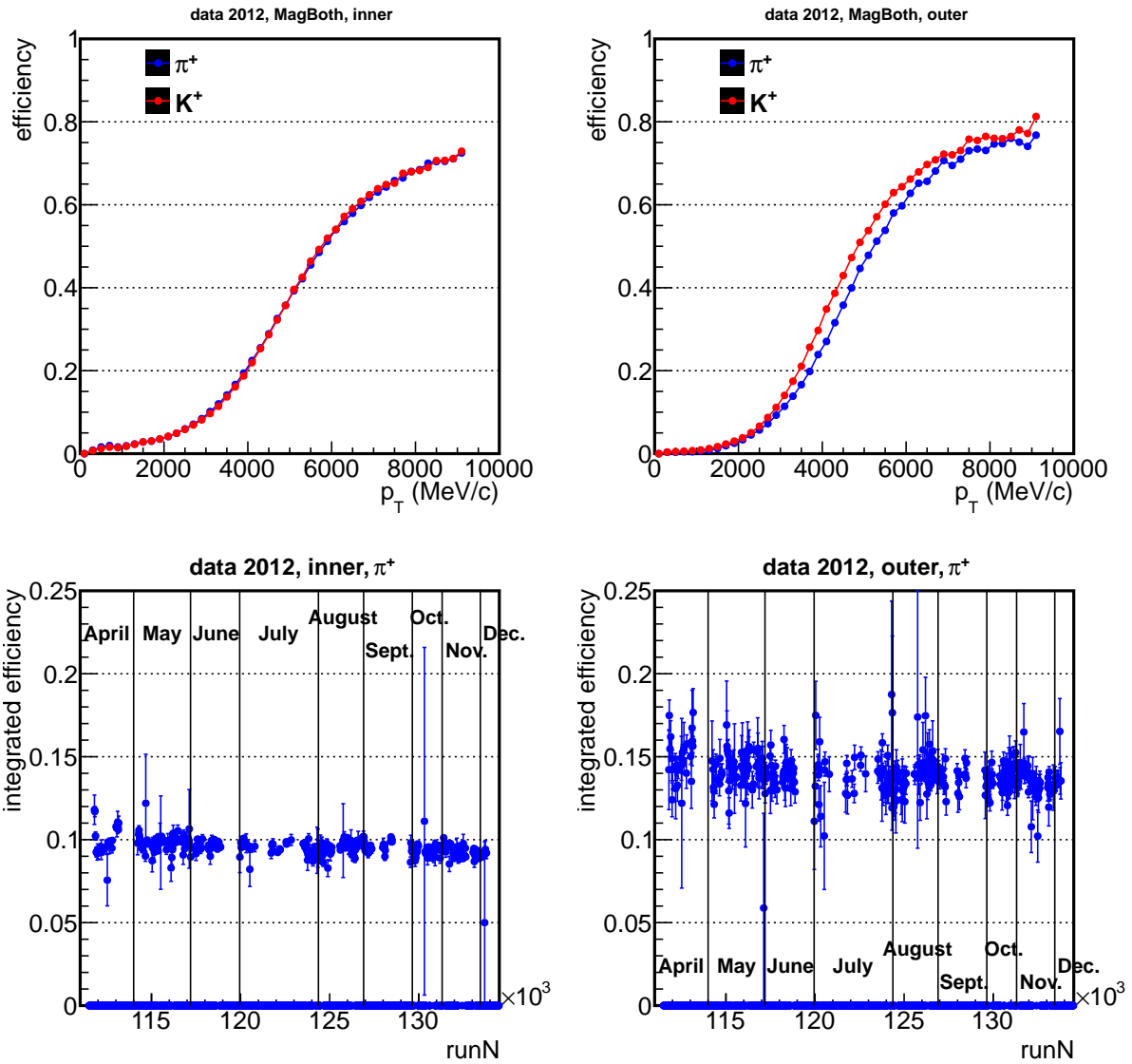
Figure 4: *Efficacité du système de déclenchement hadronique de LHCb pour des pions et kaons des données recoltées en 2012, à gauche pour la région interne du calorimétre hadronique, et à droite pour la région externe. Haut : efficacité en fonction de l'impulsion transverse p_T des particules. Bas : efficacité en fonction du temps.*
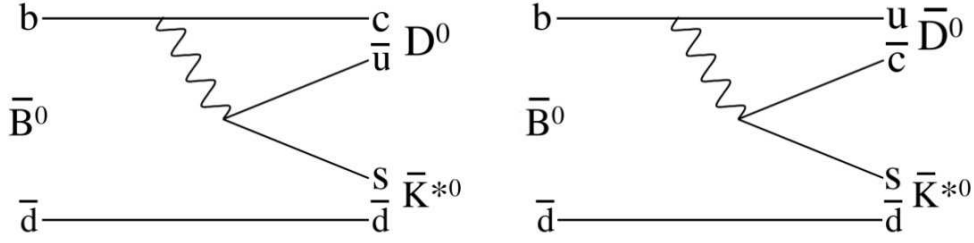
Figure 5: *Diagrammes de Feynman pour les processus $\overline{B}^0 \to D^0\overline{K}^{*0}$ (gauche), correspondant à une transition $b \to c$, et $\overline{B}^0 \to \overline{D}^0\overline{K}^{*0}$ (droite), pour $b \to u$.*

$\rho^0 \to \pi^+\pi^-$ dans le cas où un des pions est reconstruit comme un kaon, est aussi présente. Ces deux composantes sont modélisées à partir des données de simulation. Le résultat de l'ajustement est montré dans les Figures 6 et 7, pour $B^0 \to [K^+K^-]_DK^{*0}$, le mode signal, et pour le mode utilisé pour la normalisation $B^0 \to [K^+\pi^-]_DK^{*0}$, respectivement. Ce résultat est la première observation du canal de désintégration $B^0 \to [K^+K^-]_DK^{*0}$, avec une significance totale de $5,1\ \sigma$. La violation de la symétrie CP est visible dans ce mode. Les observables CP dans la méthode GLW pour le canal $B^0 \to DK^{*0}$ sont ainsi mesurées,

$$A_d^{KK} = -0,452\ ^{+0,228}_{-0,230} \pm 0,025 = A_{CP+},$$
$$R_d^{KK} = \quad 1,360\ ^{+0,366}_{-0,319} \pm 0,075 = R_{CP+},$$

où la première incertitude est statistique et la deuxième systématique. L'asymétrie CP dans le mode de normalisation $B^0 \to [K^+\pi^-]_DK^{*0}$ est compatible avec 0 comme attendu,

$$A^{\mathrm{fav}} = -0,084\ \pm 0,079 \pm 0,010.$$

Ces résultats ont été publiés dans [64].

Les 3 fb^{-1} des données récoltées par LHCb en 2011 et 2012 sont analysés pour mesurer les observables CP dans la méthode ADS. Le canal de désintégration supprimé $B^0 \to [K^-\pi^+]_DK^{*0}$ est analysé, avec le favorisé $B^0 \to [K^+\pi^-]_DK^{*0}$ comme mode de normalisation. Une analyse multivariée est utilisée ici pour sélectionner plus efficacement les événements du signal. Un algorithme « Boosted Decision Tree » (BDT) est optimisé, avec fondamentalement les mêmes variables utilisées précédemment dans l'analyse du mode $B^0 \to [K^+K^-]_DK^{*0}$. Ce BDT est mis au point avec des données de simulation pour le signal et du bruit de fond combinatoire des données 2011. Cette nouvelle sélection est appliquée à l'ensemble des données. L'ajustement de la distribution de masse invariante des candidats B est montré dans les Figures 8 et 9, respectivement pour le mode signal
$B^0 \to [K^-\pi^+]_DK^{*0}$ et le mode de normalisation $B^0 \to [K^+\pi^-]_DK^{*0}$. Le résultat préliminaire sur les observables de violation de CP dans la méthode ADS pour la désintégration $B^0 \to DK^{*0}$ est

$$A_d^{sup} = -0,094\ ^{+0,303}_{-0,318} = A_{ADS},$$
$$R_d = \quad 0,075\ ^{+0,023}_{-0,022} = R_{ADS},$$

où la seule incertitude donnée est statistique.

Figure 6: *Distribution de la masse invariante pour l'état $[K^+K^-]_D K^{*0}$ (gauche), correspondant à des candidats B^0 et $\overline{B}^0_s$, et $[K^+K^-]_D \overline{K}^{*0}$ (droite), correspondant à $\overline{B}^0$ et B^0_s. Les points noirs représentent les données, la ligne noire continue est le résultat de l'ajustement. Les différentes contributions sont visibles : le pic du signal est indiqué par une ligne noire pointillée, et les bruits de fond par les différentes zones grises qui sont, de la plus foncée à la plus claire, combinatoire, $B^0 \to D\rho^0$ erronément identifié, et $B^0_{(s)} \to D^* K^{*0}$ reconstruit partiellement à basse masse. Les lignes colorées représentent les différentes amplitudes d'hélicité qui contribuent au bruit à basse masse : rouge est "001", bleu est "010" et vert est "100" ; les lignes continues correspondent au bruit du B^0_s, les lignes pointillées à celui du B^0. Les histogrammes du bas représentent la différence entre les données et la fonction d'ajustement, divisée par l'incertitude sur le nombre d'entrées.*
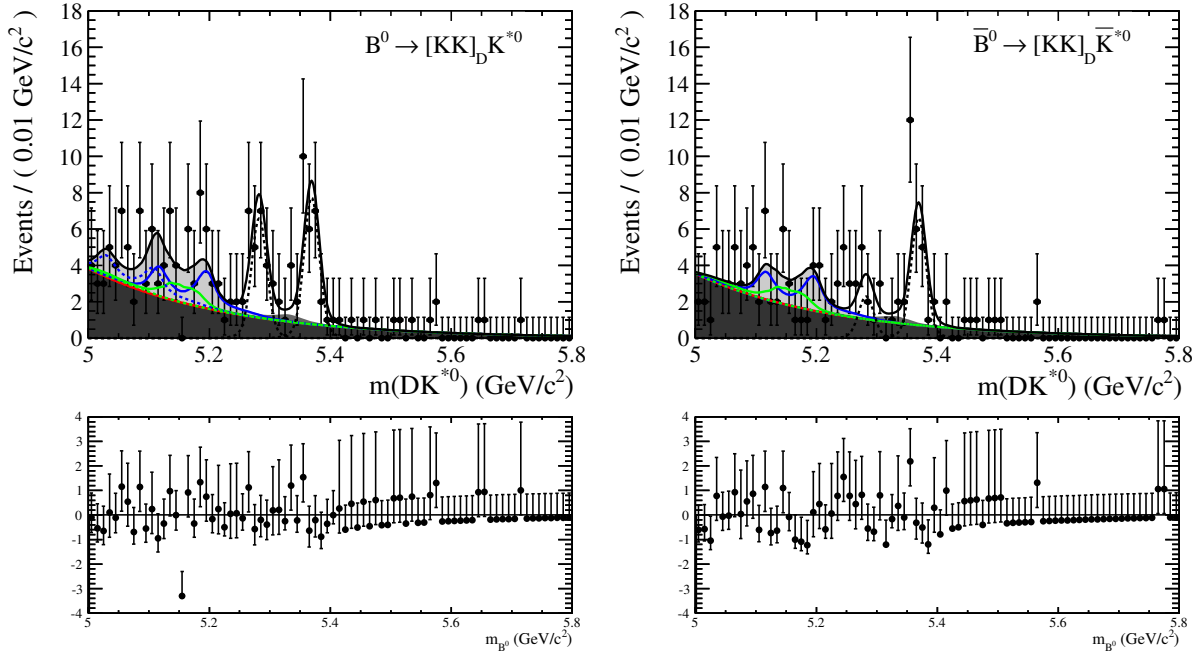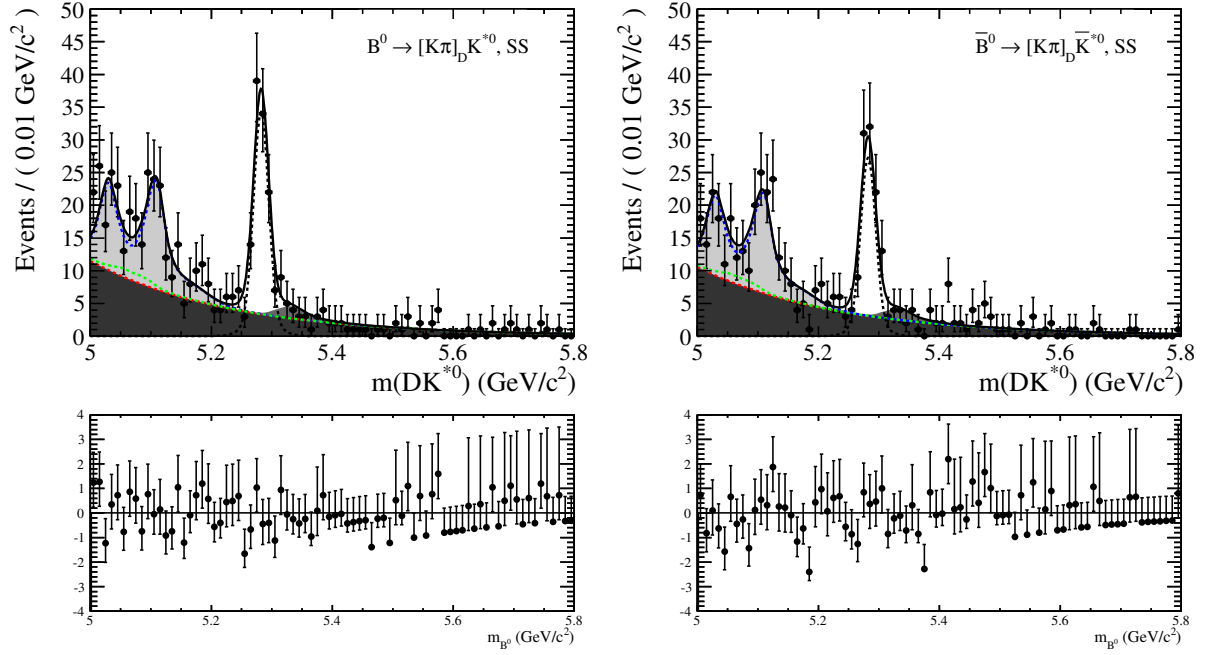
Figure 7: *Distribution de la masse invariante pour l'état $[K^+\pi^-]_D K^{*0}$ (gauche), correspondant à des candidats B^0 et $\overline{B}^0_s$, et $[K^-\pi^+]_D \overline{K}^{*0}$ (droite), correspondant à $\overline{B}^0$ et B^0_s. Les différentes contributions sont représentées comme dans la Figure 6.*

Avec 50 fb^{-1} de données que LHCb espère récolter à l'énergie nominale de collision du LHC et avec les futures améliorations du collisionneur et du détecteur, ces observables pourront être mesurés précisément pour introduire des contraintes sur l'angle γ de la théorie CKM. Avec l'étude des différents canaux de désintégration sensibles, LHCb envisage de produire une mesure combinée de γ avec une incertitude de l'ordre de 1°.

Figure 8: *Distribution de la masse invariante pour l'état $[K^-\pi^+]_D K^{*0}$ (gauche), correspondant à des candidats B^0 et $\overline{B}^0_s$, et $[K^+\pi^-]_D \overline{K}^{*0}$ (droite), correspondant à $\overline{B}^0$ et B^0_s. Les points noirs représentent les données, la ligne noire continue est le résultat de l'ajustement. Les différentes contributions sont visibles : le pic du signal est indiqué par une ligne noire pointillée, et les bruits de fond par les différentes zones grises qui sont, de la plus foncée à la plus claire, combinatoire, $B^0 \rightarrow D\rho^0$ erronément identifié, et $B^0_s \rightarrow D^*K^{*0}$ reconstruit partiellement à basse masse. Les lignes colorées représentent les différentes amplitudes d'hélicité qui contribuent au bruit à basse masse : rouge est "001", bleu est "010' ; les lignes continues correspondent au bruit du B^0_s, les lignes pointillées à celui du B^0. Les histogrammes du milieu représentent la différence entre les données et la fonction d'ajustement, divisée par l'incertitude sur le nombre d'entrées. Les histogrammes du bas présentent une échelle logarithmique pour l'axe vertical.*
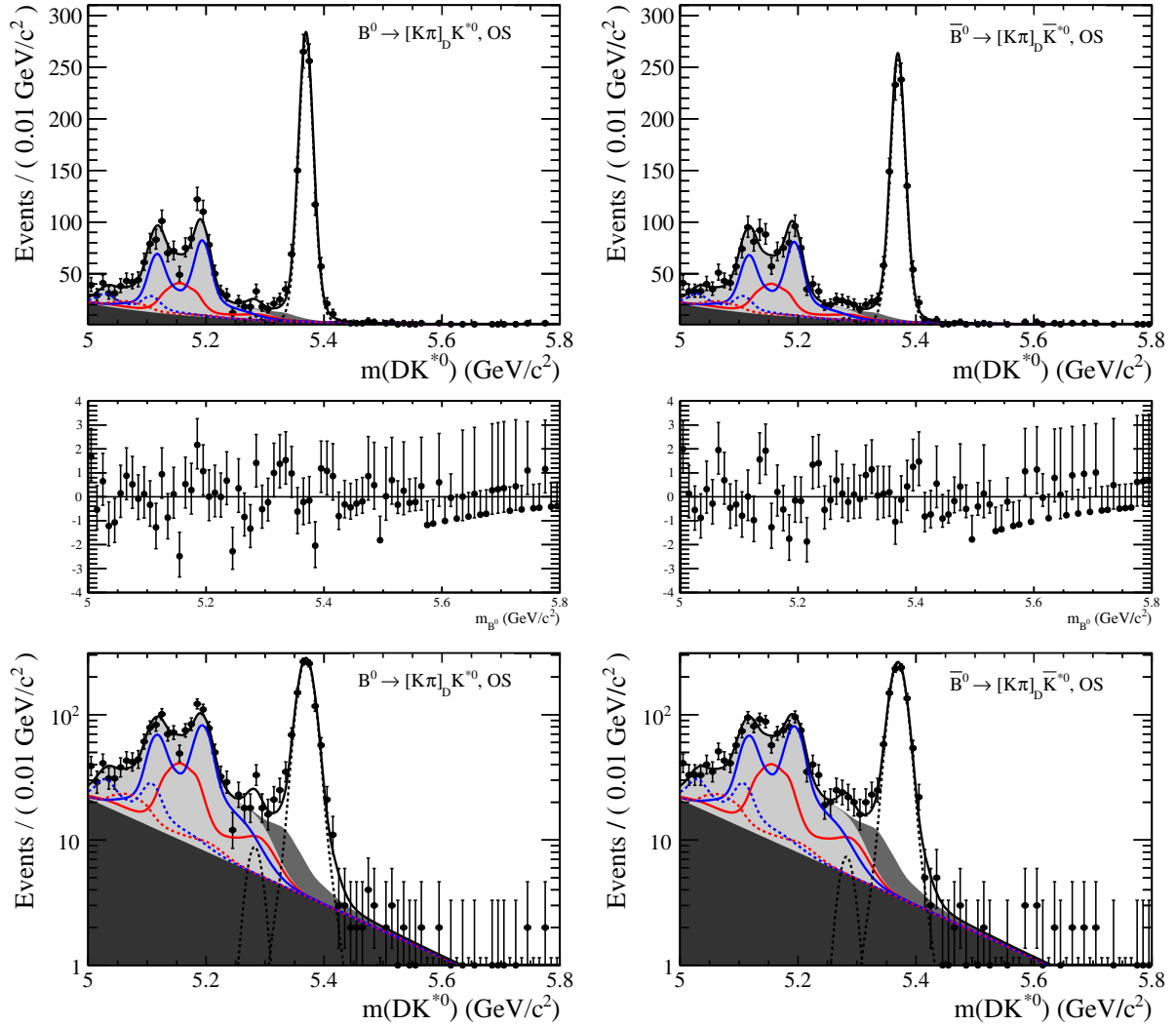
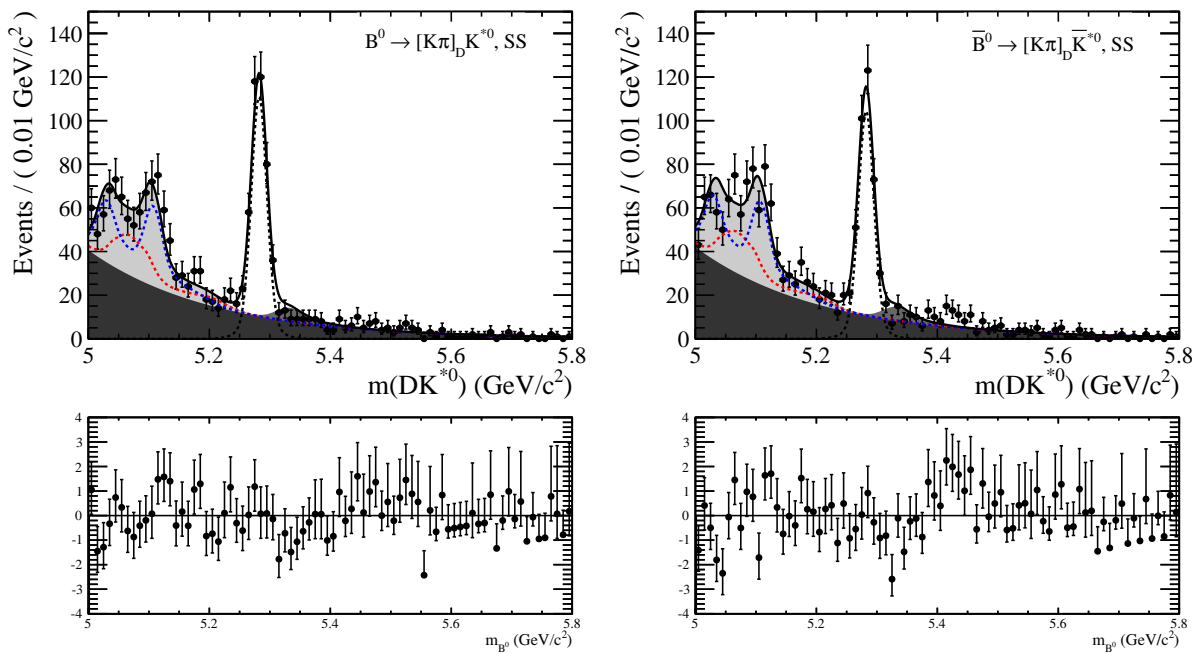Figure 9: *Distribution de la masse invariante pour l'état* $[K^+\pi^-]_D K^{*0}$ *(gauche), correspondant à des candidats* B^0 *et* $\overline{B}_s^0$, *et* $[K^-\pi^+]_D \overline{K}^{*0}$ *(droite), correspondant à* $\overline{B}^0$ *et* B_s^0. *Les différentes contributions sont représentées comme dans la Figure 8.*

Contents

Introduction

The current theory defining the fundamental structure of matter is the Standard Model of particle physics. This theory is parametrised by 18 quantities, corresponding to the mass of the particles and the couplings and constants characterising the interactions between them. The quark mixing effect, accounting for the fact that the quark mass eigenstates are different from the quark interaction eigenstates, is described inside the Standard Model framework by the Cabibbo-Kobayashi-Maskawa (CKM) matrix [27]. A Unitary Triangle can be extracted from this description. A great effort is being made by particle physics experiments in order to measure as precisely as possible the sides and angles of this triangle. Indeed, studying the Unitary Triangle is an excellent way of testing the consistency of the Standard Model, and to look for indications of new physics beyond it. The Standard Model and the CKM theory are described in Chapter 1.

We focus especially on one of the angles of the Unitary Triangle, the γ angle. While the other two are measured experimentally with a good precision, the uncertainty on the direct measurements of the γ angle is still large, of roughly $15°$. The latest experimental results are $\left(69^{+17}_{-16}\right)°$ from the BaBar experiment [38], $\left(68^{+15}_{-14}\right)°$ from Belle [39] and $(67 \pm 12)°$ from LHCb [40]. The combination of all measurements providing information on the sides and angles of the Unitary Triangle allows to extract a much more precise value of γ, with an uncertainty of a few degrees: the UTfit Collaboration obtains $(69.2 \pm 3.2)°$ [35], and the CKMfitter Collaboration $\left(67.7^{+4.1}_{-4.3}\right)°$ [36]. Experiments today are challenged to perform a precise measurement of the γ angle. This accomplishment will introduce new constraints to the Unitary Triangle and the Standard Model. In addition, an eventual inconsistency between this measurement and the result from the global combinations would open the door to physics beyond the Standard Model. The status of the measurements of the γ angle and the different methods to extract it are detailed in Chapter 2.

The Unitary Triangle involves b-physics. The LHCb experiment [69] at the LHC (CERN, Geneva) is very well suited for the study of decays involving heavy quarks, due not only to its special geometry, but also to the specific design of the different subdetectors. For instance, the silicon vertex detector allows to separate primary and secondary vertices with excellent precision, and the Ring Imaging Cherenkov detectors distinguish efficiently kaons from pions. In addition, the choice of operation conditions, that includes an instantaneous luminosity that keeps a low number of interactions per LHC bunch crossing, makes it possible to identify all the particles in the decay chain. This provides a very good scenario to perform precision measurements on the heavy flavour sector. The LHCb experiment has collected 1 fb^{-1} of proton-proton collision data at a center-of-mass energy of 7 TeV in the year 2011, and around 2 fb^{-1} at 8 TeV in 2012. The LHCb detector is described in Chapter 3.

A promising channel for the extraction of the γ angle is $\overline{B}^0 \to D\overline{K}^{*0}$, where D represents either a D^0 meson or a $\overline{D}^0$ decaying to a same final state. The time integrated study of the CP asymmetries between this decay and its charge conjugate can be done for different D decay modes, when the final state is accessible to both D^0 and $\overline{D}^0$. Sensitivity to γ arises then from

the interference of the $b \to u$ and $b \to c$ mediated amplitudes, through tree diagrams. No contributions from physics beyond the Standard Model are expected here. In this work, the CP-even final state $D \to K^+K^-$ is used, corresponding to the GLW approach to extract γ [45,46], as well as the flavour quasi-specific final state $D \to K^{\mp}\pi^{\pm}$, corresponding to the ADS approach [47]. The analyses performed during this thesis, leading to the first measurement of the CP observables from the two approaches in the $\overline{B}^0 \to D\overline{K}^{*0}$ channel, are presented in Chapters 5 and 6.

The $\overline{B}^0 \to D\overline{K}^{*0}$ mode is a purely hadronic decay. Many other decay channels under study at LHCb contain hadronic final states. However, a trigger system is needed in order to reduce the large LHC bunch crossing rate to a level that meets the storage requirements. The hardware hadronic trigger of LHCb allows to efficiently select this type of decays, by asking for high transverse momentum deposits in the calorimeters. The knowledge of the trigger efficiency is required in physics analysis. Chapter 4 presents a method for the computation of the hadronic trigger efficiencies in LHCb, for kaons and pions, and a study of the results is performed.

Chapter 1

Theoretical overview:
the Standard Model of particle physics

The Standard Model of particle physics is the theory that is currently accepted to describe the elementary blocks of matter building the Universe, together with their interactions. This model, which was introduced in the 70's, has proven to be outstandingly predictive, and some of its constituents have only been experimentally discovered decades later. However, several questions on the fundamental structure of matter are still open, and strong effort is being made to precisely measure all the parameters of the Standard Model, to further check its consistency and look for physics beyond.

This chapter introduces the fundamental interactions of Nature and the Standard Model of particle physics. Focus will be made on quarks, their interactions and the theory discribing the "heavy flavour sector" of particle physics: the Cabibbo-Kobayashi-Maskawa (CKM) matrix. These are the necessary bases leading to the parameter which is the ultimate subject of the analysis presented in this thesis: the γ angle of the CKM Unitary Triangle.

1.1   A subatomic particle classification

There are different possible ways of classifying the subatomic particles. Usually, particles are divided in groups of similar characteristics and behaviours by their spin. Particles with half-integer spin are fermions: they follow the Fermi-Dirac statistics and their quantum mechanics is described by the Dirac equation. Particles with integer spin are bosons: they follow the Bose-Einstein statistics and are described by the Klein-Gordon equation. The particles that carry the fundamental interactions are bosons. On the other hand, the fundamental matter particles, namely the quarks and the leptons, are fermions. Quarks are never observed individually, but they combine to form other particles that are called hadrons. These can be combinations of different numbers of quarks. Hadrons formed by a quark and an anti-quark are then bosons and are called mesons. Hadrons formed by three quarks or three anti-quarks are fermions, and are called baryons. This classification is summarised in Figure 1.1.

1.2   The fundamental interactions

There are four fundamental interactions applying to matter in the Universe: the gravitation, the strong interaction, the electromagnetic interaction and the weak interaction. Table 1.1 shows a
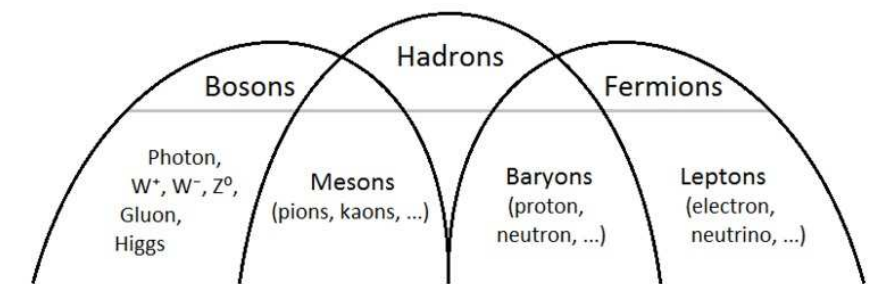
Figure 1.1: *Subatomic particles classification depending on their spin.*

force	relative strength	messenger	charge
gravitation	10^{-42}	(graviton)	mass
weak	10^{-5}	$W^{\pm}$ and Z^0 bosons	flavour
electromagnetic	10^{-2}	photon	electric charge
strong	1	gluons	colour

Table 1.1: *The four fundamental forces in Nature.*

comparison of the four of them regarding their typical strengths, and presents also their messenger particles[1] and their charges.

Gravitation is the weakest of the four interactions and, at the level of particle physics, this force does not play a role: the mass of the particles is so small that the gravitational forces between them are completely negligible. Another peculiarity of this interaction is that its messenger particle, the graviton, is for the moment only a prediction and has not been observed yet.

In the world of particle physics, the interactions that have an effect are the strong, the weak, and the electromagnetic ones. Furthermore, the weak and the electromagnetic interactions have been unified in the 70's, and are now described by a common theory. A short review of these three forces is presented in the following sections.

1.2.1 The strong interaction

The strong interaction acts on particles carrying a charge called "colour", that is to say the quarks. The typical times of strong interaction decays are 10^{-23} s. The messenger particles, the gluons, are massless but carry colour charge themselves, so they are also affected by the strong interaction. There are three possible values of the colour charge, and they are designated as red, green and blue. The colours and gluons are part of the Standard Model of particle physics and are described by a $SU(3)$ symmetry group. Eight different gluons can be formed in $SU(3)$, each one of them carrying a combination of a colour and an anti-colour.

The modern description of the strong interaction is given by Quantum Chromodynamics (QCD). Its running coupling becomes very large when the distance between the particles involved is large, and it is very small at short distance, where perturbative calculations can be made as an approximation. This translates into two features:

---

[1]The messenger of an interaction is the particle that "carries" the force and is exchanged between two other particles being affected by the interaction.

- Asymptotic freedom: the quarks interact very weakly as the energy increases and the distance decreases.

- Confinement: the strength of the strong force increases with the distance separating two quarks.

Confinement implies that the quarks are never observed individually. Instead, they form particles by combining in groups of two or three, in such a way that the result is colourless: groups of an anti-quark and a quark are possible when one carries the anti-colour of the other; groups of three quarks when each one of them carries a different colour (red + green + blue = white), and groups of three anti-quarks when each one carries a different anti-colour. When two quarks are brought away from each other, the energy between them becomes so large that new particles can be created that form new hadrons (but never individual quarks), in a process called hadronisation.

Strongly interacting hadrons can be organised in multiplets following the $SU(N)$ symmetry group of isospin, with N the number of quarks involved. The isospin I is a quantum number which is conserved by the strong interaction. Particles inside a multiplet are characterised by the isospin and the hypercharge Y, which is the sum of the baryonic number and the other quantum numbers describing the quark content of the particle (strangeness, charm, bottomness and topness). Different multiplets are built for different values of total angular momentum. The third component of the isospin explains the mass degeneration of particles with the same hypercharge in the same multiplet[2].

1.2.2   The electromagnetic interaction

Electromagnetism acts on particles carrying electromagnetic charge: the quarks and the charged leptons (electron, muon, tau). The typical lifetime of a particle decaying by this interaction is 10^{-20} s. The photon is the messenger particle, and is massless and electrically neutral. The electromagnetic interaction conserves the lepton number and the quark flavour, which means that a photon can only couple with leptons or quarks of the same type.

The modern theory describing the electromagnetic interaction is Quantum Electrodynamics (QED). It is characterised by a running coupling factor α which becomes smaller at high distance and low energy. Its asymptotic value is known as the fine structure constant for historical reasons, and it is equal to

$$\alpha \;=\; \frac{e^2}{4\pi\epsilon_0\hbar c} = \frac{1}{137}, \tag{1.1}$$

$$F \;=\; \frac{\alpha}{r^2} \tag{1.2}$$

where e is the electric charge of the electron, ϵ_0 is the vacuum permittivity, $\hbar$ is the reduced Planck constant and c is the speed of light. The electromagnetic force F is equal to this coupling divided by the square of the distance between the electrical charges involved, r.

1.2.3   The weak interaction: an introduction

Particles susceptible of interacting via the weak force are the quarks and all the leptons: all of them carry flavour charge. The typical lifetime of a particle decaying through weak interaction is of the order of 10^{-8} s, but it can be much larger or smaller. The messenger particles are the $W^{\pm}$

---

[2]For example, the proton and the neutron form an isospin doublet with $I = \frac{1}{2}$. They have common total angular momentum and parity $J^P = \frac{1}{2}^+$ and hypercharge $Y = 1$, but different isospin third component $I_3(p) = +\frac{1}{2}$ and $I_3(n) = -\frac{1}{2}$, such that their masses are different. In the same way, K^+ and K^0, with $J^P = 0^-$ form a different isospin doublet.

bosons for charged currents and the Z^0 boson for neutral currents. These bosons are massive: the $W^{\pm}$ has a mass of roughly 80 GeV/c^2, the Z^0 has a mass of around 91 GeV/c^2.

In 1932, Fermi [1] proposed a theory similar to electromagnetism to explain nuclear β-decays, where a neutron decays into a proton, an electron and an electronic antineutrino,

$$n \to p \; e^- \; \overline{\nu}_e, \tag{1.3}$$

or in its crossed form

$$p \; e^- \to n \; \nu_e. \tag{1.4}$$

He started from the expression in QED for an electron-proton scattering. The amplitude of this process is

$$
\begin{aligned}
\mathcal{M} &= (e\overline{u}_p\gamma^{\mu}u_p)\left(\frac{-1}{q^2}\right)(-e\overline{u}_e\gamma_{\mu}u_e) \tag{1.5} \\
&= -\frac{e^2}{q^2}(\overline{u}_p\gamma^{\mu}u_p)(-\overline{u}_e\gamma_{\mu}u_e) \tag{1.6} \\
&= -\frac{e^2}{q^2}(j^{em}_{\mu})_p(j^{em\;\mu})_e, \tag{1.7}
\end{aligned}
$$

where u is a Dirac spinor, γ^{μ} are the Dirac matrices, j^{em} are the electromagnetic currents and $(\frac{-1}{q^2})$ is the electromagnetic propagator of the exchanged photon, q^2 being its momentum. In an analogous way, he supposed a point interaction for the weak interaction,

$$\mathcal{M} = G_F(\overline{u}_n\gamma^{\mu}u_p)(\overline{u}_{\nu_e}\gamma_{\mu}u_e), \tag{1.8}$$

where G_F is the weak coupling factor and is called the Fermi constant. This equation follows a vector-vector structure.

This effective theory turned out to be a success at these energies, but it has also evolved to take into account larger energy scales and symmetry breaking issues, as is explained in the next section. The modern theory that describes this kind of interactions unifies the weak and the electromagnetic forces, and is explained in Section 1.5.

1.3 Symmetries and quantum number conservation

In particle physics, there are three discrete symmetries which are particularly important:

- Parity (P): space inversion, $P(\overrightarrow{r}; t) = (-\overrightarrow{r}; t)$. It corresponds to a reflexion with respect to a plane, followed by a rotation of 180° around an axis perpendicular to this plane.

- Charge conjugation (C): particle-antiparticle transformation, $C(p) = \overline{p}$.

- Time reversal (T): inversion of time, $T(\overrightarrow{r}; t) = (\overrightarrow{r}; -t)$. It swaps the initial and the final states.

The P and C transformations are unitary, while T is anti-unitary. The interest of them is that, while the combination of the three, CPT, is an exact symmetry in Nature [2], the individual transformations C and P are not conserved in the weak interaction, while they are in the strong and electromagnetic ones. The CP transformation, which combines the previous two and allows to go from a particle decay to an antiparticle decay, is also violated by the weak interaction. The CPT conservation law implies that T is also not conserved. These rules are shown in Table 1.2.

In addition to the symmetries, there are also quantum numbers that set selection rules for the different interactions. The total angular momentum J, the electromagnetic charge Q, the baryonic number B and the lepton number L are, as the energy, always conserved. Flavour is not conserved in weak interactions. Finally, the isospin I is only conserved in strong interaction. All of this is also summarised in Table 1.2.

symmetry or quantum number	strong int.	electromagnetic int.	weak int.
CPT	yes	yes	yes
P	yes	yes	no
C	yes	yes	no
CP or T	yes	yes	no
Q	yes	yes	yes
B	yes	yes	yes
L	yes	yes	yes
flavour	yes	yes	no
I	yes	no	no
J (total angular momentum)	yes	yes	yes

Table 1.2: *Conservation of symmetries or quantum numbers by the fundamental interactions in particle physics.*

1.4 Parity violation in weak interactions

In the 50's, two strange[3] particles were found with the same mass and lifetime but decaying through different modes,

$$\theta^+ \quad \rightarrow \quad \pi^+ \pi^0 \tag{1.9}$$
$$\tau^+ \quad \rightarrow \quad \pi^+ \pi^- \pi^+. \tag{1.10}$$

This is the so-called $\theta - \tau$ puzzle[4]. If, as believed at that time, parity was conserved in all interactions, the θ and τ particles would have different parity P, as inferred from their decay products. In 1956, Lee and Yang [3] came up with an easier solution: those two particles are actually the same one, the K meson, and parity is violated by the weak interaction.

Experiments were performed to confirm this idea. In 1957, C.S. Wu *et al.* [4] studied the β-transitions of polarised Cobalt nuclei,

$$^{60}\text{Co} \rightarrow^{60} \text{Ni}^* \ e^- \ \overline{\nu}_e. \tag{1.11}$$

The nuclear spins in the ^{60}Co sample were aligned by an external magnetic field. If parity was conserved, the electrons would be emitted in the same or the opposite direction to the nuclear spin in equal amounts. An asymmetry in the directions of the emitted electrons was observed, which changed sign upon reversal of the magnetic field. That is to say, electrons prefer to be emitted in a direction opposite to that of the nuclear spin. This implies that parity is violated in these decays.

Other experiments were performed on the same topic. In 1958, Goldhaber *et al.* [5] showed that neutrinos have left helicity, that is to say that there are no right-handed neutrinos (the inverse is true for antineutrinos). This automatically means that the weak interaction violates both P and C symmetries, and it only conserves CP, which transforms a left-handed neutrino into a right-handed antineutrino.

In order to take the parity violation into account, the Fermi theory needs to be slightly modified: in Equation (1.8), the γ^μ factors should be replaced by $\gamma^\mu(1 - \gamma^5)$. This means that the weak interaction does not follow a vector-vector structure, but a vector-axial (V-A)

---

[3]Containing a strange quark s. This property was discovered later, and it was named "strangeness" after the strange character of these $\theta - \tau$ particles.

[4]This τ particle does not have anything to do with the τ lepton, which was discovered decades later.

structure. This small modification is enough to include parity violation in weak interactions. Thus, the amplitude of a β-decay is described as

$$\mathcal{M} = \frac{G_F}{\sqrt{2}} [\overline{u}_n \gamma^\mu (1 - \gamma^5) u_p][\overline{u}_{\nu_e} \gamma_\mu (1 - \gamma^5) u_e], \tag{1.12}$$

where the factor $\frac{1}{\sqrt{2}}$ is added for normalisation purposes.

1.5   The electroweak interaction

Adding a propagator to the theory

The Equation (1.12), implementing the V-A structure in the weak interaction, can be further modified to move from a ponctual interaction to actual currents, produced by the exchange of the $W^\pm$ and Z^0 bosons. The Fermi constant G_F is thus replaced by a propagator. In the case of a charged current, the amplitude of the process becomes:

$$\mathcal{M} = \left(\frac{g}{\sqrt{2}} \overline{u}_n \gamma^\mu \frac{1}{2}(1 - \gamma^5) u_p \right) \frac{1}{M_W^2 - q^2} \left(\frac{g}{\sqrt{2}} \overline{u}_{\nu_e} \gamma_\mu \frac{1}{2}(1 - \gamma^5) u_e \right), \tag{1.13}$$

where g is a dimensionless coupling, M_W is the mass of the $W^\pm$ boson, q is the momentum carried by it and the factors $\frac{1}{2}$ are inserted for normalisation. The same strategy can be followed for neutral currents exchanging a Z^0 boson. The analogy between the Equations (1.13) and (1.5), where a massless photon is exchanged, is straightforward.

Now, we can compare Equations (1.12) and (1.13) in order to have a quantitative estimate of the coupling. In the case where the exchanged momentum is small, $q^2 \ll M_W^2$, that is to say when the weak currents interact essentially at a point, we find that G_F is related to the mass of the $W^\pm$ boson as

$$\frac{G_F}{\sqrt{2}} = \frac{g^2}{8M_W^2}. \tag{1.14}$$

This shows that the weak interactions are not weak because of the coupling g being small compared to the electromagnetic coupling e, but because the mass of the exchanged boson M_W^2 is large. Indeed, it is shown in the next section that essentially $g \approx e$, allowing the unification of the weak and electromagnetic forces.

The unification of electromagnetic and weak interactions

The electromagnetic and weak interactions are unified by defining a weak isospin and a weak hypercharge analogous to those of the strong interaction, proposed by Glashow in 1961 [6]. The result is a group of symmetry $SU(2)_L \times U(1)_Y$: the $SU(2)_L$ is the symmetry group for the weak isospin involving only left-handed states, while $U(1)_Y$ corresponds to the weak hypercharge Y group, involving left- and right-handed states; this incorporates the electromagnetic interaction to the weak interaction. The theory was extended by Weinberg in 1967 [7] and Salam in 1968 [8] to accomodate the massive vector bosons $W^\pm$ and Z^0.

As seen before, the electromagnetic current couples to a photon, and the weak currents couple also to vector bosons. This is implemented in the model by a triplet of vector fields W_μ^i coupled with strength g to the weak isospin current J_μ^i, together with a single vector field B_μ coupled to the weak hypercharge j_μ^Y with strength conventionally taken as $g'/2$. The W_μ^i and B_μ fields are gauge bosons. The basic electroweak interaction operator is therefore

$$- ig(J^i)^\mu W_\mu^i - i\frac{g'}{2}(j^Y)^\mu B_\mu. \tag{1.15}$$

In this representation, the massive $W^\pm$ bosons exchanged in the charged weak currents, the Z^0 boson in the neutral weak current and the photon in the electromagnetic current (denoted in the literature by A) are described by the following fields:

$$W_\mu^\pm = \sqrt{\frac{1}{2}}(W_\mu^1 \mp iW_\mu^2) \tag{1.16}$$

$$Z_\mu = -B_\mu \sin\theta_W + W_\mu^3 \cos\theta_W \tag{1.17}$$

$$A_\mu = B_\mu \cos\theta_W + W_\mu^3 \sin\theta_W, \tag{1.18}$$

where θ_W is the Weinberg or weak mixing angle.

The electroweak neutral interaction coupling between currents and exchanged bosons is therefore

$$
\begin{aligned}
-igJ_\mu^3(W^3)^\mu \quad - \quad & i\frac{g'}{2}j_\mu^Y B^\mu = \\
- \quad & i\left(g\sin\theta_W J_\mu^3 + g'\cos\theta_W \frac{j_\mu^Y}{2}\right) A^\mu \\
- \quad & i\left(g\cos\theta_W J_\mu^3 - g'\sin\theta_W \frac{j_\mu^Y}{2}\right) Z^\mu,
\end{aligned}
\tag{1.19}
$$

where the first term corresponds to the electromagnetic interaction and the second to the weak neutral interaction. In order to recover the electromagnetic interaction with coupling e, we find that

$$g\sin\theta_W = g'\cos\theta_W = e. \tag{1.20}$$

This equation gives the unification of the electroweak theory, through the Weinberg angle.

To complete the description of the theory in the conventional way, let us recall the relation given by Equation (1.14)

$$\frac{G_F}{\sqrt{2}} = \frac{g^2}{8M_W^2} \tag{1.21}$$

between the mass of the $W^\pm$ boson, the weak coupling g and the Fermi constant G_F. This expression was found by comparing the Fermi phenomenological model to the weak charged interaction including a $W^\pm$ propagator. The same can be done with neutral currents exchanging a Z^0 boson, finding the relation

$$\frac{M_W^2}{M_Z^2 \cos^2\theta_W} = 1 \tag{1.22}$$

between the masses of the weak bosons and the Weinberg angle. Equations (1.20), (1.21) and (1.22) describe and constrain the theory, and involve some of the parameters of the Standard Model of particle physics.

1.6 The Standard Model

The Standard Model of particle physics is described by a $SU(2)_L \times U(1)_Y \times SU(3)$ gauge symmetry: $SU(2)_L$ corresponding to the weak isospin involving left-handed particles, $U(1)_Y$ for the weak hypercharge, and the $SU(3)$ colour symmetry group. This structure implies that left-handed particles form doublets, right-handed ones form singlets and there is no right-handed neutrino. Table 1.3 shows the classification of the Standard Model particles of the first families and their quantum numbers.

quantum number	quarks				leptons		
	u_L	d_L	u_R	d_R	e_L^-	ν_e	e_R^-
Q	2/3	-1/3	2/3	-1/3	-1	0	-1
Y	1/3	1/3	4/3	-2/3	-1	-1	-2
I_3	1/2	-1/2	0	0	-1/2	1/2	0

Table 1.3: *Quantum numbers for the Standard Model quarks and leptons of the first families. Q is the electromagnetic charge, Y the weak hypercharge and I_3 the weak isospin third component.*

families	quarks			leptons		
	I	II	III	I	II	III
fermions (matter)	$\begin{pmatrix} u \\ d \end{pmatrix}$	$\begin{pmatrix} c \\ s \end{pmatrix}$	$\begin{pmatrix} t \\ b \end{pmatrix}$	$\begin{pmatrix} e \\ \nu_e \end{pmatrix}$	$\begin{pmatrix} \mu \\ \nu_\mu \end{pmatrix}$	$\begin{pmatrix} \tau \\ \nu_\tau \end{pmatrix}$
gauge bosons (interactions)	$g, \gamma, W^\pm, Z^0$					
Higgs boson	H					

Table 1.4: *The Standard Model particles.*

The particles contained in the Standard Model are summarised in Table 1.4. The fermionic matter particles are the quarks and the leptons, which are in both cases arranged in three generations or families of increasing mass. The six quarks are massive and are called *up*, *down*, *charm*, *strange*, *top* and *bottom*. Each family of leptons contains a massive particle, namely the *electron*, the *muon* or the *tau*, and its corresponding massless *neutrino*[5]. The gauge bosons carrying the interactions, as seen in the previous sections, are the photon γ, the gluons g, and the $W^\pm$ and Z^0 bosons. The masses and other characteristics of the Standard Model particles are shown in Figure 1.2. In addition to these particles, another one has been predicted and recently confirmed to exist, the Higgs boson, which "gives the mass to the particles" and is presented in Section 1.7.

There are 18 free parameters in the Standard Model. First, there are 9 masses for the 9 massive fermions (6 quarks and 3 leptons). The quark mixing, which is explained in Section 1.9, adds 4 parameters. The interactions add a few parameters to the theory. We have the strong coupling constant α_s. From Equations (1.20), (1.21) and (1.22), another 3 parameters at choice are needed for the electroweak sector, for example e, G_F and θ_W. Finally, the mass of the Higgs boson m_H completes the set of Standard Model parameters. The Standard Model Lagrangian can be written in a general way as

$$
\begin{aligned}
\mathcal{L} \;=\; & -\frac{1}{4} W_{\mu\nu} \cdot W^{\mu\nu} - \frac{1}{4} B_{\mu\nu} B^{\mu\nu} \\
& + \overline{L}\gamma^\mu \left(i\partial_\mu - g\frac{1}{2}\tau \cdot W_\mu - g'\frac{Y}{2}B_\mu \right) L + \overline{R}\gamma^\mu \left(i\partial_\mu - g'\frac{Y}{2}B_\mu \right) R \\
& + \left| \left(i\partial_\mu - g\frac{1}{2}\tau \cdot W_\mu - g'\frac{Y}{2}B_\mu \right) \phi \right|^2 - V(\phi) \\
& - (G_1 \overline{L}\phi R + G_2 \overline{L}\phi_c R + \text{hermitian conjugate}),
\end{aligned}
\tag{1.23}
$$

where τ represents the Pauli matrices and ϕ is the Higgs doublet (see Section 1.7). The first line gives the kinetic energies and self-interaction of the gauge bosons, the second gives the lepton

---

[5]Neutrino oscillations have been observed and would imply that neutrinos do have masses, even if very small compared to the other particles in the Standard Model. There is discussion on the fact of massive neutrinos being inside the Standard Model, or beyond.

Figure 1.2: *The Standard Model of particle physics. The Higgs boson, whose existence has been recently confirmed, is missing from this list.*

and quark kinetic energies and their interactions, the third gives the gauge boson and Higgs masses and couplings, and the fourth gives the lepton and quark masses and couplings to the Higgs boson (L denotes a left-handed fermion doublet, R a right-handed fermion singlet).

1.7 The Higgs boson

The probably most important open question about the Standard Model is how particles acquire their mass. We know experimentally that the quarks, the three charged leptons and the weak interaction vector bosons are massive, but the Standard Model Lagrangian describing the theory does not provide the corresponding terms. Dirac mass terms for fermions, with the structure

$$m\overline{\psi}\psi = m(\overline{\psi}_R\psi_L + \overline{\psi}_L\psi_R), \tag{1.24}$$

are not gauge invariant: left-handed fermions form doublets, while right-handed ones form singlets, so terms of this type break the symmetry of the Lagrangian. A similar problem appears for the gauge bosons.

The Higgs mechanism provides a way to overcome this problem. It generates gauge invariant mass terms through spontaneous symmetry breaking of the $SU(2) \times U(1)$ symmetry of the Standard Model Lagrangian. Let us take the Lagrangian,

$$\begin{aligned} \mathcal{L} &= (\partial_\mu\phi)^\dagger(\partial^\mu\phi) - V(\phi) \\ &= (\partial_\mu\phi)^\dagger(\partial^\mu\phi) - \mu^2\phi^\dagger\phi - \lambda(\phi^\dagger\phi)^2 \end{aligned} \tag{1.25}$$

which preserves the Standard Model symmetry, where ϕ is a $SU(2)$ doublet of complex scalar fields, μ represents the mass of the field when $\mu^2 > 0$ and $\lambda > 0$ is the coupling of a four-particle

1. THEORETICAL OVERVIEW:
THE STANDARD MODEL OF PARTICLE PHYSICS

vertex. We are interested in the case where $\mu^2 < 0$. The potential $V(\phi)$ has its minimum for values of ϕ such that

$$\phi^\dagger \phi = -\frac{\mu^2}{2\lambda}. \tag{1.26}$$

This represents a group of points invariant under $SU(2)$ transformations[6], thus the ground state is degenerate. One of these minima is chosen as the vacuum of the theory without loss of generality, as any other can be reached by a simple gauge transformation,

$$\phi_0 = \sqrt{\frac{1}{2}} \begin{pmatrix} 0 \\ v + H(x) \end{pmatrix}, \tag{1.27}$$

where v is the vacuum expectation value and $H(x)$ is a perturbative expansion around this minimum value. This field does not hold anymore the Standard Model symmetries. Choosing this particular field configuration out of the degeneration of the ground state is a spontaneous symmetry breaking, as the symmetry becomes hidden. Substituting this into the Lagrangian, we find that $H(x)$ represents a scalar field, the Higgs field. It introduces gauge invariant mass terms for the fermions and weak bosons, together with a scalar boson, the Higgs particle.

Precisely for the quarks and leptons, if we take the electron as an example, the following terms appear in the Standard Model Lagrangian

$$
\begin{aligned}
&- \quad G_e \left[(\overline{\nu}_e, \overline{e})_L \begin{pmatrix} \phi^+ \\ \phi^0 \end{pmatrix} e_R + \overline{e}_R (\phi^-, \overline{\phi}^0) \begin{pmatrix} \nu_e \\ e \end{pmatrix}_L \right] \\
&= \quad - \quad \frac{G_e}{\sqrt{2}} v (\overline{e}_L e_R + \overline{e}_R e_L) - \frac{G_e}{\sqrt{2}} (\overline{e}_L e_R + \overline{e}_R e_L) H \\
&= \quad - \quad m_e \overline{e} e - \frac{m_e}{v} \overline{e} e H,
\end{aligned} \tag{1.28}
$$

where G_e is an arbitrary constant, as the mass of the electron is not predicted. We see that a mass term is present, with $m_e = \frac{G_e v}{\sqrt{2}}$, together with an interaction term between the electron and the Higgs scalar, with coupling $\frac{m_e}{v}$. Thus, the Higgs couples to the fermions proportionally to their masses. Similar terms appear in the Lagrangian for the other fermions. For the vector bosons, we get

$$\left(\frac{1}{2} v g \right)^2 W_\mu^+ W^{-\mu} + \frac{1}{8} v^2 \left[g W_\mu^3 - g' B_\mu \right]^2 + m_\gamma \left[g' W_\mu^3 + g B_\mu \right]^2, \tag{1.29}$$

together with their coupling to the Higgs. The mass of the $W^\pm$ bosons appears as $m_W = \frac{1}{2} v g$, and the mass of the Z^0 boson as $m_Z = \frac{1}{2} v \sqrt{g^2 + g'^2}$. A massless term is obtained for the photon, as its mass factor becomes $m_\gamma = 0$.

In this way, the Higgs boson provides the theory with gauge invariant mass terms. The fermion masses are free parameters of the theory. In addition, a term appears for the Higgs mass or self-coupling, with $m_H = \sqrt{2v^2\lambda}$. The mass of the Higgs is also unknown, adding another free parameter.

The Higgs mechanism and the Higgs boson were predicted in 1964 by three groups of physicists: F. Englert and R. Brout [9]; P. Higgs [10,11]; G. Guralnik, C. Hagen and T. Kibble [12]. Almost 50 years later, results of an indication of this particle has been released by the ATLAS and CMS Collaborations in July 2012, with 12 fb^{-1} of data from the LHC proton-proton collisions collected in 2011 and 2012 [13,14]. A particle with the Higgs characteristics, decaying

---

[6]When $\mu^2 > 0$, only a minimum is found. Taking $\mu^2 < 0$ gives a degeneration of minima, and enables the sponateous symmetry breaking mechanism.

to the predicted channels most favoured at the LHC, has been detected, with a mass of around 125 GeV/c^2. In March 2013 new results have been presented, showing that the total angular momentum and parity of the observed particle seem to be those of the predicted Higgs boson, $J^P = 0^+$, confirming its existence. Nevertheless, efforts still need to be made in order to measure additional properties of this particle, to be able to confirm that it is actually the predicted Higgs boson in the Standard Model, or a light Higgs boson from theories beyond. In any case, the Higgs mechanism enforces the validity of the Standard Model and the great predictive strength of the physics theories of the last century.

1.8 Building the Standard Model: a historical approach

In 1897 the electron was discovered by J.J. Thomson [15]. The other subatomic particles followed: the proton was discovered in 1919 by E. Rutherford, and the neutron in 1932 by J. Chadwick [16]. These discoveries showed that there was a structure inside the atom, and even inside its nucleus. The positron was also discovered at that time, in 1933 by C.D. Anderson [17], who also discovered the muons and antimuons in 1936 [18].

The π, which was predicted by H. Yukawa in 1935 [19] as the messenger particle for the strong interaction, was first seen in 1947. The picture of subatomic particles began to get complicated, as new particles started to flow from this year on. Also in 1947, the K meson and the Λ baryon were discovered in cosmic rays. These particles were "strange", as they were produced by strong interaction (as copiously as the π) but were decaying with very long lifetimes, of the order of 10^{-10} s, that is to say by weak interaction. There should be a reason that forbids their decay through strong interaction. A new additive quantum number was introduced in order to explain this effect, the "strangeness", which would be conserved in strong interactions but violated in weak interactions. In the following years, new particles appeared with these same characteristics, such as the Σ and the Ξ. All observed particles were classified in a $SU(3)$ isospin symmetry group. To complete the isospin multiplet, another particle was predicted, the Ω, discovered in 1964.

The large number of particles already seen was an indication that these particles could not be fundamental, or at least not all of them. The quark representation was proposed by Gell-Mann [20] and Zweig [21] in 1964: the quarks u and d would form an isospin doublet, while the s would be a singlet. In this way, the u and d quarks could interact together, but not with the s singlet. This was proved to be wrong with the observation of the decay $K^- \to \mu^- \ \overline{\nu}_\mu$, where two quarks s and $\overline{u}$ in the initial state give no quarks in the final state, and thus interact with each other.

The mixing of quarks was then introduced by N. Cabibbo in 1963 [22]. He proposed a rotation of the d and s states, in such a way that, when they interact, the quarks are u, d' as a doublet and s' as a singlet,

$$\begin{pmatrix} d' \\ s' \end{pmatrix} = \begin{pmatrix} \cos\theta_C & \sin\theta_C \\ -\sin\theta_C & \cos\theta_C \end{pmatrix} \begin{pmatrix} d \\ s \end{pmatrix} = \begin{pmatrix} d\cos\theta_C + s\sin\theta_C \\ -d\sin\theta_C + s\cos\theta_C \end{pmatrix} \tag{1.30}$$

where θ_C is the Cabibbo angle, with $\theta_C \sim 13°$. The interaction between the u and s quarks is then allowed, with coupling $G_F \sin\theta_C$, which is smaller than the coupling between the u and d quarks $G_F \cos\theta_C$. The $u-d$ transitions are then "Cabibbo favoured", while the $u-s$ are "Cabibbo suppressed". Thus weak interaction in the quark sector is non-universal, but the couplings depend on the quarks involved. The Cabibbo rotation indicates that the mass eigenstates are not the same than the weak interaction eigenstates in the quark sector.

This idea introduced a new problem. The allowed couplings for neutral currents between the proposed states are

$$u\overline{u} + d\overline{d}\cos^2\theta_C + s\overline{s}\sin^2\theta_C + (d\overline{s} + \overline{d}s)\cos\theta_C\sin\theta_C, \tag{1.31}$$

that is to say, this theory predicts flavour changing neutral currents, as transitions between the d and s quarks, which were not observed experimentally. In 1970, the Glashow-Iliopoulos-Maiani (GIM) mechanism [23] was introduced, which proposes a fourth quark c forming a doublet with the s quark. Thus two quark families exist, (u, d) and (c, s) with interaction eigenstates

$$\begin{pmatrix} u \\ d\cos\theta_C + s\sin\theta_C \end{pmatrix}, \begin{pmatrix} c \\ s\cos\theta_C - d\sin\theta_C \end{pmatrix}. \tag{1.32}$$

Now, the neutral couplings become

$$\begin{aligned} u\bar{u} + d\bar{d}\cos^2\theta_C + s\bar{s}\sin^2\theta_C &\quad + \quad (d\bar{s} + \bar{d}s)\cos\theta_C\sin\theta_C + \\ c\bar{c} + s\bar{s}\cos^2\theta_C + d\bar{d}\sin^2\theta_C &\quad - \quad (d\bar{s} + \bar{d}s)\cos\theta_C\sin\theta_C \\ = u\bar{u} + d\bar{d} &+ c\bar{c} + s\bar{s}, \end{aligned} \tag{1.33}$$

and the flavour changing neutral currents (FCNC) are forbidden. The c quark was discovered almost at the same time at Brookhaven National Laboratory and SLAC in 1974 [24,25], seen as the J/ψ resonance[7] decaying to an electron-positron pair.

The third family of quarks (t b) was predicted to accomodate the CP violation seen in the K sector in 1964. The K^0 meson is a mixing of two CP eigenstates, the CP-even K_S^0 and the CP-odd K_L^0. From their CP eigenvalues, assuming CP symmetry in weak interactions, these particles are expected to decay as $K_S^0 \rightarrow \pi\pi$ and $K_L^0 \rightarrow \pi\pi\pi$, where the first one has a shorter lifetime than the second one due to the available phase space. Christenson *et al.* [26] performed an experiment that studied the angular distribution of the K_L^0 decay products and were able to observe the $K_L^0 \rightarrow \pi\pi$ mode, which implies a CP violation in K_L^0 weak decays. Thus the CP symmetry was found to be not conserved in the weak interaction.

The CP violation means that a particle and its antiparticle do not decay in the same way, which implies that a complex phase is present in the decay amplitudes. The Cabibbo rotation matrix is a unitary 2×2 matrix, which can be parametrised by one angle. An additional dimension is needed: a unitary 3×3 matrix can be parametrised by three angles and an irreducible complex phase. That is to say, in order to allow CP violation, 3 families of quarks must exist. This idea was first introduced by M. Kobayashi and T. Maskawa in 1973 [27]. The third family of quarks was directly observed in 1977, with the b quark discovery at Fermilab as the Υ resonance [28]. The t quark, which is the heaviest one and decays before hadronising, was first seen in 1994 [29] by the CDF and D0 Collaborations.

The rotation matrix is in the three family scenario replaced by the Cabibbo-Kobayashi-Maskawa (CKM) matrix, which is described in the next section. It is worth noting that mixing also happens in the neutrino sector. The corresponding matrix is the Pontecorvo-Maki-Nakagawa-Sakata (PMNS) matrix, and it explains the phenomenon of neutrino oscillations [30–32]. If the complex phase of the PMNS matrix is found to be different from zero, it will imply that CP violation also occurs in the neutrino sector.

1.9 The CKM mechanism

The charged weak interaction currents, mediated by $W^{\pm}$ vector bosons, are present in the Standard Model Lagrangian as

$$-\frac{g}{\sqrt{2}} \left(\bar{u}_L, \bar{c}_L, \bar{t}_L \right) \gamma^{\mu} W_{\mu}^{+} V_{CKM} \begin{pmatrix} d_L \\ s_L \\ b_L \end{pmatrix} + \text{hermitian conjugate.} \tag{1.34}$$

---

[7]This new resonance was called J at Brookhaven and ψ at SLAC, so the two names were retained.

The mixing of quarks is taken into account by the factor V_{CKM}. The quark mixing between the three Standard Model families is described by the Cabibbo-Kobayashi-Maskawa (CKM) matrix [27],

$$V_{CKM} = \begin{pmatrix} V_{ud} & V_{us} & V_{ub} \\ V_{cd} & V_{cs} & V_{cb} \\ V_{td} & V_{ts} & V_{tb} \end{pmatrix}. \tag{1.35}$$

It represents the change of basis between the quark interaction eigenstates and the quark mass eigenstates. This is a 3×3 matrix that can be parametrised by three angles and one complex phase. The standard parametrisation of this matrix, which is the product of three 3×3 matrix, each one of them representing a 2×2 rotation including a complex phase, is

$$
\begin{aligned}
V &= \begin{pmatrix} c_{12} & s_{12}e^{i\delta} & 0 \\ -s_{12}e^{-i\delta} & c_{12} & 0 \\ 0 & 0 & 1 \end{pmatrix} \times \begin{pmatrix} 1 & 0 & 0 \\ 0 & c_{23} & s_{23}e^{i\delta} \\ 0 & -s_{23}e^{-i\delta} & c_{23} \end{pmatrix} \times \begin{pmatrix} c_{13} & 0 & s_{13}e^{i\delta} \\ 0 & 1 & 0 \\ -s_{13}e^{-i\delta} & 0 & c_{13} \end{pmatrix} \\
&= \begin{pmatrix} c_{12}c_{13} & s_{12}c_{13} & s_{13}e^{i\delta} \\ -s_{12}c_{23}-c_{12}s_{23}s_{13}e^{i\delta} & c_{12}c_{23}-s_{12}s_{23}s_{13}e^{i\delta} & s_{23}c_{13} \\ s_{12}s_{23}-c_{12}s_{23}s_{13}e^{i\delta} & -s_{23}c_{12}-s_{12}c_{23}s_{13}e^{i\delta} & c_{23}c_{13} \end{pmatrix},
\end{aligned} \tag{1.36}
$$

where $s_{ij} = \sin\theta_{ij}$ and $c_{ij} = \cos\theta_{ij}$, with $i, j = 1, 2, 3$ and $i \neq j$. The θ_{ij} factors are the three angles of the parametrisation, and δ is the irreducible complex phase.

The angle θ_{12} can be identified with the Cabibbo angle, responsible of the $u - s$ quark mixing, with $s_{12} = 0.22$. Experimentally, the two other angles are found to be smaller than this one, $s_{23} \sim 10^{-2}$ corresponding to the $c - b$ mixing and $s_{13} \sim 10^{-3}$ for the $u - b$ mixing, with $c_{23} \sim c_{13} \sim 1$. To better state the order of magnitude of each matrix element and of the implied quark couplings, another representation is more commonly used. In 1983, L. Wolfenstein proposed a parametrisation [33],

$$V = \begin{pmatrix} 1 - \frac{\lambda^2}{2} & \lambda & A\lambda^3(\rho - i\eta) \\ -\lambda & 1 - \frac{\lambda^2}{2} & A\lambda^2 \\ A\lambda^3(1 - \rho - i\eta) & -A\lambda^2 & 1 \end{pmatrix} + \mathcal{O}(\lambda^4), \tag{1.37}$$

where the real parameters are now λ, A and ρ and the imaginary part is represented by η. This matrix is built by expanding each element as a power series in $\lambda \equiv |V_{us}| \sim \sin\theta_C$. The λ parameter states the relative strength of the interactions between the different families: the diagonal elements are of the order of 1, for transitions inside the same family; the elements involving the first and the second family are of the order of λ, the second and third families go as λ^2 and the first and third family as λ^3. This is also illustrated in Figure 1.3.

The other parameters in the matrix are so that each element agrees with the experimental observations. The important role of b-physics to constrain the CKM matrix appears already at this level: while the mixing between the first and second family only involves the Cabibbo angle, thus the λ parameter, the elements involving the third family are constrained by B hadron decays, for V_{xb} elements, or B hadron oscillations (that imply t quarks in box diagrams) for V_{tx} elements.

The CKM matrix is a rotation of eigenstates, so it is required to be unitary, that is to say to verify

$$VV^\dagger = V^\dagger V = \mathbb{I}. \tag{1.38}$$

Nine relations between CKM matrix elements can be extracted, three of which are equal to 1 corresponding to the diagonal of the matrix product, and six equal to 0 for the non-diagonal. These complex equations equal to 0 can be represented as triangles in the (ρ, η) complex plane,
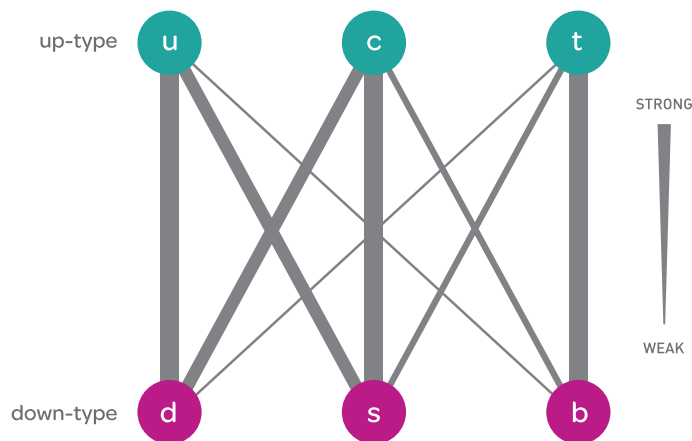
Figure 1.3: *Quark mixing in weak interactions. The strength of the interactions between each pair of families is indicated by the scale.*

and their area quantifies the amount of CP violation in the quark sector. In particular, two of them have all their terms of the same order λ^3 and result in non-flat triangles. One of these two equations involves B physics[8], as the b quark is present in all the terms,

$$V_{ud}V_{ub}^* + V_{cd}V_{cb}^* + V_{td}V_{tb}^* = 0. \tag{1.39}$$

Making a transformation of coordinates $\overline{\rho} = (1 - \lambda^2/2)\rho$, $\overline{\eta} = (1 - \lambda^2/2)\eta$, and normalising to the term $|V_{cd}V_{cb}^*|$, the resulting triangle in the $(\overline{\rho}, \overline{\eta})$ complex plane is represented in Figure 1.4.
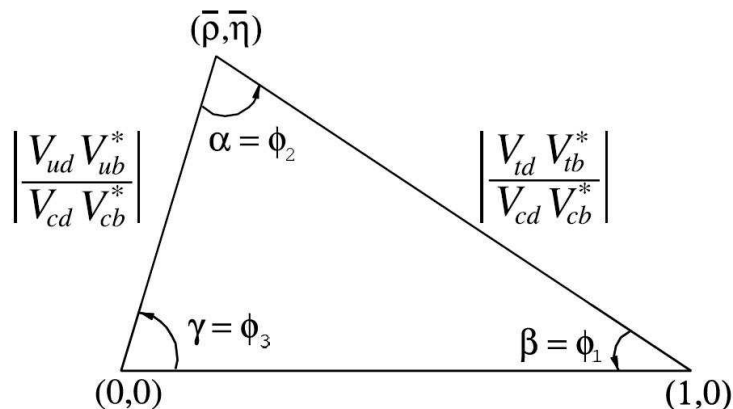
Figure 1.4: *The Unitary Triangle of the CKM mechanism.*

This triangle is known as the Unitary Triangle of the CKM mechanism. Its angles are labelled in the literature as $\phi_{1,2,3}$ or α, β and γ. The fact that this triangle involves CKM elements corresponding to the b quark states again the relevance of b-physics in the study of the CKM matrix. The $\left|\frac{V_{ud}V_{ub}^*}{V_{cd}V_{cb}^*}\right|$ side in Figure 1.4 can be measured using B decays, while the $\left|\frac{V_{td}V_{tb}^*}{V_{cd}V_{cb}^*}\right|$

---

[8]The other equation is $V_{td}V_{ud}^* + V_{ts}V_{us}^* + V_{tb}V_{ub}^* = 0$, and involves "top" physics, thus it is significantly more difficult to study, as the t quark is very heavy and decays before hadronising. However, there is another relation, $V_{ub}V_{us}^* + V_{cb}V_{cs}^* + V_{tb}V_{ts}^* = 0$, where the two last terms are of order λ^2 and the first one λ^4. This relation involves B_s^0 physics, and the triangle that can be built from it is also studied in current experiments.

side involves $B^0 - \overline{B}^0$ oscillations. The angles are defined as

$$\alpha = \text{Arg} \left(-\frac{V_{td}V_{tb}^*}{V_{ud}V_{ub}^*} \right), \tag{1.40}$$

$$\beta = \text{Arg} \left(-\frac{V_{cd}V_{cb}^*}{V_{td}V_{tb}^*} \right),$$

$$\gamma = \text{Arg} \left(-\frac{V_{ud}V_{ub}^*}{V_{cd}V_{cb}^*} \right).$$

It should be noted that in the CKM matrix only V_{ub} and V_{td} are complex (when we use the Wolfenstein parametrisation given by Equation (1.37)). These two elements are present in the expression of each one of the angles, which are measured precisely through CP violating decays.

Effort is currently made in particle physics to measure the sides and the angles of the Unitary Triangle, in order to constrain it as much as possible. If eventually all the measurements do not converge in a closed triangle, this will be an indication of physics beyond the Standard Model. The subject of this thesis is the measurement of the $\overline{B}^0 \to D\overline{K}^{*0}$ decay[9], where the interference between $b \to u$ (CKM suppressed) and $b \to c$ (CKM favoured) mediated amplitudes induces sensitivity to the γ angle of the CKM Unitary Triangle. This angle is also called the weak phase γ. Quantifying the CP violation in this decay provides valuable information that, if large statistics are available, can be used together with other sensitive decays to extract a measurement of the γ angle.

---

[9]Charge conjugation is implied throughout this document unless otherwise stated.

Chapter 2

Towards a measurement of the CKM weak phase γ from $\overline{B}^0 \to D\overline{K}^{*0}$ decays. Experimental status

The γ angle of the CKM Unitary Triangle is one of the Standard Model parameters which is less well constrained. In order to verify the consistency of the Standard Model and of the CKM mechanism, the Unitary Triangle needs to be measured accurately. Effort is being made nowadays in particle physics to improve the precision on the γ angle measurement and to check its compatibility with the value that can be extracted from global fits. Using tree-level diagrams allows to measure γ inside the Standard Model, avoiding the effect of eventual new physics contributions, which can appear at the loop-level.

The LHCb experiment is designed to perform measurements of the CKM mechanism parameters, and one of its most important physics goals is to produce a precise measurement of the CKM γ angle. B-meson decays involving only tree diagrams are expected to provide a large sensitivity on this parameter, although large statistics are needed to compensate for the small branching fractions involved. The object of this thesis is the study of the $\overline{B}^0 \to D\overline{K}^{*0}$ decay, sensitive to the weak phase γ. The experimental status of the CKM Unitary Triangle, focussing especially on the γ parameter, is presented in this chapter. A description of how the γ angle can be extracted from decays of the type of $\overline{B}^0 \to D\overline{K}^{*0}$ is also given.

2.1   The CKM mechanism experimental status

The Cabibbo-Kobayashi-Maskawa (CKM) matrix [27] describes the quark mixing in the weak sector of particle physics, which states that the quark weak interaction eigenstates are a unitary transformation of the mass eigenstates. The CKM matrix is defined as

$$V = \begin{pmatrix} V_{ud} & V_{us} & V_{ub} \\ V_{cd} & V_{cs} & V_{cb} \\ V_{td} & V_{ts} & V_{tb} \end{pmatrix} = \begin{pmatrix} 1 - \frac{\lambda^2}{2} & \lambda & A\lambda^3(\rho - i\eta) \\ -\lambda & 1 - \frac{\lambda^2}{2} & A\lambda^2 \\ A\lambda^3(1 - \rho - i\eta) & -A\lambda^2 & 1 \end{pmatrix} + \mathcal{O}(\lambda^4), \qquad (2.1)$$

where the Wolfenstein parametrisation [33] has been used (*c.f* Section 1.9). The unitarity of this matrix implies, among others, the relation

$$V_{ub}^* V_{ud} + V_{cb}^* V_{cd} + V_{tb}^* V_{td} = 0, \qquad (2.2)$$
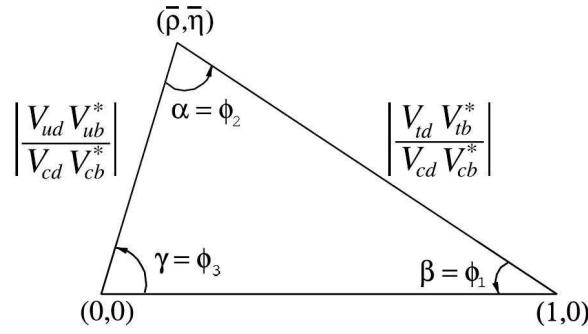
Figure 2.1: *The Unitary Triangle of the CKM mechanism.*

which can be represented as a triangle in the complex plane, known as the Unitary Triangle, is shown in Figure 2.1.

Different measurements are used to determine the value of each CKM matrix element (and the sides of the Unitary Triangle), together with theoretical calculations and QCD factors. The main channels are [34]

- $|V_{ud}| = 0.97425 \pm 0.00022$: superallowed $0^+ \to 0^+$ nuclear beta decays and neutron lifetime measurements.

- $|V_{us}| = 0.2252 \pm 0.0009$: decays of the type $K_L^0 \to \pi l\nu$ and $K/\pi \to \mu\nu(\gamma)$.

- $|V_{cd}| = 0.230 \pm 0.011$: semileptonic charm decays, in particular $D \to K/\pi l\nu$.

- $|V_{cs}| = 1.006 \pm 0.023$: semileptonic D decays of the type $D \to K l\nu_l$ and leptonic D_s decays of the type $D_s \to l\nu_l$.

- $|V_{cb}| = (40.9 \pm 1.1) \times 10^{-3}$: exclusive and inclusive semileptonic B decays to charm.

- $|V_{ub}| = (4.15 \pm 0.49) \times 10^{-3}$: inclusive and exclusive decays of the type $B \to X_u l\overline{\nu}$.

- $|V_{td}| = (8.4 \pm 0.6) \times 10^{-3}$ and $|V_{ts}| = (42.9 \pm 2.6) \times 10^{-3}$: $B - \overline{B}$ oscillations mediated by box diagrams, or loop-mediated rare K and B decays[1].

- $|V_{tb}| = 0.89 \pm 0.07$: t quark decays and electroweak decays of the type $Z \to b\overline{b}$ dominated by loop contributions involving t quarks.

The angles of the Unitary Triangle are measured from the following modes:

- $\alpha = \left(89.0^{+4.4}_{-4.2}\right)^\circ$: decays of the type $b \to u\overline{u}d$, where penguin contributions are sizeable, in particular $B \to \pi\pi$, $B \to \rho\rho$ and $B \to \rho\pi$.

- β, $\sin(2\beta) = 0.679 \pm 0.020$: CP violating B decays involving charmonium modes of the type $b \to c\overline{c}s$, and penguin dominated modes of the type $b \to sq\overline{q}$.

- $\gamma = \left(68^{+10}_{-11}\right)^\circ$: tree-level B decays[2], in particular decays of the type $B \to D^{(*)}K^{(*)}$, which contain the interference between the $b \to c\overline{u}s$ and $b \to u\overline{c}s$ processes, using transitions to final states accessible to both D^0 and $\overline{D}^0$; also time-dependent analysis of the decays $B \to D^{(*)}\pi$.

---

[1]The t quark is very heavy, and decays before hadronising. That is the reason why the determination of CKM matrix parameters involving t quarks is easier to be made through loop-level processes than through tree-level ones.

[2]The t quark is not involved in the definition of the γ angle, so no loops are needed for its measurement.
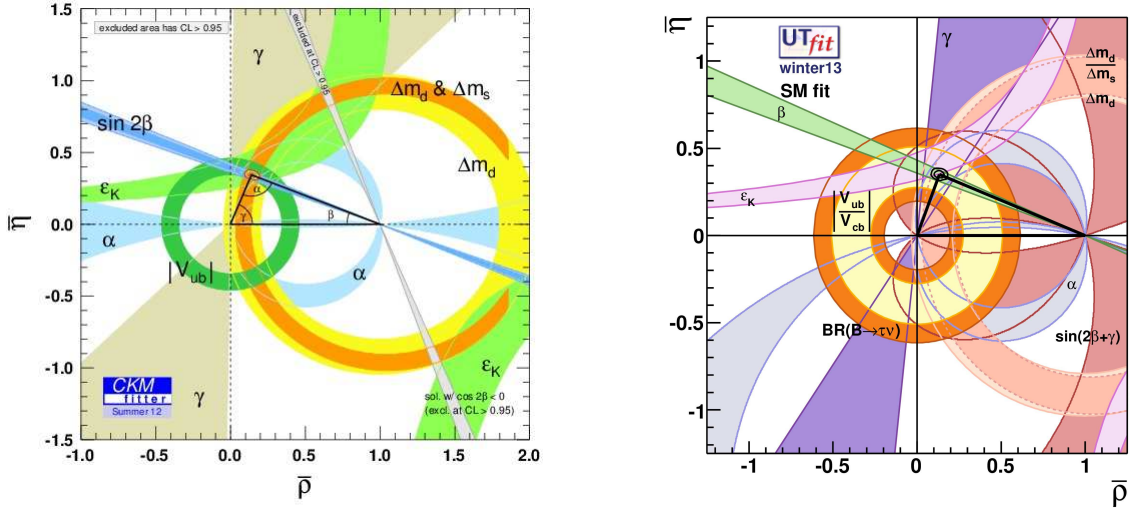
Figure 2.2: *Global fit of the CKM Unitary Triangle (in black, indicating the apex of the triangle), using the available experimental measurements on the CKM parameters (coloured regions). Left: CKMfitter collaboration. Right: UTfit collaboration.*

Two collaborations exist that put together all the different measurements to check the consistency of the Unitary Triangle and the CKM mechanism: the CKMfitter collaboration and the UTfit collaboration. They perform global fits using all available measurements of the CKM elements and angles and imposing Standard Model constraints, in order to extract a more precise determination of each parameter. CKMfitter follows a frequentist approach, while UTfit uses a bayesian method. Both approaches give similar outcomes. The latest results[3] of the global fits from both collaborations are available in Figure 2.2 [35,36]. The consistency of the CKM theory needs all measurements to converge in one point for the apex of the triangle. If this is proven not to be the case, it will be an indication of the existence of physics beyond the Standard Model.

2.2 The γ angle: state of the art

A close look at Figure 2.3, where the experimental results on the CKM angles are included, allows to see that γ is the angle of the Unitary Triangle which is experimentally known with the largest uncertainty. Nevertheless, the results of the global fits, taking into account all the available measurements of the sides and angles of the triangle, give [35,36]

$$\gamma_{\text{fit}}^{\text{UTfit}} \quad = \quad (69.2 \pm 3.2)^{\circ}\,, \tag{2.3}$$

$$\gamma_{\text{fit}}^{\text{CKMfitter}} \quad = \quad \left(67.7^{+4.1}_{-4.3}\right)^{\circ}\,. \tag{2.4}$$

The most precise direct measurements of the γ angle up to date come from the *B*-factories, namely the BaBar and Belle experiments, and from recent LHCb results [37–40],

$$\gamma_{\text{direct}}^{\text{BaBar}} \quad = \quad \left(69^{+17}_{-16}\right)^{\circ}\,, \tag{2.5}$$

$$\gamma_{\text{direct}}^{\text{Belle}} \quad = \quad \left(68^{+15}_{-14}\right)^{\circ}\,, \tag{2.6}$$

$$\gamma_{\text{direct}}^{\text{LHCb}} \quad = \quad (67 \pm 12)^{\circ}\,. \tag{2.7}$$

---

[3]The CKMfitter result corresponds to summer 2012, at the moment of the ICHEP conference. That of UTfit corresponds to winter 2013, before the Moriond conference.
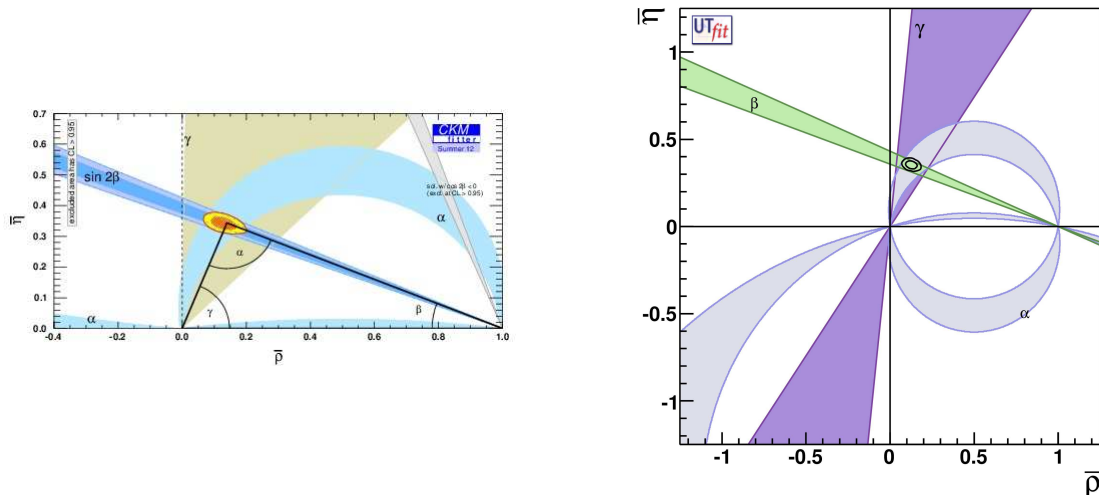
Figure 2.3: *Global fit of the CKM Unitary Triangle (in black, indicating the apex of the triangle), including only the three angle measurements (coloured regions). Left: CKMfitter collaboration. Right: UTfit collaboration.*

experiment	r_B	δ_B	γ	ref.
BaBar	$0.092^{+0.013}_{-0.012}$	$(105^{+16}_{-17})^\circ$	$(69^{+17}_{-16})^\circ$	[38]
Belle	$0.112^{+0.014}_{-0.015}$	$(116^{+18}_{-21})^\circ$	$(68^{+15}_{-14})^\circ$	[39]
LHCb	$0.0923^{+0.0078}_{-0.0080}$	$(114.3^{+12.0}_{-13.0})^\circ$	$(67 \pm 12)^\circ$	[40]

Table 2.1: *Summary of the γ measurement from different experiments, together with the parameters related to the $D^\pm \to DK^\pm$ mode that are extracted together with γ.*

The above results show that, while the global fits manage to constrain γ up to an uncertainty of a few degrees, the direct measurements are still far from this precision. Accurate measurements of the CKM γ angle are needed in order to further constrain the Unitary Triangle. These results are consistent with the Standard Model predictions.

The γ weak phase is extracted along with two other parameters involved in the CP observables. These are the magnitude of the amplitudes ratio r_B of the suppressed to favoured $B^\pm \to DK^\pm$ decay on which these measurements are performed, and the corresponding relative strong phase δ_B, see Section 2.4.2. The measured values of these parameters corresponding to the quoted γ results in Equations (2.5) to (2.7) are given in Table 2.1.

2.3 Measuring γ from loop diagrams

Although this is not the most straightforward way to perform the measurement, γ can be extracted from charmless charged two-body B decays proceeding through both trees and loop diagrams. The study of the CP observables of these decays can improve the knowledge on γ and on other CKM parameters. The loop pollution through penguin diagrams makes more difficult to extract a clean measurement of γ, but on the other hand loop diagrams are interesting as they can be sensitive to sizeable contributions of physics beyond the Standard Model. This new physics would show in the case that γ measurements at the loop-level differ substantially from tree-level results.

The corresponding decays are of the type $H_b \to h^+ h'^-$, where H_b can be either a B^0 meson, a B_s^0 meson or a Λ_b baryon and h, h' stand for π, K or p [41]. The study of time-dependent CP asymmetries under the assumption of U-spin symmetry (invariance of the strong interaction dynamics under the exchange of the d and s quarks) can be used to determine γ [42]. The different possible diagrams corresponding to this type of decays are presented in Figure 2.4. Sensitivity to γ arises from the measurement of the time-dependent CP asymmetry [43]

$$A_{CP}(t) = \frac{S_f \sin(\Delta m_{(s)} t) - C_f \cos(\Delta m_{(s)} t)}{\cosh(\frac{\Delta \Gamma_{(s)}}{2} t) + D_f \sinh(\frac{\Delta \Gamma_{(s)}}{2} t)}, \tag{2.8}$$

where t is the proper time, and $\Delta m_{(s)}$ and $\Delta \Gamma_{(s)}$ are the $B_{(s)}^0$ mixing parameters. The factors S_f and C_f parametrise the direct and mixing-induced CP violation respectively, and can be written in terms of the amplitudes of the decay of $B_{(s)}^0$ and $\overline{B}_{(s)}^0$ to the same considered final state. D_f is constrained from the relation $(C_f)^2 + (S_f)^2 + (D_f)^2 = 1$. The weak phase γ appears in these parameters through the expression of the decay amplitudes; for example, for $B^0 \to \pi^+\pi^-$,

$$\mathcal{A}(B^0 \to \pi^+\pi^-) \quad \propto \quad e^{i\gamma} - de^{i\delta}, \tag{2.9}$$
$$\mathcal{A}(\overline{B}^0 \to \pi^+\pi^-) \quad \propto \quad e^{-i\gamma} - de^{i\delta}, \tag{2.10}$$

where $de^{i\delta}$ is the ratio of the penguin and tree amplitudes involved in the decay.

As the CP asymmetries in these decays are measured as a function of the $B_{(s)}^0$ proper time, the flavour of the $B_{(s)}^0$ meson at the moment of its production needs to be known. Flavour tagging methods are developed by the experiments in order to extract this information. One possible technique is the "opposite side" tagging, which relies on the fact that the b and $\bar{b}$ quarks are produced in pairs. The flavour of the signal $B_{(s)}^0$ meson is thus inferred by identifying the flavour of the other b-hadron in the event. The "same side" tagging method makes use of the other tracks from hadronisation processes in the same jet as the signal $B_{(s)}^0$. These algorithms need to be efficient, so that they can be reliably used for precise time-dependent measurements without loosing too much statistics.

2.4 Measuring γ from tree diagrams

A clean γ measurement can be extracted from the interference between tree-level diagrams involving $b \to u$ and $b \to c$ transitions. The effect of physics beyond the Standard Model at tree-level is not expected to be significant[4].

2.4.1 Time-dependent analysis

Time-dependent measurements of CP asymmetries are used when the same final state is reachable from both $B_{(s)}^0$ and $\overline{B}_{(s)}^0$ [41]. In particular, the $B_s^0 \to D_s^\pm K^\mp$ mode, shown in Figure 2.5, allows to extract γ when using as input the CP violating B_s^0 mixing phase $-2\beta_s$, which is well constrained from $B_s^0 \to J/\psi \phi$ decays [44]. The sensitivity to γ arises from the interference between the direct decay and the decay after mixing, and a time-dependent analysis is required.

---

[4]New physics at tree-level is not excluded and can happen from a charged Higgs boson mediating the decay, instead of a $W^\pm$. However, the large mass expected for the Higgs particle makes this contribution rather small. Also eventual new physics in the D mixing can affect this type of decays, but its existence is not yet confirmed.
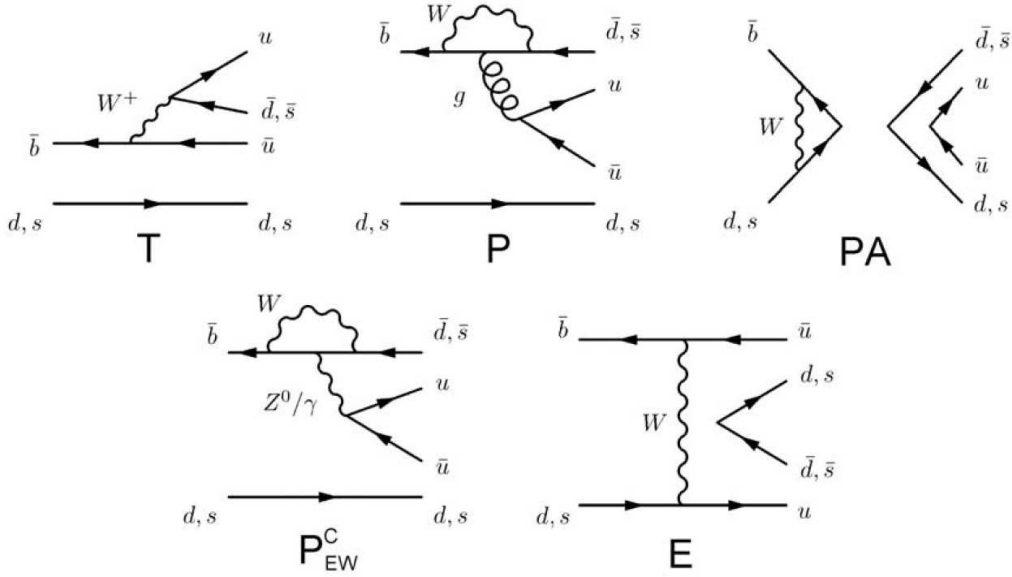
Decay mode	Contributing diagrams
$B^0 \to \pi^+\pi^-$	$T,\ P,\ PA,\ P_{EW}^C,\ E$
$B^0 \to K^+\pi^-$	$T,\ P,\ P_{EW}^C$
$B_s^0 \to \pi^+K^-$	$T,\ P,\ P_{EW}^C$
$B_s^0 \to K^+K^-$	$T,\ P,\ PA,\ P_{EW}^C,\ E$
$B^0 \to K^+K^-$	$PA,\ E$
$B_s^0 \to \pi^+\pi^-$	$PA,\ E$

Figure 2.4: *Top: diagrams for charmless decays of the type $H_b \to h^+h'^-$, where H_b can be either a B^0 meson, a B_s^0 meson or a Λ_b baryon and h, h' can be a π, K or p. The capital letters stand for: Tree (T), Penguin (P), Penguin Annihilation (PA), Colour-suppressed Electroweak Penguin (P_{EW}^C) and Exchange (E). Bottom: table that details the diagrams contributing to each one of the quoted charmless $B_{(s)}^0$ decay. A γ measurement at the loop-level can be extracted from the study of these decays [41].*
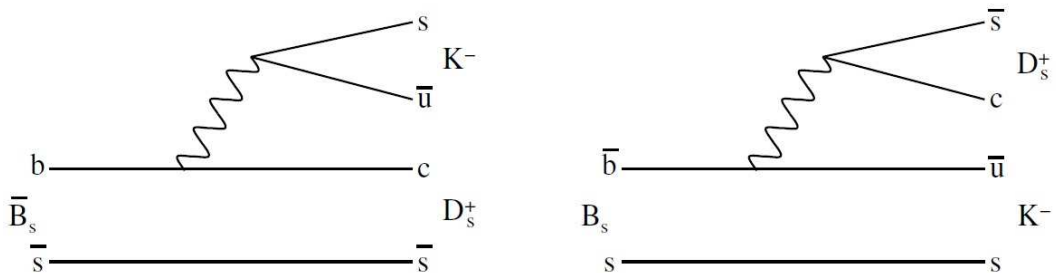
Figure 2.5: *Feynman diagrams for $\overline{B}_s^0 \to D_s^+K^-$ (left) and $B_s^0 \to D_s^+K^-$ (right).*

The time-dependent decay rates of these decays are given by [43]

$$
\begin{aligned}
\Gamma_{B_s^0(\overline{B}_s^0)\to f}(t) \;=\;& \frac{e^{-\Gamma_s t}}{2}|A_f|^2(1+|\lambda_f|^2) \\
&\times\; \left[\cosh\left(\frac{\Delta\Gamma_s t}{2}\right) - D_f\sinh\left(\frac{\Delta\Gamma_s t}{2}\right) \pm C_f\cos(\Delta m_s t) \mp S_f\sin(\Delta m_s t)\right],
\end{aligned}
\tag{2.11}
$$

where t is the proper time, Γ_s, $\Delta\Gamma_s$ and Δm_s are the mixing parameters of the B_s^0 system and D_f, C_f and S_f are CP asymmetry observables depending on λ_f. This factor is given by

$$
\lambda_f = \frac{\overline{A}_f}{A_f} = \left(\frac{V_{ts}V_{tb}^*}{V_{tb}V_{ts}^*}\right)\left(\frac{V_{ub}V_{cs}^*}{V_{us}V_{cb}^*}\right)\left|\frac{A_2}{A_1}\right|e^{i\Delta} = |\lambda_f|e^{i(\Delta-(\gamma-2\beta_s))},
\tag{2.12}
$$

where A_f is the decay amplitude of the B_s^0 meson decay to the final state f, $\overline{A}_f$ is the amplitude of the $\overline{B}_s^0$ meson decay to the same final state f, $|A_2/A_1|$ is the ratio of hadronic amplitudes between $B_s^0 \to D_s^- K^+$ and $B_s^0 \to D_s^+ K^-$, and Δ is the relative strong phase between these amplitudes. The sensitivity to the weak phase difference $\gamma - 2\beta_s$ arises from λ_f as shown in Equation (2.12).

In an analogous way, the time-dependent CP asymmetries in $B^0 \to D^\pm\pi^\mp$ allow to measure $\gamma + 2\beta$ [41], and γ can then be extracted due to β being already well constrained. Nevertheless, the sensitivity to γ from this decay is reduced, as the ratio between the interfering amplitudes is smaller.

In both cases, a time dependent analysis is needed, thus an excellent decay time resolution is essential for experiments aiming at these measurements. Also flavour tagging techniques need to be used here, as already discussed in Section 2.3.

2.4.2 Time-integrated analysis: GLW, ADS and GGSZ methods

A measurement of γ can be extracted from CP observables in decays of the type $B^- \to DK^-$ and $\overline{B}^0 \to D\overline{K}^{*0}$, where D can be either a D^0 or a $\overline{D}^0$ meson depending if it happens through a $b \to c$ transition, involving V_{cb}, or a $b \to u$ transition, involving V_{ub}. The sensitivity to γ arises when the same final state is accessible to both D^0 and $\overline{D}^0$.

A nice feature of these decays is that they are self-tagged, that is to say that the flavour of the B meson at the time of its decay can be known by just looking at the sign of the K in the final state for the charged B decay, or the K from the K^{*0} in the neutral B decay (since $\mathcal{BR}(K^{*0} \to K^+\pi^-) \sim 66.6\,\%$). Thus no time-dependent analysis or sophisticated flavour tagging methods are needed.

The diagrams corresponding to these decays are shown in Figure 2.6. The charged decay $B^- \to DK^-$ has a larger branching fraction and is thus easier to observe than the neutral decay $\overline{B}^0 \to D\overline{K}^{*0}$. On the other hand, in the case of $B^- \to DK^-$ one of the diagrams is colour suppressed and the other one is colour allowed, which reduces the ratio between the two interfering amplitudes $r_B = \frac{1}{3}\frac{|V_{ub}\times V_{cs}|}{|V_{cb}\times V_{us}|} \sim 0.1$ and so the sensitivity to γ. For $\overline{B}^0 \to D\overline{K}^{*0}$ both interfering diagrams are colour suppressed, the ratio of their amplitudes becomes $r_{B^0} \sim 0.3$, and the interference and the sensitivity to γ are enhanced, even though the branching fractions are smaller.

Depending on the D mode, several methods have been proposed for the extraction of γ with time-integrated analyses at tree-level. These are originally applied to the $B^- \to DK^-$ decay, and can be extended to $\overline{B}^0 \to D\overline{K}^{*0}$. The $B^- \to DK^-$ channel is used in the following to illustrate the different methods.
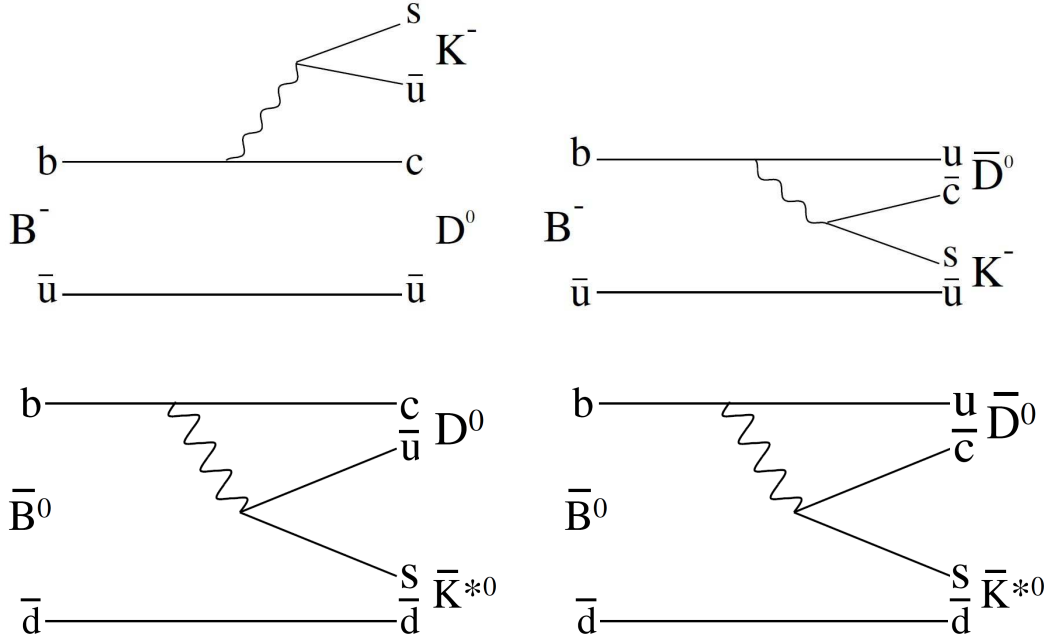
Figure 2.6: *Top: Feynman diagrams for $B^- \to D^0 K^-$ (left), $B^- \to \overline{D}^0 K^-$ (right). Bottom: Feynman diagrams for $\overline{B}^0 \to D^0 \overline{K}^{*0}$ (left), $\overline{B}^0 \to \overline{D}^0 \overline{K}^{*0}$ (right).*

GLW method (Gronau, London and Wyler)

The GLW method [45, 46] for measuring γ considers D meson decays to a CP eigenstate, such as $K^+ K^-$ and $\pi^+ \pi^-$, which are CP-even, or $K_S^0 \pi^0$ and $K_S^0 \phi$, which are CP-odd. In this case, the branching fraction for the D decay is the same in both interfering diagrams, assuming no CP violation in the D meson sector. The widths for the $B^\pm \to DK^\pm$ decays are

$$\Gamma(B^+ \to [CP^\pm]_D K^+) = \Gamma_0^{GLW}(1 + r_B^2 \pm 2r_B \cos(\delta_B + \gamma)), \tag{2.13}$$

$$\Gamma(B^- \to [CP^\pm]_D K^-) = \Gamma_0^{GLW}(1 + r_B^2 \pm 2r_B \cos(\delta_B - \gamma)), \tag{2.14}$$

where $[CP^\pm]_D$ denotes either a D^0 or a $\overline{D}^0$ decaying to a CP eigenstate ($+$ for even, $-$ for odd), $r_B e^{i\delta_B}$ is the ratio of the suppressed to favoured $B^\pm \to DK^\pm$ amplitudes and Γ_0^{GLW} represents normalisation factors. The dependence with γ is visible in the equations.

The observables that are traditionally used for the γ extraction with this method are

$$A_{CP\pm} = \frac{\Gamma(B^- \to [CP^\pm]_D K^-) - \Gamma(B^+ \to [CP^\pm]_D K^+)}{\Gamma(B^- \to [CP^\pm]_D K^-) + \Gamma(B^+ \to [CP^\pm]_D K^+)} \tag{2.15}$$

$$= \frac{\pm 2r_B \sin\delta_B \sin\gamma}{1 + r_B^2 \pm 2r_B \cos\delta_B \cos\gamma}, \tag{2.16}$$

$$R_{CP\pm} = \frac{\Gamma(B^- \to [CP^\pm]_D K^-) + \Gamma(B^+ \to [CP^\pm]_D K^+)}{\Gamma(B^- \to DK^-) + \Gamma(B^+ \to DK^+)} \tag{2.17}$$

$$= 1 + r_B^2 \pm 2r_B \cos\delta_B \cos\gamma, \tag{2.18}$$

The $A_{CP\pm}$ observable provides a direct quantification of the amount of CP violation in this decay mode, while $R_{CP\pm}$ indicates the sensitivity of the method.

ADS method (Atwood, Dunietz and Soni)

The ADS method [47] makes use of D meson decays to a flavour specific eigenstate f_D such as $K^+\pi^-$. This decay is Cabibbo favoured in the case of a $\overline{D}^0$, and doubly Cabibbo suppressed for D^0, but available for both states. Two parameters are added with respect to the GLW method, which are the magnitude of the ratio of amplitudes r_D between the D^0 and $\overline{D}^0$ decays to the same final state, and the corresponding relative strong phase δ_D. These two parameters are usually taken from existing measurements, as the charm sector at this level is already well constrained from previous experiments.

The $B^\pm \to DK^\pm$ widths are thus parametrised as

$$\Gamma(B^+ \to f_D K^+) = \Gamma_0^{ADS}(1 + r_B^2 r_D^2 + 2r_B r_D \cos(\delta_B + \delta_D + \gamma)), \tag{2.19}$$

$$\Gamma(B^- \to \overline{f}_D K^-) = \Gamma_0^{ADS}(1 + r_B^2 r_D^2 + 2r_B r_D \cos(\delta_B + \delta_D - \gamma)), \tag{2.20}$$

$$\Gamma(B^+ \to \overline{f}_D K^+) = \Gamma_0^{ADS}(r_B^2 + r_D^2 + 2r_B r_D \cos(\delta_B - \delta_D + \gamma)), \tag{2.21}$$

$$\Gamma(B^- \to f_D K^-) = \Gamma_0^{ADS}(r_B^2 + r_D^2 + 2r_B r_D \cos(\delta_B - \delta_D - \gamma)). \tag{2.22}$$

The CP observables from which γ is traditionally extracted become for the ADS method

$$A_{ADS} = \frac{\Gamma(B^- \to f_D K^-) - \Gamma(B^+ \to \overline{f}_D K^+)}{\Gamma(B^- \to f_D K^-) + \Gamma(B^+ \to \overline{f}_D K^+)} \tag{2.23}$$

$$= \frac{2r_B r_D \sin(\delta_B - \delta_D)\sin\gamma}{r_B^2 + r_D^2 + 2r_B r_D \cos(\delta_B - \delta_D)\cos\gamma}, \tag{2.24}$$

$$R_{ADS} = \frac{\Gamma(B^- \to f_D K^-) + \Gamma(B^+ \to \overline{f}_D K^+)}{\Gamma(B^- \to \overline{f}_D K^-) + \Gamma(B^+ \to f_D K^+)} \tag{2.25}$$

$$= \frac{r_B^2 + r_D^2 + 2r_B r_D \cos(\delta_B - \delta_D)\cos\gamma}{1 + r_B^2 r_D^2 + 2r_B r_D \cos(\delta_B + \delta_D)\cos\gamma}. \tag{2.26}$$

Also multi-body decays of the same type, such as $D \to K^+\pi^-\pi^+\pi^-$ can be used, where one needs to take into account the effect of the various interfering intermediate resonances contributing.

GGSZ method (Giri, Grossman, Soffer and Zupan)

The GGSZ method [48] considers D meson decays to multi-body final states such as $K_S^0\pi^+\pi^-$. A Dalitz plot analysis can then be performed, and the sensitivity to γ is enhanced thanks to the resonant structure. Two possibilities exist to obtain γ: a model-dependent method, which performs a likelihood fit to the Dalitz plot and requires a model of the resonances, and a model-independent method, which performs a binning of the Dalitz plot and relies on the knowledge of the strong phase difference between D^0 and $\overline{D}^0$ within each bin.

The widths for these decays become [43]

$$\Gamma(B^\mp \to [K_s^0\pi^+\pi^-]_D K^\mp) \propto |f_\mp|^2 + r_B^2 |f_\pm|^2 + 2[x_\mp \Re[f_\mp f_\pm^*] + y_\mp \Im[f_\mp f_\pm^*]], \tag{2.27}$$

with

$$x_\pm = \Re[r_B e^{i(\delta_B \pm \gamma)}] \quad , y_\pm = \Im[r_B e^{i(\delta_B \pm \gamma)}]. \tag{2.28}$$

The factors $f_\pm$ represent the D decay amplitudes to the final state $f = K_s^0\pi^+\pi^-$, that is to say $f_\pm = f(m_\pm^2, m_\mp^2)$ with $f_+ = A_{\overline{f}}e^{i\delta_{\overline{f}}}$, $f_- = A_f e^{i\delta_f}$. The factors m_+^2 and m_-^2 are the squared masses of the $K_s^0\pi^+$ and $K_s^0\pi^-$ combinations respectively. Using these decay widths, CP asymmetries and ratios can be built in an analogous way to the GLW and ADS methods.

An example of Dalitz plots for these decays, taken from BaBar results on this channel [49], is shown in Figure 2.7.
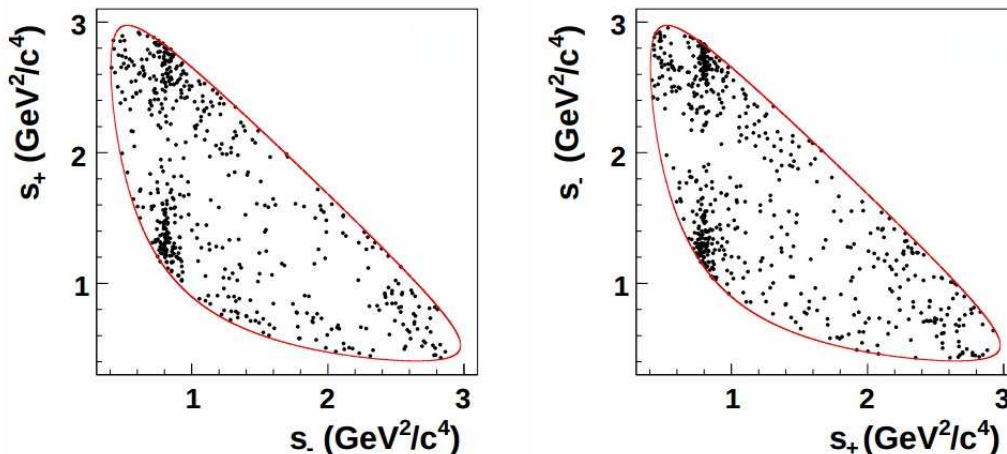
Figure 2.7: *Dalitz plots for the decays $B^- \to DK^-$ (left) and $B^+ \to DK^+$ (right), with $D \to K_s^0\pi^+\pi^-$, taken from the BaBar experiment results [49], where only events in the $B^\pm$ signal region are used. s_+ is the square of the invariant mass of the $K_s^0\pi^+$ combination, while s_- is the square of the invariant mass of the $K_s^0\pi^-$ combination. The resonant structure is visible, as well as the different populations between B^+ and B^-.*

2.5   LHCb perspectives for a precise measurement of γ

The LHCb experiment (*c.f.* Section 3.2) has updated its measurement of the CKM weak phase γ in April 2013 [40],

$$\gamma = (67 \pm 12)^\circ \tag{2.29}$$

modulo 180°. This result is produced by combining several sensitive analyses based on 3 fb^{-1} of 2011 and 2012 LHCb data from proton-proton collisions at $\sqrt{s} = 7$ TeV and 8 TeV respectively. A frequentist approach is used for this combination. The modes entering this combination are those of the type $B^- \to DK^-$, at the tree-level, where D indicates either a D^0 or a $\overline{D}^0$ meson corresponding to the two interfering diagrams. In particular, the D decays accessible to both intermediate states that are used are K^+K^-, $\pi^+\pi^-$, $K^\pm\pi^\mp$, $K_S^0K^+K^-$, $K_S^0\pi^+\pi^-$ and $K^\pm\pi^\mp\pi^+\pi^-$, that is to say that γ is extracted combining the three time-integrated methods described above. Hadronic parameters of the D systems are taken from the CLEO experiment measurements, and the ΔA_{CP} parameter accounting for CP asymmetries in $D \to K^+K^-, \pi^+\pi^-$ decays[5] is taken from the HFAG combination [37].

Although results are already available for the $\overline{B}^0 \to D\overline{K}^{*0}$ channel, as is discussed in this thesis (*c.f.* Chapter 5), they are still not used in the LHCb γ combination. As previouly stated, the sensitivity to γ is enhanced in these decays, but the branching fractions involved are very small. Adding these results brings up new unknown variables that need to be extracted together with γ, which are the ratio of amplitudes of the two interfering diagrams r_{B^0}, the corresponding relative strong phase δ_{B^0} and a coherence factor for the K^{*0} resonance. In order to extract useful information from the $\overline{B}^0 \to D\overline{K}^{*0}$ observables, statistics larger than the current ones are needed to compensate for the lack of knowledge on the additional unknown parameters. With a larger LHCb data sample, these decays will provide important insight to the γ parameter determination.

---

[5]The ΔA_{CP} factor is defined as $\Delta A_{CP} = A_{CP}(D \to K^+K^-) - A_{CP}(D \to \pi^+\pi^-)$. Recent measurements of this quantity might indicate CP violation effects in the charm sector [50–53], but this is yet to be confirmed by upcoming measurements.

When nominal operation of the LHC machine will be reached (*c.f.* Section 3.1), LHCb will accumulate at least 10 fb^{-1} of proton-proton collision data at a center-of-mass energy of 14 TeV. Furthermore, the upgrade of the LHCb detector is already being designed. With the final 50 fb^{-1} of integrated luminosity that LHCb foresees to collect, and combining all the sensitive channels that can be studied at this experiment, the expected sensitivity on γ is of the order of 1°, greatly improving the accuracy of the γ direct measurements with respect to the current one.

2.6 Extracting γ from the $\overline{B}^0 \to D\overline{K}^{*0}$ channel

The GLW and ADS analyses of the decay $\overline{B}^0 \to D\overline{K}^{*0}$ at the LHCb experiment is the object of this thesis. The dependence on γ in this channel using these methods is detailed in this section.

The starting point is the amplitudes of the B^0 decay for each one of the two interfering diagrams, shown on the bottom of Figure 2.6,

$$\mathcal{A}(B^0 \to \overline{D}^0 K^{*0}) = A_c e^{i\delta^c_{B^0}} = A_{B^0}, \tag{2.30}$$

$$\mathcal{A}(\overline{B}^0 \to D^0 \overline{K}^{*0}) = A_c e^{i\delta^c_{B^0}} = A_{B^0}, \tag{2.31}$$

$$\mathcal{A}(B^0 \to D^0 K^{*0}) = A_u e^{i(\delta^u_{B^0}+\gamma)} = A_{B^0} r_{B^0} e^{i(\delta_{B^0}+\gamma)}, \tag{2.32}$$

$$\mathcal{A}(\overline{B}^0 \to \overline{D}^0 \overline{K}^{*0}) = A_u e^{i(\delta^u_{B^0}-\gamma)} = A_{B^0} r_{B^0} e^{i(\delta_{B^0}-\gamma)}, \tag{2.33}$$

where the A_c, A_u are real and A_{B^0} is complex. The r_{B^0} factor represents the relative amplitude magnitude of the suppressed diagram to the favoured one, and δ_{B^0} is the relative strong phase between the two amplitudes, $\delta_{B^0} = \delta^u_{B^0} - \delta^c_{B^0}$. The CP violating phase γ is by definition only involved in the diagram concerning the V_{ub} CKM matrix element, which is the bottom right one on Figure 2.6.

Now, we need to write down also the amplitudes of the D meson decays. In the GLW method, this step can be skipped, as the D^0 and $\overline{D}^0$ decays are exactly the same process in absence of CP violation in the charm sector, and so the amplitudes are the same for the CP-even case, or differ only by a sign for the CP-odd. We denote this decay amplitude as A_D^{CP}. In the ADS method, for a definite final state f_D, we have

$$\mathcal{A}(\overline{D}^0 \to f_D) = \mathcal{A}(D^0 \to \overline{f}_D) = A_D^{K\pi}, \tag{2.34}$$

$$\mathcal{A}(D^0 \to f_D) = \mathcal{A}(\overline{D}^0 \to \overline{f}_D) = A_D^{K\pi} r_D e^{i\delta_D}, \tag{2.35}$$

where, in an analgous way to the B^0 decay, the $r_D e^{i\delta_D}$ factor represents the ratio of amplitudes between the suppressed and the favoured D decays, assuming no CP violation at the D level. These parameters are well constrained by previous experiments and are then taken from external inputs: r_D is the square root of the ratio of the suppressed to favoured branching fractions, $r_D^{K\pi} = (6.16 \pm 0.16) \times 10^{-2}$ [34] for $f_D = K^+\pi^-$, while δ_D has been measured by the CLEO Collaboration and is $\delta_D^{K\pi} = \left(151.5^{+9.6}_{-9.5}\right)^{\circ}$ [54,55].

For the GLW method, combining the previous expressions, the total amplitudes down to the common final state reached by the two interfering diagrams are

$$\mathcal{A}(B^0 \to [CP^{\pm}]_D K^{*0}) = A_{B^0} A_D^{CP} \left[1 \pm r_{B^0} e^{i(\delta_{B^0}+\gamma)}\right], \tag{2.36}$$

$$\mathcal{A}(\overline{B}^0 \to [CP^{\pm}]_D \overline{K}^{*0}) = A_{B^0} A_D^{CP} \left[1 \pm r_{B^0} e^{i(\delta_{B^0}-\gamma)}\right]. \tag{2.37}$$

Taking the square of these two expressions, the observable widths for the GLW decays are

$$\Gamma(B^0 \to [CP^{\pm}]_D K^{*0}) = |A_{B^0}|^2 |A_D^{CP}|^2 \left[1 + r_{B^0}^2 \pm 2\kappa r_{B^0} \cos(\delta_{B^0}+\gamma)\right], \tag{2.38}$$

$$\Gamma(\overline{B}^0 \to [CP^{\pm}]_D \overline{K}^{*0}) = |A_{B^0}|^2 |A_D^{CP}|^2 \left[1 + r_{B^0}^2 \pm 2\kappa r_{B^0} \cos(\delta_{B^0}-\gamma)\right]. \tag{2.39}$$

where κ is a coherence factor that is introduced to take into account non-resonant contributions under the K^{*0} resonance and is discussed later.

For ADS, the corresponding amplitudes become

$$\mathcal{A}(B^0 \to f_D K^{*0}) = A_{B^0} A_D^{K\pi} \left[1 + r_{B^0} r_D e^{i(\delta_{B^0} + \delta_D + \gamma)} \right], \tag{2.40}$$

$$\mathcal{A}(\overline{B}^0 \to \overline{f}_D \overline{K}^{*0}) = A_{B^0} A_D^{K\pi} \left[1 + r_{B^0} r_D e^{i(\delta_{B^0} + \delta_D - \gamma)} \right], \tag{2.41}$$

$$\mathcal{A}(B^0 \to \overline{f}_D K^{*0}) = A_{B^0} A_D^{K\pi} \left[r_D e^{i\delta_D} + r_{B^0} e^{i(\delta_{B^0} + \gamma)} \right], \tag{2.42}$$

$$\mathcal{A}(\overline{B}^0 \to f_D \overline{K}^{*0}) = A_{B^0} A_D^{K\pi} \left[r_D e^{i\delta_D} + r_{B^0} e^{i(\delta_{B^0} - \gamma)} \right], \tag{2.43}$$

and the widths

$$\Gamma(B^0 \to f_D K^{*0}) = |A_{B^0}|^2 |A_D^{K\pi}|^2 \left[1 + r_{B^0}^2 r_D^2 + 2\kappa r_{B^0} r_D \cos(\delta_{B^0} + \delta_D + \gamma) \right], \tag{2.44}$$

$$\Gamma(\overline{B}^0 \to \overline{f}_D \overline{K}^{*0}) = |A_{B^0}|^2 |A_D^{K\pi}|^2 \left[1 + r_{B^0}^2 r_D^2 + 2\kappa r_{B^0} r_D \cos(\delta_{B^0} + \delta_D - \gamma) \right], \tag{2.45}$$

$$\Gamma(B^0 \to \overline{f}_D K^{*0}) = |A_{B^0}|^2 |A_D^{K\pi}|^2 \left[r_{B^0}^2 + r_D^2 + 2\kappa r_{B^0} r_D \cos(\delta_{B^0} - \delta_D + \gamma) \right] \tag{2.46}$$

$$= |A_{B^0}|^2 |A_D^{K\pi}|^2 r_{B^0}^2 \left[1 + \frac{r_D^2}{r_{B^0}^2} + 2\kappa \frac{r_D}{r_{B^0}} \cos(\delta_{B^0} - \delta_D + \gamma) \right],$$

$$\Gamma(\overline{B}^0 \to f_D \overline{K}^{*0}) = |A_{B^0}|^2 |A_D^{K\pi}|^2 \left[r_{B^0}^2 + r_D^2 + 2\kappa r_{B^0} r_D \cos(\delta_{B^0} - \delta_D - \gamma) \right] \tag{2.47}$$

$$= |A_{B^0}|^2 |A_D^{K\pi}|^2 r_{B^0}^2 \left[1 + \frac{r_D^2}{r_{B^0}^2} + 2\kappa \frac{r_D}{r_{B^0}} \cos(\delta_{B^0} - \delta_D - \gamma) \right].$$

A coherence factor κ is introduced in Equations (2.38), (2.39) and (2.44)-(2.47) to take into account non-resonant contributions under the K^{*0} resonance [56]. Indeed, the K^{*0} resonance has a natural width which is large ($\Gamma = (48.7 \pm 0.8)$ MeV$/c^2$ [34]), and thus the resonant $\overline{B}^0 \to D\overline{K}^{*0}$ and non-resonant $\overline{B}^0 \to DK^-\pi^+$ processes interfere, and are both present in the K^{*0} mass region. The r_{B^0}, δ_{B^0} and κ factors are defined in this scenario as

$$r_{B^0}^2 = \frac{\int A_u^2(p)\mathrm{d}p}{\int A_c^2(p)\mathrm{d}p}, \tag{2.48}$$

$$\kappa e^{i\delta_{B^0}} = \frac{\int A_c(p) A_u(p) e^{\delta_{B^0}(p)}\mathrm{d}p}{\sqrt{\int A_c^2(p)\mathrm{d}p \int A_u^2(p)\mathrm{d}p}}, \tag{2.49}$$

where the integrals are performed over all points p of the phase space of $DK\pi$. The Schwarz inequality[6] applied to Equation (2.49) implies $0 \leq \kappa \leq 1$. The case where $\kappa = 1$ would give identical equations for the $\overline{B}^0 \to D\overline{K}^{*0}$ mode as for the $B^- \to DK^-$ mode. The distribution of the κ parameter can be obtained by simulation studies based on realistic models for the different resonance contributions to the $\overline{B}^0 \to DK^-\pi^+$ decays, and is estimated to be 0.95 ± 0.03 when a region within ± 48 MeV$/c^2$ around the nominal K^{*0} mass is used [57].

The number of events measured by an experiment in these channels is directly proportional to the widths quoted above. From Equations (2.44)-(2.47), it can be seen that the interference term governed by the γ phase is enhanced in the suppressed modes of (2.46) and (2.47), where the dominant term is multiplied by $r_{B^0}^2$. If we take $f_D \equiv K^+\pi^-$, this means that CP violation is

---

[6]The Schwarz inequality states that, for two functions $\psi_1(x), \psi_2(x)$ integrable in $[a, b]$, the relation $\left[\int_a^b \psi_1(x)\psi_2(x)dx \right]^2 \leq \int_a^b [\psi_1(x)]^2 dx \int_a^b [\psi_2(x)]^2 dx$ is always verified.

maximal in the case where the two K mesons in the final state[7] have opposite charge, while the effect is diluted in the modes that give same charge K mesons in the final state. For the GLW method, we only consider CP-even final states for the D meson, namely K^+K^-.

We can finally write the CP violation observables sensitive to γ analogous to those shown in Section 2.4.2, for the GLW and the ADS methods applied to the $\overline{B}^0 \to D\overline{K}^{*0}$ mode. We get

$$
\begin{aligned}
A_{CP+} &= \frac{\Gamma(\overline{B}^0 \to [K^+K^-]_D\overline{K}^{*0}) - \Gamma(B^0 \to [K^+K^-]_DK^{*0})}{\Gamma(\overline{B}^0 \to [K^+K^-]_D\overline{K}^{*0}) + \Gamma(B^0 \to [K^+K^-]_DK^{*0})} & (2.50) \\
&= \frac{2\kappa r_{B^0} \sin\delta_{B^0} \sin\gamma}{1 + r_{B^0}^2 + 2\kappa r_{B^0} \cos\delta_{B^0} \cos\gamma}, \\
R_{CP+} &= \frac{\Gamma(\overline{B}^0 \to [K^+K^-]_D\overline{K}^{*0}) + \Gamma(B^0 \to [K^+K^-]_DK^{*0})}{\Gamma(\overline{B}^0 \to [K^-\pi^+]_D\overline{K}^{*0}) + \Gamma(B^0 \to [K^+\pi^-]_DK^{*0})} & (2.51) \\
&= \frac{1 + r_{B^0}^2 + 2\kappa r_{B^0} \cos\delta_{B^0} \cos\gamma}{1 + r_{B^0}^2 r_D^2 + 2\kappa r_{B^0} r_D \cos(\delta_{B^0} + \delta_D) \cos\gamma}, \\
A_{ADS} &= \frac{\Gamma(\overline{B}^0 \to [K^+\pi^-]_D\overline{K}^{*0}) - \Gamma(B^0 \to [K^-\pi^+]_DK^{*0})}{\Gamma(\overline{B}^0 \to [K^+\pi^-]_D\overline{K}^{*0}) + \Gamma(B^0 \to [K^-\pi^+]_DK^{*0})} & (2.52) \\
&= \frac{2\kappa r_{B^0} r_D \sin(\delta_{B^0} - \delta_D) \sin\gamma}{r_{B^0}^2 + r_D^2 + 2\kappa r_{B^0} r_D \cos(\delta_{B^0} - \delta_D) \cos\gamma}, \\
R_{ADS} &= \frac{\Gamma(\overline{B}^0 \to [K^+\pi^-]_D\overline{K}^{*0}) + \Gamma(B^0 \to [K^-\pi^+]_DK^{*0})}{\Gamma(\overline{B}^0 \to [K^-\pi^+]_D\overline{K}^{*0}) + \Gamma(B^0 \to [K^+\pi^-]_DK^{*0})} & (2.53) \\
&= \frac{r_{B^0}^2 + r_D^2 + 2\kappa r_{B^0} r_D \cos(\delta_{B^0} - \delta_D) \cos\gamma}{1 + r_{B^0}^2 r_D^2 + 2\kappa r_{B^0} r_D \cos(\delta_{B^0} + \delta_D) \cos\gamma}.
\end{aligned}
$$

Experimentally, the factors r_{B^0}, δ_{B^0} and γ are extracted together from the CP observables. Indeed, the knowledge of r_B^0 and δ_B^0 is also poor and inherent to this measurement, and can not be taken from external inputs. This means that a single measurement of CP observables from either the GLW or the ADS method is not enough. The fact that there are three unknowns (r_{B^0}, δ_{B^0} and γ) implies that measuring the observables from both methods is needed (which would provide four equations to constrain these unknowns, two from each method). The current measurements for r_{B^0} and δ_{B^0} are given in Table 2.2, together with the rest of inputs involved in the CP observable computation.

In addition, the phases only contribute through cosine functions in Equations (2.46) and (2.47), so ambiguities arise in the determination of γ. There are four ambiguities, as the relations are invariant when flipping signs or exchanging terms in the following ways:

$$
\begin{aligned}
(\delta_{B^0} - \delta_D, \gamma) &\to (\delta_{B^0} - \delta_D, \gamma), & (2.54) \\
(\delta_{B^0} - \delta_D, \gamma) &\to (-\delta_{B^0} + \delta_D, -\gamma), & (2.55) \\
(\delta_{B^0} - \delta_D, \gamma) &\to (\gamma, \delta_{B^0} - \delta_D), & (2.56) \\
(\delta_{B^0} - \delta_D, \gamma) &\to (-\gamma, -\delta_{B^0} + \delta_D). & (2.57)
\end{aligned}
$$

Furthermore, an irreducible global π ambiguity is present, that can be added to each one of the four previous cases. The ambiguities from Equations (2.54) to (2.57) can be reduced to two by using Equations (2.44) and (2.45), that contain the phase $\delta_{B^0} + \delta_D$. These two remaining

---

[7]The K^{*0} meson decays to $K^{*0} \to K^+\pi^-$ with a branching fraction of ~ 66.6 %. With the given choice of f_D, there are two K mesons in the final state: one coming from the D decay, an another one from the K^{*0} decay.

parameter	value	source	ref.
r_{B^0}	$\in [0.07, 0.41]$ @ 95 % CL	BaBar	[37,58]
δ_{B^0}	$(62 \pm 57)^\circ$	BaBar	[59]
$r_D^{K\pi}$	$(6.16 \pm 0.16) \times 10^{-2}$	PDG	[34]
$\delta_D^{K\pi}$	$\left(151.5^{+9.6}_{-9.5}\right)^\circ$	CLEO	[54,55]
κ	0.95 ± 0.03	phenomenology estimate	[57]

Table 2.2: *Summary of the current measurements on the different parameters contributing to the $\overline{B}^0 \to D\overline{K}^{*0}$ CP observables together with γ.*

ambiguities can be resolved by measuring the $\overline{B}^0 \to D\overline{K}^{*0}$ CP observables with additional modes for the D meson decay.

The work of this thesis has been centred in measuring these observables. These analyses are presented in Chapters 5 and 6.

2.7 *CP* observables experimental status

The experimental status of the CP observables for the GLW method and the ADS method for the discussed decays is summarised in Table 2.3. The result concerning the GLW observable for the $\overline{B}^0 \to [CP^+]_D\overline{K}^{*0}$ is the product of this thesis analysis.

mode	experiment	A_{CP+}	R_{CP+}	ref.
$B^- \to [CP^+]_D K^-$	BaBar	$0.25 \pm 0.06 \pm 0.02$	$1.18 \pm 0.09 \pm 0.05$	[60]
	Belle	$0.29 \pm 0.06 \pm 0.02$	$1.03 \pm 0.07 \pm 0.03$	[39]
	CDF	$0.39 \pm 0.17 \pm 0.04$	$1.30 \pm 0.24 \pm 0.12$	[61]
	LHCb	$0.14 \pm 0.03 \pm 0.01$	$1.01 \pm 0.04 \pm 0.01$	[62]
	HFAG average	0.19 ± 0.03	1.03 ± 0.03	[63]
$\overline{B}^0 \to [CP^+]_D\overline{K}^{*0}$	LHCb	$-0.47^{+0.24}_{-0.25} \pm 0.02$	$1.42^{+0.41}_{-0.35} \pm 0.07$	[64]
mode	experiment	A_{ADS}	R_{ADS}	ref.
$B^- \to [K^+\pi^-]_D K^-$	BaBar	$-0.86 \pm 0.47^{+0.12}_{-0.16}$	$0.011 \pm 0.006 \pm 0.002$	[65]
	Belle	$-0.39^{+0.26}_{-0.28}\,{}^{+0.04}_{-0.03}$	$0.0163^{+0.0044}_{-0.0041}\,{}^{+0.0007}_{-0.0013}$	[66]
	CDF	$-0.82 \pm 0.44 \pm 0.09$	$0.0220 \pm 0.0086 \pm 0.0026$	[67]
	LHCb	$-0.52 \pm 0.15 \pm 0.02$	$0.0152 \pm 0.0020 \pm 0.0004$	[62]
	HFAG average	-0.54 ± 0.12	0.0153 ± 0.0017	[63]
$\overline{B}^0 \to [K^+\pi^-]_D\overline{K}^{*0}$	BaBar	-	< 0.244 @ 95 % CL	[58]
	Belle	-	< 0.16 @ 95 % CL	[68]

Table 2.3: *Status of the measurements of the CP observables from the GLW and ADS methods.*

Chapter 3

The LHCb experiment

The LHCb detector [69] at the CERN Large Hadron Collider is designed for precision measurements in the heavy flavour sector of particle physics. Diverse searches are being performed with the data recorded in 2011 and 2012, looking at processes involving b or c quarks. The LHCb detector is particularly well suited to study b decays to final states containing open charm mesons, which are the subject of the analysis of this thesis. An overview of the experimental setup is presented in this chapter.

3.1   The LHC machine

The Large Hadron Collider (LHC) is a two ring superconducting proton accelerator. It is installed in the existing tunnel of the former Large Electron-Positron Collider (LEP) at the French-Swiss border close to Geneva in Switzerland at CERN (European Organization for Nuclear Research): it has 26.7 km of circumference and lies around 100 m underground. Two separate rings allow to accelerate counter-rotating protons beams[1]. They are fed by a chain of smaller accelerators, part of the full CERN accelerator complex, as shown in Figure 3.1: protons are obtained by removing electrons from hydrogen atoms; they are then injected from the linear accelerator (LINAC2) into the PS Booster, then the Proton Synchrotron (PS), and finally the Super Proton Synchrotron (SPS), before reaching the LHC rings. The LHC has 8 circular sectors, 4 of which contain an interaction point, installed in the middle of long straight lines, as shown in Figure 3.2. The LHC is designed to reach a nominal centre-of-mass energy of the collisions of 14 TeV and an instantaneous luminosity of 10^{34} cm^{-2}s^{-1}.

Several experiments are installed at the LHC. The very large ATLAS (A Toroidal LHC ApparatuS) and CMS (Compact Muon Solenoid) detectors, installed at Point 1 and Point 5 respectively, are general purpose experiments, aiming at discovering and studying the Higgs boson, performing direct searches of physics beyond the Standard Model and continuing the measurements in the electroweak sector. LHCb (Large Hadron Collider beauty), at Point 8, is a heavy flavour physics oriented experiment. ALICE (A Large Ion Collider Experiment), at Point 2, aims for reasearch on quark-gluon plasma from heavy ion collisions, which are also provided by the LHC. Smaller than these are: TOTEM (TOTal Elastic and diffractive cross-section Measurement) experiment, at Point 5, to study the total proton-proton cross-section, elastic scattering and diffractive dissociation and also to monitor the LHC luminosity; LHCf (Large Hadron Collider forward), at Point 1, for engineering measurements useful for astroparticle

---

[1]As a difference compared to particle-antiparticle colliders, where the two beams can share the same ring.
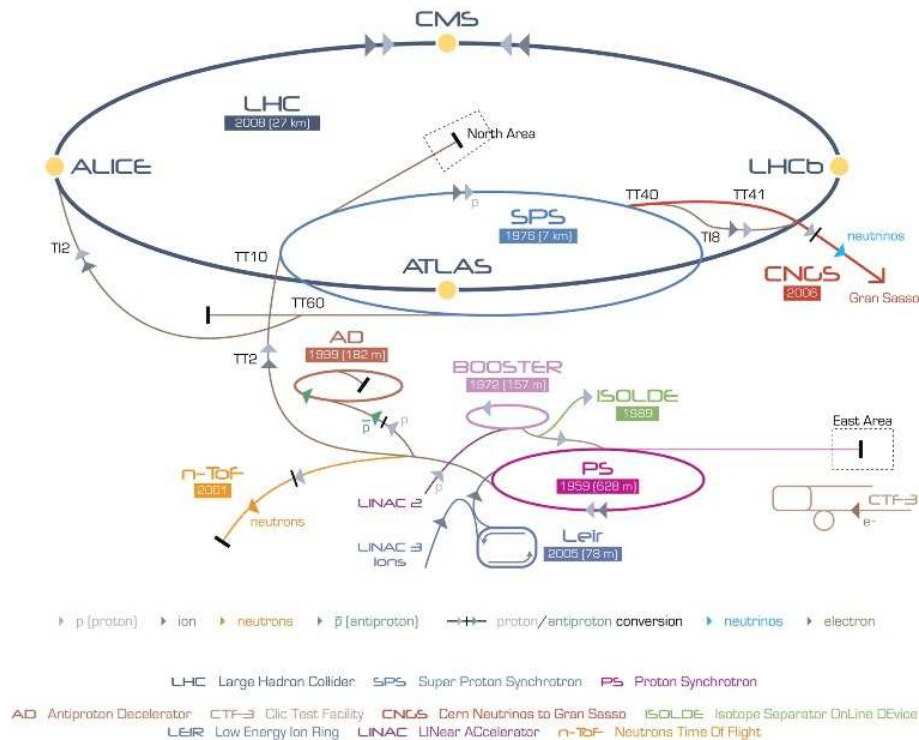
Figure 3.1: *CERN acceleration complex.*

experiments, which simulates cosmic rays in laboratory conditions; MoEDAL (Monopole and Exotics Detector At the LHC), at Point 8, which looks for the magnetic monopole.

Proton beams were injected for the first time in the LHC in September 2008, but a few weeks later a quench in one of the superconducting magnets produced a leak of liquid helium in the tunnel, inducing some damage in the accelerator that forced to halt the LHC operation. After this incident was fixed, the LHC began providing collisions to the experiments in 2010. This first data taking period has lasted until the beginning of 2013, when the LHC stopped to prepare for nominal design conditions. In 2012, the centre-of-mass energy of the collisions was 8 TeV (7 TeV in 2010 and 2011) and the intensity of the colliding beams was of the order of 10^{14} protons per beam. The peak instantaneous luminosity delivered to the ATLAS and CMS experiments was of 6000 $(\mu b \times s)^{-1}$, while the instantaneous luminosity delivered to LHCb was 400 $(\mu b \times s)^{-1}$, approximately constant[2]. More details on the LHCb operations during this first period of data taking are given in Section 3.5.

The expected $b\bar{b}$ production cross-section at a centre-of-mass collision energy of $\sqrt{s} = 14$ TeV is around 500 μb; this makes the LHC the most prolific source of B mesons in the world, quite more significant than the B-factories (BaBar, Belle). LHCb measured with the 2010 data set the cross-section at $\sqrt{s} = 7$ TeV to be $\sigma(pp \to b\bar{b}X) = (284 \pm 20 \pm 49)$ μb [70]. The LHC provides LHCb with a large sample of b- and also c-hadrons (as in addition to b also an even larger sample of c quarks are produced) to perform the searches of its physics program. For the nominal LHCb luminosity of 2×10^{32} cm^{-2}s^{-1} and centre-of-mass energy of 14 TeV, 10^{12} $b\bar{b}$ pairs are produced in a canonical year of data taking (10^7 s). In addition, the large LHC collision energy allows to produce all types of b-hadrons: not only $B^{\pm}$ and B^0 mesons, but also B_s^0 and $B_c^{\pm}$ mesons, and b-baryons, in contrast to the B-factories, which worked mainly at an energy corresponding to the $\Upsilon(4S)$ resonance.

---

[2]1 μb $= 10^{-30}$ cm^2.
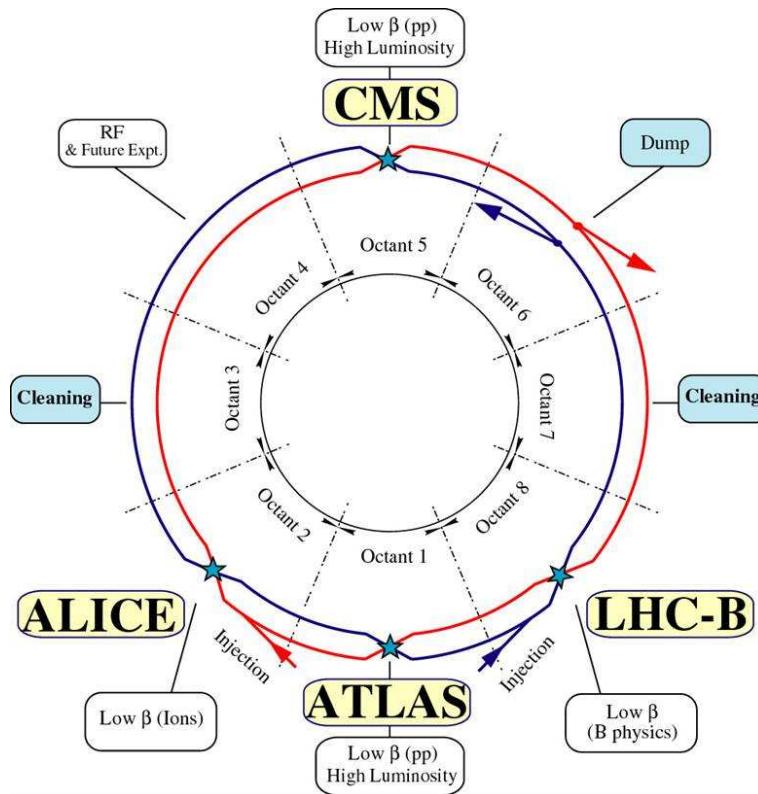
Figure 3.2: *Schematic view of the LHC.*

3.2 The LHCb detector

LHCb is a single arm spectrometer designed to perform precision measurements in the area of heavy flavour particle physics. In particular, the experiment aims at further constraining the Unitary Triangle of the CKM matrix and to study CP violation by looking at processes involving b and c quarks decays, and it also searches for physics beyond the Standard Model in this sector.

LHCb has an angular coverage from 10 mrad to 300 (250) mrad in the bending (non-bending) plane[3] (equivalent to a pseudorapidity[4] region of $2 < \eta < 5$); this particular geometry is adopted to account for the fact that, at high energy collisions, $b\bar{b}$ pairs are mostly produced in a narrow cone in the forward or backward direction of the collision point, as shown by simulation, see Figure 3.3.

The design instantaneous luminosity of LHCb is of 2×10^{32} cm^{-2}s^{-1}. This is a particularity of this experiment, as the LHC provides two orders of magnitude more to ATLAS and CMS (10^{34} cm^{-2}s^{-1}). This modest instantaneous luminosity is chosen to benefit from the advantage that, at this value, events are dominated by a single proton-proton interaction per bunch crossing, as shown in Figure 3.4. Analyses are then more manageable than when events present multiple primary interactions: the production vertex can be identified and reconstructed more easily, as well as the whole decay chain. In addition, the occupancy in the detector remains low, reducing the radiation damage. A "luminosity leveling" system that controls the separation between the

---

[3]According to the dipole magnetic field, the bending plane is the horizontal one, while the non-bending corresponds to the vertical plane. The minimum acceptance covered by the subdetectors is conditioned by the high radiation dose levels close to the beampipe.

[4]The pseudorapidity is defined as $\eta = -\ln\left[\tan\left(\frac{\theta}{2}\right)\right]$, where θ is the angle between a particle momentum and the beam axis. This quantity is commonly used to characterise the geometry of a detector in particle physics, using (ϕ, η) coordinates with ϕ the polar angle rather than Cartesian ones.
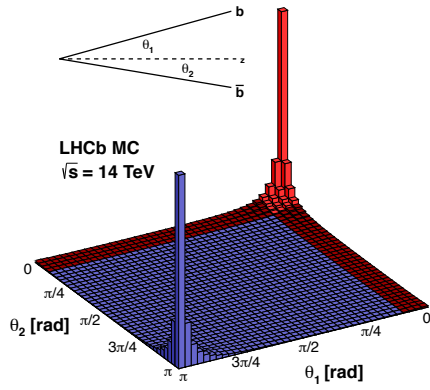
Figure 3.3: *Polar angles of the b- and $\bar{b}$-hadrons from proton-proton collisions, calculated by simulation using the PYTHIA event generator.*
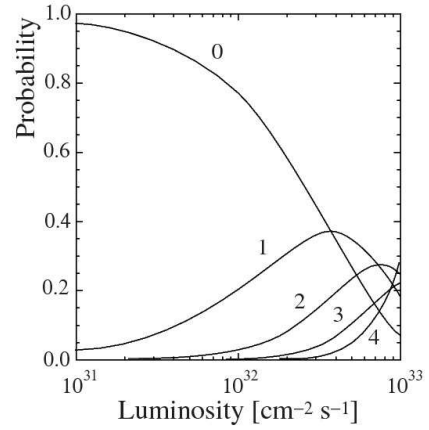
Figure 3.4: *Probability of having 0, 1, 2, 3 and 4 proton-proton interactions per bunch crossing as a function of the luminosity at LHCb.*
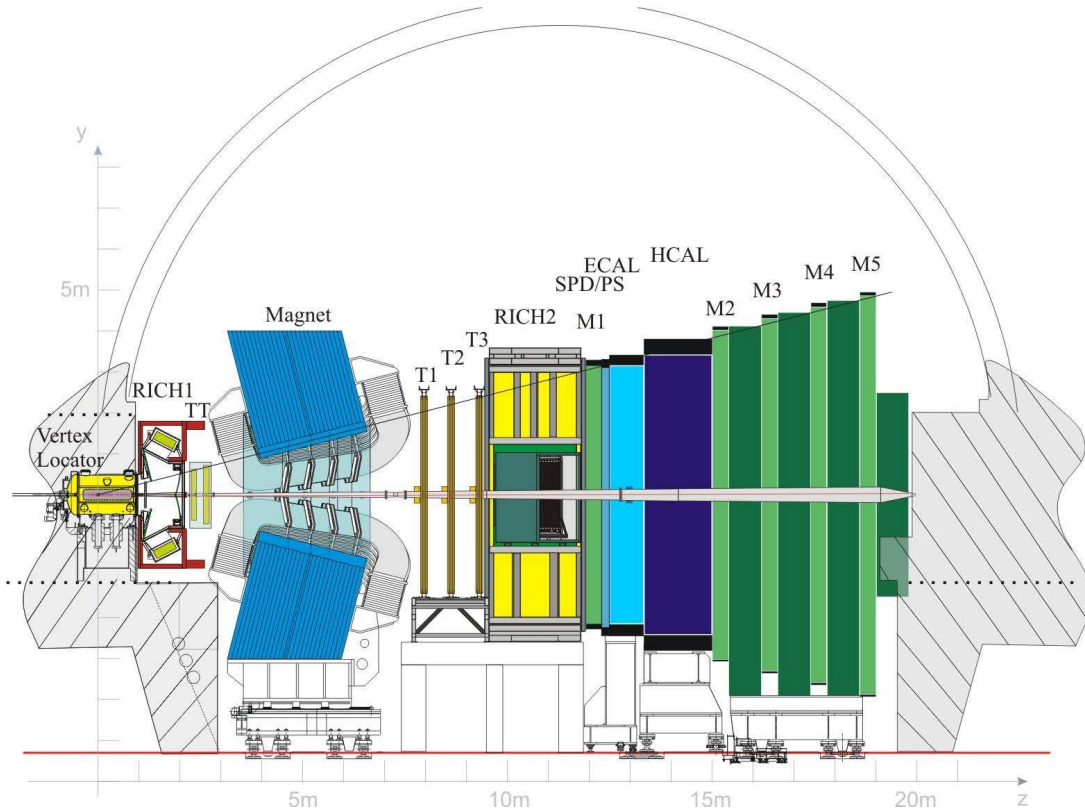
Figure 3.5: *The LHCb detector. The different subdetectors are indicated.*

two beams at the interaction point perpendicularly to the collision plane allows to keep the instantaneous luminosity constant in LHCb, see Section 3.5. This is a major difference with respect to the other LHC experiments.

LHCb is located at the interaction Point 8 of the LHC. An overview of the LHCb detector is shown in Figure 3.5. It is composed of several subdetectors to measure the trajectory of the particles passing through (vertex locator, trackers) and to identify them (RICHs, calorimeters, muon system). The whole detector is described in this section, together with the trigger system. The LHCb experiment is described in greater detail in [69].

3.2.1   VErtex LOcator

The closest subdetector to the beam interaction region is the VErtex LOcator (VELO). It is conceived to reconstruct displaced vertices, characteristic of b- and c-hadrons decays, in an extreme radiation environment. The good performance of this subdetector is vital for LHCb, as the identification of primary and secondary vertices allows to measure the decay lifetimes of these hadrons, and also to know the impact parameter of particles, which is one of the main discriminating variables to control the background in physics analyses. In addition, it has a role in the trigger, due to two pile-up sensors installed upstream of the interaction region, see Section 3.3.1. The VELO measures precisely the position of the vertices in (R, ϕ) coordinates.

The VELO layout is shown in Figure 3.6. It is 1 m long and is divided in two halves, each one of them containing 21 half-circular stations (Figure 3.7) placed along the beam direction[5], 5 of which are located before the interaction point. Each station contains a R-sensor, to measure the radial distance to the beam axis R of the hits of the traversing particles, and a ϕ-sensor, to measure the azimuthal coordinate around the beam axis; the third spatial coordinate is provided by the position of the sensors. One of the halves is shifted 1.5 cm with respect to the other on the z-axis, so that the two halves overlap to cover the full azimuthal acceptance.

Each sensor is composed of 2,048 silicon strips. They operate inside vacuum vessels that play the role of beampipe in this region[6]. A system of RF-foils provides shielding against beam radiations. The sensors have an external radius of 42 mm and an internal one of 8 mm, being this the closest possible distance of the sensitive material to the beam. The distance between the stations in the interaction region is 3.5 cm, set to fulfill the requirement that any particle must cross at least three stations. The VELO covers a pseudorapidity range of $1.6 < \eta < 4.9$.

The two halves of the VELO are retractable, allowing to put the subdetector in the shadow of the beam pipe during the injection of the beams (when the beams do not have yet their optimal sizes and characteristics, and so the sensors need to be protected), separating the halves up to 6 cm. The closing and opening of the VELO is done fully automatically from the LHCb control room under the supervision of the shifter. However, very good alignment of the stations is crucial. In spite of the fact that it is retracted for every LHC fill, the alignment of the two VELO halves is stable over time to better than 5 μm.

The VELO is required to have high signal to noise ratio S/N, efficiency and impact parameter

---

[5]The beam direction corresponds to the z-axis in the LHCb reference system.

[6]These vessels can be filled with gas in dedicated periods to perform absolute luminosity measurements with the Beam-Gas Imaging (BGI) method. The absolute luminosity needs to be known in order to determine the absolute cross-sections of the collision processes and is also an estimate of the performance of the accelerator. In the BGI, relatively light elements such as hydrogen, carbon and oxygen are injected, and the beam-gas interaction is used to measure the beam parameters to extract the absolute luminosity. The VELO plays a crucial role here, as its high resolution allows to measure precisely the beam profiles and positions. The BGI method is an alternative to the "van der Meer scan" method, which provides a direct measurement of the effective cross-section by scanning the two coliding beams, one with the other, in both transverse directions. Special fills are scheduled for this in LHCb. In the end, the results from both methods are combined [71].
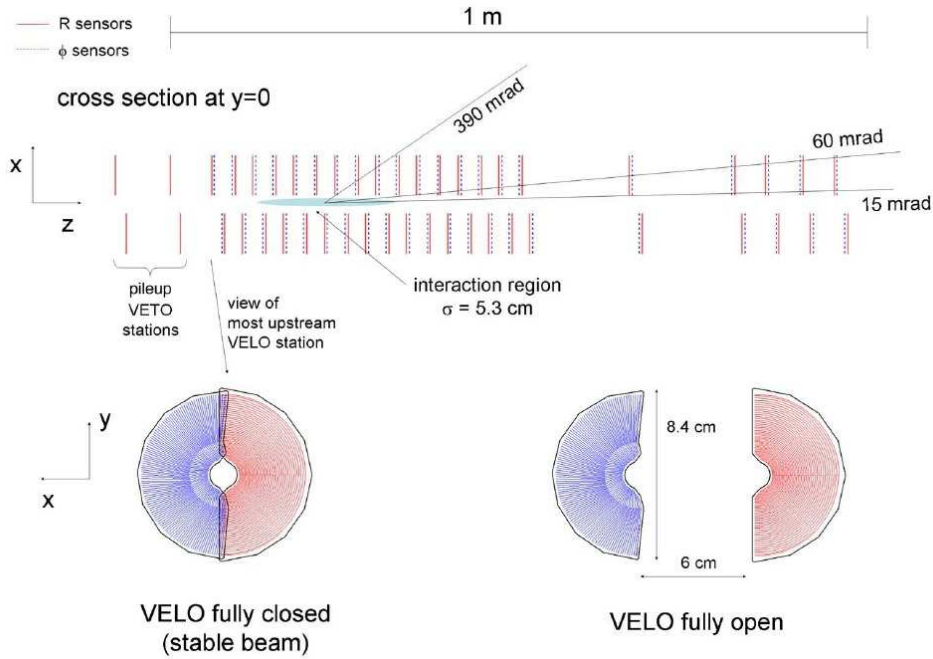
Figure 3.6: *Scheme of the VELO subdetector layout, seen from the top. Also the front face of the sensors is shown (in blue a ϕ-sensor, in red a R-sensor).*

resolution. In 2012, the VELO was showing a signal to noise ratio $S/N > 17$, an impact parameter resolution of 20 μm for high p_T tracks and a primary vertex resolution of 12 μm in the x- and y-axis for a 35 track vertex.

3.2.2 Trackers

Magnet

LHCb uses a warm dipole magnet, shown in the left panel of Figure 3.8, to bend the trajectory of the charged particles traversing the detector in order to measure their momentum. It consists of two identical coils of conical saddle shape placed mirror-symmetrically to each other in a
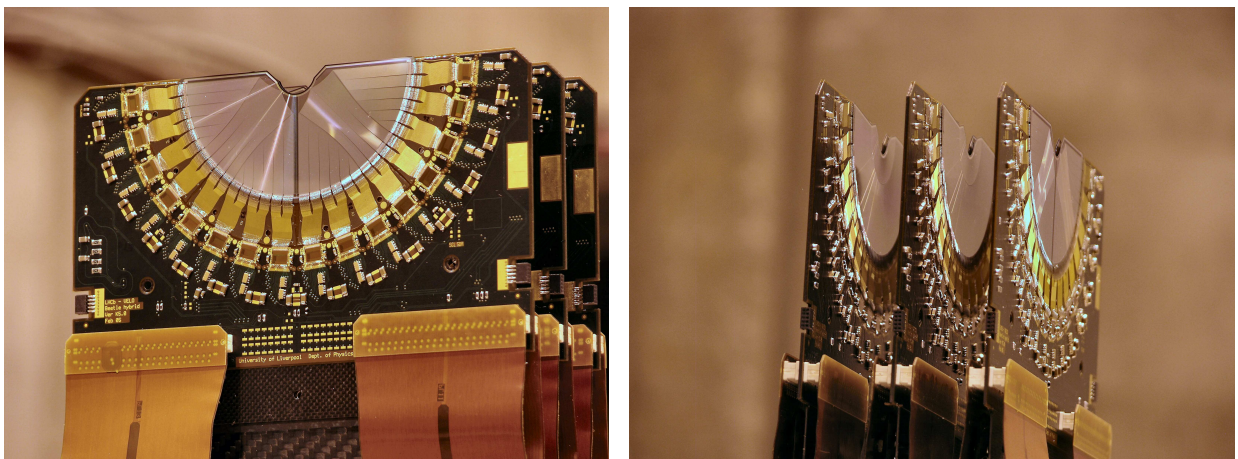
Figure 3.7: *VELO sensors.*
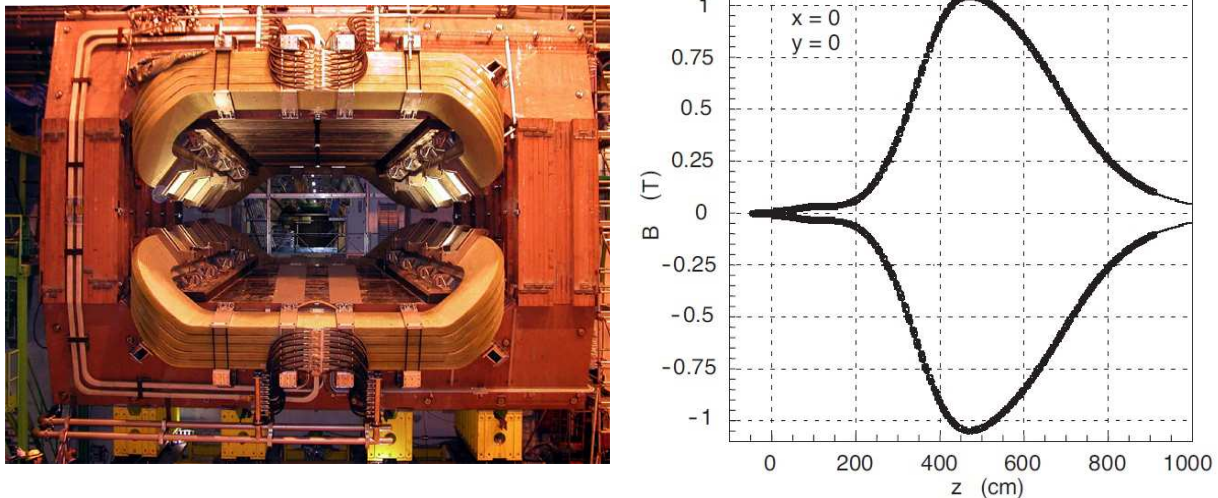
Figure 3.8: *(left) Picture of the LHCb magnet, installed in the cavern. (right) Mapping of the y component of the magnetic field B_y along the z axis, for the two magnet polarities.*

window-frame yoke with sloping poles. The conductor has a specific ohmic resistance below 28 Ωm and works at a nominal current of 5.85 kA.

The integrated magnetic field is 4 Tm. Mapping measurements have been performed for the three spatial components; as an example, the y component field mapping measurement is shown in the right panel of Figure 3.8 for both magnet polarities. The non-uniformities of the field are of the order of 1 %. To control the detector systematic uncertainties related to the left-right detection asymmetries, the polarity of the field is reversed periodically.

The Silicon Tracker: Tracker Turicensis and Inner Tracker

Precise track detection in a high occupancy environment is achieved in LHCb by means of the Silicon Tracker (ST), which is composed of the Tracker Turicensis (TT) and the Inner Tracker (IT). Both of them consist of silicon microstrip sensors with a strip pitch of 200 μm optimised to meet the 50 μm single hit spatial resolution required for this subdetector. There is one station in the TT, placed upstream of the magnet, and three in the IT, downstream of the magnet. The TT station is a rectangular area of 150 cm (width) × 130 cm (height), covering the full LHCb acceptance, and has an active region of 8.4 m^2, while the IT is a 120 cm wide and 40 cm high cross-shaped plane with a 4.0 m^2 active region.

Schematic representations of a TT and an IT detection layer are shown in Figure 3.9. Each one of the four stations has four detection layers, formed by strip sensors which are vertical in the first and the last, while the second is rotated by a stereo angle of $-5°$ and the third by $+5°$ ($x-u-v-x$ geometry). The length of the readout strips is chosen in each case to keep maximum strip occupancies at the level of the percent with a minimum number of readout channels. Each TT half detection module is composed of basic blocks of 7 sensors grouped in 2 or 3 readout sectors, covering half of the LHCb acceptance in height. There is one such block above and one under the beampipe, and 7 (in the two first layers) or 8 (in the two last layers) full detection modules of 14 sensors at each side. Each one of the three IT stations is formed by four individual detector boxes arranged around the beampipe (in a cross shape), with an overlap between them to avoid gaps and for alignment purposes. The boxes above and below the beampipe contain single silicon sensors, while the ones at the left and the right have two rows of them.

The TT and IT share the same readout electronics, power distribution and control, and

39
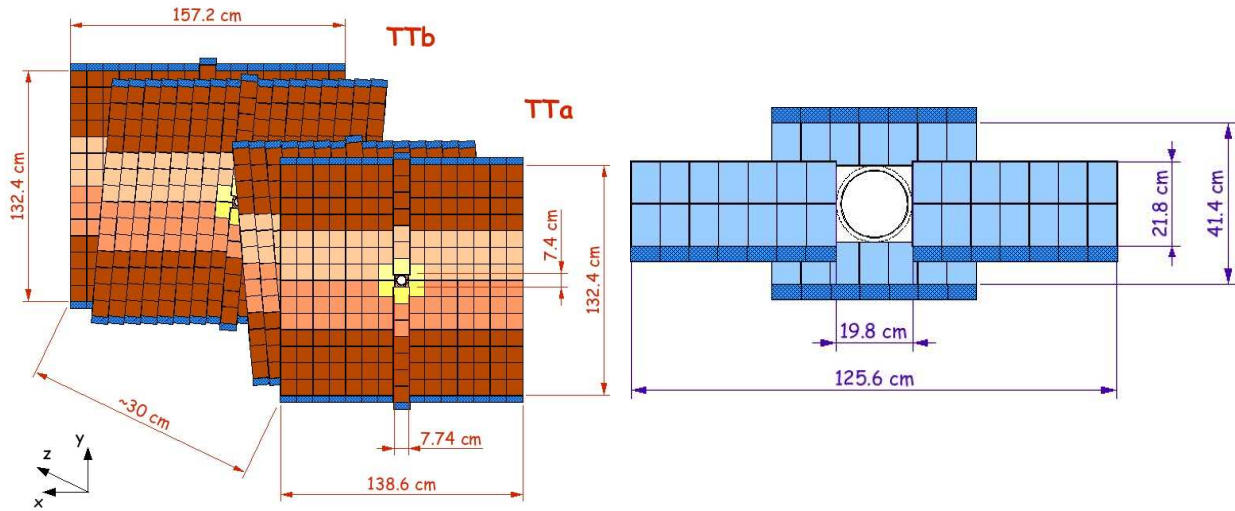
Figure 3.9: *Scheme of Silicon Tracker detection layers: from the TT station (left) and an IT station (right).*

monitoring systems. They are light tight and thermally and electrically insulated, and they operate at 5 °C to minimise radiation damage. In addition to a 50 μm spatial resolution, they are required to provide full single-hit efficiency for minimum ionising particles while keeping the noise hit rate low; this means to achieve a signal-to-noise ratio higher than 12. This requirement was nicely met in 2012.

The Outer Tracker

The Outer Tracker (OT) is a drift-time device for track detection and precise momentum measurement, covering an acceptance of 300 mrad in the bending plane and 250 mrad in the non-bending plane. Its three stations are placed at the IT positions, covering the outer acceptance around the IT modules, where the occupancy is lower, Figure 3.10. Each OT station is composed of four layers of 64 drift tubes of 4.9 mm diameter, placed following a $x - u - v - x$ geometry. The total active area covered is 5,971 × 4,850 mm^2. The gas in each straw-tube is a mixture of 70 % Argon and 30 % CO_2, which provides fast drift time, smaller than 50 ns, and a good drift-coordinate resolution of 200 μm.

In 2012, LHCb was showing a momentum resolution of $\Delta p/p \sim 0.4$ % at 5 GeV/c to 0.6 % at 100 GeV/c. Track reconstruction efficiency was 96 % for long tracks[7]. The impact parameter resolution was 20 μm for high-p_{T} tracks.

3.2.3 Ring Imaging Cherenkov detectors

Two Ring Imaging CHerenkov detectors (RICHs) have the role of separating pions from kaons in hadron decays, task which is fundamental in LHCb. Charged particles going through this subdetector, when travelling faster than the speed of light in the material that fills it, produce a cone of Cherenkov light, from which the velocity of the particle can be extracted[8]. The

---

[7]Long tracks are tracks with reconstructed hits in the VELO and all the tracking stations.

[8]The Cherenekov angle θ is defined as $\cos\theta = \frac{1}{n\beta}$, where n is the refractive index of the medium and β the ratio between the speed of the particle in this medium, or velocity, and the speed of ligt, $\beta = \frac{v_p}{c}$.
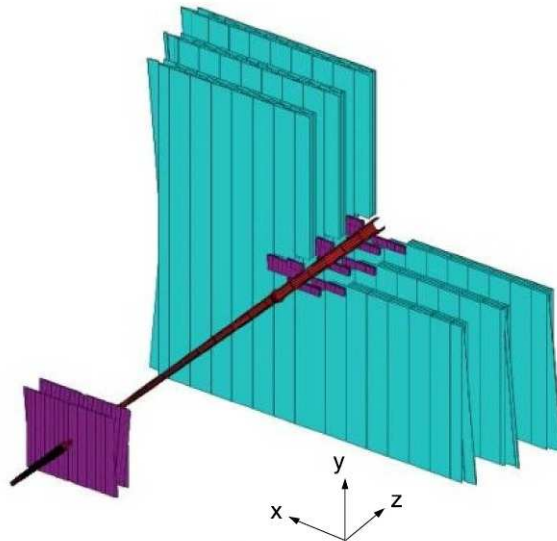
Figure 3.10: *Illustration of the LHCb tracking subdetectors: the Outer Tracker (green) and the ST (purple); the IT deals with the central, higher occupancy region, while the OT covers the surrounding area.*

tracking system provides an independent measurement of the momentum; combining velocity and momentum allows to deduce the mass of the particle, which identifies it. Tilted spherical mirrors collect this light, which is then guided by planar mirrors to photon detectors, located outside of the LHCb acceptance. A schematic description of each one of the two RICHs is available in the left and central panels of Figure 3.11.

Two RICHs are needed to cover the full momentum range. RICH1, placed upstream of the LHCb magnet, is low-momentum oriented, covering a range from 1 to 60 GeV/c, which corresponds to large polar angles; it extends over the full LHCb acceptance, from 25 to 300 (250) mrad in the bending (non-bending) plane. It uses an aerogel and C_4F_{10} radiators. RICH2 is located downstream of the magnet and is high-momentum oriented: it covers a range from 15 to 100 GeV/c and has a limited angular acceptance, covering small polar angles from 15 to 120 (100) mrad; it uses CF_4 radiators. The choice of the radiators is illustrated in the right panel of Figure 3.11.

Each RICH has two Hybrid Photon Detector (HPD) boxes, which are placed outside the acceptance and are shielded with iron to protect them from the magnetic field. The RICH1 is arranged in a vertical layout, with the HPD boxes above and under the beampipe, while the RICH2 has a horizontal layout, with the HPD boxes at the left and the right sides of the beampipe. The system of spherical and flat mirrors focuses the Cherenkov light emitted by the crossing particles and reflects the image out to the HPDs (only the spherical mirrors are inside the acceptance, all other optical components are outside). These are vacuum photon detectors in which an electron, released from the conversion of an incident photon in the photocathode, is accelerated by an applied high voltage to a silicon detector. Each RICH1 plane comprises 7 rows of 14 HPDs hexagonally closely packed, with centres separated by 89.5 mm; RICH2 planes have 9 rows of 16 HPD each, Figure 3.12. The HPD main characteristics are large coverage, high active-to-total area ratio, high granularity and high speed.

Very good RICH performance is crucial for LHCb, as it is very important for its physics program to identify all the particles in a B hadron decay chain. In 2012, the kaon identification efficiency was excellent, of 95 %, for 10 % pion to kaon mis-identification probability over a momentum range of 2 to 100 GeV/c^2.
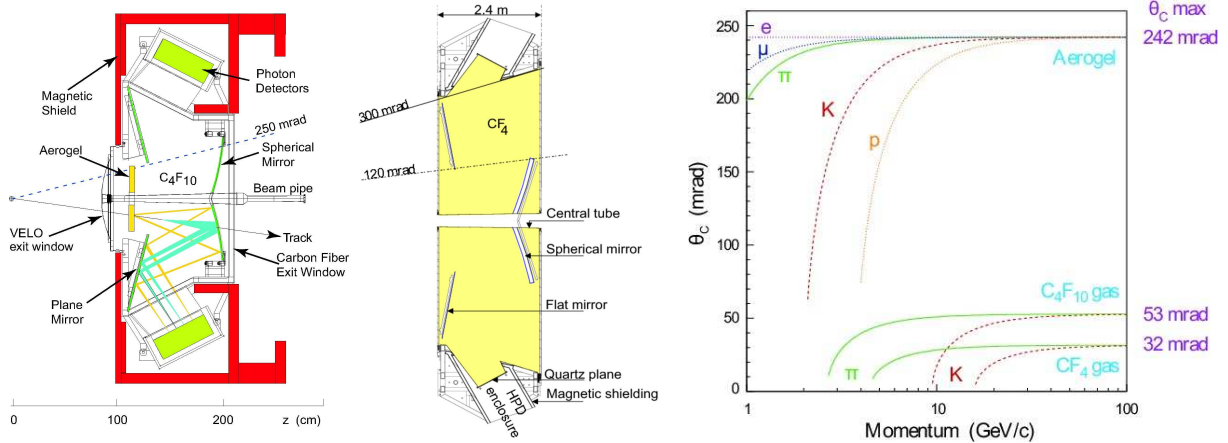
Figure 3.11: *(left) Scheme of RICH1. (centre) Scheme of RICH2. (right) Cherenkov angle as a function of the momentum for different particle identities, justifying the choice of the radiators in each RICH detector.*
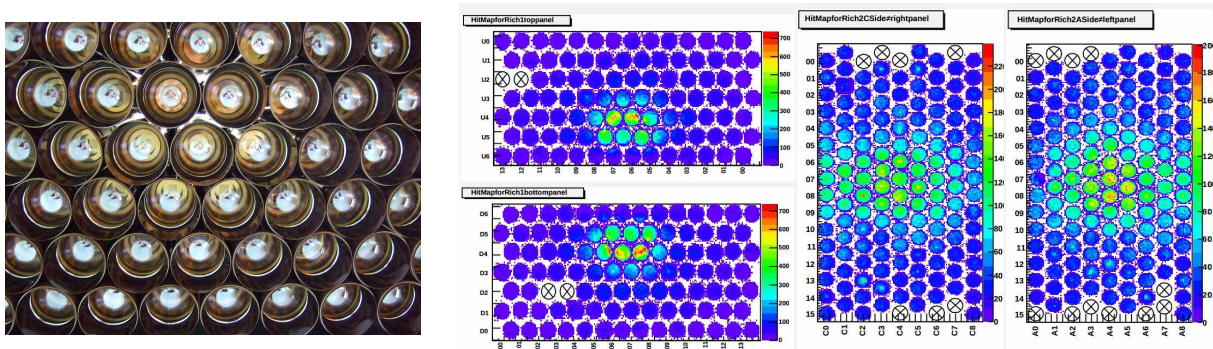
Figure 3.12: *(left) Photograph of RICH1 upper box HPDs. (right) RICH online monitoring plots. Each plot corresponds to one RICH box, the circles being the HPDs. The colour scale represents the hit multiplicity.*
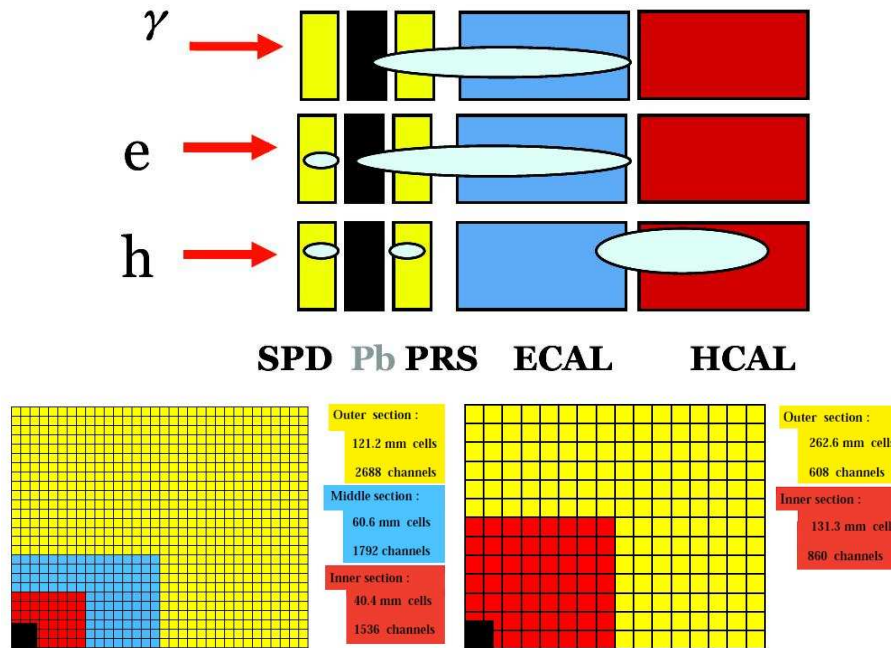
Figure 3.13: *(top) Illustration of the shower development in the calorimeter system for different particle identities. (bottom left) ECAL and (bottom right) HCAL cell sizes.*

3.2.4   Calorimeters

The goal of the calorimeter system is the identification of electrons, photons and hadrons and a measurement of their energies and positions, but it is also used in the trigger, having as a task the selection of high transverse energy electron, photon and hadron candidates, as described in Section 3.3.1. Photons and neutral pions are also reconstructed.

An electromagnetic (ECAL) and a hadronic (HCAL) calorimeter are installed, required to have good resolution and particle shower separation. For the identification of electrons, the rejection of charged pion background needs longitudinal segmentation of the electromagnetic shower detection, thus a preshower detector (PS) is present in front of the ECAL. A scintillator pad detector (SPD) located before the PS identifies charged particles. A lead converter is placed between the SPD and the PS. All the four subdetectors work with shashlik technology: they are sampling devices using scintillator material, and the scintillation light is transmitted to photomultiplier tubes (PMT) by wavelength-shifting (WLS) fibres. The electronics of this system of subdetectors is designed to be as fast as possible, for trigger purposes, see Section 3.3.1.

The top panel of Figure 3.13 provides a simple explanation of the particle identification done by the calorimeter system. In 2012, the invariant mass resolution provided by the detector to the LHCb physics analysis was ~ 100 MeV/c^2 for $B_s^0 \to \phi\gamma$; the electron identification efficiency was of 90 %, for 5 % electron to hadron mis-identification probability. Each calorimeter component is described in the following.

Scintillator pad detector and preshower detector

SPD and PS are two almost identical planes of rectangular scintillator pads of high granularity (12,032 channels), separated by a distance of 56 mm, with a 15 mm lead converter of 2.5 radiation lengths thickness placed between them. The sensitive area is 7.6 m wide and 6.2 m high. All SPD dimensions are 0.45 % smaller than the PS ones to achieve a projective geometry. To match the ECAL segmentation, the SPD and PS are divided into three regions: Inner (composed of
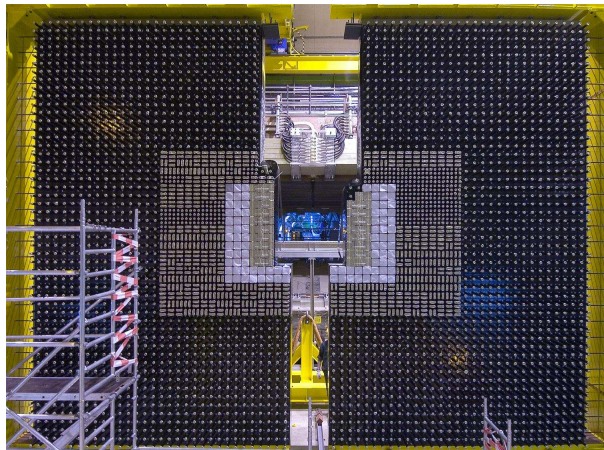
Figure 3.14: *Picture of the ECAL at the time of its installation in the pit. The three regions corresponding to different cell sizes are visible.*

3,072 cells), Middle (3,584) and Outer (3,376). The WLS fibres are read out by multianode photomultiplier tubes (MAPMT), which makes them fast, multi-channel detectors.

Electromagnetic calorimeter

The ECAL (Figure 3.14) is placed at 12.5 m of the interaction point, covering an acceptance of 300 (250) mrad in the bending (non-bending) plane to match projectively the tracking system geometry; it is 7.8 m wide and 6.3 m high. As the hit density is a function of the distance to the beampipe, and it varies by two orders of magnitude over the active surface of the calorimeters, this subdetector is divided into three regions. They have different dimensions and cell sizes in order to provide good granularity, see bottom left panel of Figure 3.13.

The ECAL modules alternate 2 mm thick lead layers and 4 mm thick scintillator tiles. It is 84 cm deep, equivalent to 25 radiation lengths, which guarantees full containment of high energy photon showers. This detector design choice provides modest energy resolution but fast response, uniformity, acceptable radiation resistance and reliability. The energy resolution of the ECAL is $\frac{\sigma_E}{E} = \frac{10 \ \%}{\sqrt{E}} \bigoplus 1 \ \%$, where E is expressed in GeV.

Hadronic calorimeter

The HCAL is located at 13.33 m of the interaction point and is 8.4 m height, 6.8 m width and 1.65 m depth, equivalent to 5.6 interaction lengths (the ECAL upstream adds 1.2 interaction lengths to this value). It is transversally segmented in two regions, with double cell size in the Outer region with respect to the Inner one, see Figure 3.13 bottom right (HCAL cell borders match ECAL ones, in a non-projective way). It is a sampling device made from tiles of scintillator as active material and iron as absorber. As the light yield in the HCAL is a factor 30 smaller than in the ECAL, the HCAL PMTs operate at higher gain. The resolution is $\frac{\sigma_E}{E} = \frac{65 \ \%}{\sqrt{E}} \bigoplus 9 \ \%$ (E expressed in GeV).

An interesting feature of the HCAL is its embedded self-calibration system equipped with a ^{137}Cs gamma source. The periodic calibration of the calorimeters has become an important task during operation, to recover from ageing effects that have appear in both HCAL and ECAL in 2011, and to maintain good performances and constant trigger rates.
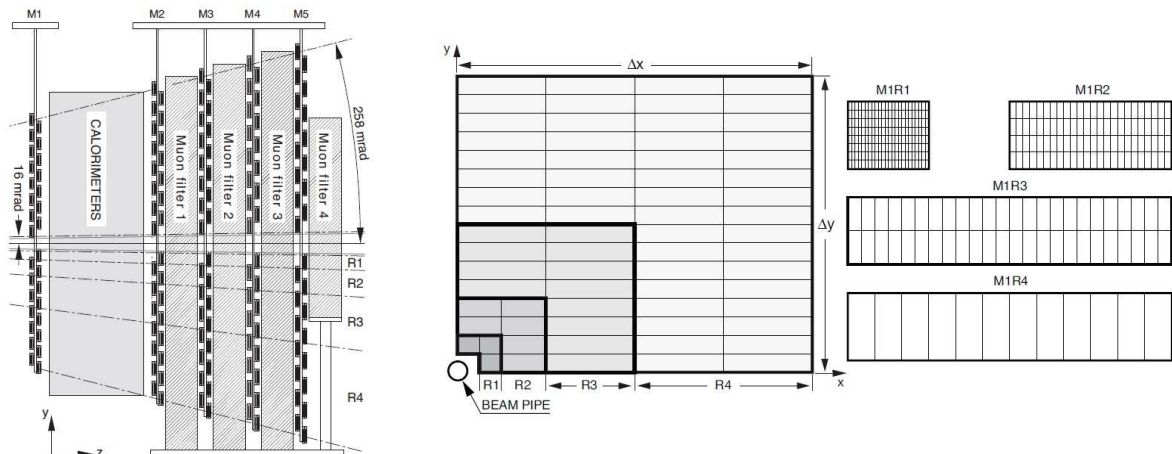
Figure 3.15: *(left) Schematic muon system overview. (right) A quadrant of one of the muon stations, where each square represents one muon chamber. The segmentation of the chambers for each different region is shown on the right-hand side of the picture, for M1.*

3.2.5 Muon system

LHCb has five muon stations (M1 to M5), placed along the beam axis, dedicated to the identification of muons. The transverse geometry is projective between the stations, and their angular acceptance is of 306 (258) mrad in the bending (non-bending) dimension. The muon chambers are used also for trigger purposes, and their design is strongly conditioned by this. The muon system layout is illustrated in Figure 3.15.

M1 is located upstream of the calorimeter system, to provide a better transverse momentum measurement (for trigger purposes), while stations M2 to M5 are placed downstream of the calorimeters. 80 mm thick iron absorbers are inserted between these last four stations in order to select penetrating muons; the total absorber thickness of the whole muon system (including the calorimeters) is equivalent to 20 interaction lengths, which means that the minimum momentum of a muon crossing all the five stations is 6 GeV/c. Each station is divided into four regions (R1 to R4). The dimensions and segmentation scale from the inner (R1) to the outer (R4) region as 1:2:4:8, see right panel of Figure 3.15, in order to have uniform particle flux and channel occupancy over the four regions of the same station. They are all multi-wire proportional chambers (MWPC) except for the R1 of M1, which uses triple-GEM detectors due to the higher particle rates in this region (for radiation protection issues). There are 1,380 chambers in total, covering a full active surface of 435 m^2.

The muon trigger requires hit coincidence in the five chambers in a certain time window and is based on stand-alone muon track reconstruction and transverse momentum measurement, *c.f* Section 3.3.1. Stations M1 to M3 are designed to have high spatial resolution along the horizontal direction, to define the track direction and to calculate the transverse momentum of the muon candiate with a 20 % resolution. Stations M4 and M5 do the identification of penetrating particles, and therefore they can have more limited spatial resolution. High efficiency in the five stations is important in order to meet the 5-hit coincidence. Other important features required to the muon system are time resolution, rate capability, ageing resistance, and fast electronics.

In 2012, the muon identification efficiency was excellent: 97 %, for 1-3 % pion to muon mis-identification probability.

3.3 The LHCb trigger system

The LHC bunch crossing frequency is 40 MHz. For LHCb, this means 10 MHz of crossings containing visible interactions in the detector. A trigger system is necessary to reduce this rate to 5 kHz, which can be written to storage. At a luminosity of 2×10^{32} cm^{-2}s^{-1}, 100 kHz of $b\bar{b}$ pairs are expected; only 15 % of them includes at least one b-hadron with all its decay products contained in the spectrometer acceptance. Thus, the trigger has the task of efficiently selecting interesting events for physics analysis while rejecting as much as possible uninteresting background.

Two trigger levels are present in LHCb, Figure 3.16. The Level 0 (L0) is implemented in hardware using custom made electronics, and operates synchronously with the 40 MHz bunch crossing frequency, reducing it to 1 MHz, at which the whole detector can be read out. The L0 selects events containing particles of high transverse momentum, using the information from the VELO pile-up system, the calorimeters and the muon chambers. The High Level Trigger (HLT) is implemented in software using commercially available equipment; it uses the full event information and its algorithms are executed asynchronously on a processor farm. The combination of trigger selections or "trigger lines" to be used during operation, both for the L0 and the HLT, are configured in the Trigger Configuration Key (TCK), which is preloaded before each fill. The trigger source information of each event is saved for off-line analyses.

The final output rate of the LHCb trigger is 5 kHz [9]. The trigger efficiencies at the end of 2012 were around 90 % for dimuon channels and around 30 % for multi-body hadronic final states.

3.3.1 L0 trigger

The first level of trigger at LHCb, the Level 0 (L0), is a fully synchronous hardware trigger that uses the information of the VELO pile-up system, the calorimeters and the muon system to reduce the 40 MHz LHC crossing rate to 1 MHz. As the B hadrons that LHCb aims to study have large masses, their decay products are particles with large transverse momentum ($p_{\rm T}$) or transverse energy ($E_{\rm T}$); the calorimeter and muon triggers reconstruct and select the highest $E_{\rm T}$ electron, photon and hadron and the two highest $p_{\rm T}$ muons of the event, respectively. In addition to this, a few global quantities are extracted: the total observed energy is calculated by the calorimeters and an estimate of the total number of tracks is performed using the number of hits in the SPD; the number of primary proton-proton interactions in each bunch crossing is estimated by the pile-up system. The L0 Decision Unit (DU) evaluates the final trigger decision for each bunch crossing.

The pile-up system distinguishes between crossings with single and multiple visible interactions. It is composed of two planes (A and B) perpendicular to the beam line, upstream of the VELO, Figure 3.6. Each plane contains two R-sensors, see Section 3.2.1, measuring the radial position of the tracks, which are then extrapolated to the beam axis to identify the position of the primary vertices with a resolution of 3 mm. This allows to measure the backward charged track multiplicity and to detect multiple interaction events, to be vetoed.

The calorimeter trigger system looks for high $E_{\rm T}$ particles. It builds clusters of 2×2 cells and selects the highest $E_{\rm T}$ candidate, whose type (electron, photon, π^0 or hadron) is determined using the information of the different calorimeter elements (SPD, PS, ECAL, HCAL). A measurement of the total $E_{\rm T}$ in the HCAL and the total SPD multiplicity of the event is also performed. As

---

[9] This value corresponds to the end of 2012 operation. The output trigger rate evolved during this first period of data taking, from 2 kHz in 2010, which was the design output rate, to this final value. The deferred HLT, explained later in this section, helped remarkably to achieve this larger rate.

LHC bunch crossing
40 MHz

LØ TRIGGER (HARDWARE)
Readout electronics
High E_T, p_T signatures

$h^{\pm}$ 450 kHz	$\mu/\mu\mu$ 400 kHz	e/γ 150 kHz

1 MHz

HIGH LEVEL (SOFTWARE)
Online CPU Farm

HLT1

VELO track and primary vertex reconstruction
At least one track passing p, p_T, impact parameter and track quality cuts

HLT2

Full reconstruction
Mixture of inclusive and exclusive selections

INCLUSIVE TOPOLOGICAL 2 kHz	INCLUSIVE / EXCLUSIVE CHARM 2 kHz	$\mu/\mu\mu$ 1 kHz

5 kHz

STORAGE

Figure 3.16: *Scheme of the LHCb trigger system.*

L0 decision line	2011 threshold	2012 threshold	SPD multiplicity
L0Muon	$p_\mathrm{T} > 1.48$ GeV/c	$p_\mathrm{T} > 1.76$ GeV/c	< 600
L0DiMuon	$p_\mathrm{T}^{12} > 1.296$ GeV/c	$p_\mathrm{T}^{12} > 1.6$ GeV/c	< 900
L0Hadron	$E_\mathrm{T} > 3.6$ GeV	$E_\mathrm{T} > 3.5 - 3.74$ GeV	< 600
L0Electron	$E_\mathrm{T} > 2.5$ GeV	$E_\mathrm{T} > 2.5 - 2.86$ GeV	< 600
L0ElectronHi	$E_\mathrm{T} > 4.2$ GeV	$E_\mathrm{T} > 4.2$ GeV	< 600
L0Photon	$E_\mathrm{T} > 2.5$ GeV	$E_\mathrm{T} > 2.5 - 2.96$ GeV	< 600
L0PhotonHi	$E_\mathrm{T} > 4.2$ GeV	$E_\mathrm{T} > 4.2$ GeV	< 600

Table 3.1: *L0 trigger cuts for each type of decision as set on the TCKs in 2011 and 2012.*

part of the work of this thesis concerns the L0 hadronic trigger, more details on the L0 calorimeter system are given in Chapter 4.

The muon trigger performs a stand-alone muon reconstruction, with a p_T resolution of ~ 20 %, to select the two muon tracks with largest p_T in each quadrant of the muon detector. It looks for hits defining a straight line through the five muon stations (with hits in all of them) and pointing towards the interaction point. The first two stations perform the p_T measurement. The algorithm starts from the hits in M3, which are extrapolated to M2, M4 and M5 by a straight line to the interaction point, searching for hits in a defined interest window in the surroundings of the extrapolation points. The hits in M1 are found by extrapolating the ones in M2 and M3. The two tracks reconstructed in this way with the highest p_T values are selected to perform the trigger decision.

The cuts[10] applied for each L0 decision line configured in the TCKs for operation during 2011 and 2012 are available in Table 3.1. The L0 Decision Unit collects the information of each L0 system, at 40 MHz, and performs a logical computation to combine all signatures into one decision per crossing. It allows overlap of different trigger conditions (OR computation) and prescaling of them. The DU decision is sent to the Read Out Supervisor, which makes the ultimate decision of accepting the event depending on the status of the different detector components, in order to prevent overflows. The system latency[11] is fixed to 4 µs, which includes the time of flight of the particles as well as cables and electronic delays, meaning that 2 µs are left in the end for the L0 data processing.

3.3.2 High Level Trigger

The second trigger level at LHCb, the High Level Trigger (HLT), is a software trigger. It consists of a C++ application running on each one of the CPUs that form the so-called Event Filter Farm (EFF). It reduces the 1 MHz output rate of the L0 trigger to 5 kHz to be stored on disk. Each HLT application has access to the whole data in each event, but due to CPU limitations it uses only a part of the full event information to reject uninteresting events in the most optimal possible way. The limit time for an event to be processed by the HLT is fixed to ~ 30 ms. As it is fully implemented in software, the HLT is flexible and can evolve to meet the changing experiment needs and physics priorities.

The HLT consists of independent trigger lines, which are optimised to cover different types of interesting events, containing dedicated selection parameters and scaling factors. It is implemented in two levels: the HLT1 performs a partial event reconstruction by using primary vertex

---

[10] p_T^{12} is defined as $p_\mathrm{T}^{12} = \sqrt{p_\mathrm{T}^{largest} \times p_\mathrm{T}^{2nd\ largest}}$, that is to say the square root of the product of the p_T of the two muons with largest values for this quantity.

[11] The system latency is the time between a proton-proton interaction and the moment when the L0 delivers its decision to the Front End electronics.

identification together with the information from the trackers, and the HLT2 uses the whole event information to select interesting inclusive and exclusive decays. The HLT performance is checked on "no bias" samples, recorded without any trigger requirements applied.

The HLT1 uses the VELO reconstruction algorithm to perform a full 3D pattern recognition. Vertices with at least 5 VELO tracks originating from them and within a radius of 300 μm from the reconstructed mean position of the proton-proton interaction envelope are considered to be primary vertices. Tracks are selected by minimising their impact parameter to any primary vertex, and additional cuts are applied on the vertex quality based on the number of hits per track. In the case of muon dedicated lines, a fast muon identifiction is performed to tag VELO tracks associated to muons. For each selected VELO track, its track-segment is reconstructed in the trackers to determine their momentum, and minimum momentum criteria are applied. A simplified fit is performed on reconstructed tracks, and their χ^2 and convariance matrix are measured. The output rate at this stage is around 30 kHz.

The HLT2 can perform a full event reconstruction, as the rate coming from HLT1 is low enough to allow it. VELO tracks are built using a seeding algorithm, and their measured momentum from the trackers is required to be $p > 5$ GeV/c and $p_{\mathrm{T}} > 0.5$ GeV/c. An identification algorithm is applied for muons, and also electrons are identified by matching tracks with ECAL clusters. Finally, a set of lines are run to select particular types of events. The so-called topological lines are defined for triggering on partially reconstructed b-hadron decays, in an inclusive way: they require at least two charged particles in the final state and a displaced decay vertex. Exclusive lines also exist that require all particles in the decay to be reconstructed, mainly oriented for prompt c-hadron production studies, as well as dedicated lines for decays containing muons in the final state.

In 2012 the so-called "deferred HLT" was implemented: the idea was to take profit of the time between two LHC fills to process data by the HLT trigger and so to increase the output trigger rate. As explained before, the HLT rate is limited by the event processing time; instead of throwing the excess away, some of the data selected by the L0 trigger was temporary written to disk waiting to be processed by the HLT during the next interfill period. The HLT deferral fraction was around 35 % at the end of the year.

3.4 The LHCb software: data processing, stripping, simulation

The different LHCb applications are built in a software framework called Gaudi [72], see Figure 3.17. Data recorded by the LHCb detector is reconstructed with the Brunel application and stored in "data summary tape" (dst) files for physics analysis. The stripping is a first, very loose selection which is applied on these files, dividing the data in different groups or streams depending on the type of analysis for which the set of cuts is conceived. Doing this first selection centrally notably reduces the processing time for analysis. In each stream, different stripping lines are written that select candidates for specific decays on which exhaustive physics analyses will be performed. The selected candidates from one stream are stored in output files, ready to be used by analysts. Examples of stripping streams are "calibration", "charm", "Bhadron", "semileptonic" and so on. Stripping selections are revisited and broadened from time to time and new processings and stripping versions are released and run periodically, for new and older data.

B hadron candidates selected by the stripping for physics analysis are retrieved by running the DaVinci application on the stripped data files. The decay of interest is specified inside a Python script using LHCb specific classes, and a ROOT[12] tree [73] is produced that contains as

---

[12]ROOT is a C++ object-oriented program and library developed by CERN. It was originally designed for
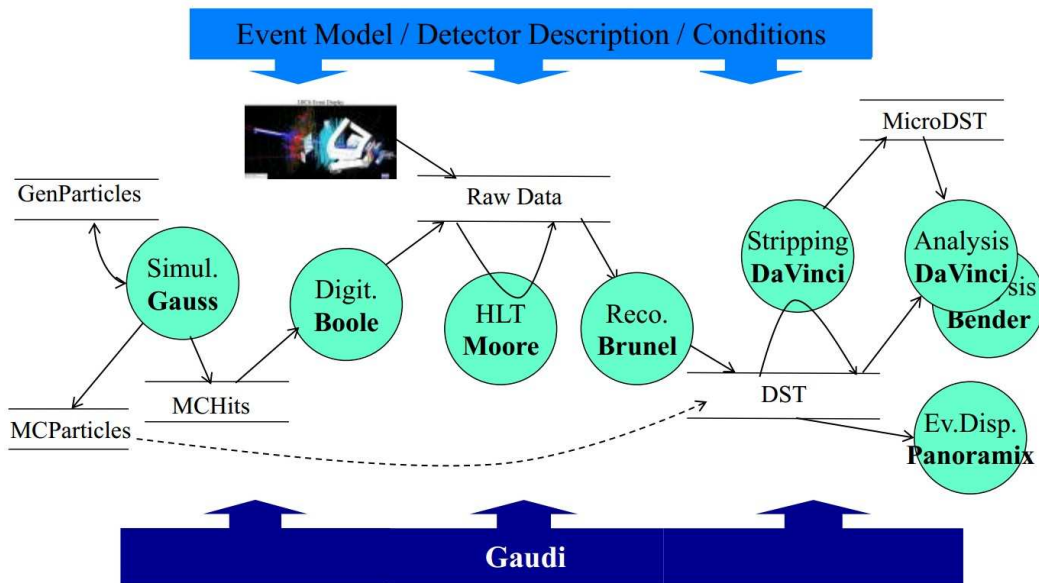
Figure 3.17: *LHCb software applications.*

leaves the properties of each one of the particles in the decay chain. The physics analyses are then performed on these ROOT files.

Monte Carlo simulation is also produced in LHCb, which models real data. Physics processes are generated within the Gauss application [74] using the PYTHIA package[13] [75] for proton collisions and the EvtGen package[14] [76] for particle decays. The detector response (its geometry and the interactions of the particles with the matter in it) is simulated using the Geant4 package[15] [77, 78], interfaced also to Gauss. The digitisation of the simulated data is done by the Boole application, in order to obtain raw data similar to that produced by the detector. During this thesis some work has been done on the calibration of the calorimeter simulation, which is detailed in Appendix A.

Other applications are available inside the Gaudi architecture. Moore, for example, is the HLT application. Bender is an alternative to DaVinci to perform physics analysis in a more interactive way. Finally, Panoramix is the event display application of LHCb. It allows to show physics events in a 3-dimensional representation of the LHCb detector, where vertices, tracks and hits can be seen. This can be done live on prompt data, but can also be useful for analysts to investigate particular events in detail in a more visual and intuitive way.

---

particle physics data analysis and contains several features specific to this field, but it is also used in other areas such as astronomy and data mining.

[13]PYTHIA is a package for simulation of particle collisions in accelerators, taking into account parton distributions and the interactions involved in such a physics process. Originally written in FORTRAN 77, the latest versions are now released in C++ language.

[14]EvtGen is an event generator designed for the simulation of the physics of B decays. It was initially developed for the CLEO and BaBar experiments.

[15]The Geant4 (GEometry ANd Tracking) package is an object oriented C++ program for simulation of the passage of particles through matter. In addition to particle physics, it also has applications in the fields of nuclear, space and medical physics.
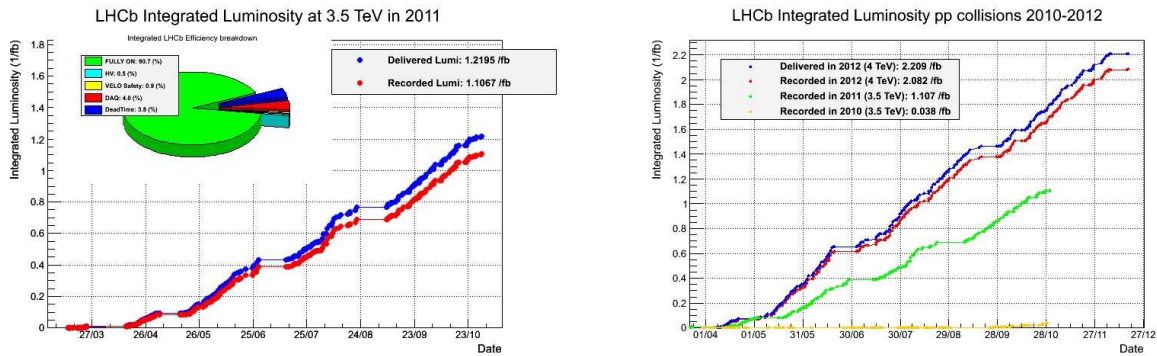
Figure 3.18: *Integrated luminosity delivered by the LHC to the LHCb experiment and recorded by the detector in 2011 (left) and 2012 (right).*

3.5 LHCb performance between 2010 and 2012

LHCb data taking

LHCb has taken proton collisions data from Mars 2010 to December 2012 [16]. The instantaneous luminosity has evolved in time within this period, increasing from the cautious few $(\mu b \times s)^{-1}$ at the start-up to 400 $(\mu b \times s)^{-1}$ at the end of 2012 (which corresponds to approximately twice the design instantaneous luminosity value). The data taking efficiency has been in average higher than 90 %, and 99 % of the data has been checked to be good for analysis. The recorded luminosity on disk is 38 pb^{-1} in 2010, 1 fb^{-1} in 2011 and 2.2 fb^{-1} in 2012. The energy of the collisions has not been constant either: in 2010 and 2011 it was of 7 TeV at the centre-of-mass (each beam circulating at 3.5 TeV), while in 2012 the choice was made of increasing this energy to 8 TeV (each beam at 4 TeV), for physics reasons[17] but also as a technologic challenge. The Figure 3.18 shows the evolution of the integrated luminosity of LHCb as a function of time. Also important in LHCb are the μ parameter, or average number of visible proton-proton interactions per bunch crossing, and the pile-up, or average number of proton-proton interactions in visible events. The design μ value of LHCb was around 0.6, but even if the LHCb design aims to keep these quantities low to facilitate analysis, in 2012 it was coping very well with a maximum pile-up of 1.7, thanks to the good performance of the LHCb reconstruction software.

As a member of the LHCb Collaboration, I have been involved in the data taking of the experiment as Data Manager. I have done several series of shifts in the LHCb control room (on the surface of Point 8), where my role is to check and interpret the histograms that monitor the data being taken, in order to make sure that every element of the detector is working fine.

Luminosity Leveling

As previously pointed out, the LHCb instantaneous luminosity has two particularities with respect to that of the other experiments of the LHC: it is lower, and approximatively constant in time. These are provided by the so-called "luminosity leveling" mechanism. This procedure consists simply in separating the beams perpendicularly to the collision plane, to avoid head-on

---

[16]The LHC stopped its operation in February 2013, but the collisions scheduled during these last months were of protons with heavy ions.

[17]The main reason to raise the collision energy in 2012 is to increase the cross-section of the Higgs boson production; its discovery was the major goal of the ATLAS and CMS experiments. Of course LHCb searches also benefit from this higher energy, as the $b\bar{b}$ cross-section becomes larger.
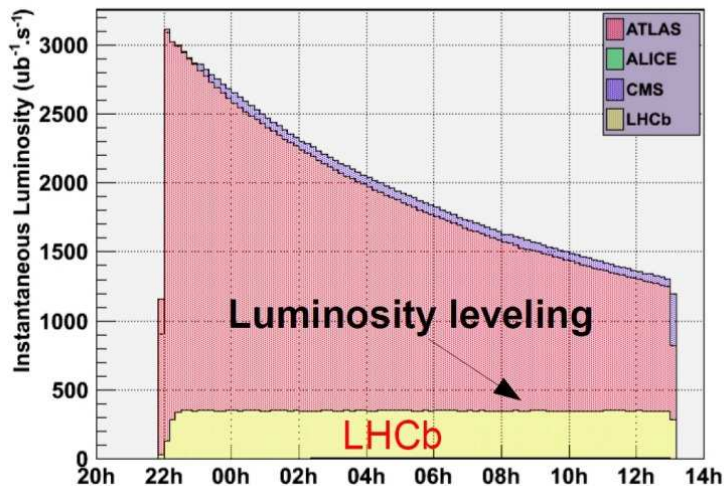
Figure 3.19: *Instantaneous luminosity of a fill as a function of time, for the different LHC experiments. While the instantaneous luminosity in ATLAS and CMS decreases exponentially, the luminosity leveling technique allows to have an approximately constant value in LHCb.*

collisions and so to operate at a luminosity lower than the total available. Beam separation is done fully automatically in communication with the LHC. First, the distance betweem beams is set to be quite large, then the beams are gradually brought closer to the optimal positions by steps that are chosen taking into account the beam size. As the fill goes, the luminosity drops due to the dispersion of the beams and the collisions themselves, so beams are again moved closer to each other periodically to maintain the luminosity level. When the fill is a long one (more then 12 hours approximatively), beams will eventually collide head-on, the leveling will be disabled and luminosity will begin to drop with time as it does in the other experiments. This is illustrated in Figure 3.19.

It is important to take into account that other parameters of the machine play a role on the luminosity seen by an experiment, which makes that the LHCb head-on luminosity is not the same than the one in ATLAS or CMS. The β^* parameter regulates the focusing of the beams in the interaction point[18]. It is set to 3 m in LHCb, while in these other experiments it is around 1 m. This means that luminosity leveling could also be achieved tuning this parameter instead of varying the beams separation. On the other hand, this has implications on the pile-up of the experiment and the divergences of the beams. The different technical choices have to be studied for operation after the long technical stop, when luminosity will be nominal and new settings will be necessary.

---

[18]This parameter, together with the emittance ϵ, determines the beam transverse size as $\sigma = \sqrt{\epsilon\beta^*}$ which is equal to 40 μm in LHCb.

Chapter 4

L0 Hadron trigger efficiencies

The trigger system is a fundamental element in a hadronic machine environement such as that of LHCb. As explained in Section 3.3, it reduces the huge amount of data produced by the proton-proton collisions to a reasonable size that can be written to disk. This is done by means of dedicated trigger decisions that select interesting events for the LHCb offline analysis, while maximising the background rejection. The L0 Hadron is part of the calorimeter hardware-implemented trigger, and it is of prime importance for the selection of hadronic B decays.

A significant task of this thesis is the computation of the L0 Hadron trigger efficiencies: not only for monitoring the calorimeters and its trigger-related behaviour, but also for offline analysis use when hadronic channels are involved. A tool has been created in order to provide the LHCb Collaboration with a simple way of computing the L0 Hadron trigger efficiencies that enter physics results computations. The L0 Hadron trigger architecture, the algorithm for efficiency computation and the interpretation of the efficiency curves are presented in this chapter.

4.1 The calorimeter trigger system

The L0 calorimeter trigger [79] identifies and selects the highest transverse energy E_{T} deposit associated to an electron, a photon, a π^0 or a hadron candidate. Two types of π^0 candidates are considered, local and global, which depend on the separation of the energy deposits of the two photons that the π^0 decays to[1]. The system uses the information of the four calorimeter detectors (*c.f.* Section 3.2.4): the SPD, which identifies charged particles and thus differenciates electron from photons; the PreShower, which identifies electromagnetic particles; the ECAL, which measures electromagnetic showers; and the HCAL, which measures hadronic showers. The calorimeter trigger is hardware-implemented, and operates synchronously with the LHC collisions.

A schematic overview of the L0 calorimeter trigger is presented in Figure 4.1. A trigger candidate is a cluster of 2×2 cells. Considering the typical size of the particle showers in the calorimeter, this choice is large enough to contain most of the shower energy (95 %), and at the same time small enough to avoid overlaps between different particles[2]. The selection of the final candidates is performed in three steps, in different electronics boards:

---

[1]The architecture for the local and global π^0 triggers is in place. However, these are not used for the moment in LHCb.

[2]However, in for offline analysis 3×3 cell clusters are considered, so that no energy is lost. The 2×2 cell cluster choice in the trigger is a good compromise and reduces the complexity in the electronics.
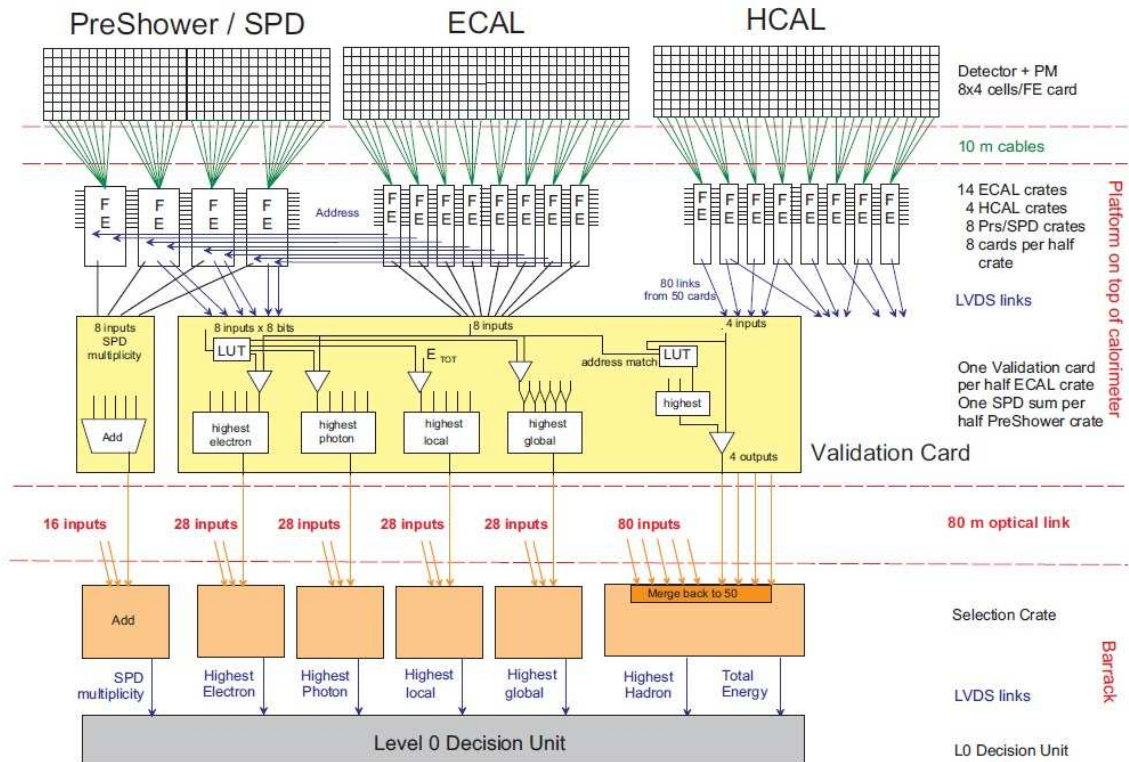
Figure 4.1: *The L0 calorimeter trigger system. The scheme shows the electronics architecture, which provides an overview of the system operation.*

- The Front End (FE) Cards: the highest E_T 2×2 cell cluster in each card is selected as a trigger candidate.

- The Validation Cards: the type of electromagnetic candidate is identified; the ECAL energy deposit is added to each HCAL candidate; the SPD multiplicity of each card is computed.

- The Selection Crate: the final highest E_T candidate of each type over the whole calorimeter is selected; the total E_T in the HCAL is computed; the total SPD multiplicity is computed.

A single energy deposit can produce several trigger candidates, as the electron, photon or π^0 triggers are not mutually exclusive. In addition, a hadron leaving a large energy deposit in the ECAL can produce an electromagnetic candidate. This overlap is useful for the robustness of the system, although it makes the study of the trigger performance of each candidate type difficult.

The FE Cards and the Validation Cards are located on the platform of the calorimeter and are designed to cope with the radiation dose resulting from the collisions in this area; the Selection Crate is located in the barracks behind the detector, which are radiation safe. The latency of the system, taking into account the internal processing time, the transport time and the delays for synchronisation of the inputs, is 750 ns. Once the final candidates are selected, the L0 Decision Unit (L0DU) produces a trigger decision. This is done by comparing the energy of each type of selected candidate to the thresholds set in the Trigger Configuration Key (TCK) (*c.f.* Section 3.3.1). In addition to the calorimeter trigger, the L0DU receives the inputs from the muon and the pile-up trigger systems, and produces also decisions from them.
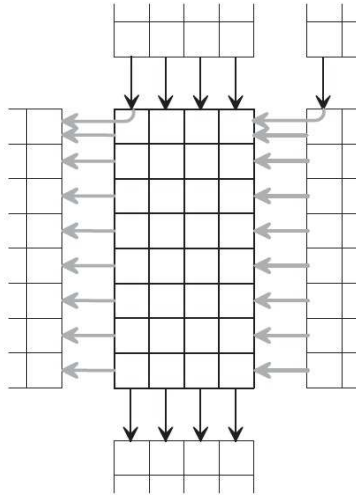
Figure 4.2: *Neighbour access scheme for the Front End Cards, required to perform the 32 E_{T} sums corresponding to the 2 × 2 cell clusters.*

4.1.1   The Front End Cards

A Front End (FE) Card covers an area of 8 × 4 ECAL or HCAL cells. There are 188 FE Cards in the ECAL, and 50 in the HCAL. After digitisation of the energy deposit measurements from the calorimeter PMTs, the sum of the E_{T} in each 2 × 2 cell cluster is performed, in parallel for the 32 possible clusters. To do so, access to the neighbour cards is needed, more precisely to 8 right neighbour cells, 4 top ones, and the top-right one, as shown in Figure 4.2. It should be noted that cells of different sizes are not connected, to avoid introducing too much complexity; neither are the two halves of the detector, which needs to be opened regularly for maintenance. The inefficiency due to these missing connections is very small, of the order of 0.1 %.

The 2 × 2 cell cluster E_{T} sums are saturated at 5.1 GeV. This does not have an effect on the trigger performance, as the trigger thresholds are always kept below this value. The highest of the 32 sums is selected by performing a 5 step binary comparison (first, 16 comparisons of 2 sums, then 8 comparisons of the previous results, and so on).

Besides, the total E_{T} of the card is calculated by summing the E_{T} of the appropriate 2 × 2 cell clusters. This sum is the input for the local π^0 trigger. Finally, three pieces of information per card are sent to the next stage: the highest E_{T} sum, its position and the total E_{T} of the card.

A different FE Card deals with the PreShower and SPD information. It covers an area of 8 × 8 cells. For the two selected candidates from the corresponding ECAL FE Cards, the PreShower FE assigns the boolean PreShower and SPD information: the PreShower and SPD signals are compared to a threshold, and are classified as "hits" when they pass it[3]. The total SPD multiplicity of a card is also computed, by counting how many cells have fired.

4.1.2   The Validation Cards

The Validation Card has two tasks: to determine the type of the electromagnetic candidates, and to add the corresponding ECAL deposit to each HCAL candidate.

---

[3]The reader should keep in mind that the PreShower detect electromagnetic showers, and the SPD identifies charged particles; no energy measurement from these two detectors is used in the trigger. A "hit" signals an electromagnetic candidate for the PreShower, and a charged particle for the SPD.

There are 28 Validation Cards, each one of them connected to a maximum of 8 ECAL FE Cards. To determine the type of the electromagnetic candidates, it uses the information provided by the PreShower FE Card. A photon flag is assigned when PreShower hits are present but there are no SPD hits. An electron flag is assigned when there are hits in both the PreShower and the SPD. No PreShower or SPD conditions are required for a π^0 trigger. In the case of the local-π^0 decision, the two photons coming from it are expected to be on the same FE Card, and the E_T sum of this card is used as a measurement of the π^0 E_T. For a global-π^0 candidate, the two photons will appear on two neighbouring FE Cards, and its E_T is obtained by adding the E_T of the candidates of these two cards. The position of the global-π^0 candidates is chosen arbitrarily as the position of the candidate in the first card. For each type of electromagnetic trigger candidate, the one with highest E_T out of the 8 FE Cards associated with each Validation Card is kept, and sent to the next stage together with its position.

Regarding the HCAL candidates, the Validation Card adds to each one of them the E_T deposit from the ECAL candidate in front. To do so, the information on the HCAL candidates is sent to the Validation Cards. As the cell size is different in the ECAL and the HCAL, sometimes more than one ECAL candidate can be in front of an HCAL one. In such a situation, the candidate is duplicated to save all cases.

In addition, the SPD multiplicity of each group of 8 PreShower FE Cards is computed at this level, in the SPD Control Boards.

4.1.3   The Selection Crate

The Selection Crate identifies the highest E_T candidate of each type, by successive binary comparisons, out of 28 inputs from the ECAL and 50 from the HCAL. In the case of the HCAL, the duplicate candidates from the Validation Cards are removed beforehand, by keeping the one with highest E_T out of each pair. The final candidates and their positions are sent to the L0 Decision Unit. The total SPD multiplicity is also computed, adding the information from all the SPD Control Boards. The E_T of each HCAL FE Card is added, to compute the total E_T deposited in the event in the HCAL. This information is used for two purposes: on one hand, to detect minimal activity in the detector, by comparing the total E_T with a threshold of a few hundreds of MeV, and on the other hand to identify and veto dirty events.

4.1.4   The L0 Decision Unit

The L0 Decision Unit (L0DU) receives the inputs from the calorimeter, muon and pile-up L0 trigger systems, in order to perform the decision of keeping or rejecting the event. The subdetectors send their information synchronously with the bunch crossing frequency. The latency of the L0DU is 500 ns. The L0DU performs a simple algorithm to combine all the signatures into one decision per crossing. The different conditions set to select different trigger types are called trigger lines. Several thresholds can be set for each trigger type, and downscaling[4] of the trigger lines is also possible. In addition, events with high SPD multiplicity are rejected, as they take too long to be processed in the HLT (*c.f.* Section 3.3.2). The different trigger lines are added by a logic OR, which means that overlap between them is allowed. The thresholds for each trigger decision are set in the Trigger Configuration Keys (TCKS), and detailed in Section 3.3.1. The thresholds for the L0 Hadron trigger line in 2011 were $E_T > 3.6$ GeV and SPD multiplicity < 600, while in 2012 $E_T > 3.5 - 3.74$ GeV and SPD multiplicity < 600.

---

[4]To meet the limitations of the system, the output of the trigger lines can be reduced by a proportional factor, or "downscaled". In this case not all the events passing the line thresholds are kept, but only the chosen proportion. For example, if the downscaling is 0.5, only one out of every two events will be selected, in a random way.

On top of the L0DU, the Readout Supervisor controls the trigger rate, taking into account the status of the different components in order to prevent overflows. Thus the final decision of keeping the event is done here: the Readout Supervisor can disable triggers, send a forced trigger, etc.

The readout of the detector data is done by TELL1 boards. If the L0 trigger decision is positive, the event is then sent to the next stage, the HLT1 trigger (*c.f.* Section 3.3.2). The global output rate of the L0 trigger system is 1 MHz.

4.2   The role of L0 Hadron trigger efficiency in physics analysis

Knowing accurately the efficiency of the trigger in an experiment is essential, for several reasons. First of all, the performance of the trigger needs to be watched and understood, to make sure that the detector is working properly througout the data taking. Looking at the trigger efficiencies is a way of monitoring the trigger and the relevant subdetectors behaviour.

In addition to this, the trigger efficiencies need to be known for physics analysis. As the trigger rejects inevitably some signal events together with the undesired background, the efficiency of this "cut" is used in physics analysis to recover the real number of events decaying to a certain channel produced by the proton-proton collisions.

Most of the searches in LHCb are based on measuring ratios and asymmetries between branching ratios. Classically, an analysis consists on the application of a certain selection criterion to the data, optimised to increase the significance of a certain decay channel with respect to the background in the sample, followed by a fit to the invariant mass of the selected B candidates. The yields extracted by the fit are related to the branching fraction of the decay of interest as

$$N = L_{int} \times \sigma_{b\bar{b}} \times 2 \times f_q \times BR_{vis} \times \epsilon_{tot}, \tag{4.1}$$

where N is the measured number of events from the fit, L_{int} is the integrated luminosity on which the analysis is based, $\sigma_{b\bar{b}}$ is the cross-section of the production of a $b\bar{b}$ pair from the proton-proton collisions ($\sigma(pp \to b\bar{b}X) = (284 \pm 20 \pm 49)$ μb measured by LHCb at the centre-of-mass energy $\sqrt{s} = 7$ TeV [70]), the factor 2 is needed to take into account the decay and its charge-conjugate at the same time (ignoring CP violation), f_q is the probability of a b-quark to hadronise into a given type of B meson, BR_{vis} is the visible branching fraction of the decay, which takes into account the sequence of subdecays down to the final particles visible by the detector, and ϵ_{tot} is the product of the efficiency of all the cuts applied to the data sample. In its most general way, this efficiency can be written as

$$\epsilon_{tot} = \epsilon_{acc} \times \epsilon_{rec} \times \epsilon_{sel} \times \epsilon_{trig}, \tag{4.2}$$

that is to say the product of the geometrical acceptance, the reconstruction efficiency, the selection efficiency and the trigger efficiency. ϵ_{trig} should include the efficiency of the L0 trigger and the efficiency of any specific HLT trigger lines to the channel of interest.

The analysis presented in this thesis studies a B meson decay to purely hadronic final states. The efficiency of the L0 Hadron trigger is one of the inputs needed in the computation of the final result. The study of the L0 Hadron trigger efficiency, together with the implementation of a method for the LHCb Collaboration to work out the L0 Hadron efficiency corresponding to any hadronic decay, has been an important part of this thesis work, which is presented in the following sections.

4.3   Trigger simulation

A great amount of effort has been made in order to simulate the calorimeter trigger system in the LHCb Monte Carlo productions. Every step, from the Front End electronics to the different possible trigger configurations, is included and implemented in the simulation. This is extremely useful to understand the trigger behaviour and also to monitor the trigger performance during operation. However, this simulation, as exhaustive as it is, can not include all effects playing a role in the trigger. Elements like ageing, disabled cells or occupancy strongly influence the trigger behaviour, but they are very difficult to predict and model, and implementing them in the simulation becomes a hardly conceivable task. This is also the case for other elements of the LHCb detector.

This is the reason why trigger related quantities can not be rigourously extracted from Monte Carlo simulation, and data-driven methods are necessary. Measurements such as L0 trigger efficiencies, necessary in physics analysis as explained in Section 4.2, can only be reliably performed using real data. More details on this subject are given in Section 4.5.5 and 4.6.

4.4   "Real" transverse energy: what the HCAL measures

The measurements given by the calorimeter cells correspond to transverse energies[5]: the hadrons arrive to the HCAL and are stopped there, depositing their energy in the cells, which is then transformed into transverse energy using the coordinates of these cells. Let (x, y, z) be the position of the centre of the cell in cartesian coordinates (for the HCAL, $z = 13.33$ m measured from the interaction point), then the transverse energy is calculated as

$$
\begin{aligned}
E_{\mathrm{T}} &= E \times \sin\theta, \\
\sin\theta &= \sqrt{\frac{x^2 + y^2}{x^2 + y^2 + z^2}},
\end{aligned}
\tag{4.3}
$$

where E is the energy carried by a particle that it deposits in the calorimeter cells, and θ is the angle between the beam direction and an imaginary straight line linking the centre of the cell and the interaction point. This energy corresponds to $E = \sqrt{p^2 + m^2}$, where p is the momentum of the particle and m is its invariant mass. The same is true for electromagnetic particles being stopped by the ECAL.

In addition to the energy of the particles, LHCb also measures their momentum. The magnet bends the trajectory of charged tracks, which allows the tracking system to measure the corresponding momentum p and transverse momentum p_{T} (*c.f.* Section 3.2.2). It is important to note that, while the energy is conserved, the same is not true for transverse quantities, due to the magnet bending the particle tracks. One should be careful when studying calorimeter performances, as the p_{T} of a particle is not the same when crossing the tracking system and at the HCAL level, and thus it is not directly correlated to the E_{T} that the HCAL measures.

This is illustrated in Figure 4.3. Tracks of particles with opposite charge are bent by the magnet in opposite directions: in the picture, the pink and green tracks correspond to particles of same charge, as well as the blue and grey tracks (with opposite charge to the previous two). If we take into account the angle θ computed from the HCAL cells coordinates, we can see that a transverse magnitude associated to the grey track (supposing magnet polarity "Up", charge $+$, positive half of the HCAL $x > 0$) will be overestimated with respect to the same quantity measured in the trackers. In the case of the green track (charge $-$, $x > 0$) a transverse quantity

---

[5]Transverse with respect to the beam direction.

Figure 4.3: *Diagram representing tracks coming from the interaction point and impacting on the HCAL, seen from the top. The tracks are bent by the magnetic field in one direction or the other depending on their charge Q. The dashed lines show the difference between the transverse energy carried by the particles when produced at the interaction point and the E_T measured by the HCAL. The same effect applies to any other transverse quantity. The conclusions are the opposite if the magnet polarity is reversed (up in the scheme).*

will be underestimated at the HCAL level with respect to the trackers measurement. For the same charge, the conclusions are the opposite when taking into account the other half of the HCAL: the blue track (charge $+$, negative half of the HCAL $x < 0$) will be underestimated, the pink track (charge $-$, negative half of the HCAL $x < 0$) overestimated. It should also be noted that all these statements become the opposite when reversing the magnet polarity.

In order to perform a correct comparison between the transverse energy carried by a particle and the associated transverse energy E_T measured by the HCAL as shown in Equation (4.3), it is necessary to compute the first one using tracking information, but at the HCAL z position. We call this quantity E_T^{real},

$$E_\mathrm{T}^{real} = \sin\theta^{track} \times \sqrt{p^2 + m^2},\tag{4.4}$$

where θ^{track} is computed as in Equation (4.3) but using the coordinates of the particle track projection from the tracking system to the HCAL, p is measured by the trackers and m is the mass of the particle.

The L0 Hadron trigger efficiencies are not constant throughout the E_T spectrum, due to the fact that there is a threshold that rejects particles not carrying enough energy. That is why these

efficiencies need to be given as a function of the energy or, for practical reasons, as a function of a transverse quantity. To avoid inconsistencies, the efficiencies need to be given as a function of E_{T}^{real} computed at the HCAL level using Equation (4.4), instead of the more straightforward p_{T} measured by the tracking system.

4.5 L0 Hadron trigger efficiencies computation: algorithm development

To study the L0 Hadron trigger behaviour, a part of the work of this thesis has been dedicated to develop an algorithm that retrieves the calorimeter information related to the trigger for selected particles. Two different methods resulted, which are detailed and compared in this section. Before this, the concept of "trigger independent of signal" is introduced, needed in the efficiency algorithms.

4.5.1 An important concept: triggering independently of signal

As discussed in Section 4.3, to study the detector performance, and particularly the trigger, we need to use real data. But, in order to be kept and written on disk to be analysed, any data needs to trigger. In other words, all available data has necessarily been triggered by a L0 line.

When we study the performance of the L0 Hadron trigger, we need to make sure that we are not allowing any bias. This can happen when using data that has been mostly triggered by the L0 Hadron line, which would give misleadingly high efficiencies. That is to say, we need to ensure that we use a data set which corresponds to a "trigger independent of signal", or TIS data set, where the "signal" are the tracks that we use for the L0 Hadron efficiency computation.

Several TIS methods have been developed and tested. The way to test them is to use simulation data, where a trigger requirement is not applied beforehand and so they are not biased by default, without needing additional requirements. The three TIS methods that have been studied are:

- TIS Hadron: requires that there is at least one L0 Hadron trigger object (*i.e.* one 2×2 cell cluster candidate) above the threshold in the event which is independent of the signal (where the signal is defined as a 3×3 cell cluster around the cell corresponding to the track projection).

- TIS Muon/Dimuon: requires that there is at least one L0 Muon or one L0 Dimuon trigger object above the threshold in the event which is independent of the signal.

- TIS from distance: requires that, in addition to the L0 Hadron candidate associated to the track projection to the HCAL using the method explained in Section 4.5.2, there is another one in the event above the threshold which is at least 450 mm away from the projection (the 450 mm cut is chosen taking into account the size of the HCAL cells).

The L0 Hadron efficiency is computed for simulation data as a function of p_{T}, for four different cases: without TIS, which gives the "true" efficiency (*i.e.* no signal events are rejected by the trigger), and with each one of the TIS requirements applied. The results are all fully compatible.

The TIS Hadron and TIS Muon/Dimuon methods are implemented using the L0 TISTOS tool that is explained in Section 4.5.3; the implementation of TIS from distance is part of the work of this thesis and has been developed together with the efficiency computation method of Section 4.5.2.

4.5.2   Method 1: efficiency computation using distances

The L0 Hadron trigger can be studied through the distance between particle projections on the HCAL and the available trigger candidates. Tracks measured in the tracking system are projected to the HCAL, to the plane of maximum particle shower development, $z = 13.33$ m from the interaction point. This allows to identify the cell hit by the particle, which deposits its energy in it and in the surrounding ones. In parallel, the trigger readout system allows to retrieve offline all the L0 Hadron trigger candidates, that is to say all the selected 2×2 cell clusters of highest E_T per Front End Card, see Section 4.1.1.

The distances between the track projection and each one of the L0 Hadron candidates is computed. The candidates close to this projection by a distance lower than 250 mm (450 mm) if looking at the Inner (Outer) region are retrieved, and the highest E_T candidate among them is kept. These distances are set taking into account the size of the HCAL cells, and are slightly larger than a cell diagonal[6]: they can be understood as the maximum distance between a projection and the trigger candidate that it creates. In the case that no candidate appears inside this distance, the closest candidate to the projection is selected. When making these projection-candidate pairs, only L0 Hadron candidates with E_T higher than the L0 Hadron threshold set for the event, and particles with projection inside the HCAL acceptance, are looked at. In addition, a requirement to avoid biases, which can happen when taking into account a too large proportion of L0 Hadron triggered events, needs to be applied, as discussed in Section 4.5.1.

The distributions of the distance dr between the particle projections and their associated L0 Hadron candidate are represented for simulation data in the two right hand panels of Figure 4.4. The top panel corresponds to particles with projection in the Inner region of the HCAL, and the bottom panel corresponds to the Outer region. There is a peak or accumulation of entries at low values of the distributions, which contains particles where the association projection-candidate is the correct one. Particles entering the distribution to higher dr values have their associated candidate too far away, and are just random associations.

Using these distributions, the L0 Hadron trigger efficiency can be computed as

$$\epsilon = \frac{\text{events under the peak}}{\text{total number of events}}, \tag{4.5}$$

where again only events inside the HCAL acceptance are considered. To do so, the distributions are fitted in order to reproduce the shape at best and to count the number of signal events in the peak at low distances, corresponding to good projection-candidate associations. Two components are present in these distributions: the signal, which is fitted using three Gaussian distributions with different mean and resolution, and the background.

To model the background, random associations are generated using mirror events, as shown in Figure 4.5: for each particle, its projection is replaced by its mirror one, that is to say, each pair of projection coordinates (x, y) is replaced by $(-x, -y)$; then the associated L0 Hadron trigger candidate to this mirror projection is searched as previously explained. The distribution of the projection-candidate distance for these random associations is shown for simulation data in the left hand panels of Figure 4.4, where the top distribution corresponds to projections in the Inner region of the HCAL, and the bottom distribution to the Outer. Each distribution is fitted using a polynomial function of order 3 with all parameters floating. The fitted shape for each HCAL region is then used to fit the background component of the real projection-candidates association distributions of the right hand side of Figure 4.4, fixing all the parameters except the normalisation.

---

[6]These values can be checked to be appropriate *a posteriori* when looking at the projection-candidate distance distributions, shown in Figure 4.4.
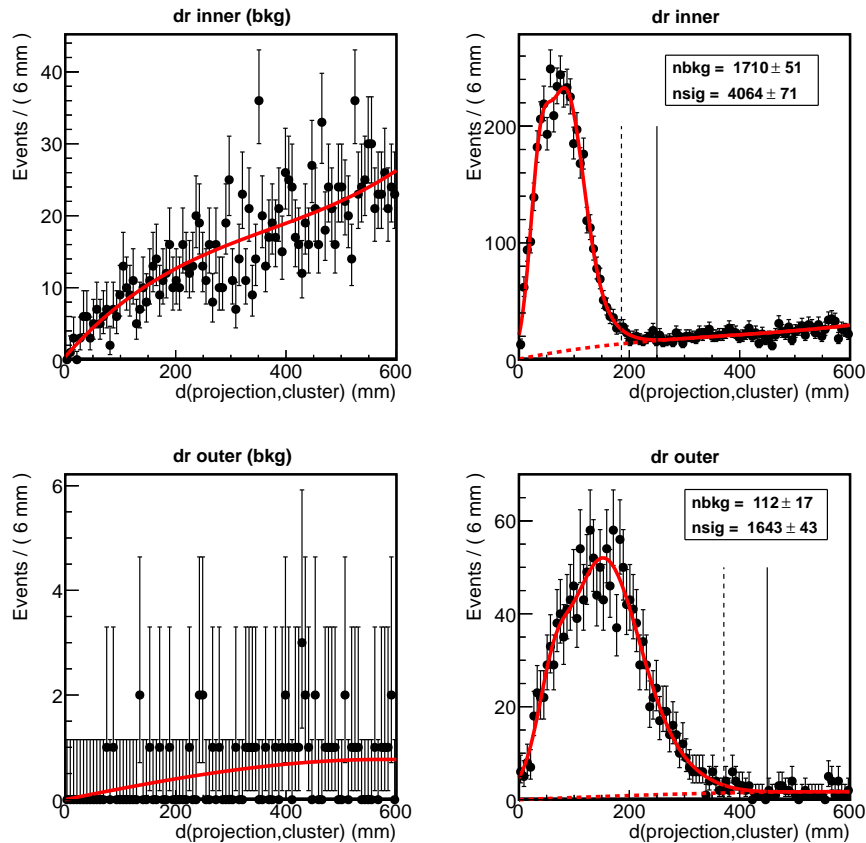
Figure 4.4: *Distributions of the distance between a projection of a particle to the HCAL and the associated L0 Hadron trigger candidate cluster above the threshold, for $\pi^{\pm}$ from simulation. The two left panels correspond to random distributions, generated from the mirror projections, used to model the background in the right hand side plots. The two top panels use projections in the Inner region of the HCAL, while the two bottom ones use projections in the Outer region. The dashed vertical lines in the right-hand plots illustrate the distance corresponding to a cell diagonal; the continuous vertical lines mark 250 mm in the Inner region and 450 mm in the Outer, which indicate approximately the maximum distance between a projection and its corresponding trigger candidate when the association is correct.*
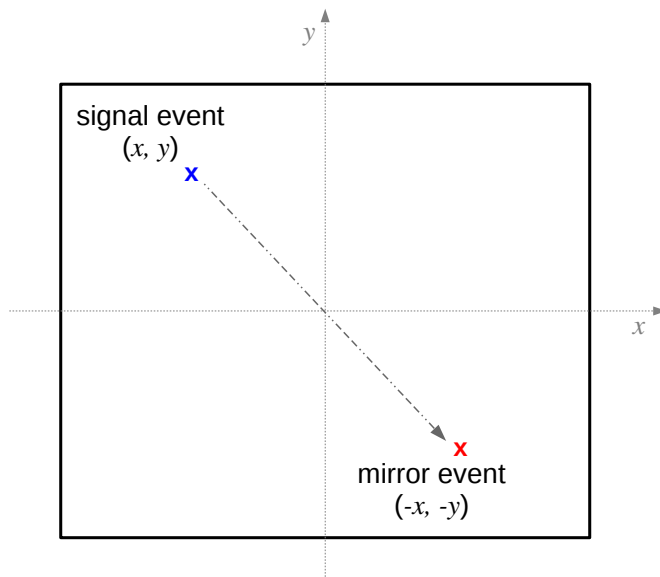
Figure 4.5: *Schematic explanation of mirror events: the coordinates of each projection on the HCAL are reversed, then treated normally to look for the associated L0 Hadron candidate. This generates random projection-candidate associations, which are used to model the background as explained in the text.*

4.5.3 Method 2: efficiency computation using the "L0 TISTOS tool"

L0 TISTOS tool: a trigger class in the LHCb software

The LHCb software, which is developed and constantly enlarged in a collaborative way, contains a wide variety of C++ classes to access information from the different detector subsystems. One of the classes concerning the trigger is the so-called L0 TISTOS tool.

This class takes a particle as signal input, and allows to know if this particle is responsible for triggering the event with respect to a given L0 trigger line or trigger decision. To do so, in the case of the L0 Hadron trigger, the particle is projected to the HCAL and a 3×3 cell cluster is built around the cell corresponding to the track projection; this is the signal. In parallel, all the L0 Hadron trigger candidates from the FE Cards which have an E_{T} above the L0 Hadron threshold are kept: as explained in Section 4.1.1, these are 2×2 cell clusters, and only the one with highest E_{T} per FE Card is kept as a candidate. The signal 3×3 cell cluster is compared with the trigger objects, and the event can be classified in two non-exclusive categories:

- Trigger On Signal (TOS): The particle could be responsible of triggering the event. This means that at least one of the trigger objects has one or more cells in common with the signal.

- Trigger Independent of Signal (TIS): The particle is not responsible (or not responsible alone) of triggering the event. Trigger objects exist, but at least one of them has no cell in common with the signal cluster[7].

---

[7]An event can not be TIS if there are no trigger candidates of the requested type (we focus on the L0 Hadron line, so in our case they are 2×2 HCAL cell clusters) above the threshold. This category tells us that the L0 Hadron trigger conditions are fullfiled, by asking that at least one trigger object exists, but that it does not correspond to the given signal particle. The TIS and TOS classifications depend on each particular trigger line.
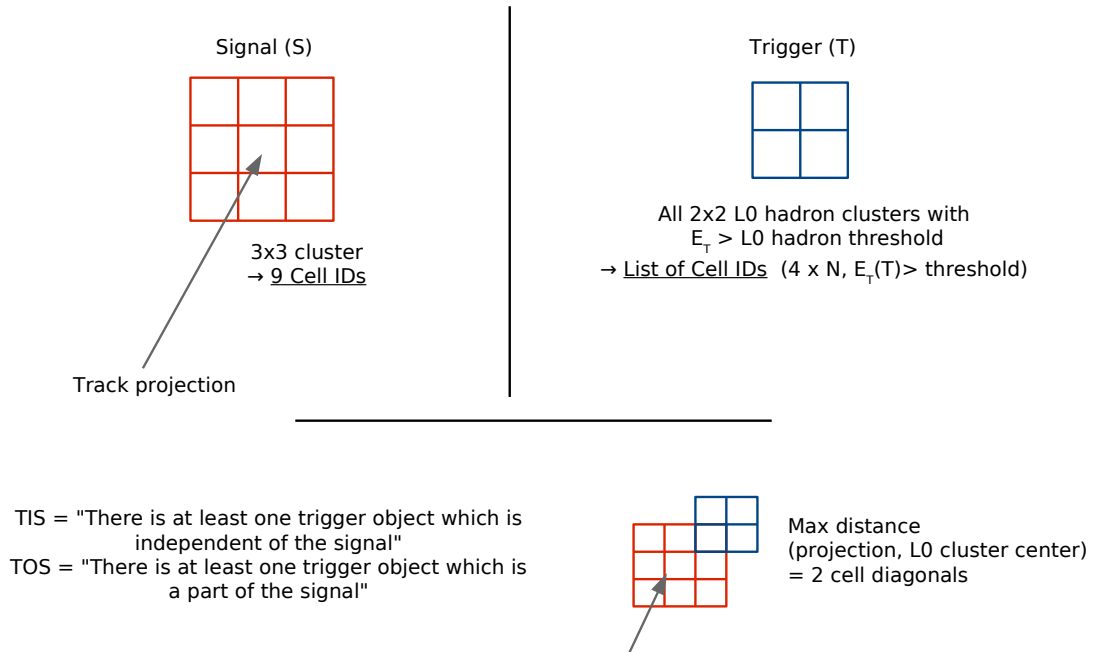
Figure 4.6: *Schematic explanation of the L0 TISTOS tool algorithm.*

This is illustrated also in Figure 4.6. It is important to note that an event can be TIS and TOS at the same time. Furthermore, an event being TOS does not mean that the trigger would not have fired without the signal particle, but only provides the information that the particle gives a trigger object above the threshold. Other particles can exist in the event that produce a trigger, of hadronic type or other type. The same algorithm exists for the Muon trigger lines, which projects the particle track to the muon chambers and compares it to the L0 Muon trigger candidates, to perform the same type of classification.

Efficiency computation using TISTOS

The L0 TISTOS tool can be used to build an alternative method for the L0 Hadron trigger efficiency computation. This second method is also part of the work of this thesis. The efficiency can be defined as

$$\epsilon = \frac{\text{number of (TOS \& TIS) events}}{\text{number of TIS events}}, \tag{4.6}$$

always using only particles with projection inside the HCAL acceptance. The TOS classification is obviously made with respect to the L0 Hadron line; TIS uses one of the three possibilities listed in Section 4.5.1. The implementation of this method is much simpler than the one explained in Section 4.5.2, as it is only a counting exercise and no fits need to be performed, which avoids problems when the statistics available are low.

4.5.4 Method comparison

At this point, two methods are available for the computation of the L0 Hadron trigger efficiencies:

- Projection-candidate distance method, detailed in Section 4.5.2. It uses the LHCb track projection algorithm and takes into account the cell sizes to interpret the distance between the projection and the trigger candidates. A fit to the projection-candidate distribution is needed for each p_T bin when computing the efficiencies as a function of this variable.

- TISTOS method, detailed in Section 4.5.3. Based on the L0 TISTOS class available in the LHCb software, it counts the number of particles that trigger or not the event and computes their ratio. It is much faster and less resource consuming that the previous one, allowing to use a much larger number of p_T bins. On the other hand, it is less transparent.

The two methods are compared in order to cross-check each other. We should recall now that both methods use a TIS requirement applied to the data set, in order to avoid biases, as explained in Section 4.5.1. The L0 Hadron efficiency curves as a function of p_T are given in Figure 4.7, requiring either TIS Hadron or TIS Muon/DiMuon[8], for well identified pions from $D^0 \rightarrow \pi^+ K^-$ decays for 2010 calibration data and simulation. The efficiency goes up with p_T, as expected from the effect of the L0 Hadron threshold. The two regions of the HCAL are treated separately, and the two methods described are shown.

Let us analyse these plots. If we focus on the TIS Hadron data set (top panels of Figure 4.7), we can see that there is a difference between the distance and the TISTOS method for both data and simulation. This is due to the background modelled from mirror events in the fit for the distance method: these events are not counted as signal, while they are TOS in the TISTOS method, and thus this latter gives a higher efficiency. This effect is more noticeable in the Inner region (left panel) than in the Outer (right panel), which is expected as there is more background in the projection-candidate distance distribution for the Inner region than for the Outer one, as shown in Figure 4.4. The two plots for the TIS Muon/DiMuon data set (bottom panels of Figure 4.7) show a better agreement between the two methods, which is again explained due to the background, much more reduced in this case (the larger error bars here show that this TIS requirement rejects a larger number of events than the Hadron one).

We conclude that both methods are understood, as well as the small disagreement between them. We choose the TISTOS method for a more exhaustive analysis of the L0 Hadron trigger efficiencies, as it is easier to implement and more functional. To avoid biases in the efficiency computation on real data, we will require the data sets to be classified as TIS by the Muon/DiMuon line decision. Moreover, in LHCb analysis the data are usually required to be TOS by the appropriate L0 line, to enforce the quality of the events being studied, so what is needed to be known in physics analysis is the L0 Hadron TOS efficiency, which we actually compute with the TISTOS method.

There is another important issue that we remark when looking at these plots: the efficiencies on real data are always lower than the ones on simulation. This is discussed in the next section.

4.5.5 Differences between trigger simulation and data

The plots in Figure 4.7 show a difference between the L0 Hadron trigger efficiencies computed on real data from those computed on simulation: the trigger appears to be more efficient on simulation than what it is on real data. This subject has been broadly discussed and it indicates that the trigger model in simulation is not accurate enough.

Several tests have been made to understand the reason for this, which are shown in Figure 4.8. The ratio of efficiencies on real data divided by efficiencies on simulation data is shown as a function of p_T. Different L0 Hadron thresholds, namely 2.6 GeV, 3.6 GeV, 4.0 GeV and 4.9 GeV, have been tested, which are shown on the two top panels, for each one of the HCAL regions. The

---

[8] An additional requirement needs to be made in the case of TIS Muon/DiMuon. In the TISTOS method, we are using the Hadron decision for the TOS category. The Muon/DiMuon and Hadron lines decisions do not apply the same SPD cut, as shown in Table 3.1, the cut being tighter for the Hadron line. In order to prevent cutting additional events when asking for TOS Hadron in the TIS Muon/DiMuon data set, we need to require that the SPD multiplicity of the event is smaller than the SPD multiplicity threshold of the Hadron trigger line.
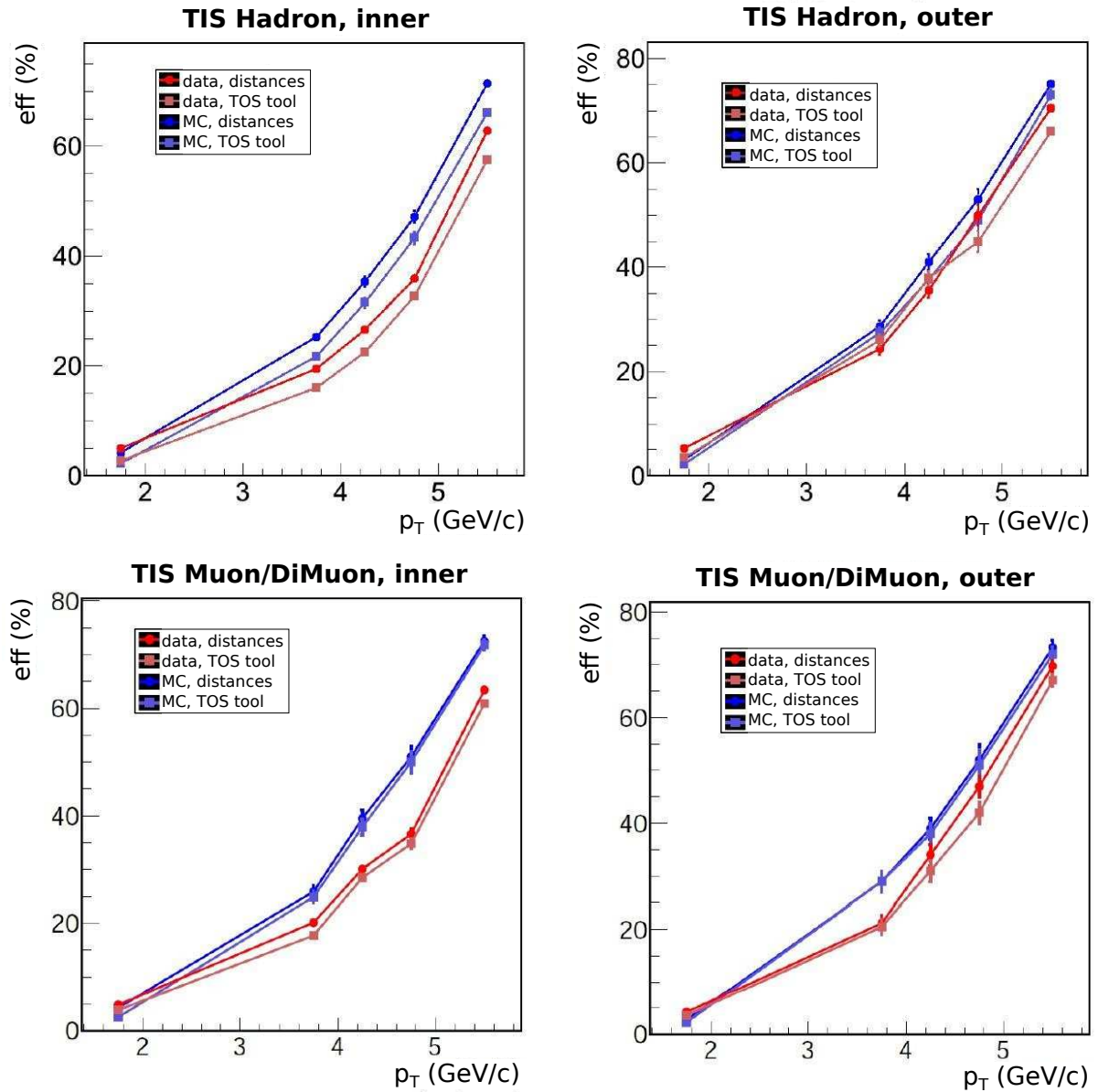
Figure 4.7: *L0 Hadron trigger efficiencies as a function of the transverse momentum for $\pi^{\pm}$ for 2010 real data and simulation, computed requiring the data set to be TIS by the L0 Hadron decision (top) or by the Muon/DiMuon decisions (bottom). The two panels on the left correspond to particles with projection inside the Inner region of the HCAL, while the two on the right correspond to the Outer. Data are represented in red, while Monte Carlo simulation is in blue. The efficiencies computed with each one of the two methods explained in the text are shown, in bright colours for the TISTOS method, in faded colours for the projection-candidate distance method, as indicated in the legends.*
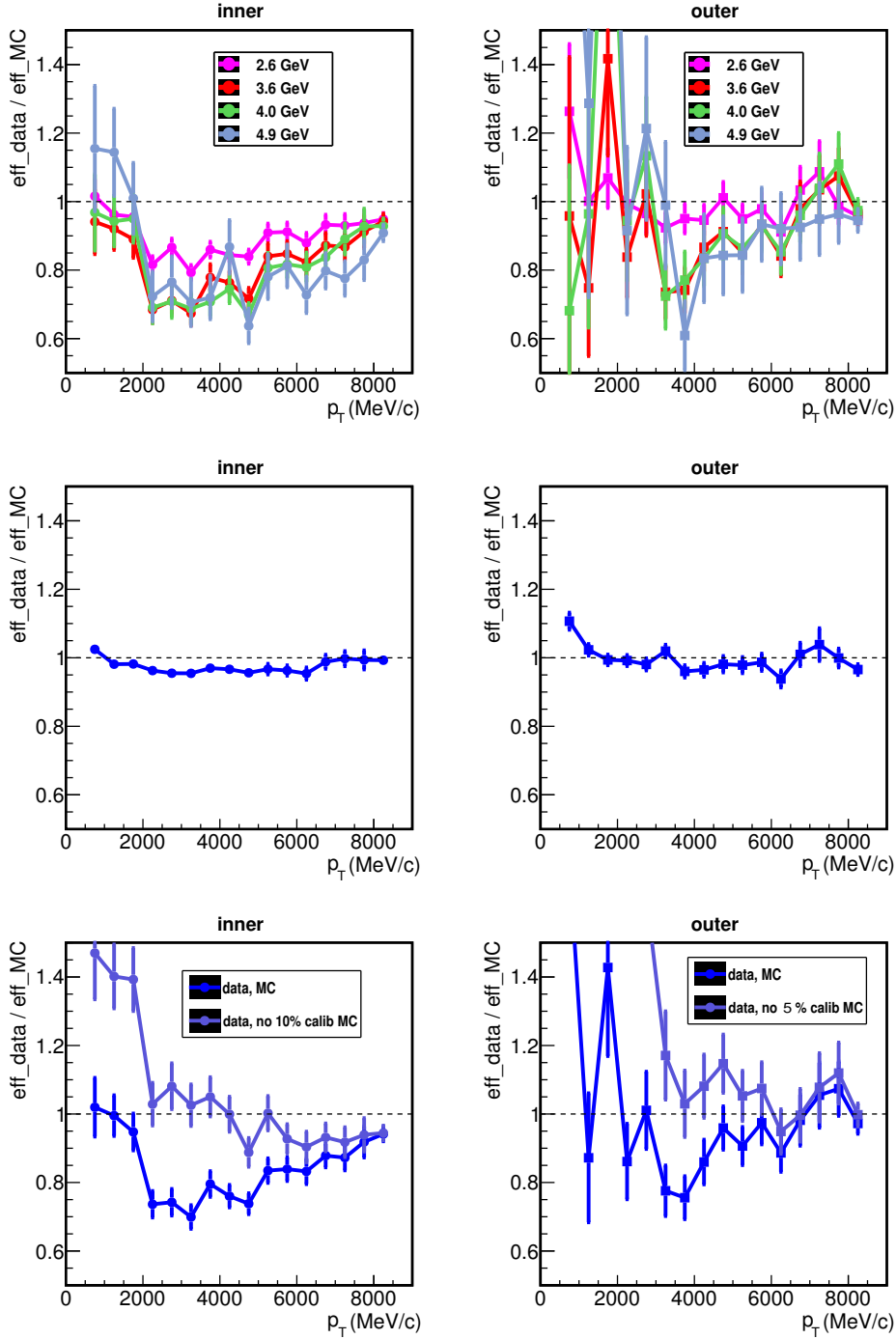
Figure 4.8: *Ratio of L0 Hadron trigger efficiencies for real data over simulation, as a function of the transverse momentum, for $\pi^{\pm}$ for 2010 data and simulation. Panels on the left correspond to the Inner region of the HCAL, while panels on the right correspond to the Outer. Top: for different L0 Hadron thresholds, namely 2.6 GeV, 3.6 GeV, 4.0 GeV and 4.9 GeV. Middle: for a very low L0 Hadron threshold, fixed at 0.4 GeV, insensitive to calibration effects. Bottom: for usual Monte Carlo simulation data, and for simulation corrected for a 10 % calibration factor in the Inner region and 5 % in the Outer region, for the 2010 L0 Hadron threshold, of 3.6 GeV.*

discrepancy between data and simulation, manifesting in a ratio different than 1, is visible in all four cases, especially in the Inner plot, and it does not disapear for high p_T values (far from the effect of the threshold). This can be an indication of a calibration problem (in addition to the other aspects not considered in the Monte Carlo, as discussed in Section 4.3). We test a much lower threshold, down to 0.4 GeV, which is too low to be sensitive to calibration effects: this is what is shown in the middle panels of the figure, and the agreement becomes remarkably better.

In the LHCb simulation, there is an obsolete 5 % global calibration factor applied to the energies, to account for former differences between real data and simulation. In addition, another 5 % factor is applied only in the Inner region, to account for the different cell sizes in the Inner and Outer zones of the HCAL. This makes a total 10 % calibration factor in the Inner region, and 5 % in the Outer, of energy increase in simulation which do not exist in data. We test the real data over simulation efficiency ratios removing these factors in the bottom plots of Figure 4.8: the corrected curve, in faded blue, shows a much better agreement between data and simulation than the default bright blue one, confirming that the difference comes mainly from calibration.

All of this shows that L0 Hadron trigger efficiencies can not be reliably calculated from simulation. This implies that a data-driven method is needed to compute the efficiencies to be used in physics analysis.

4.6 L0 Hadron trigger efficiency for LHCb physics analysis: a data-driven method

4.6.1 Simulation data reweighting

As explained in Section 4.2, the L0 Hadron trigger efficiencies are needed in the computation of results in physics analysis: as the trigger rejects inevitably a fraction of signal together with the undesired background, this fraction needs to be known and taken into account. The philosophy is the same as for any other cut used in the analysis (acceptance, selection, etc.).

The straightforward way to compute these efficiencies, including the one corresponding to the trigger, is to use simulation. As a difference with respect to data, simulation does not have any cuts applied *a priori*, and so all the events produced in the simulated proton-proton collisions are present in the data set. The trigger is then also simulated and the effect can be easily estimated.

This would be right if the L0 Hadron trigger behaviour was correctly reproduced in the simulation, which as we have seen in Section 4.5.5 is not the case. A method has been developed during this thesis to overcome this problem. The starting point is always a simulation data set of the signal which is the object of each physics analysis. Now, instead of making use of the simulation of the trigger effect, look-up tables are generated which give the L0 Hadron trigger efficiency as a function of p_T or E_T^{real} (defined in Section 4.4) for hadronic final particles arriving to the HCAL and thus sensitive of triggering the L0 Hadron line, namely pions and kaons. Combining the final particles from the signal simulation sample, taking into account their p_T or E_T^{real} distribution, the efficiency of triggering on the B hadron event can be computed: the simulation data set is reweighted by means of the efficiency tables.

For example, let us take the simple case of a B decaying to two hadronic particles p_1 and p_2. The efficiency of triggering on the B will be the sum of three terms: triggering on only p_1 and not on p_2, triggering only on p_2 and not on p_1, and triggering on both p_1 and p_2 at the same time:

$$\epsilon_{trig}(B) = \epsilon_{trig}(p_1) \times [1 - \epsilon_{trig}(p_2)] + \epsilon_{trig}(p_2) \times [1 - \epsilon_{trig}(p_1)] + \epsilon_{trig}(p_1) \times \epsilon_{trig}(p_2). \quad (4.7)$$

The mean value computed over all the B events of the data set can now be used as an input for physics computations, as part of ϵ_{trig} in Equations (4.1), (4.2).

This method has been used in the physics analysis object of this thesis, and its application will be shown in Chapter 5 (*c.f.* Section 5.4.3).

4.6.2 L0 Hadron efficiency tables

Look-up tables of the L0 Hadron efficiency in bins of p_T or E_T^{real} have been produced[9] from real data and released to the Collaboration for pions and kaons for the three years of data taking [80], accounting for the different trigger conditions (*i.e.* the different L0 Hadron thresholds) used in each one of them. Pions and kaons are taken from well identified D^0 mesons from D^{*+} decays, with D^0 decaying as $D^0 \to K^- \pi^+$. These D^{*+} data belong to the calibration stream of the LHCb stripping (*c.f.* Section 3.4).

The method applied for the efficiency computation is the one using the L0 TISTOS tool, detailed in Section 4.5.3. The TIS requirement applied to the data set to avoid biases is L0 Muon/DiMuon decision. The binning of the tables is chosen accordingly with the statistics available in the data set: small bins are preferred, but at the same time they need to be large enough in order to avoid bins with 0 % or 100 % efficiency calculated over a too small number of events to be reliable. The efficiency is given for each region of the HCAL, either Inner or Outer. Tables are produced separately for each particle type, for each charge, and the choice is given with respect to the magnet polarity, either up and down separately, either altogether. A look-up table is shown in Figure 4.9. Example plots of these tables are given in Figure 4.10 for 2012 data.

4.6.3 L0 Calo Tuple Tool

At first, tables have been released to the Collaboration as a function of p_T. Even if this is not the optimal quantity for HCAL-related computations, as illustrated in Section 4.4, this variable was preferred at the begining, as it is a common one and always present in reconstructed data for physics analysis by default. The difference in efficiency when using one or the other variable is on average around 2 %.

Nevertheless, LHCb is an experiment dedicated to perform precision measurements. In order to achieve this goal and do things precisely, E_T^{real} should be used. Also the HCAL region hit by the particle needs to be taken into account. This information is not directly present in reconstructed data, but need to be computed through each particle projection. A tool has been written, as part of the work of this thesis in order to make them available for each final particle of a decay, providing the following variables: E_T^{real}, the HCAL region containing the track projection, and the corresponding coordinates (x, y) of this projection[10]. This tool, called "L0 Calo Tuple Tool" (as reconstructed data for physics analysis are given as ROOT nTuples), is coded in C++ and has been added to the LHCb software to make it accessible for the Collaboration. These variables allow to reweight the simulation data as explained in Section 4.6.1, using the L0 Hadron efficiency tables as function of E_T^{real} and taking into account the two different HCAL regions.

---

[9]As explained in Section 4.4, the correct quantity to take into account when looking at particles arriving to the HCAL is E_T^{real}. These tables are an important part of the work of this thesis. Initially, tables have been also produced as a function of p_T, as this quantity is a very commonly used one that is always present in data sets, while making E_T^{real} available needed some code developing, see Section 4.6.3.

[10]Extending the tool to use projections on ECAL instead of HCAL is straightforward, thus the tool gives the choice between the two calorimeters. This allows to extend the trigger efficiency computing data-driven procedure for L0 electromagnetic trigger lines in the future.

ETr_min (MeV)	ETr_max (MeV)	Eff(inner)	err(inner)	Eff(outer)	err(outer)
0	200	0.0146204	0.000938777	0	0
200	400	0.0141047	0.000301756	0.00496278	0.0035005
400	600	0.0144046	0.000200325	0.00323574	0.000504519
600	800	0.0150358	0.000174224	0.00244982	0.000310746
800	1000	0.018558	0.000167859	0.00479006	0.000289213
1000	1200	0.0223123	0.000164199	0.00651918	0.000276069
1200	1400	0.024834	0.000164878	0.00985244	0.000330862
1400	1600	0.0263069	0.000159767	0.0114542	0.000307345
1600	1800	0.0290733	0.000166059	0.0132013	0.000304891
1800	2000	0.0331743	0.000185797	0.0172288	0.000360955
2000	2200	0.0371684	0.000202486	0.021631	0.000423865
2200	2400	0.0413458	0.000213217	0.0275093	0.000488184
2400	2600	0.0485537	0.000230864	0.0352573	0.000552476
2600	2800	0.0577751	0.000268261	0.0457023	0.000679341
2800	3000	0.0701683	0.000317857	0.06146	0.000857621
3000	3200	0.0856358	0.000380541	0.0787205	0.00105105
3200	3400	0.102318	0.000451205	0.10279	0.00128928
3400	3600	0.124942	0.000536513	0.13394	0.00156619
3600	3800	0.150705	0.000631121	0.171331	0.00186374
3800	4000	0.179999	0.000736282	0.216586	0.00216216
4000	4200	0.213996	0.000854025	0.252424	0.00242547
4200	4400	0.249287	0.000976799	0.304556	0.00271919
4400	4600	0.286948	0.00110858	0.357391	0.00299327
4600	4800	0.325954	0.0012344	0.400954	0.00324266
4800	5000	0.361984	0.00136931	0.437208	0.00344415
5000	5200	0.40266	0.00150149	0.486054	0.00364298
5200	5400	0.435023	0.00162861	0.524021	0.00384627
5400	5600	0.469525	0.00176792	0.54899	0.00400298
5600	5800	0.502131	0.00188764	0.585225	0.00418884
5800	6000	0.524106	0.00202308	0.603913	0.00438873
6000	6200	0.54707	0.00215711	0.633582	0.00449187
6200	6400	0.569847	0.00229999	0.647621	0.00471712
6400	6600	0.591803	0.00243493	0.668951	0.00486934
6600	6800	0.609006	0.00258712	0.682502	0.0050479
6800	7000	0.626348	0.00273261	0.689405	0.00522509
7000	7200	0.642176	0.00286559	0.711867	0.00542514
7200	7400	0.650514	0.00302865	0.719503	0.00556489
7400	7600	0.666576	0.00318154	0.719374	0.00589357
7600	7800	0.678264	0.00332437	0.734797	0.00604771
7800	8000	0.683097	0.00350819	0.743868	0.00618909
8000	8200	0.690908	0.00367968	0.751919	0.00648904
8200	8400	0.697093	0.00388806	0.739536	0.00678756
8400	8600	0.702165	0.00406467	0.750863	0.00704883
8600	8800	0.718516	0.00422187	0.763406	0.00729497
8800	9000	0.722479	0.00443734	0.771252	0.00738482
9000	-	0.727779	0.00131549	0.767963	0.00201162

Figure 4.9: *Example of an efficiency look-up table, giving the L0 Hadron trigger efficiency in bins of E_{T}^{real} for π^+ from the 2012 data set, where the L0 Hadron threshold was 3.5 - 3.74 GeV, for both magnet polarities combined.*
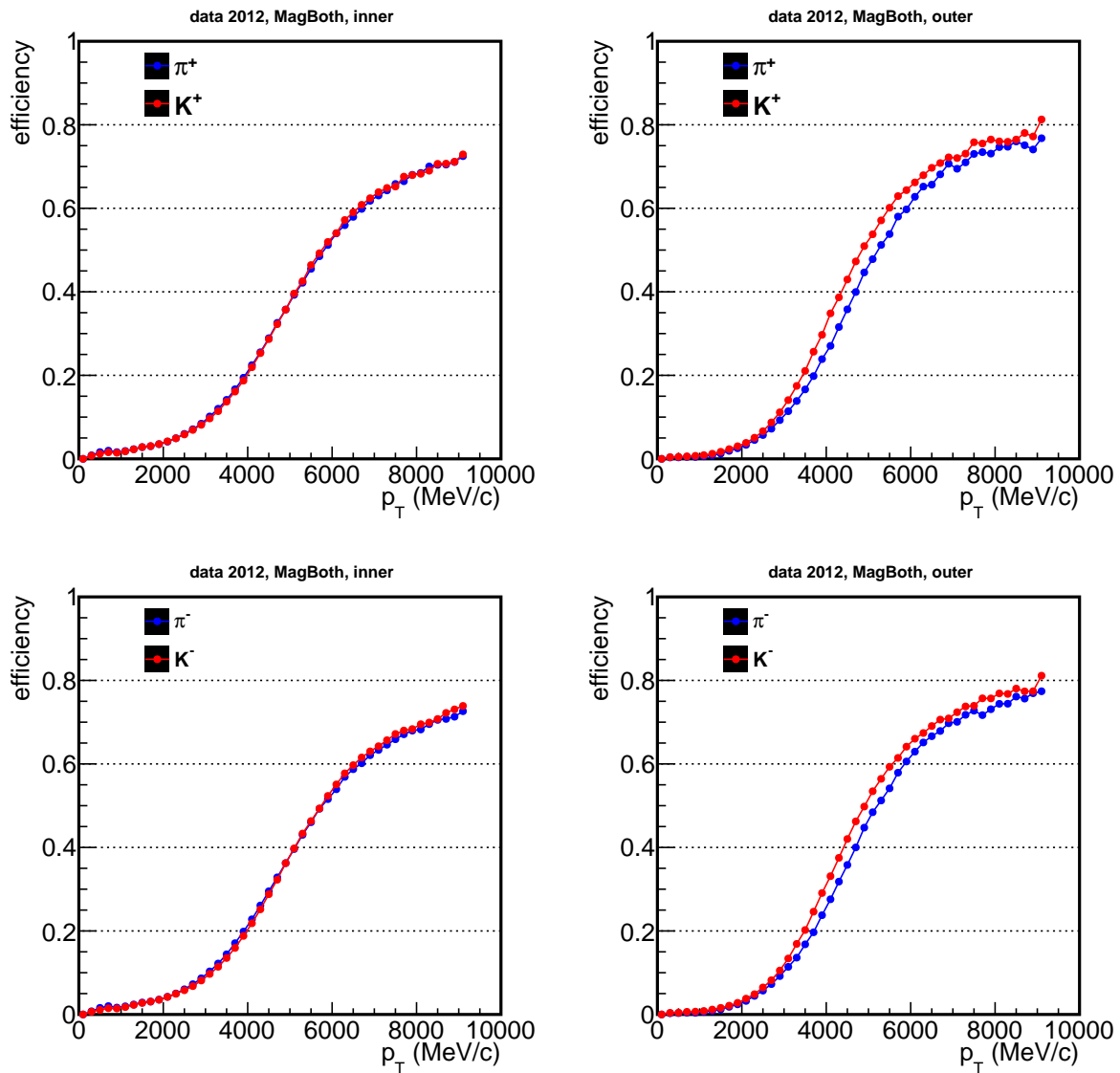
Figure 4.10: *L0 Hadron trigger efficiencies as a function of p_T for pions and kaons for 2012 data, where the L0 Hadron E_T threshold was 3.5 - 3.74 GeV. Both magnet polarities are combined. The top plots give the efficiency for particles charged $+$, while bottom plots are for particles charged $-$. Left-hand panels correspond to the Inner region of the HCAL, right-hand to the Outer.*

4.7 Interpretation of the L0 Hadron efficiency tables

4.7.1 Comment on inefficiency

When looking at the L0 Hadron efficiency curves, one can be surprised that the efficiency is never 100 %, not even for high p_T particles. Actually, its maximum value is never higher than around 80 %. Qualitative studies have been made to understand this loss of efficiency, leading to the conclusion that the occupancy together with the HCAL resolution are responsible for most of this effect.

As there are a lot of particles hitting the HCAL at the same time for a single event, a sort of masking effect appears. Let us imagine two particles, p_1 and p_2, with one over the L0 Hadron threshold $E_T(p_1) > E_T^{L0Hadron}$ and the other one under $E_T(p_2) < E_T^{L0Hadron}$, arriving alone to the same HCAL FE Card. Normally p_1 should trigger the L0 Hadron line. But it can happen that p_2 leaves a larger E_T deposit in the HCAL FE than p_1, that is to say p_1 deposits a large fraction of its energy in the ECAL. In this case, the highest E_T cluster of the FE Card will be the one corresponding to p_2, and as its energy is below the L0 Hadron threshold, there is finally no trigger candidate kept in this FE Card. In this case, p_2 has masked p_1 and p_1 does not trigger, even if its total E_T was over the L0 Hadron threshold.

All of this is due to the fact that the L0 Hadron trigger uses both HCAL and ECAL. This example illustrates how the ECAL effect is important in the hadronic trigger. As explained in Section 4.1, one should remember that the ECAL energy is added to the HCAL clusters only after the FE Card selection of the highest E_T candidate.

The size of the calorimeter clusters considered in the trigger, set to 2×2 cells, is another element playing a role. Although this is enough to detect a large fraction of the energy carried by a particle, a part of it spills out and is missed. Some particles carrying a transverse energy higher than the L0 Hadron threshold do not deposit in this 2×2 cell area a fraction large enough to trigger the L0 Hadron line. This effect also reduces the trigger efficiency.

Another thing to take into account is that the L0 Hadron trigger efficiency defined in this chapter is, strictly speaking, the efficiency of a particle of being responsible of a hadronic trigger, or what we call TOS. This efficiency needs to be known for its application for physics analysis. However, the quantity to take into account for a rigorous analysis of the trigger behaviour are the trigger rates, more than looking at a particular set of particles. Note that a hadron not being TOS does not mean that the L0 Hadron trigger did not fire, but another hadron in the event can have fired it independently of the first one.

4.7.2 Charge and magnet polarity studies

The L0 Hadron trigger efficiency has been studied for particles of both charges and for the two different magnet polarities. The corresponding plots, for pions from 2012 data as an example, are shown in Figure 4.11: no difference is seen between the efficiency for π^+ and for π^-; also the efficiencies for "Up" polarity of the magnet and for "Down" polarity are compatible[11]. The same is true for kaons.

4.7.3 Efficiency evolution and HCAL ageing

A problem that LHCb had to deal with during this first period of data taking has been the calorimeter ageing: both ECAL and HCAL degrade due to radiation from the proton-proton collisions, translating into a loss of gain of the photomultipliers (PMT). In order to overcome

---

[11]For simplicity, not all the different combinations of charge and magnet polarities are shown, even if they have been looked at. They all lead to the same conclusions explained in the text.
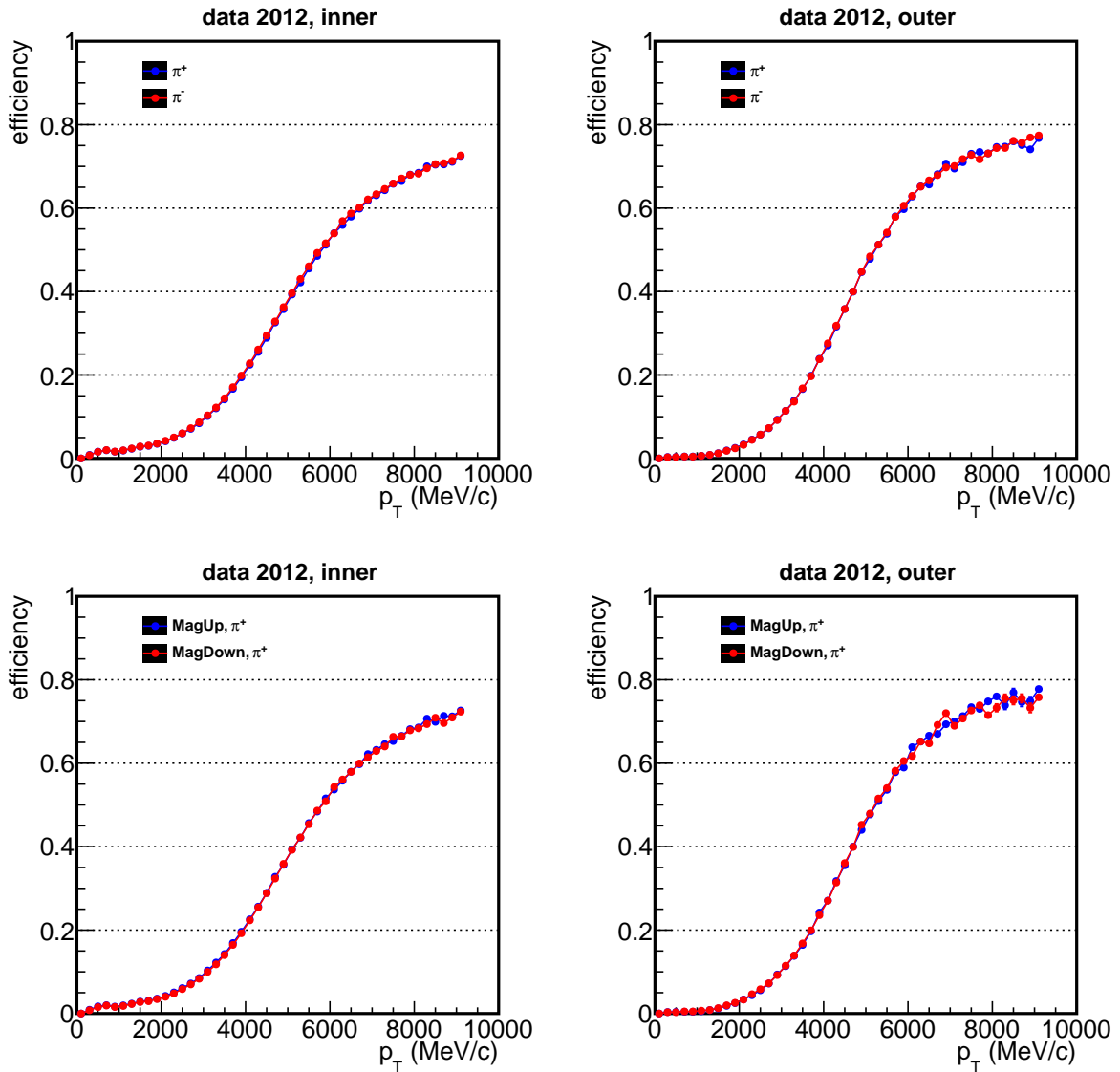
Figure 4.11: *L0 Hadron trigger efficiencies for pions as a function of p_T for 2012 data, where the L0 Hadron threshold was 3.5 - 3.74 GeV. Top: efficiency comparison for different charge (both magnet polarities combined). Bottom: efficiency comparison for different magnet polarities (for π^+).*

this problem, the high voltages of the PMTs need to be readjusted periodically, to maintain the particle detection rates as constant as possible.

The drop in HCAL gain between two adjustments means that particles will be detected with less energy than what they actually carry. This leads to a drop in the L0 Hadron trigger efficiencies. The L0 Hadron trigger efficiencies integrated over p_{T} as a function of time are shown in Figure 4.12, for 2011 and 2012, for π^+; kaons give similar results. The ageing was found to be faster than expected during 2011, especially for the Inner region, where the occupancy and then the radiation levels are higher than assumed from design. Drops in efficiency of the order of 5 % are visible from March to August. Calibrations of the high voltages were performed during Technical Stops: between June and July, and in August. The increase in efficiency due to those calibrations is also visible on the plot. Calibrations were much more frequent in 2012, providing much more stable L0 Hadron efficiencies, as can be seen in Figure 4.12. More precisely, HCAL calibrations were performed approximately every 100 pb^{-1} recorded.

However, ECAL calibrations happened only during Technical Stops, and they were done in such a way that the ECAL is overcalibrated, to delay the next calibration. When this occurs, the L0 Hadron threshold needs to be raised, in order to keep the trigger rate constant[12]: as the energy deposits in the ECAL are added to each HCAL trigger candidate, a raise in the ECAL gains translates into a raise of the energy detected and thus a raise of the number of particles passing the trigger. This explains why the L0 Hadron threshold was not constant in 2012. Indeed, while in 2011 it was set to 3.6 GeV, in 2012 it was initially 3.5 GeV and then raised periodically up to a value of 3.74 GeV at the end of the year. The initial lower value in 2012 was due to a collaboration choice, in order to increase the L0 Hadron trigger rate. The subsequent updates raising the threshold (3.62 GeV in May, 3.68 GeV in September, 3.74 GeV in November) were performed after ECAL calibrations, to compensate for the overcalibration introduced and thus keep the L0 Hadron trigger rate stable.

---

[12]In order to meet the system limitations for data storage.
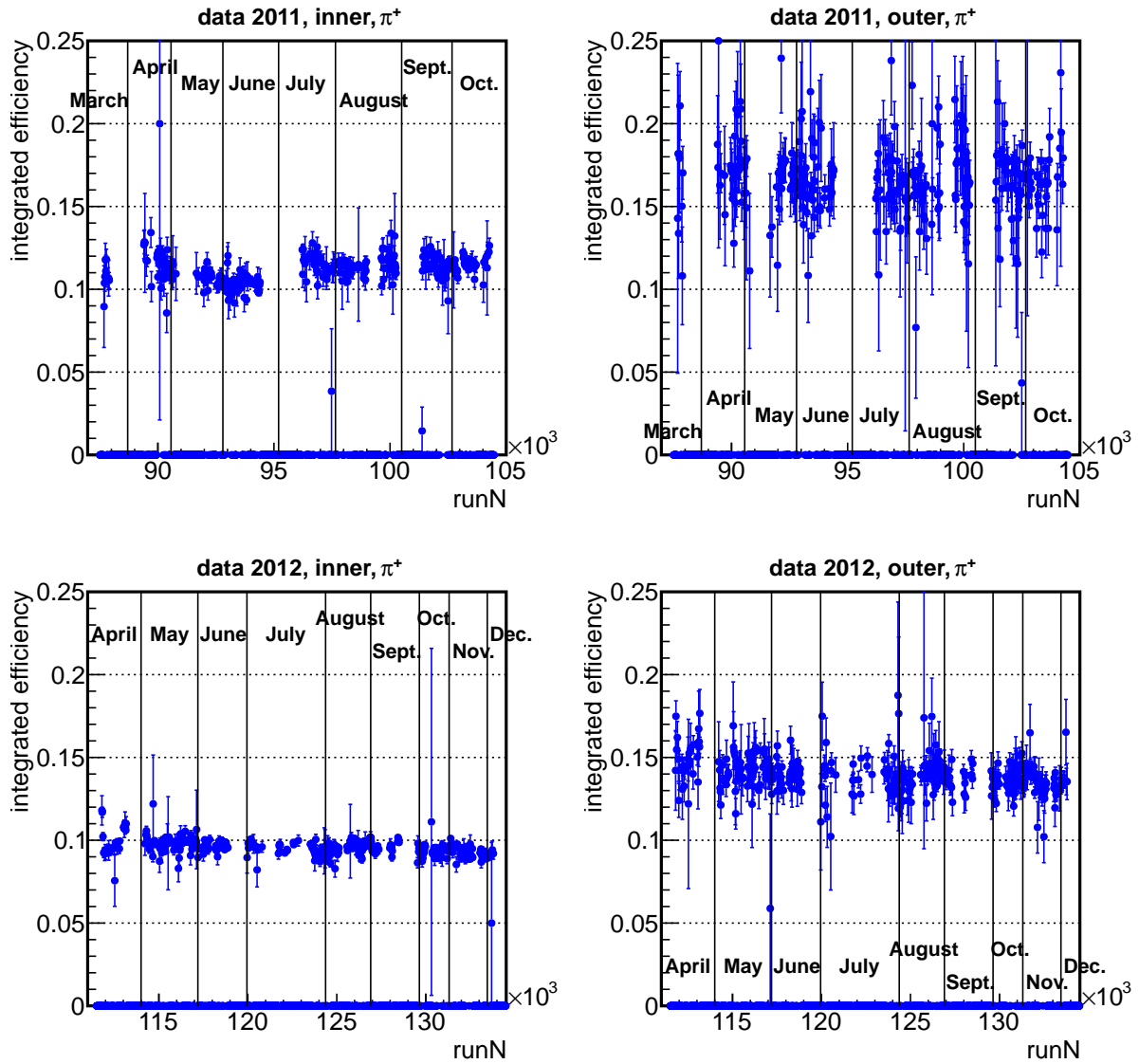
Figure 4.12: *L0 Hadron trigger efficiencies for π^+ as a function of the run number for the 2011 (top) and the 2012 (bottom) data taking periods. Left-hand panels correspond to the Inner region of the HCAL, right-hand to the Outer. The ageing effect is visible especially for the Inner region and in 2011, with drops in efficiency up to 5 %. Efficiencies in 2012 are much more steady due to the frequent calibrations. Periods with null efficiency correspond to Technical Stops.*

Chapter 5

Measurement of CP observables in $\overline{B}^0 \to D\overline{K}^{*0}$ with $D \to K^+K^-$

This chapter presents the main physics analysis which is the product of the work of this thesis. It consists in the study of the CP asymmetries and ratios of partial widths of the decay[1] $B^0 \to DK^{*0}$ with $D \to K^+K^-$, using 1 fb^{-1} of proton-proton collision data from the LHC at 7 TeV centre-of-mass energy, recorded by the LHCb experiment during 2011. This decay mode is interesting because it is sensitive to the γ angle of the CKM Unitary Triangle at the tree-level, through the CP observables. The so-called time-integrated GLW approach (c.f. Section 2.4.2) is followed in this analysis.

5.1 Analysis introduction

This analysis describes the first measurements of CP observables with B^0 and $\overline{B}_s^0$ decays to the DK^{*0} final state at LHCb, where D can be a D^0 or a $\overline{D}^0$. Both in the B^0 and in the $\overline{B}_s^0$ systems, direct CP violation can arise from the interference between colour-suppressed $b \to u$ (CKM suppressed) and $b \to c$ (CKM favoured) mediated amplitudes at tree-level, which gives access to the relative weak phase γ (c.f. Section 2.4.2). The sensitivity to CP violation is sizeable in the B^0 system given the relatively large value of $r_{B^0} = |V_{ub} \times V_{cs}|/|V_{cb} \times V_{us}| \sim 0.3$, the magnitude of the ratio between the suppressed and favoured amplitudes (where the colour suppression factors cancel), which governs the size of the interference between the two amplitudes. In the $\overline{B}_s^0$ system, $r_{B_s^0}$ is suppressed by λ^2, where $\lambda = \sin\theta_C \sim 0.22$ with θ_C the Cabibbo angle. Thus, interferences and CP violation effects for the $\overline{B}_s^0$ decay are very small and can be neglected with the current LHCb data sample size. However, the $\overline{B}_s^0$ are good control channels and can be used as normalisation modes. The involved interfering diagrams for the B^0 and the $\overline{B}_s^0$ channels are shown in Figure 5.1.

We select neutral D decays to two-body final states, which are the CP-even $D \to K^+K^-$ as the signal channel under study and the quasi-specific flavour eigenstates $D \to K^{\mp}\pi^{\pm}$ as control channels[2]. The GLW [45, 46] method can be used for extracting γ and the other un-

---

[1] Charge conjugation is implied throughout this thesis unless otherwise stated.

[2] The CP-even $D \to \pi^+\pi^-$ decay was also studied as signal channel together with $D \to K^+K^-$ and the control channels $D \to K^{\mp}\pi^{\pm}$. As the branching ratio for this mode is smaller than for the others, very few events were selected and the result on the CP observables was strongly dominated by the statistical uncertainty. Hence this mode was later dropped for publication. However, the preliminary results obtained by this first stage of the analysis, where all the quoted D decay modes were studied simultaneously, are detailed in the appendix to this chapter, see Section 5.8.
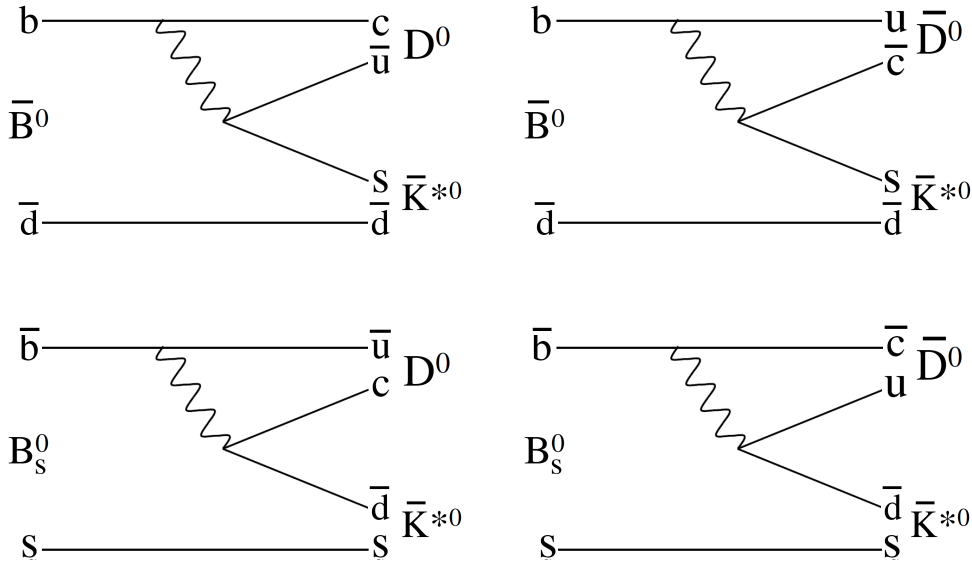
Figure 5.1: *Top: Feynman diagrams for* $\overline{B}^0 \rightarrow D^0\overline{K}^{*0}$ *(left),* $\overline{B}^0 \rightarrow \overline{D}^0\overline{K}^{*0}$ *(right). Bottom: Feynman diagrams for* $B_s^0 \rightarrow D^0\overline{K}^{*0}$ *(left),* $B_s^0 \rightarrow \overline{D}^0\overline{K}^{*0}$ *(right), where only the second one is expected to contribute with the current statistics.*

known hadronic quantities with these decays. In this analysis we do not attempt to measure quantities related to the suppressed $\overline{B}^0 \rightarrow D^0\overline{K}^{*0}$ with $D \rightarrow K^{\mp}\pi^{\pm}$ channels, corresponding to the ADS [47] method to measure γ. We consider only the favoured modes, *i.e.* those characterised by same sign (SS) kaons in the final state $\overline{B}^0 \rightarrow [K^+\pi^-]_D K^{*0}(K^+\pi^-)$, where sensitivity to γ is not expected with the current statistics, and the CP-even modes $\overline{B}^0 \rightarrow [K^+K^-]_D K^{*0}$ and $\overline{B}_s^0 \rightarrow [K^+K^-]_D K^{*0}$. The suppressed modes involving opposite sign (OS) kaons in the final state $\overline{B}^0 \rightarrow [K^-\pi^+]_D K^{*0}(K^+\pi^-)$ are themselves sensitive to γ. However, in the analysis presented here, they are only used to constrain specific backgrounds but no results are computed for them (the $\overline{B}^0$ region is kept blind at all times), as this signal is difficult to observe with the size of the 2011 data set[3].

From the partial widths of the considered decays, we can build the five observables listed below. These are related to the physics parameters to be measured (*c.f.* Section 2.6) and do not require the knowledge of absolute efficiencies, but can be measured from ratios of reconstructed signal yields, relative efficiencies and relative D^0 branching fractions. They are the two CP asymmetries for the $D \rightarrow K^+K^-$ mode for $\overline{B}^0$ and $\overline{B}_s^0$

$$A_d^{KK} = \frac{\Gamma(\overline{B}^0 \rightarrow [K^+K^-]_D \overline{K}^{*0}) - \Gamma(B^0 \rightarrow [K^+K^-]_D K^{*0})}{\Gamma(\overline{B}^0 \rightarrow [K^+K^-]_D \overline{K}^{*0}) + \Gamma(B^0 \rightarrow [K^+K^-]_D K^{*0})} \tag{5.1}$$

$$= A_{CP+},$$

$$A_s^{KK} = \frac{\Gamma(\overline{B}_s^0 \rightarrow [K^+K^-]_D K^{*0}) - \Gamma(B_s^0 \rightarrow [K^+K^-]_D \overline{K}^{*0})}{\Gamma(\overline{B}_s^0 \rightarrow [K^+K^-]_D K^{*0}) + \Gamma(B_s^0 \rightarrow [K^+K^-]_D \overline{K}^{*0})}, \tag{5.2}$$

---

[3]The analysis of the $\overline{B}^0 \rightarrow D\overline{K}^{*0}$ channel with $D \rightarrow K^+\pi^-$ using the total 2011 and 2012 LHCb data is presented in Chapter 6, where preliminary measurements of the related CP observables are obtained.

the ratio of B^0 widths for the $D \to K^+ K^-$ over $D \to K^{\mp} \pi^{\pm}$ SS favoured modes

$$
\begin{aligned}
R_d^{KK} &= \frac{\Gamma(\overline{B}^0 \to [K^+ K^-]_D \overline{K}^{*0}) + \Gamma(B^0 \to [K^+ K^-]_D K^{*0})}{\Gamma(\overline{B}^0 \to [K^- \pi^+]_D \overline{K}^{*0}) + \Gamma(B^0 \to [K^+ \pi^-]_D K^{*0})} \\
&= R_{CP+},
\end{aligned}
\tag{5.3}
$$

the ratio of B^0 and $\overline{B}_s^0$ widths for the $D \to K^+ K^-$ modes

$$
R_{ds}^{KK} = \frac{\Gamma(\overline{B}^0 \to [K^+ K^-]_D \overline{K}^{*0}) + \Gamma(B^0 \to [K^+ K^-]_D K^{*0})}{\Gamma(\overline{B}_s^0 \to [K^+ K^-]_D K^{*0}) + \Gamma(B_s^0 \to [K^+ K^-]_D \overline{K}^{*0})},
\tag{5.4}
$$

and the B^0 CP asymmetry in the favoured $D \to K^{\mp} \pi^{\pm}$ SS mode

$$
A^{\text{fav}} = \frac{\Gamma(\overline{B}^0 \to [K^- \pi^+]_D \overline{K}^{*0}) - \Gamma(B^0 \to [K^+ \pi^-]_D K^{*0})}{\Gamma(\overline{B}^0 \to [K^- \pi^+]_D \overline{K}^{*0}) + \Gamma(B^0 \to [K^+ \pi^-]_D K^{*0})}.
\tag{5.5}
$$

The branching fraction of the K^{*0} decay is $\mathcal{B}(K^{*0} \to K^+ \pi^-) \sim 66.6$ %. For the considered decays of the D^0 meson, we have $\mathcal{B}(D^0 \to K^- \pi^+) = (3.88 \pm 0.05) \times 10^{-2}$ (Cabibbo favoured), $\mathcal{B}(D^0 \to K^+ \pi^-) = (1.47 \pm 0.07) \times 10^{-4}$ (doubly Cabibbo suppressed), and $\mathcal{B}(D^0 \to K^+ K^-) = (3.96 \pm 0.08) \times 10^{-3}$ [34].

In order to reduce any risk of bias, a blind analysis is performed on the B^0 and $\overline{B}^0$ signal mass windows of the $D \to K^+ K^-$: the extracted values and errors of the GLW B^0 and $\overline{B}^0$ yields, sensitive to γ, were hidden during the first phase of the studies and unblinded only after all the analysis choices were made and fixed.

As both B^0 and $\overline{B}_s^0$ contributions are expected, we denote by B the candidate events entering this analysis, in a more general way.

5.2 Data sets and event selection

5.2.1 Data and simulation samples

The analysis described here uses $1.03 \pm 0.04\,\text{fb}^{-1}$ of data recorded at the LHCb experiment (*c.f.* Chapter 3) from the LHC proton-proton collisions at a centre-of-mass energy of $\sqrt{s} = 7\,\text{TeV}$ during the year 2011. These data were taken in stable running conditions, with a mean number of visible interactions per bunch-crossing equal to $\mu = 1.5$.

The $B^0 \to DK^{*0}$ candidates used for this analysis are built from combinations of charged hadrons reconstructed in the detector. These candidates are preselected by the stripping software (using the DaVinci application, *c.f.* Section 3.4) by a stripping line dedicated to select decays of B hadrons to particles containing c quarks in the final state. Table 5.1 details this stripping selection[4]. The events are required to be triggered at the hardware trigger level L0 by the signal candidate (Trigger On Signal, "TOS") by any line. Concerning the software trigger, events must be triggered at the first level HLT1 by a specific line relying on track information, and at the second level HLT2 by the topological lines, which select b-hadron decays in an inclusive

---

[4]Most of the symbols used in this table are explained in the following sections describing the specific selection. Those not included there are: the particle lifetime τ; the track momentum p; the χ^2 distance significance with respect to the related primary vertex (PV); the maximum distance of closest approach "Max DOCA" or impact parameter significance with respect to any primary vertex; the Boosted Decision Tree output. This last one corresponds to the value of the classification of events in signal or background performed by a multivariate algorithm, trained on $B \to Dh$ 2011 real data (the sidebands of the D mesons in these decays are used to model the background), using kinematic, vertex, track quality and RICH variables for the D meson and its daughters.

Meson	Variable	Cut value
Charged track	p_{T}	$> 100 \,\mathrm{MeV}/c$
	p	$> 1000 \,\mathrm{MeV}/c$
	Track χ^2/ndf	< 4
	Min IPχ^2	> 4
D^0	$\sum_{K^{\pm},\pi^{\pm}} p_T$	$> 1.8 \,\mathrm{GeV}/c$
	Max DOCA(h^+, h^-)	$< 0.5 \,\mathrm{mm}$
	Vertex χ^2/ndf	< 10
	Distance to PV significance	> 36
	$\cos(\theta_{\mathrm{dira}})$	> 0
	$\left| M(K^{\mp}\pi^{\pm} - M(D^0) \right|$	$< 100 \,\mathrm{MeV}/c^2$
K^{*0}	$p(K^{\pm}, \pi^{\pm})$	$> 2000 \,\mathrm{MeV}/c$
	Max DOCA$(K^{\pm}, \pi^{\mp})$	$< 0.5 \,\mathrm{mm}$
	Vertex χ^2/ndf	< 16
	Distance to PV significance	> 16
	$\cos(\theta_{\mathrm{dira}})$	> 0
	$p_{\mathrm{T}}(K^{\pm}) + p_{\mathrm{T}}(\pi^{\mp})$	$> 1000 \,\mathrm{MeV}/c$
	$M(K^+\pi^-)$	$< 5.2 \,\mathrm{GeV}/c^2$
B^0	Max DOCA(D^0, K^{*0})	$< 1 \,\mathrm{mm}$
	$p_{\mathrm{T}}(D^0) + p_{\mathrm{T}}(K^{*0})$	$> 5 \,\mathrm{GeV}/c$
	Vertex χ^2/ndf	< 10
	Min IPχ^2	< 25
	τ	$> 0.2 \,\mathrm{ps}$
	$\cos(\theta_{\mathrm{dira}})$	> 0.999
	$M(D^0 K^{*0})$	$> 4.75 \,\mathrm{GeV}/c^2$
		$< 7 \,\mathrm{GeV}/c^2$
	Boosted decision tree output	> 0.05

Table 5.1: *Stripping selection for $B^0 \to DK^{*0}$ candidates.*

way by requiring at least two charged particles in the final state and a displaced decay vertex (*c.f* Section 3.3).

The Monte Carlo simulation samples used to determine efficiencies and to model B invariant mass distribution components were produced with the Gauss software [74]. The signal samples were obtained requiring all charged tracks from the signal decay to be in the LHCb acceptance at generator level.

On top of the stripping selection, further specific criteria are applied, which are described in the following sections and summarised in Table 5.2. These selection criteria are based on that optimised for the $\overline{B}_s^0 \to [K^{\mp}\pi^{\pm}]_D K^{*0}$ analysis from [81,82]. B and $\overline{B}$ candidates are treated together along all the selection and background studies procedure.

5.2.2 D^0 selection

D^0 or $\overline{D}^0$ mesons are reconstructed in the decay modes $D \to K^\mp \pi^\pm$ and $D \to K^+ K^-$. The transverse momentum p_{T} of the D daughter hadrons (K and π) is required to be greater than $400 \, \mathrm{MeV}/c$. Particle identification (PID) criteria are applied to distinguish π from K, namely the difference between the logarithmic likelihoods[5] of the K and π hypotheses, the $\mathrm{DLL}_{K\pi}$, must be larger than 0 for K and smaller than 4 for π.

   A fit to a common vertex is applied to the two-track combination, requiring the corresponding χ^2/ndf value to be less than 5. In order to separate D mesons coming from a B decay from prompt D mesons, the candidates are required to have a minimal impact parameter significance $\mathrm{IP}\chi^2$ with respect to all primary vertices (PV) greater than 4. To suppress background from charmless decays ($B^0 \to K^+ K^- K^{*0}$ for example), for which all four charged hadrons are produced at the B decay vertex[6], a condition on the D flight distance (FD) significance with respect to the B vertex is applied. This quantity is requested to be larger than 2.5, that is to say we require the D daughters to come from a D vertex, displaced with respect to the B vertex (see Section 5.3.1). Finally, only D candidates with an invariant mass within $\pm 20 \, \mathrm{MeV}/c^2$ of the D^0 nominal mass ($1864.8 \, \mathrm{MeV}/c^2$ [84]) are kept to form B candidates.

5.2.3 K^{*0} selection

K^{*0} mesons are reconstructed in the mode $K^{*0} \to K^+ \pi^-$. The p_{T} of the K and π must be larger than $300 \, \mathrm{MeV}/c$. Concerning particle identification, the $\mathrm{DLL}_{K\pi}$ is required to be larger than 3 for the K and lower than 3 for the π. Possible contamination from protons in the K sample ($\Lambda_b^0 \to \overline{D}^0 p h^-$ decays, see Section 5.3.4) is reduced by keeping only K candidates with a difference between the logarithmic likelihoods of the proton and K hypotheses DLL_{pK} smaller than 10.

   To select a K^{*0} coming from a B decay, its minimal $\mathrm{IP}\chi^2$ with respect to all PV must be larger than 25. K^{*0} candidates with an invariant mass within $\pm 50 \, \mathrm{MeV}/c^2$ of the nominal mass ($891.66 \, \mathrm{MeV}/c^2$ [84]) are selected. This cut value was used in the $\overline{B}^0_s \to D^0 K^{*0}$ analysis [81]. It is chosen as it offers a reasonable compromise between the efficiency loss and the amount of non-resonant background which dilutes the CP asymmetry (see Section 5.3.3). It corresponds to an expected value of the coherence factor $\kappa = 0.95$ [57], involved in Equations (5.1) to (5.5) (*c.f.* Section 2.6).

5.2.4 B^0 selection

B hadron candidates are formed combining D and K^{*0} candidates selected with the above requirements. Events are required to be triggered by any particle in the $B^0 \to [h^\pm h^\mp]_D K^{*0}(K^+ \pi^-)$ final state by the L0 Hadron line ("TOS"), or by any L0 line by the other B hadron decay in the same event ("OtherB") (see Section 5.4.3). A fit to a common vertex is done, keeping only combinations with a χ^2/ndf lower than 4. Since B mesons are produced at the PV, only candidates with a minimal impact parameter significance $\mathrm{IP}\chi^2$ with respect to all PV lower than 9 are

---

[5]The DLL are the typical variables used in LHCb to apply particle identification requirements. As explained in Section 3.2.3, the information coming from the RICH subdetectors is combined with the momentum measured by the tracking system in order to determine the particle species associated to each track. To cope with the high occupancy in the RICHs, an overall event logarithmic likelihood algorithm is employed [83] to treat the overlap of Cherenkov cones properly, in order to achieve an efficient reconstruction of events. For each track, the DLL gives the difference in the overall event logarithmic likelihood when that track is changed from the pion hypothesis to each of the electron, muon, kaon and proton hypotheses. These values are then used to identify particle types.

[6]The K^{*0} meson has a very short lifetime compared to the D or the B^0 ones, so it decays very fast and it does not produce a displaced vertex with respect to the B vertex.

retained. Additionally, the momentum of the reconstructed B is requested to be pointing back to the PV, requiring the cosine of the pointing angle θ_{dira} to be larger than 0.99995, corresponding to an angle of 10 mrad. θ_{dira} is defined as the angle between the B momentum direction and the direction of flight of the B candidate from the PV of smallest IPχ^2. Furthermore, the sum of the square roots of the IPχ^2 of the four charged tracks with respect to this PV must be larger than 32.

Using the fact that the signal decay modes are decays of a pseudo-scalar particle (B^0) to a pseudo-scalar particle (D^0) and a vector particle (K^{*0}), the helicity angle θ^* of the K from the K^{*0} is required to have an absolute value of the cosine larger than 0.4. The helicity angle is defined as the angle between the K momentum direction in the K^{*0} rest frame, and the K^{*0} direction in the B rest frame. This variable is expected to follow a flat distribution for the combinatorial background and to follow a $\cos^2\theta^*$ distribution for the signal candidates. It should be noted that the distribution of this variable is modified by the transverse momentum cuts.

Specific peaking backgrounds from $B^0 \to D^-_{(s)}\pi^+$ or $B^0 \to D^-_{(s)}K^+$ decays are eliminated by applying a veto on candidates for which the invariant mass of three of the four charged mesons in the final state is compatible with them being produced by a $D^{\mp}$ or a $D^{\mp}_s$ decay (see Section 5.3.4). Namely, candidates are rejected when the invariant mass $M(K^{\pm}\pi^{\mp}\pi^{\mp})$ is within ± 15 MeV/c^2 of the $D^{\mp}$ nominal mass or when the invariant mass $M(K^{\mp}K^{\pm}\pi^{\mp})$ is within ± 15 MeV/c^2 of the $D^{\mp}_s$ or $D^{\mp}$ nominal mass, corresponding to a mass window approximatively equal to ± 2.5 times the D mass resolution.

After all selections are applied, 0.5 % of the events contain more than one B candidate. For the final measurement, and in particular for the mass fit described later, only one candidate per event is retained, keeping the one with the largest B flight distance significance with respect to the PV of smallest IPχ^2.

5.2.5 Selection optimisation

As already mentioned, the selection presented before is based on the optimal selection developed for the $\overline{B}^0_s \to [K^{\mp}\pi^{\pm}]_D K^{*0}$ analysis from [81]. In addition to the $D \to K^{\mp}\pi^{\pm}$ decay modes, the analysis that is presented here also uses $D \to K^+K^-$. Due to the differing kinematics of its decay products, the selections specific to the D daughters are reoptimised for this mode, namely the PID and p_{T} requirements.

The optimisation process makes use of the $\overline{B}^0_s \to [K^+K^-]_D K^{*0}$ signal and of the background contribution in the B^0 blind signal region, both from data. The expected signal yield in the $B^0 \to [K^+K^-]_D K^{*0}$ blind signal region is calculated from the yield of the $\overline{B}^0_s$ control sample multiplied by a factor which depends on the r_{B^0}, r_D, δ_{B^0}, δ_D and γ parameters[7], for which sensible estimates are taken from the experimentally allowed ranges for these parameters. This factor is calculated using a value for the strong phase δ_{B^0} that results in the highest possible signal yield, $\delta_{B^0_{\mathrm{max}}} = 0$, since no δ_{B^0} estimate is available.

All offline selections are applied apart from the cuts on $\mathrm{DLL}_{K\pi}$ and p_{T} on the D daughters in the $D \to K^+K^-$ mode. The expected significance of the blind signal, defined as $S/\sqrt{S+B}$ where S is the expected B^0 signal computed as explained and B the background in the B^0 signal region, is then represented as a function of both of these cuts as shown in Figure 5.2. Both the yield of $\overline{B}^0_s$ signal and the background B are estimated using a simplified version of the fit presented in Section 5.5. The selections for the $D \to K^+K^-$ mode favoured by this procedure are $\mathrm{DLL}_{K\pi}(K) > 0$, $p_{\mathrm{T}}(K) > 400$ MeV/c, since they maximise the significance. These requirements are identical to those applied to the π in the $D \to K^{\mp}\pi^{\pm}$ mode.

---

[7]The factor $r^0_B e^{i\delta^0_B}$ is the ratio of the suppressed to favoured $B^0 \to DK^{*0}$ amplitudes, while $r_D e^{i\delta_D}$ is the ratio of the suppressed to favoured $D^0 \to K^{\mp}\pi^{\pm}$ decay amplitudes (*c.f.* Section 2.6).

Meson	Variable	Cut value
D^0	$p_{\mathrm{T}}(K^\pm, \pi^\pm)$	$> 400\,\mathrm{MeV}/c$
	$\mathrm{DLL}_{K\pi}(K^\pm)$	> 0
	$\mathrm{DLL}_{K\pi}(\pi^\pm)$	< 4
	Vertex χ^2/ndf	< 5
	Min $\mathrm{IP}\chi^2$	> 4
	Flight distance significance	> 2.5
	$\left\vert M(K^\mp \pi^\pm) - M(D^0) \right\vert$	$< 20\,\mathrm{MeV}/c^2$
K^{*0}	$p_{\mathrm{T}}(K^\pm, \pi^\pm)$	$> 300\,\mathrm{MeV}/c$
	$\mathrm{DLL}_{K\pi}(K^\pm)$	> 3
	$\mathrm{DLL}_{K\pi}(\pi^\pm)$	< 3
	$\mathrm{DLL}_{pK}(K^\pm)$	< 10
	Min $\mathrm{IP}\chi^2$	> 25
	$\left\vert M(K^+ \pi^-) - M(K^{*0}) \right\vert$	$< 50\,\mathrm{MeV}/c^2$
B	Vertex χ^2/ndf	< 4
	Min $\mathrm{IP}\chi^2$	< 9
	$\cos(\theta_{\mathrm{dira}})$	> 0.99995
	$\sum_{\mathrm{tracks}} \sqrt{\mathrm{IP}\chi^2}$	> 32
	$\vert \cos\theta^* \vert$	> 0.4
	$\vert M(K^\mp \pi^\pm \pi^\pm) - M(D^\pm) \vert$	$> 15\,\mathrm{MeV}/c^2$
	$\vert M(K^\pm K^\mp \pi^\pm) - M(D_s^\pm, D^\pm) \vert$	$> 15\,\mathrm{MeV}/c^2$

Table 5.2: *Selection criteria for $B^0 \to DK^{*0}$ candidates.*
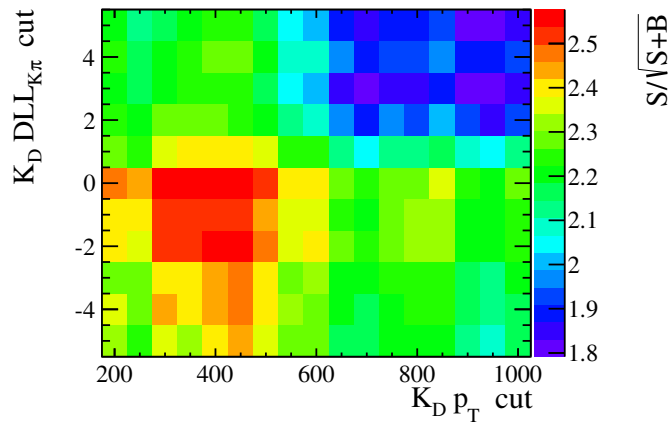
Figure 5.2: *Expected significance $S/\sqrt{S+B}$ of $B^0 \to [K^+ K^-]_D K^{*0}$ as a function of the $\mathrm{DLL}_{K\pi}$ and p_{T} cuts on the D daughter tracks, calculated using a value for the strong phase δ_{B^0} that results in the highest possible signal yield, $\delta_{B^0_{\max}} = 0$.*

5.3 Specific backgrounds studies

5.3.1 Charmless background

Peaking backgrounds are anticipated from charmless $B^0 \to hh'K^{*0}$ decays ($h, h' = K^{\pm}, \pi^{\pm}$). To keep this source of background at a negligible level, a tight flight distance significance cut at > 2.5 on the D is applied, as mentioned in Section 5.2.2. The D flight distance significance is defined as the difference in the longitudinal direction z of the D and the B decay vertices, divided by the square root of the sum of the squares of their uncertainties,

$$\text{FDS}_D = \frac{z_D - z_B}{\sqrt{\sigma_D^2 + \sigma_B^2}}. \tag{5.6}$$

To study this source of background and determine this requirement, the D flight distance significance cut and mass window are relaxed. A simple fit to the D mass is performed using a Gaussian function for the signal, a linear function for the combinatorial background and a Crystall Ball function for contributions due to particle misidentification (mis-ID). Figure 5.3 allows to identify the D mass sidebands which do not contain real D events (no requirements on the $B^0_{(s)}$ mass is applied, that is to say the whole B mass distribution is considered). The sidebands are defined as $|M(K^{\mp}\pi^{\pm}) - M(D^0)| > 40\,\text{MeV}/c^2$ in the $D \to K^{\mp}\pi^{\pm}$ categories and $M(K^+K^-) < 1\,835\,\text{MeV}/c^2$ in the $D \to K^+K^-$ category.

The background from charmless B decays is assessed from the reconstructed B mass of the events in these D sidebands. The B invariant mass distribution for each mode is fitted with a linear combinatorial background and double Gaussian functions for the B^0 and $\overline{B}^0_s$ signals, the parameters of which are taken and fixed from the full fit to data described in Section 5.5, with B and $\overline{B}$ candidates added together. The yields of any peaking backgrounds from charmless decays, resulting from these fits, are then scaled to give an expected number of charmless background candidates for events selected in the D signal region, using the relative sizes of this signal region and of the sidebands.

Figure 5.4 shows that, when the flight distance significance cut is relaxed, there is considerable peaking background from charmless decays, as can be seen from the peaks at the B^0 and $\overline{B}^0_s$ nominal mass positions. From Figures 5.5 and 5.6, which show the scaled yield of the peaking B^0 and $\overline{B}^0_s$ charmless background as a function of the D flight distance significance cut, one can see that the category most affected is the B^0 for the $D \to K^+K^-$ mode. The scaled yield of this peaking background goes to zero at a flight distance significance cut greater than 2.5 on the

Figure 5.3: *Fit to the D invariant mass distribution after all offline cuts, relaxing the D mass window and the D flight distance significance cut, for $D \to K^{\mp}\pi^{\pm}$ (SS) (left), $D \to K^{\mp}\pi^{\pm}$ (OS) (middle) and $D \to K^+K^-$ (right). The black line superimposed on the distributions is the fit result, sum of a linear combinatorial background (dashed blue line), a Gaussian function for the signal (red line) and a Crystal Ball function for the mis-ID of $D \to K^{\mp}\pi^{\pm}$ into $D \to K^+K^-$ (green line, right only). The grey arrows indicate the sideband region defined in the text.*

D, thereby motivating its inclusion in the event selection criteria. This cut also serves to reduce combinatorial background, as shown by the much cleaner D samples in Figure 5.7 compared with Figure 5.3.
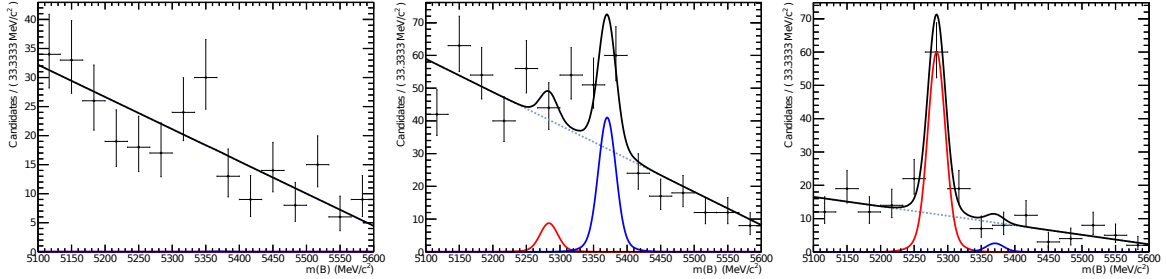
Figure 5.4: *Fit to the B invariant mass of the reconstructed events in the D sidebands as defined in the text, relaxing the requirement on the D flight distance significance, for $D \to K^{\mp}\pi^{\pm}$ (SS) (left), $D \to K^{\mp}\pi^{\pm}$ (OS) (middle) and $D \to K^{+}K^{-}$ (right). The black line superimposed on the distributions is the fit result, sum of a linear combinatorial background (dashed grey line) and two double Gaussian functions, one for the B^{0} signal (red line) and the other for $\overline{B}_{s}^{0}$ signal (blue line).*
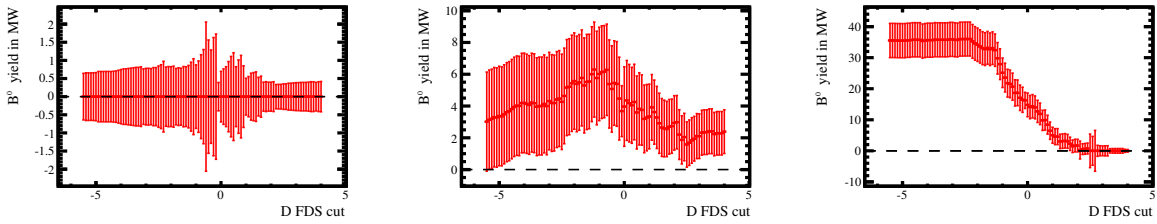
Figure 5.5: *Yields of peaking backgrounds from charmless B^{0} decays scaled to the D signal region in all three categories, as a function of the flight distance significance cut on the D. The uncertainties are subject to fluctuations from the fit procedure on Figure 5.3, as when a peak is not found the likelihood curve for the yield is not well-behaved. Categories are (left to right): $D \to K^{\mp}\pi^{\pm}$ (SS), $D \to K^{\mp}\pi^{\pm}$ (OS) and $D \to K^{+}K^{-}$.*
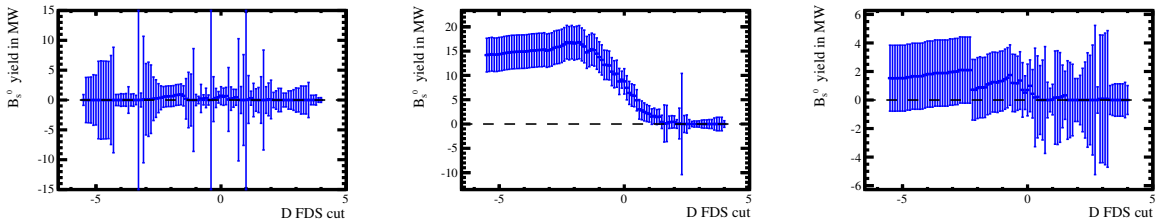
Figure 5.6: *Yields of peaking backgrounds from charmless $\overline{B}_{s}^{0}$ decays scaled to the D signal region in all three categories, as a function of the flight distance significance cut on the D. The uncertainties are subject to fluctuations from the fit procedure on Figure 5.3, as when a peak is not found the likelihood curve for the yield is not well-behaved. Categories are (left to right): $D \to K^{\mp}\pi^{\pm}$ (SS), $D \to K^{\mp}\pi^{\pm}$ (OS) and $D \to K^{+}K^{-}$.*
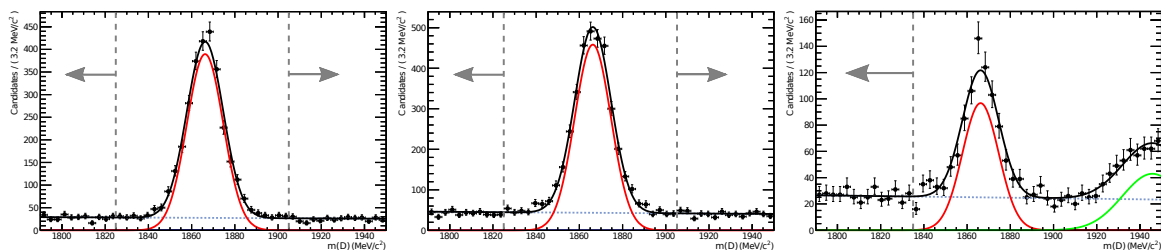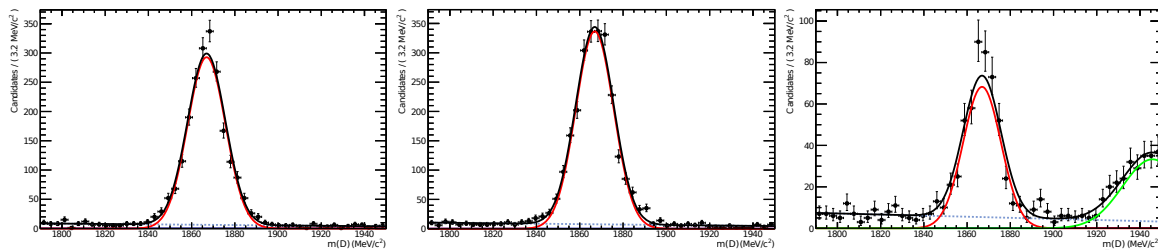
Figure 5.7: *Fit to the D invariant mass distribution after all offline cuts, relaxing the D mass window but applying the flight distance significance cut on the D at > 2.5, for $D \to K^\mp\pi^\pm$ (SS) (left), $D \to K^\mp\pi^\pm$ (OS) (middle) and $D \to K^+K^-$ (right). The black line superimposed on the distributions is the fit result, sum of a linear combinatorial background (dashed blue line), a Gaussian function for the signal (red line) and a Crystal Ball function for the mis-ID of $D \to K^\mp\pi^\pm$ into $D \to K^+K^-$ (green line, right only).*

5.3.2 Cross-feed of D modes

From the PID selections listed in Table 5.2, the same event can eventually be reconstructed in both $D \to K^\pm\pi^\mp$ and $D \to K^+K^-$, since the regions of phase space allowed by the cuts overlap. The cross-feed background of $D \to K^\pm\pi^\mp$ into the $D \to K^+K^-$ mode can be assessed from Figure 5.7, which shows the D invariant mass distribution after all cuts except the D mass window cut, in the [5.1;5.6] GeV/c^2 B mass window. The yield of the $D \to K^\pm\pi^\mp$ mis-ID inside the ± 20 MeV/c^2 signal region of the $D \to K^+K^-$ mode is found to be approximately 0.005 % of the signal yield.

One expects the mis-ID shape for the cross-feed of $D \to K^+K^-$ into $D \to K^\pm\pi^\mp$ to be slightly different, as the momentum distribution of the daughters is not the same. However, the lower branching fraction ($\mathcal{B}(D^0 \to K^+K^-) = (3.96 \pm 0.08) \times 10^{-3}$, compared to $\mathcal{B}(D^0 \to K^-\pi^+) = (3.88 \pm 0.05) \times 10^{-2}$ [34]) means that it is not expected to contribute more than 0.005 % of the signal yield in $D \to K^\pm\pi^\mp$.

We can therefore assume that all D cross-feed backgrounds are negligible.

5.3.3 Non-resonant K^{*0} background

Possible background from decays of the type $B^0 \to DK^+\pi^-$, that is to say a non-resonant $K^\pm\pi^\mp$ contribution, is studied analysing the K^{*0} invariant mass distribution, where the background is subtracted using the *sPlot* technique [85]. All selection cuts are applied to the data sample except the K^{*0} mass window cut. The K^{*0} mass distributions are studied for the most favoured modes in the analysis, namely $\overline{B}^0_s \to [K^-\pi^+]_D K^{*0}$ and $B^0 \to [K^+\pi^-]_D K^{*0}$, adding B and $\overline{B}$ together. A simplified version of the B invariant mass distribution fit presented in Section 5.5 is used to determine the weights for the background subtraction.

The background subtracted $K^\pm\pi^\mp$ mass distributions are fitted using a relativistic Breit-Wigner function,

$$f_{\text{BW}}(x; M, \Gamma, J, R) =$$

$$\frac{\Gamma M}{x} \left(\frac{M}{x} \sqrt{\frac{\left(x^2 - (M_\pi + M_K)^2\right)\left(x^2 - (M_\pi - M_K)^2\right)}{\left(M^2 - (M_\pi + M_K)^2\right)\left(M^2 - (M_\pi - M_K)^2\right)}} \right)^{2J+1}$$

$$\times \frac{1 + \frac{R^2}{4x^2}\left(x^2 - (M_\pi + M_K)^2\right)\left(x^2 - (M_\pi - M_K)^2\right)}{1 + \frac{R^2}{4M^2}\left(M^2 - (M_\pi + M_K)^2\right)\left(M^2 - (M_\pi - M_K)^2\right)}, \quad (5.7)$$

Function	Parameter	Value
Relativistic Breit-Wigner	$M(K^{*0})$ ($\overline{B}_s^0$ mode)	$902 \pm 2 \, \text{MeV}/c^2$
	$M(K^{*0})$ (B^0 mode)	$900 \pm 3 \, \text{MeV}/c^2$
	$\Gamma(K^{*0})$	$49.7 \, \text{MeV}/c^2$ [Fixed]
	$J(K^{*0})$	1 [Fixed]
	R (Radius)	4 [Fixed]
	M_π	$140 \, \text{MeV}/c^2$ [Fixed]
	M_K	$494 \, \text{MeV}/c^2$ [Fixed]
Gaussian (resolution)	σ	$9 \, \text{MeV}/c^2$ [Fixed]
Polynomial (background)	slope ($\overline{B}_s^0$ mode)	$1 \pm 19 \, (\text{MeV}/c^2)^{-1}$
	slope (B^0 mode)	$5 \pm 250 \, (\text{MeV}/c^2)^{-1}$

Table 5.3: *Parameters of the fit model for the background subtracted K^{*0} invariant mass distributions.*

Mode	Yield	Result	Scaled
$\overline{B}_s^0 \rightarrow [K^-\pi^+]_D K^{*0}$	N(resonant)	602 ± 28	462 ± 21
	N(non − resonant)	61 ± 27	16 ± 7
$B^0 \rightarrow [K^+\pi^-]_D K^{*0}$	N(resonant)	283 ± 31	217 ± 24
	N(non − resonant)	42 ± 31	11 ± 8

Table 5.4: *Result of the fit to the background subtracted K^{*0} invariant mass distribution. The last column shows the result scaled to the K^{*0} mass window applied in the selection.*

convolved with a Gaussian resolution function for the resonant K^{*0} component (signal) and a first-order polynomial for the non-resonant component (background). The Breit-Wigner parameters are the mass M and width Γ of the resonance, its total angular momentum J, the mass of the two decay products M_K and M_π and the range parameter R; σ is the resolution of the Guassian. The list of the parameters used in this model is shown in Table 5.3: all parameters except the background slopes and the mean M of the Breit-Wigner are fixed. The results of this fit for each one of the two studied categories are shown in Table 5.4 and in Figures 5.8 and 5.9. The non-resonant $K^\pm\pi^\mp$ contribution to the signal in the K^{*0} mass window ($\pm 50 \, \text{MeV}/c^2$) used in the selection is found to be (3.3 ± 1.4) % in the $\overline{B}_s^0 \rightarrow [K^-\pi^+]_D K^{*0}$ mode and (4.8 ± 3.4) % in the $B^0 \rightarrow [K^+\pi^-]_D K^{*0}$. Since these fractions are small, they are neglected in the final result of this analysis.

5.3.4 Other backgrounds

$\Lambda_b^0 \rightarrow D^0 p h^-$ ($h = \pi, K$) background

A potential background is anticipated from $\Lambda_b^0 \rightarrow D^0 p h^-$ decays where the proton in the final state is misidentified as the K or the π from the K^{*0} decay. Indeed, from signal Monte Carlo samples of $\Lambda_b^0 \rightarrow D^0 p h^-$ some events are reconstructed as $B^0 \rightarrow DK^{*0}$ candidates. It is found
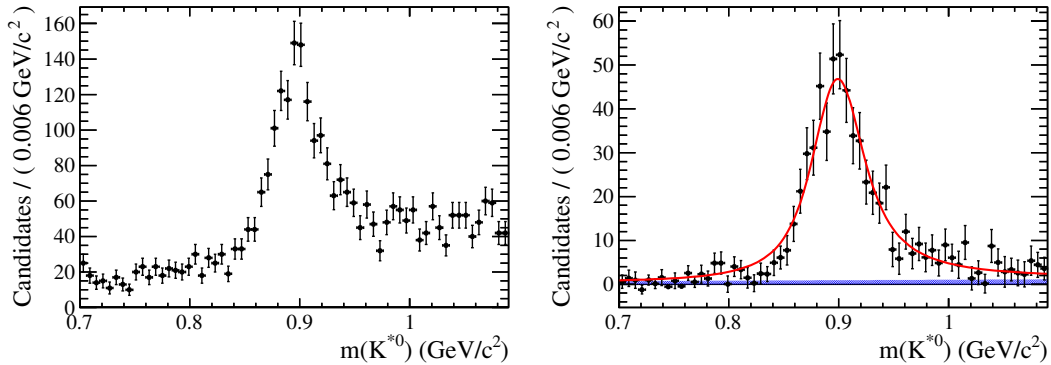
Figure 5.8: K^{*0} *invariant mass distribution for the* $\overline{B}^0_s \to [K^-\pi^+]_D K^{*0}$ *mode before (left) and after background subtraction (right). All selection cuts are applied except the* K^{*0} *mass window cut. On the right-hand plot, the red line represents the result of the fit, and the blue area corresponds to the non-resonant contribution.*
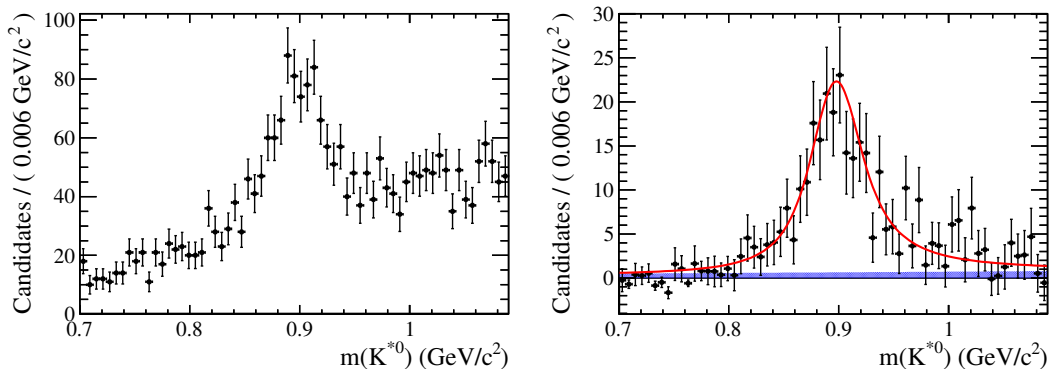
Figure 5.9: K^{*0} *invariant mass distribution for the* $B^0 \to [K^+\pi^-]_D K^{*0}$ *mode before (left) and after background subtraction (right). All selection cuts are applied except the* K^{*0} *mass window cut. On the right-hand plot, the red line represents the result of the fit, and the blue area corresponds to the non-resonant contribution.*

that, after all stripping selections and offline cuts except PID, the only background that is expected to contribute significantly is $\Lambda^0_b \to D^0 p\pi^-$ with the proton misidentified as a K. The number of events expected in the $D \to K^\mp\pi^\pm$ category after all kinematic selections is approximately 20 (split equally between Same Sign and Opposite Sign categories) and approximately 2 in the $D \to K^+K^-$ category. These numbers are estimated from the yield of B^0 events in the $D \to K^\mp\pi^\pm$ Same Sign mode, extracted from a simplified version of the fit in Section 5.5, scaled using the ratio of branching fractions and selection efficiencies of the $\Lambda^0_b \to D^0 ph^-$ decay [86] with respect to $B^0 \to DK^{*0}$.

Therefore a PID cut designed to veto protons, namely $\mathrm{DLL}_{pK} < 10$, is applied to the K from the K^{*0} to remove this background. The number of expected background events in both the $D \to K^\mp\pi^\pm$ Same Sign and Opposite Sign categories is reduced by this requirement to 2.4, and in $D \to K^+K^-$ to 0.44. This contamination is small and neglected in the final result.

$\Lambda_b^0 \rightarrow \Lambda_c^+ \left(pK^- \pi^+ \right) h^-$ ($h = \pi, K$) background

Events of the type $\Lambda_b^0 \rightarrow \Lambda_c^+ \left(pK^- \pi^+ \right) h^-$ can potentially become a background to $B^0 \rightarrow DK^{*0}$ when the proton in the final state is misidentified as a K or π. It is studied in exactly the same way as the $\Lambda_b^0 \rightarrow D^0 ph^-$ background and is not expected to contribute significantly after offline selection. The tight flight distance significance cut on the D meson is observed to be the most powerful kinematic selection in discriminating against this background.

$B^0 \rightarrow D_{(s)}^{\mp} \left(h'h''h''' \right) h$ ($h, h', h'', h''' = \pi^\pm, K^\pm$) background

Peaking background could arise from $B^0 \rightarrow D^- \left(h'h''h''' \right) h^+$ and $B^0 \rightarrow D_s^+ \left(h'h''h''' \right) h^-$, since they have exactly the same final state as the signal. This background source is studied from all possible $K\pi\pi$ and $KK\pi$ invariant mass combinations with three out of the four particles in the final state in data. Very few events are found in the invariant mass region around the $D_s^\pm$ and $D^\pm$ nominal masses. Nevertheless, a $\pm 15\,\mathrm{MeV}/c^2$ cut on the difference between the $K^\pm K^\mp \pi^\pm$ invariant mass and the $D_s^\pm$ or $D^\pm$ nominal mass is applied, and also between the $K^\mp \pi^\pm \pi^\pm$ and the $D^\pm$ nominal mass (see Table 5.2), since these decays represent respectively the favoured decays of the $D_s^\pm$ and $D^\pm$ mesons. The efficiency of these cuts on signal is higher than 99 %.

5.4 Efficiencies

The efficiencies are split into three categories: the efficiency of the geometrical acceptance and the kinematic selections ϵ_{sel}, including stripping and High Level Trigger (HLT), which is reproduced correctly by the Monte Carlo simulation, and the efficiencies of the particle identification ϵ_{PID} and of the Level 0 (L0) trigger ϵ_{L0}, that need to be determined directly from data. The total efficiency is the product of the three terms,

$$\epsilon_{\mathrm{tot}} = \epsilon_{\mathrm{sel}} \times \epsilon_{\mathrm{PID}} \times \epsilon_{\mathrm{L0}}. \tag{5.8}$$

5.4.1 Kinematic selections

The efficiencies of the kinematic criteria ϵ_{sel} applied at the stripping or at the selection level (except PID or trigger efficiencies) are computed from Monte Carlo simulation, using reconstructed candidates matched to a true B signal. Only one kinematic cut is added at a time on these true signal events, and the remaining number of them is used to calculate the efficiency. The results are shown in Tables 5.5, 5.6 and 5.7, where the uncertainties are statistical. The total kinematic selection efficiency for each mode is simply the product of all the lines in the corresponding table. It can be seen from the tables that B^0 and $\overline{B}^0$ efficiencies are compatible. The ratio of efficiencies between the $B^0 \rightarrow [K^\mp \pi^\pm]_D K^{*0}$ and $B^0 \rightarrow [K^+ K^-]_D K^{*0}$ modes is computed from these tables to be

$$r_{\mathrm{sel}} \left(R_d^{KK} \right) = \frac{\epsilon_{sel}(B^0 \rightarrow [K^\mp \pi^\pm]_D K^{*0})}{\epsilon_{sel}(B^0 \rightarrow [K^+ K^-]_D K^{*0})} = 0.94 \pm 0.03. \tag{5.9}$$

This factor is used in the computation of the R_d^{KK} observable of Equation (5.3).

5.4.2 Particle identification

The DLL distributions are not well reproduced in the Monte Carlo simulation, thus a data driven method is used to determine the efficiencies of the PID cuts ϵ_{PID}. Control channels containing specific particle types exist in LHCb, where high purity samples can be isolated without the use of the RICHs particle identification information. The channel used in this

Cut	B^0 Efficiency	$\overline{B}^0$ Efficiency
Acceptance	$0.1580\,^{+0.00040}_{-0.00040}$	$0.1570\,^{+0.00040}_{-0.00040}$
Stripping	$0.0274\,^{+0.00033}_{-0.00032}$	$0.0277\,^{+0.00033}_{-0.00033}$
Vertex $\chi^2/\mathrm{ndf}\left(B^0\right) < 4$	$0.9610\,^{+0.00230}_{-0.00250}$	$0.9550\,^{+0.00250}_{-0.00260}$
Min IP$\chi^2\left(B^0\right) < 9$	$0.9610\,^{+0.00240}_{-0.00250}$	$0.9580\,^{+0.00250}_{-0.00260}$
$\cos(\theta_{\mathrm{dira}}) > 0.99995$	$0.9780\,^{+0.00180}_{-0.00200}$	$0.9770\,^{+0.00190}_{-0.00200}$
$|\cos\theta^*| > 0.4$	$0.9220\,^{+0.00340}_{-0.00350}$	$0.9310\,^{+0.00320}_{-0.00340}$
$\sum_{\mathrm{tracks}} \sqrt{\mathrm{IP}\chi^2} > 32$	$0.9740\,^{+0.00210}_{-0.00230}$	$0.9710\,^{+0.00220}_{-0.00240}$
$|M(K^{\mp}\pi^{\pm}\pi^{\pm}) - M(D^{\pm})| > 15\,\mathrm{MeV}/c^2$	$0.9940\,^{+0.00100}_{-0.00120}$	$0.9960\,^{+0.00090}_{-0.00110}$
$|M(K^{\pm}K^{\mp}\pi^{\pm}) - M(D^{\pm})| > 15\,\mathrm{MeV}/c^2$	$1.0000\,^{+0.00000}_{-0.00030}$	$1.0000\,^{+0.00000}_{-0.00030}$
$|M(K^{\pm}K^{\mp}\pi^{\pm}) - M(D_s^{\pm})| > 15\,\mathrm{MeV}/c^2$	$1.0000\,^{+0.00000}_{-0.00030}$	$1.0000\,^{+0.00000}_{-0.00030}$
Min IP$\chi^2\left(K^{*0}\right) > 25$	$0.9920\,^{+0.00120}_{-0.00140}$	$0.9920\,^{+0.00120}_{-0.00140}$
$\left|M(K^+\pi^-) - M(K^{*0}_{PDG})\right| < 50\,\mathrm{MeV}/c^2$	$0.7640\,^{+0.00570}_{-0.00580}$	$0.7600\,^{+0.00580}_{-0.00590}$
$p_{\mathrm{T}}(K_{K^{*0}}) > 300\,\mathrm{MeV}/c$	$0.9980\,^{+0.00070}_{-0.00100}$	$0.9990\,^{+0.00050}_{-0.00080}$
$p_{\mathrm{T}}(\pi_{K^{*0}}) > 300\,\mathrm{MeV}/c$	$0.9220\,^{+0.00410}_{-0.00430}$	$0.9160\,^{+0.00430}_{-0.00440}$
Vertex $\chi^2/\mathrm{ndf}\left(D^0\right) < 5$	$0.9550\,^{+0.00330}_{-0.00360}$	$0.9560\,^{+0.00330}_{-0.00360}$
Flight distance significance$(D^0) > 2.5$	$0.7380\,^{+0.00730}_{-0.00740}$	$0.7170\,^{+0.00750}_{-0.00760}$
Min IP$\chi^2\left(D^0\right) > 4$	$0.9980\,^{+0.00080}_{-0.00120}$	$0.9980\,^{+0.00090}_{-0.00140}$
$\left|M(D^0) - M(D^0_{PDG})\right| < 20\,\mathrm{MeV}/c^2$	$0.9530\,^{+0.00410}_{-0.00440}$	$0.9520\,^{+0.00420}_{-0.00450}$
$p_{\mathrm{T}}(K_D) > 400\,\mathrm{MeV}/c$	$0.9820\,^{+0.00260}_{-0.0030}$	$0.9840\,^{+0.00250}_{-0.00290}$
$p_{\mathrm{T}}(\pi_D) > 400\,\mathrm{MeV}/c$	$0.9630\,^{+0.00370}_{-0.00410}$	$0.9650\,^{+0.00370}_{-0.00410}$
Total Efficiency	$0.0015\,^{+3.2\,10^{-5}}_{-3.1\,10^{-5}}$	$0.0015\,^{+3.1\,10^{-5}}_{-3.0\,10^{-5}}$

Table 5.5: *Efficiencies of the kinematic selection on* $B^0 \to [K^{\mp}\pi^{\pm}]_D K^{*0}$.

analysis is $D^{*+} \to D^0\left(K^-\pi^+\right)\pi^+$. The large charm cross-section at the LHC, together with the unique decay kinematics of this mode, allows high statistics samples of K and π to be unambiguously identified through kinematic requirements alone. These pure samples of K and π are used for calibration, and since no PID cuts have been applied, their true DLL distributions in data can be known.

It is assumed that the efficiency of a cut on $\mathrm{DLL}_{K\pi}$ on a particular track depends on a small set of kinematic or event variables. Here, the total momentum p and the pseudorapidity η are used, because it is found from simulation that the performance of the RICH has the strongest dependence on these variables. The efficiency of the PID cuts used in this analysis is computed by applying them on the control channel, and this is done as a function of p and η. To account for variations in the performance of the RICH over the course of the data taking period, different run ranges are considered.

Signal $B^0 \to DK^{*0}$ Monte Carlo samples are used to compute the total PID efficiency for each one of the D modes in study. It is assumed that the p and η distributions of the tracks in the signal modes are well simulated in the Monte Carlo. For each event in the signal Monte Carlo sample, an efficiency is assigned depending on its particular kinematics. It is computed as the product of the individual efficiencies of the final tracks, which are determined from the results on the calibration sample by taking the efficiency for the concerned type of particle and

Cut	B^0 Efficiency	$\overline{B}^0$ Efficiency
Acceptance	$0.1570\ ^{+0.00040}_{-0.00040}$	$0.1570\ ^{+0.00040}_{-0.00040}$
Stripping	$0.0279\ ^{+0.00033}_{-0.00033}$	$0.0286\ ^{+0.00034}_{-0.00033}$
Vertex $\chi^2/\text{ndf}\left(B^0\right) < 4$	$0.9610\ ^{+0.00230}_{-0.00240}$	$0.9620\ ^{+0.00230}_{-0.00240}$
Min IP$\chi^2\left(B^0\right) < 9$	$0.9660\ ^{+0.00220}_{-0.00230}$	$0.9550\ ^{+0.00250}_{-0.00260}$
$\cos(\theta_{\text{dira}}) > 0.99995$	$0.9740\ ^{+0.0020}_{-0.00200}$	$0.9770\ ^{+0.00190}_{-0.00200}$
$|\cos\theta^*| > 0.4$	$0.9220\ ^{+0.00340}_{-0.00350}$	$0.9240\ ^{+0.00330}_{-0.00340}$
$\sum_{\text{tracks}}\sqrt{\text{IP}\chi^2} > 32$	$0.9720\ ^{+0.00220}_{-0.00230}$	$0.9770\ ^{+0.00190}_{-0.00210}$
$|M(K^{\mp}\pi^{\pm}\pi^{\pm}) - M(D^{\pm})| > 15\,\text{MeV}/c^2$	$0.9950\ ^{+0.00090}_{-0.00110}$	$0.9950\ ^{+0.00090}_{-0.00110}$
$|M(K^{\pm}K^{\mp}\pi^{\pm}) - M(D^{\pm})| > 15\,\text{MeV}/c^2$	$1.0000\ ^{+0.00000}_{-0.00030}$	$1.0000\ ^{+0.00000}_{-0.00030}$
$|M(K^{\pm}K^{\mp}\pi^{\pm}) - M(D_s^{\pm})| > 15\,\text{MeV}/c^2$	$1.0000\ ^{+0.00000}_{-0.00030}$	$1.0000\ ^{+0.00000}_{-0.00030}$
Min IP$\chi^2\left(K^{*0}\right) > 25$	$0.9930\ ^{+0.00110}_{-0.00130}$	$0.9920\ ^{+0.00120}_{-0.00140}$
$\left|M(K^+\pi^-) - M(K_{PDG}^{*0})\right| < 50\,\text{MeV}/c^2$	$0.7710\ ^{+0.00560}_{-0.00570}$	$0.7600\ ^{+0.00570}_{-0.00580}$
$p_{\text{T}}(K_{K^{*0}}) > 300\,\text{MeV}/c$	$0.9970\ ^{+0.00080}_{-0.00110}$	$0.9980\ ^{+0.00060}_{-0.00090}$
$p_{\text{T}}(\pi_{K^{*0}}) > 300\,\text{MeV}/c$	$0.9210\ ^{+0.00410}_{-0.00430}$	$0.9220\ ^{+0.00410}_{-0.00430}$
Vertex $\chi^2/\text{ndf}\left(D^0\right) < 5$	$0.9560\ ^{+0.00320}_{-0.00350}$	$0.9520\ ^{+0.00340}_{-0.00360}$
Flight distance significance$(D^0) > 2.5$	$0.7320\ ^{+0.00720}_{-0.00740}$	$0.7280\ ^{+0.00720}_{-0.00740}$
Min IP$\chi^2\left(D^0\right) > 4$	$0.9990\ ^{+0.00050}_{-0.00090}$	$0.9960\ ^{+0.00120}_{-0.00160}$
$\left|M(D^0) - M(D_{PDG}^0)\right| < 20\,\text{MeV}/c^2$	$0.9650\ ^{+0.00350}_{-0.00380}$	$0.9500\ ^{+0.00410}_{-0.00450}$
$p_{\text{T}}(K_D) > 400\,\text{MeV}/c$	$0.9810\ ^{+0.00260}_{-0.00300}$	$0.9820\ ^{+0.00260}_{-0.00300}$
$p_{\text{T}}(\pi_D) > 400\,\text{MeV}/c$	$0.9680\ ^{+0.00340}_{-0.00380}$	$0.9650\ ^{+0.00360}_{-0.00400}$
Total Efficiency	$0.0016\ ^{+3.2\,10^{-5}}_{-3.1\,10^{-5}}$	$0.0016\ ^{+3.2\,10^{-5}}_{-3.1\,10^{-5}}$

Table 5.6: *Efficiencies of the kinematic selection on* $\overline{B}_s^0 \to [K^{\mp}\pi^{\pm}]_D K^{*0}$.

cut, from the corresponding p and η bin. The overall efficiency for that particular mode is taken as the mean of all individual event efficiencies. Therefore, the efficiency of the PID cuts are given as global efficiencies on each mode rather than individual cuts.

The combined PID efficiencies on all signal modes are summarised in Table 5.8, where the quoted uncertainty is statistical only. As the efficiencies between the different modes are not compatible within the statistical uncertainty, correction factors are obtained, to be applied in the observables measurement. These corrections are computed as ratios of efficiencies,

$$\hat{\epsilon}_{\text{PID}}^{KK} = \frac{\epsilon_{\text{PID}}(B^0 \to [K^+K^-]_D K^{*0})}{\epsilon_{\text{PID}}(\overline{B}^0 \to [K^+K^-]_D \overline{K}^{*0})} = 0.99958 \pm 0.00010 \pm 0.00988, \quad (5.10)$$

$$\hat{\epsilon}_{\text{PID}}^{K\pi} = \frac{\epsilon_{\text{PID}}(B^0 \to [K^{\mp}\pi^{\pm}]_D K^{*0})}{\epsilon_{\text{PID}}(\overline{B}^0 \to [K^{\mp}\pi^{\pm}]_D \overline{K}^{*0})} = 0.98421 \pm 0.00010 \pm 0.01553, \quad (5.11)$$

$$r_{\text{PID}}\left(R_d^{KK}\right) = \frac{\epsilon_{\text{PID}}(B^0 \to [K^{\mp}\pi^{\pm}]_D K^{*0})}{\epsilon_{\text{PID}}(B^0 \to [K^+K^-]_D K^{*0})} = 1.00964 \pm 0.00010 \pm 0.01553. \quad (5.12)$$

The first uncertainty is statistical and the second systematic. This systematic uncertainty is computed as the variation between the efficiency values when using $D^{*+} \to D^0\left(K^-\pi^+\right)\pi^+$ calibration data and the result when the PID calibration procedure is done instead on a $D^{*+} \to D^0\left(K^-\pi^+\right)\pi^+$ Monte Carlo sample.

Cut	B^0 Efficiency	$\overline{B}^0$ Efficiency
Acceptance	$0.1650 \, ^{+0.00040}_{-0.00040}$	$0.1640 \, ^{+0.00040}_{-0.00040}$
Stripping	$0.0273 \, ^{+0.00032}_{-0.00032}$	$0.0269 \, ^{+0.00032}_{-0.00032}$
Vertex $\chi^2/\mathrm{ndf}\,(B^0) < 4$	$0.9590 \, ^{+0.00240}_{-0.00250}$	$0.9560 \, ^{+0.00250}_{-0.00260}$
Min IP$\chi^2\,(B^0) < 9$	$0.9640 \, ^{+0.00230}_{-0.00240}$	$0.9610 \, ^{+0.00240}_{-0.00250}$
$\cos(\theta_{\mathrm{dira}}) > 0.99995$	$0.9760 \, ^{+0.00190}_{-0.00200}$	$0.9780 \, ^{+0.00180}_{-0.00200}$
$|\cos\theta^*| > 0.4$	$0.9240 \, ^{+0.00330}_{-0.00350}$	$0.9270 \, ^{+0.00330}_{-0.00340}$
$\sum_{\mathrm{tracks}} \sqrt{\mathrm{IP}\chi^2} > 32$	$0.9730 \, ^{+0.00210}_{-0.00230}$	$0.9680 \, ^{+0.00230}_{-0.00250}$
$|M(K^\pm K^\mp \pi^\pm) - M(D^\pm)|(K_D^+) > 15\,\mathrm{MeV}/c^2$	$0.9990 \, ^{+0.00040}_{-0.00060}$	$0.9960 \, ^{+0.00080}_{-0.00100}$
$|M(K^\pm K^\mp \pi^\pm) - M(D^\pm)|(K_D^-) > 15\,\mathrm{MeV}/c^2$	$0.9950 \, ^{+0.00100}_{-0.00110}$	$0.9970 \, ^{+0.00070}_{-0.00090}$
$|M(K^\pm K^\mp \pi^\pm) - M(D_s^\pm)|(K_D^+) > 15\,\mathrm{MeV}/c^2$	$0.9980 \, ^{+0.00050}_{-0.00070}$	$0.9970 \, ^{+0.00080}_{-0.00100}$
$|M(K^\pm K^\mp \pi^\pm) - M(D_s^\pm)|(K_D^-) > 15\,\mathrm{MeV}/c^2$	$0.9960 \, ^{+0.00090}_{-0.00100}$	$0.9980 \, ^{+0.00060}_{-0.00080}$
Min IP$\chi^2\,(K^{*0}) > 25$	$0.9930 \, ^{+0.00110}_{-0.00130}$	$0.9930 \, ^{+0.00110}_{-0.00130}$
$\left|M(K^+\pi^-) - M(K^{*0}_{PDG})\right| < 50\,\mathrm{MeV}/c^2$	$0.7680 \, ^{+0.00570}_{-0.00580}$	$0.7730 \, ^{+0.00570}_{-0.00580}$
$p_\mathrm{T}(K_{K^{*0}}) > 300\,\mathrm{MeV}/c$	$0.9980 \, ^{+0.00070}_{-0.00100}$	$0.9970 \, ^{+0.00080}_{-0.00110}$
$p_\mathrm{T}(\pi_{K^{*0}}) > 300\,\mathrm{MeV}/c$	$0.9170 \, ^{+0.00420}_{-0.00440}$	$0.9220 \, ^{+0.00410}_{-0.00430}$
Vertex $\chi^2/\mathrm{ndf}\,(D^0) < 5$	$0.9550 \, ^{+0.00330}_{-0.00350}$	$0.9530 \, ^{+0.00340}_{-0.00360}$
Flight distance significance$(D^0) > 2.5$	$0.7200 \, ^{+0.00740}_{-0.00750}$	$0.7020 \, ^{+0.00760}_{-0.00770}$
Min IP$\chi^2\,(D^0) > 4$	$0.9970 \, ^{+0.00100}_{-0.00140}$	$0.9980 \, ^{+0.00080}_{-0.00130}$
$\left|M(D^0) - M(D^0_{PDG})\right| < 20\,\mathrm{MeV}/c^2$	$0.9790 \, ^{+0.00270}_{-0.00310}$	$0.9790 \, ^{+0.00280}_{-0.00320}$
$p_\mathrm{T}(K_D^+) > 400\,\mathrm{MeV}/c$	$0.9860 \, ^{+0.00230}_{-0.00270}$	$0.9860 \, ^{+0.00230}_{-0.00270}$
$p_\mathrm{T}(K_D^-) > 400\,\mathrm{MeV}/c$	$0.9860 \, ^{+0.00230}_{-0.00270}$	$0.9870 \, ^{+0.00230}_{-0.00270}$
Total Efficiency	$0.0016 \, ^{+3.3\,10^{-5}}_{-3.2\,10^{-5}}$	$0.0016 \, ^{+3.2\,10^{-5}}_{-3.2\,10^{-5}}$

Table 5.7: *Efficiencies of the kinematic selection on $B^0 \to [K^+K^-]_D K^{*0}$.*

Mode	B^0 Efficiency	$\overline{B}^0$ Efficiency
$B^0 \to [K^\mp \pi^\pm]_D K^{*0}$	0.7169 ± 0.0001	0.7284 ± 0.0001
$\overline{B}^0_s \to [K^\mp \pi^\pm]_D K^{*0}$	0.7244 ± 0.0001	0.7137 ± 0.0001
$B^0 \to [K^+ K^-]_D K^{*0}$	0.7156 ± 0.0001	0.7159 ± 0.0001

Table 5.8: *Efficiencies of the PID selection cuts on each considered decay mode.*

5.4.3 L0 trigger

Regarding the requirements on the L0 trigger, events are selected and classified into two categories: "OtherB" when the trigger is due to the other B hadron in the event, and "TOS" when the event is triggered by the signal B candidate through the L0 hadronic calorimeter trigger[8].

---

[8]Events are usually classified in LHCb with respect to the trigger as Trigger On Signal (TOS) and Trigger Independent of Signal (TIS) for a considered trigger line (*c.f.* Section 4.5.3).

Mode	B^0 Efficiency	$\overline{B}^0$ Efficiency
$B^0 \to [K^{\mp}\pi^{\pm}]_D K^{*0}$	0.529 ± 0.006	0.528 ± 0.006
$\overline{B}^0_s \to [K^{\mp}\pi^{\pm}]_D K^{*0}$	0.533 ± 0.006	0.534 ± 0.006
$B^0 \to [K^+K^-]_D K^{*0}$	0.537 ± 0.006	0.533 ± 0.006

Table 5.9: *TOS efficiencies of the L0 Hadron trigger line, for each considered decay mode.*

- The "OtherB" category is defined requiring that any TIS decision is satisfied (`L0Global_TIS`, where the L0 decision can be due to the `Electron`, `Photon`, `Hadron`, `Muon` or `DiMuon` L0 trigger lines); 56.6 % of the candidates (including background and combining the two decay modes considered for the D meson) after selection belong to this category. The efficiency of this trigger category is assumed to be equal between all D decay modes and also between B^0 and $\overline{B}^0$, thus not affecting the measurement of the asymmetries.

- The "TOS" category contains the events that satifisfy the TOS decision on the L0 Hadron line (`L0HadronDecision_TOS`), that is to say when at least one of the charged tracks of the signal decay gives a cluster of high enough transverse energy in the HCAL to pass the L0 Hadron trigger threshold. 62.2 % of events after selection belong to the "TOS" category. The efficiency of this trigger requirement depends on the D decay mode and can potentially show asymmetries between positive and negative tracks, as explained below.

Selected events in the "OtherB" or "TOS" categories are kept. The candidates that are both in the "OtherB" and in the "TOS" categories represent 23.1 % of the total sample. Around 4.3 % of events after all selection criteria are found not to be in either category, and they are not considered in this analysis[9].

The "TOS" efficiency is extracted from signal Monte Carlo samples for $B^0 \to DK^{*0}$ modes where the D meson decays as $D \to K^{\mp}\pi^{\pm}$ or $D \to K^+K^-$, following the procedure presented in Section 4.6. After applying the selection, each Monte Carlo sample is reweighted to account for differences seen in the L0 Hadron performance between data and simulation, using efficiency tables that provide the L0 Hadron trigger efficiency as a function of the transverse momentum for an individual track, depending on its type (K or π) and its charge. These efficiency tables are computed using K and π from prompt D^0 out of the calibration stream [79,80]. The total "TOS" efficiency of triggering on the B event is computed by combining the efficiencies corresponding to the four final tracks supposing that at least one triggers (*c.f* Section 4.6.1). The final efficiency for each decay mode is computed as the mean efficiency over the B events in the corresponding Monte Carlo sample. The L0 Hadron efficiencies computed in this way are summarized in Table 5.9, for the different B meson flavours and the different D decay modes considered.

The total L0 trigger efficiency is the sum of the "OtherB" and "TOS" efficiencies,

$$\epsilon_{\text{L0}} = (1 - f)\epsilon_{\text{OtherB}} + f\epsilon_{\text{TOS}}, \qquad (5.13)$$

where f is the fraction of events that belong to the "TOS" category but not to the "OtherB" category, that is to say "TOSOnly". This fraction and the efficiency of the "OtherB" category are computed using the number of signal events in the $B^0 \to [K^+\pi^-]_D K^{*0}$ and $\overline{B}^0_s \to [K^-\pi^+]_D K^{*0}$

---

[9]These are events where the L0 decision is due to particles from the signal B but not from the hadron line (electron or photon for example). For these events, the computation of the trigger efficiency would be too complex and difficult to control.

Mode	B^0 Efficiency	$\overline{B}^0$ Efficiency
$B^0 \to [K^\mp\pi^\pm]_D K^{*0}$	0.48 ± 0.03	0.48 ± 0.03
$\overline{B}^0_s \to [K^\mp\pi^\pm]_D K^{*0}$	0.48 ± 0.03	0.48 ± 0.03
$B^0 \to [K^+K^-]_D K^{*0}$	0.48 ± 0.03	0.48 ± 0.03

Table 5.10: *Total L0 trigger efficiencies computed for the different decay modes, measured with respect to the events passing all selection cuts.*

Decay mode	Efficiency
$B^0 \to [K^\mp\pi^\pm]_D K^{*0}$	0.00052 ± 0.00003
$\overline{B}^0_s \to [K^\mp\pi^\pm]_D K^{*0}$	0.00055 ± 0.00004
$B^0 \to [K^+K^-]_D K^{*0}$	0.00055 ± 0.00004

Table 5.11: *Total efficiencies.*

modes on data, extracted from the result of the fit described in Section 5.5 performed separately for each trigger requirement.

The fraction of "TOSOnly" events is computed as

$$f = \frac{N_{\text{TOSOnly}}}{N_{\text{TOS or OtherB}}}, \tag{5.14}$$

and it is found to be $f = 0.43 \pm 0.02$. This fraction is assumed to be identical for all the modes, as the same p_{T} cuts are applied to the four particles in the final state everywhere. The efficiency of the "OtherB" category is computed as

$$\epsilon_{\text{OtherB}} = \frac{N_{\text{OtherB}}}{N_{\text{TOS}}} \times \epsilon_{\text{TOS}}. \tag{5.15}$$

This efficiency is assumed to be identical for all B modes and for the two B flavours, as it does not depend on the signal. It is found to be equal to $\epsilon_{\text{OtherB}} = 0.44 \pm 0.03$. The total trigger efficiencies computed in this way for each mode are shown in Table 5.10. It can be seen that these efficiencies are compatible for all the modes and therefore they cancel when taking the ratio.

5.4.4 Total efficiencies

The total efficiencies, including geometrical acceptance, reconstruction, stripping, selection and trigger effects are summarized in Table 5.11, for all decay modes used in this analysis. The mean value of the efficiencies between B and $\overline{B}$ decays is taken when these are different. These total efficiencies are not used for the final observable computation, but are shown here for illustration purposes.

5.5 Fit strategy

The event yields necessary to compute the ratios and asymetries presented in Section 5.1 are extracted from an extended unbinned maximum likelihood fit to the mass distributions of the reconstructed and selected events. The DK^{*0} invariant mass of the B candidates is computed from the combination of the four final state particles. A constraint on the D meson mass is applied, forcing it to be equal to D^0 nominal mass (1864.84 ± 0.17) MeV/c^2 [84], in order to improve the B signal resolution. The B candidates invariant mass window considered is defined as $[5.0; 5.8]$ GeV/c^2.

5.5.1 Categories

$B \to DK^{*0}$ events are grouped into categories, according to the D decay mode in which they are reconstructed and the flavour of the B-hadron at its decay time. The following categories are defined (the signal contributions in each category are also indicated):

- B ($K\pi$) Opposite Sign (OS):
  $B^0 \to [K^-\pi^+]_D K^{*0}(K^+\pi^-)$ and $\overline{B}_s^0 \to [K^-\pi^+]_D K^{*0}(K^+\pi^-)$;

- $\overline{B}$ ($K\pi$) Opposite Sign (OS):
  $\overline{B}^0 \to [K^+\pi^-]_D \overline{K}^{*0}(K^-\pi^+)$ and $B_s^0 \to [K^+\pi^-]_D \overline{K}^{*0}(K^-\pi^+)$;

- B ($K\pi$) Same Sign (SS):
  $B^0 \to [K^+\pi^-]_D K^{*0}(K^+\pi^-)$ and $\overline{B}_s^0 \to [K^+\pi^-]_D K^{*0}(K^+\pi^-)$;

- $\overline{B}$ ($K\pi$) Same Sign (SS):
  $\overline{B}^0 \to [K^-\pi^+]_D \overline{K}^{*0}(K^-\pi^+)$ and $B_s^0 \to [K^-\pi^+]_D \overline{K}^{*0}(K^-\pi^+)$;

- B (KK):
  $B^0 \to [K^+K^-]_D K^{*0}(K^+\pi^-)$ and $\overline{B}_s^0 \to [K^+K^-]_D K^{*0}(K^+\pi^-)$;

- $\overline{B}$ (KK):
  $\overline{B}^0 \to [K^+K^-]_D \overline{K}^{*0}(K^-\pi^+)$ and $B_s^0 \to [K^+K^-]_D \overline{K}^{*0}(K^-\pi^+)$.

Events in the $D \to K^\mp\pi^\pm$ Opposite Sign categories are used to constrain with a high statistics sample the shape of the low mass $\overline{B}_s^0$ background described in Section 5.5.2.3, but they are not entering any physical observable measured in this analysis (in particular, the yield of B^0 and $\overline{B}^0$ signal candidates will be kept blind, since they are the sensitive modes for the ADS analysis).

5.5.2 Fit probability density function components

For each category of events, the mass distribution is fit with a model which is the sum of probability density functions (PDF) describing the different types of contributions. They are detailed in this Section. The B invariant mass variable on which the fit is performed is denoted as M.

5.5.2.1 Signal

The PDF describing the signal is, for each category, a sum of two double Gaussian functions, one for the B^0 signal peak and one for the $\overline{B}_s^0$ signal peak. A double Gaussian function is the

sum of two Gaussians with a common mean value. The PDF for the signal is then

$$f_{\text{signal}}(M; N^{B^0}, N^{\overline{B}_s^0}, \mu, \sigma) = N^{B^0}\left[\frac{f_{\text{core}}}{\sigma\sqrt{2\pi}}e^{-\frac{(M-\mu)^2}{2\sigma^2}} + \frac{1-f_{\text{core}}}{\sigma\kappa\sqrt{2\pi}}e^{-\frac{(M-\mu)^2}{2\sigma^2\kappa^2}}\right] + $$
$$N^{\overline{B}_s^0}\left[\frac{f_{\text{core}}}{\sigma\sqrt{2\pi}}e^{-\frac{(M-\mu-\Delta M)^2}{2\sigma^2}} + \frac{1-f_{\text{core}}}{\sigma\kappa\sqrt{2\pi}}e^{-\frac{(M-\mu-\Delta M)^2}{2\sigma^2\kappa^2}}\right], \quad (5.16)$$

where

- N^{B^0} is the number of signal B^0 events.

- $N^{\overline{B}_s^0}$ is the number of signal $\overline{B}_s^0$ events.

- μ is the central value of the Gaussian function for the B^0 peak.

- σ is the resolution of the Gaussian function out of the doublet which has the smallest one, or "core" resolution. The same value is used for the B^0 and the $\overline{B}_s^0$ peaks[10].

- κ is the ratio of the largest resolution to the smallest resolution of the double Gaussian function. It is fixed to the value obtained from Monte Carlo simulation, $\kappa = 2.1$, and the same value is used for B^0 and $\overline{B}_s^0$.

- f_{core} is the fraction of signal events in the Gaussian with the smallest resolution. It is fixed to the value obtained from Monte Carlo simulation, $f_{\text{core}} = 0.87$, and the same value is used for B^0 and $\overline{B}_s^0$.

- ΔM is the mass difference between the mean values of the $\overline{B}_s^0$ peak and B^0 peak. It is fixed to the nominal value $\Delta M = 87.35 \, \text{MeV}/c^2$ [84].

Except for the signal yields, N^{B^0} and $N^{\overline{B}_s^0}$, the values of all the other parameters are common between all the fit categories. The B_s^0 and $\overline{B}_s^0$ signal yields for the $D \to K^{\mp}\pi^{\pm}$ Same Sign category are fixed to 0 since no signal is expected with the current size of the data sample.

5.5.2.2 Combinatorial background

The combinatorial background is parameterised by a decreasing exponential function with slope parameter c,

$$f_{\text{comb}}(M; N_{comb}, c) = N_{\text{comb}}e^{Mc} \times |c|, \quad (5.17)$$

where N_{comb} is the number of combinatorial background events. The value of the slope c is the same for all event categories, and the numbers of combinatorial background candidates are constrained to be equal between B and $\overline{B}$. Using the same slope for all modes can be done as there are in all cases four particles in the final state; a previous version of the fit with different slopes for each D decay mode resulted in compatible values for all of them. The upper limit of the B invariant mass window used in the fit is set to 5.8 GeV/c^2 in order to take into account a large region at high mass, where only the combinatorial background contribution is present, which constrains this slope to a proper value.

---

[10]It was checked that this is justified on Monte Carlo simulation samples: the core resolution for both signal $B^0 \to [K^{\mp}\pi^{\pm}]_D K^{*0}$ and signal $\overline{B}_s^0 \to [K^{\mp}\pi^{\pm}]_D K^{*0}$ is (10.8 ± 0.2) MeV/c^2.
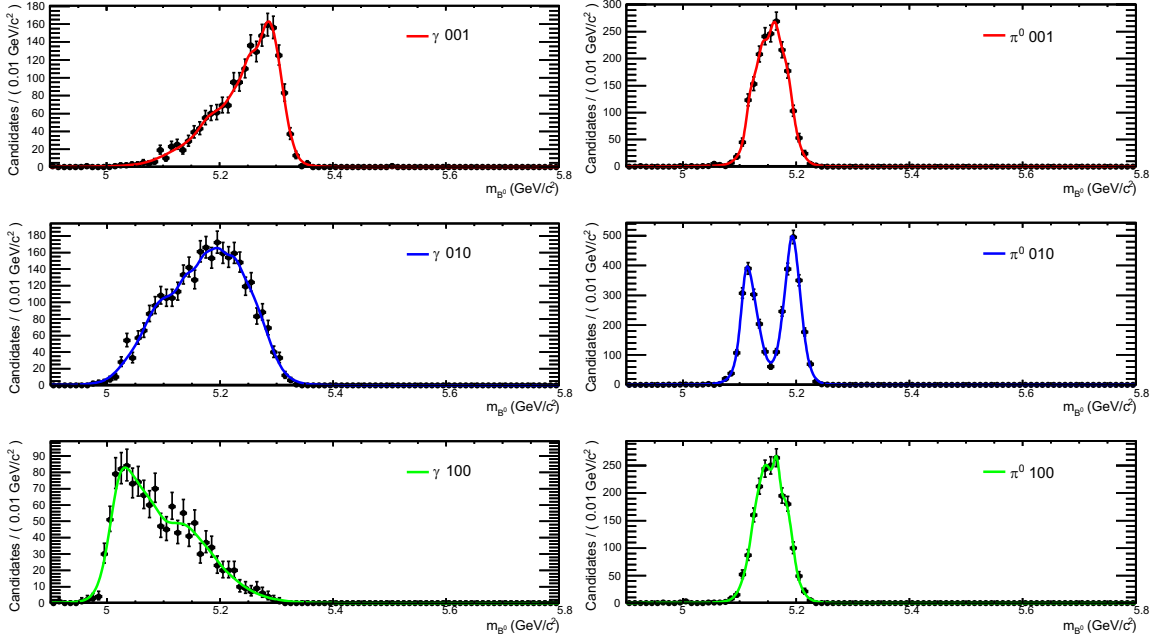
Figure 5.10: $\overline{B}_s^0 \to DK^{*0}$ invariant mass distributions for fully simulated $\overline{B}_s^0 \to D^*K^{*0}$ decays selected by the analysis selection with $D^{*0} \to D^0\gamma$ (left) and $D^{*0} \to D^0\pi^0$ (right) and $D \to K^-\pi^+$ in the "001" configuration (top), "010" configuration (middle) and the "100" configuration (bottom). The superimposed curves are non-parametric PDFs describing the distributions.

5.5.2.3 Low mass background from partially reconstructed $B^0 \to D^*K^{*0}$ decays

This category of background is due to $B^0_{(s)}$ decaying to $B^0 \to D^*K^{*0}$ or $\overline{B}_s^0 \to D^*K^{*0}$, where D^* denotes either a D^{*0} or a $\overline{D}^{*0}$, with $D^{*0} \to D^0\gamma$ or $D^{*0} \to D^0\pi^0$, and reconstructed as $B^0 \to DK^{*0}$ or $\overline{B}_s^0 \to DK^{*0}$. Because of the missing soft γ or π^0 momentum, the invariant mass of such candidates peaks at values below the nominal B^0 and B_s^0 masses.

Total angular momentum conservation in $B^0 \to D^*K^{*0}$ or $\overline{B}_s^0 \to D^*K^{*0}$, which are decays of a pseudo-scalar particle into two vector particles, implies three non zero (but unknown) helicity amplitudes:

- $\mathcal{A}_{001}$, the amplitude for the decay where the D^{*0} is produced in helicity state -1 and the K^{*0} in helicity state $+1$ (configuration "001", $\lambda(D^{*0}) = -1$, $\lambda(K^{*0}) = +1$).

- $\mathcal{A}_{010}$, the amplitude for the decay where the D^{*0} is produced in helicity state 0 and the K^{*0} in helicity state 0 (configuration "010", $\lambda(D^{*0}) = 0$, $\lambda(K^{*0}) = 0$).

- $\mathcal{A}_{100}$, the amplitude for the decay where the D^{*0} is produced in helicity state $+1$ and the K^{*0} in helicity state -1 (configuration "100", $\lambda(D^{*0}) = +1$, $\lambda(K^{*0}) = -1$).

Each helicity configuration results in different shapes of the reconstructed $B^0 \to DK^{*0}$ or $\overline{B}_s^0 \to DK^{*0}$ mass. The shape for the $D^{*0} \to D^0\gamma$ decay is also different from the shape for the $D^{*0} \to D^0\pi^0$ decay. Figure 5.10 shows the invariant mass distributions obtained with fully simulated events generated in the configurations "001", "010" and "100", and selected by the analysis selection, for the $D^{*0} \to D^0\gamma$ decay in the left panels and $D^{*0} \to D^0\pi^0$ in the rigth panels.

The function describing this background category is thus chosen, without interference between the different helicity configurations, as

$$
\begin{aligned}
f_{\text{pb}}(M; N_{\text{pb}}^{\overline{B}_s^0}, N_{\text{pb}}^{B^0}) = N_{\text{pb}}^{\overline{B}_s^0} &\left\{ \alpha_{001} \left[\frac{G_{001}}{G_{001} + P_{001}} f_{001}^\gamma(M) + \frac{P_{001}}{G_{001} + P_{001}} f_{001}^{\pi^0}(M) \right] + \right. \\
&\quad \alpha_{010} \left[\frac{G_{010}}{G_{010} + P_{010}} f_{010}^\gamma(M) + \frac{P_{010}}{G_{010} + P_{010}} f_{010}^{\pi^0}(M) \right] + \\
&\quad \left. (1 - \alpha_{010} - \alpha_{001}) \left[\frac{G_{100}}{G_{100} + P_{100}} f_{100}^\gamma(M) + \frac{P_{100}}{G_{100} + P_{100}} f_{100}^{\pi^0}(M) \right] \right\} + \\
N_{\text{pb}}^{B^0} &\left\{ \beta_{001} \left[\frac{G_{001}}{G_{001} + P_{001}} f_{001}^\gamma(M - \Delta M) + \frac{P_{001}}{G_{001} + P_{001}} f_{001}^{\pi^0}(M - \Delta M) \right] + \right. \\
&\quad \beta_{010} \left[\frac{G_{010}}{G_{010} + P_{010}} f_{010}^\gamma(M - \Delta M) + \frac{P_{010}}{G_{010} + P_{010}} f_{010}^{\pi^0}(M - \Delta M) \right] + \\
&\quad \left. (1 - \beta_{010} - \beta_{001}) \left[\frac{G_{100}}{G_{100} + P_{100}} f_{100}^\gamma(M - \Delta M) + \frac{P_{100}}{G_{100} + P_{100}} f_{100}^{\pi^0}(M - \Delta M) \right] \right\}.
\end{aligned}
$$
$$(5.18)$$

$N_{\text{pb}}^{B^0}$ and $N_{\text{pb}}^{\overline{B}_s^0}$ are the the number of partially reconstructed background events from the $B^0 \to D^*K^{*0}$ and $\overline{B}_s^0 \to D^*K^{*0}$ contributions respectively. In this function, f_X^γ and $f_X^{\pi^0}$ are non-parametric functions reproducing the mass distribution of fully simulated $\overline{B}_s^0 \to D^*K^{*0}$ events[11], with $D^{*0} \to D^0\gamma$ and $D^{*0} \to D^0\pi^0$ respectively and D^0 decaying to $K^\mp\pi^\pm$ Opposite Sign mode, and generated in the configuration "X" ("001", "010" or "100"), reconstructed as $\overline{B}_s^0 \to DK^{*0}$. These functions are the ones superimposed on the invariant mass distributions shown in Figure 5.10. The mass distributions obtained from the Monte Carlo simulation are smeared and shifted to take into account the different mass resolutions of the data[12], $\sigma = 12.4\,\text{MeV}/c^2$ and of the simulation $\sigma = 10.8\,\text{MeV}/c^2$, and the different mean values of the B_s^0 peaks, $M = 5\,368.7\,\text{MeV}/c^2$ for the data and $M = 5\,366.2\,\text{MeV}/c^2$ for the simulation.

The G_X and P_X factors in Equation (5.18) are the products of the branching fraction of $D^{*0} \to D^0\gamma$ or $D^{*0} \to D^0\pi^0$ decays respectively and of the corresponding efficiency factors in order to correctly normalise the different helicity amplitudes contributions,

$$
G_X = \mathcal{B}(D^{*0} \to D^0\gamma)\,\epsilon_{\text{acc}}(D^0\gamma)\,\epsilon_{\text{sel}}^X(D^0\gamma) \text{ and} \tag{5.19}
$$

$$
P_X = \mathcal{B}(D^{*0} \to D^0\pi^0)\,\epsilon_{\text{acc}}(D^0\pi^0)\,\epsilon_{\text{sel}}^X(D^0\pi^0), \tag{5.20}
$$

where ϵ_{acc} and ϵ_{sel} are the geometrical acceptance and the selection efficiency, respectively, both computed from fully simulated events for each configuration. Table 5.12 shows the value of each one of the factors entering this computation. The geometrical acceptance is computed as the number of events with all the final tracks inside the detector acceptance, over the total number of simulated events. The selection efficiency is computed as the number of events remaining after all selection cuts, over the number of simulated events with all the tracks inside the acceptance.

---

[11]These non-parametric functions are implemented using the "RooKeysPdf" class from the RooFit package in ROOT. It provides a one-dimensional estimation which models the distribution of an arbitrary input data set, by superposing Gaussian functions.

[12]This value of the mass resolution is found with a modified version of the fit, where B and $\overline{B}$ are not separated, and therefore is slightly different from the final value presented in Table 5.15.

Quantity	$D^{*0} \to D^0 \pi^0$	$D^{*0} \to D^0 \gamma$
Branching fraction	62 %	38 %
ϵ_{acc}	13.7 %	15.6 %
$\epsilon_{\mathrm{sel}}^{001}$	0.369 %	0.356 %
$\epsilon_{\mathrm{sel}}^{010}$	0.657 %	0.602 %
$\epsilon_{\mathrm{sel}}^{100}$	0.357 %	0.244 %

Table 5.12: *Branching fractions and efficiencies of the $B_s^0 \to D^* K^{*0}$ modes, with $D \to K^{\mp} \pi^{\pm}$.*

The same functions $f_X^{\pi^0}$ and f_X^{γ} are used to fit all categories, as well as the values of the parameters α_{001}, α_{010}, β_{001} and β_{010}, that give the relative normalisation between the different helicity configurations, are common to all of them. A first fit is performed letting these parameters free, leading to the values

- $\alpha_{001} = 0.00 \pm 0.11$,

- $\alpha_{010} = 0.67 \pm 0.07$,

- $\beta_{001} = 0.0 \pm 0.6$,

- $\beta_{010} = 0.93 \pm 0.10$,

where each value is constrained to be between 0 and 1. These results are constrained mainly by the $D \to K^{\mp} \pi^{\pm}$ Opposite Sign category. In order to avoid introducing too much complexity and control possible background correlations, these parameters are fixed to these values for the final iteration of the fit.

The yields of partially reconstructed candidates for the $\overline{B}_s^0$ background are constrained to the same value for the B and $\overline{B}$ categories. The same constraint is applied to the yields of partially reconstructed candidates for the B^0 background in the $D \to K^{\mp} \pi^{\pm}$ Same Sign category, where the CP violation effects are expected to be negligible. However, this can not be done for the other B and $\overline{B}$ yields of partially reconstructed background candidates, because of the expected sizeable CP violation effects to which they are sensitive. This is due to the interference between the $b \to u$ and $b \to c$ amplitudes in $D^* K^{*0}$ final states, which follows the same pattern as that in DK^{*0} (the Feynman diagrams are the same). Hence CP violation effects can be significant for $B^0 \to D^* K^{*0}$ in the $D \to K^{\mp} \pi^{\pm}$ Opposite Sign category or the $D \to K^+ K^-$ category.

The following yields of partially reconstructed background are left free in the fit: $N_{\mathrm{pb}}^{\overline{B}_s^0 + B_s^0 \ (K\pi OS)}$, $N_{\mathrm{pb}}^{B^0 + \overline{B}^0 \ (K\pi SS)}$, $N_{\mathrm{pb}}^{B^0 \ (K\pi OS)}$, $N_{\mathrm{pb}}^{\overline{B}^0 \ (K\pi OS)}$, $N_{\mathrm{pb}}^{B^0 \ (KK)}$, $N_{\mathrm{pb}}^{\overline{B}^0 \ (KK)}$. The B_s^0 and $\overline{B}_s^0$ yields in the $D \to K^{\mp} \pi^{\pm}$ Same Sign categories are fixed to 0 as for the corresponding signal yields, since these modes have a much lower branching fraction than the other ones. The yield of partially reconstructed $\overline{B}_s^0 + B_s^0$ background in the $D \to K^+ K^-$ category is constrained from the $\overline{B}_s^0 + B_s^0$ yields in the $D \to K^{\mp} \pi^{\pm}$ Opposite Sign category, using the branching fractions and relative selection efficiencies,

$$N_{\mathrm{pb}}^{\overline{B}_s^0 + B_s^0 \ (KK)} = N_{\mathrm{pb}}^{\overline{B}_s^0 + B_s^0 \ (K\pi OS)} \times \frac{\mathcal{B}(D^0 \to K^+ K^-)}{\mathcal{B}(D^0 \to K^- \pi^+)} \times \frac{\epsilon_{\mathrm{sel}}(B^0 \to [K^+ K^-]_D K^{*0})}{\epsilon_{\mathrm{sel}}(B^0 \to [K^{\mp} \pi^{\pm}]_D K^{*0})}, \quad (5.21)$$

assuming that the efficiencies are equal between the B^0 and the $\overline{B}_s^0$ decay modes. The values used are $\mathcal{B}(D^0 \to K^+ K^-) = 0.396$ % and $\mathcal{B}(D^0 \to K^- \pi^+) = 3.78$ % [84]. The efficiencies are
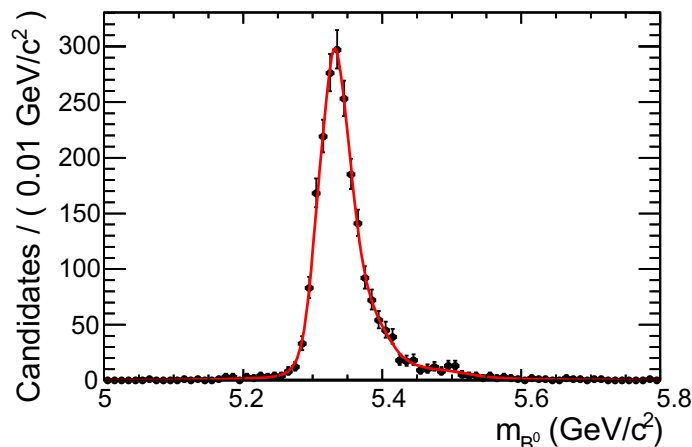
Figure 5.11: *$B^0 \to DK^{*0}$ invariant mass distribution for fully simulated $B^0 \to D\rho^0$ decays with $D \to K^{\mp}\pi^{\pm}$, selected by the analysis selection. The red line is the non-parametric function describing the distribution, used in the mass fit to model the cross-feed background component.*

measured from fully simulated Monte Carlo events and found to be $\epsilon_{\text{sel}}(B^0 \to [K^+K^-]_D K^{*0}) = 0.827$ % and $\epsilon_{\text{sel}}(B^0 \to [K^-\pi^+]_D K^{*0}) = 0.830$ %. Because of possible sizeable CP violation, the B^0 partially reconstructed background yields for $D \to K^+K^-$ cannot be directly related to the B^0 background yields for $D \to K^{\mp}\pi^{\pm}$ Opposite Sign.

5.5.2.4 Cross-feed background from $B^0 \to D\rho^0$

The last source of background considered is that due to $B^0 \to D\rho^0$ decays with $\rho^0 \to \pi^+\pi^-$, when one π from the ρ^0 is misidentified as a K and used to reconstruct the K^{*0} in the $B^0 \to DK^{*0}$ decay. Similarly, the invariant mass shape of these events is modelled with a non-parametric PDF $f_{\rho}^{\text{cross}-\text{feed}}(M)$ extracted from $B^0 \to D\rho^0$ Monte Carlo simulated events, with a K mass hypothesis assigned to one of the π from the ρ^0, applying a selection as close as possible to the one used for $B^0 \to DK^{*0}$ events[13]. The resulting distribution is shown in Figure 5.11. It has also been smeared and shifted to account for the differences between data and simulation, using the same factors as in Section 5.5.2.3.

The function used to model this background category is

$$f_{\text{cross}-\text{feed}}(M; N_{\text{cross}-\text{feed}}) = N_{\text{cross}-\text{feed}} f_{\rho}^{\text{cross}-\text{feed}}(M). \qquad (5.22)$$

The numbers of cross-feed candidates are constrained to be equal in the B and $\overline{B}$ candidates in the $D \to K^{\mp}\pi^{\pm}$ Opposite Sign and Same Sign categories,

$$N_{\text{cross}-\text{feed}}^{B\ (K\pi OS)} = N_{\text{cross}-\text{feed}}^{\overline{B}\ (K\pi OS)} = N_{\text{cross}-\text{feed}}^{B\ (K\pi SS)} = N_{\text{cross}-\text{feed}}^{\overline{B}\ (K\pi SS)}. \qquad (5.23)$$

$N_{\text{cross}-\text{feed}}^{(K\pi)}$ is constrained in the fit by means of a Gaussian constraint to the expected value, $N_{\text{cross}-\text{feed}}^{(K\pi)} = 52 \pm 2$, computed from:

- The number of signal $B^0 \to D\rho^0$, $D^0 \to K^-\pi^+$ candidates reconstructed in the same data sample. This number is extracted from a maximum likelihood fit to the $D\rho^0$ invariant mass distribution with a probability distribution function which is the sum of a double

---

[13]In practice, only the PID requirements have been relaxed in order to select enough events to compute the shape of the cross-feed distribution.

Gaussian representing the signal and an exponential function describing the background. The number of signal $D\rho^0$ candidates is equal to $N^{D\rho^0} = 4\,106 \pm 95$.

- The efficiency to reconstruct a $B^0 \to D\rho^0$, $D^0 \to K^-\pi^+$ signal candidate as a $B^0 \to DK^{*0}$, $D \to K^\mp\pi^\pm$ with the selection described above. This efficiency is computed from fully Monte Carlo simulation samples, using PID calibration tables for the PID efficiencies and mis-ID fractions, and is found to be equal to $\epsilon_{cross-feed} = (1.26 \pm 0.02)$ %.

The numbers of cross-feed candidates in the $D \to K^+K^-$ category are constrained from the $D \to K^\mp\pi^\pm$ one using the branching fractions and relative selection efficiencies measured from simulation, reported in Section 5.5.2.3,

$$N^{B^0+\overline{B}^0 \ (KK)}_{\text{cross-feed}} = N^{B^0+\overline{B}^0 \ (K\pi SS+OS)}_{\text{cross-feed}} \times \frac{\mathcal{B}(D^0 \to K^+K^-)}{\mathcal{B}(D^0 \to K^-\pi^+)} \times \frac{\epsilon_{\text{sel}}(B^0 \to [K^+K^-]_D K^{*0})}{\epsilon_{\text{sel}}(B^0 \to [K^\mp\pi^\pm]_D K^{*0})}. \quad (5.24)$$

5.5.3 Fit results

The total fit function is the sum of the individual PDFs described above, and all categories are fit simultaneously. The 23 free parameters are summarized in Tables 5.13 and 5.14. The result of the unbinned extended likelihood fit to the DK^{*0} invariant mass distributions of the B candidates in data is shown in Table 5.15 and Figures 5.12 to 5.14.

5.5.4 Validation of the fit procedure

In order to test the fitting procedure, toy Monte Carlo simulations have been generated. This method consists in generating samples following the fit model to be tested, using the result of

Group	Parameter	Description	Category
Signal	μ	Central value of the B^0 mass	Common to all
	σ	Core resolution for B^0 and $\overline{B}^0_s$	Common to all
	$N^{B^0 \ (KK)}$	Number of B^0 signal candidates	$B \ (KK)$
	$N^{\overline{B}^0 \ (KK)}$	Number of $\overline{B}^0$ signal candidates	$\overline{B} \ (KK)$
	$N^{\overline{B}^0_s \ (KK)}$	Number of $\overline{B}^0_s$ signal candidates	$B \ (KK)$
	$N^{B^0_s \ (KK)}$	Number of B^0_s signal candidates	$\overline{B} \ (KK)$
	$N^{B^0 \ (K\pi SS)}$	Number of B^0 signal candidates	$B \ (K\pi SS)$
	$N^{\overline{B}^0 \ (K\pi SS)}$	Number of $\overline{B}^0$ signal candidates	$\overline{B} \ (K\pi SS)$
(blind)	$N^{B^0 \ (K\pi OS)}$	Number of B^0 signal candidates	$B \ (K\pi OS)$
(blind)	$N^{\overline{B}^0 \ (K\pi OS)}$	Number of $\overline{B}^0$ signal candidates	$\overline{B} \ (K\pi OS)$
	$N^{\overline{B}^0_s \ (K\pi OS)}$	Number of $\overline{B}^0_s$ signal candidates	$B \ (K\pi OS)$
	$N^{B^0_s \ (K\pi OS)}$	Number of B^0_s signal candidates	$\overline{B} \ (K\pi OS)$

Table 5.13: *Free fit parameters of the invariant mass distribution (signal).*

Group	Parameter	Description	Category
Combinatorial background	c	Exponential slope	Common to all
	$N_{\text{comb}}^{(KK)}$	N. combinatorial background candidates	$B + \overline{B}\ (KK)$
	$N_{\text{comb}}^{(K\pi SS)}$	N. combinatorial bkg. cand.	$B + \overline{B}\ (K\pi SS)$
	$N_{\text{comb}}^{(K\pi OS)}$	N. combinatorial bkg. cand.	$B + \overline{B}\ (K\pi OS)$
Low mass background	$N_{\text{pb}}^{B^0\ (KK)}$	N. $B^0 \to D^*K^{*0}$ candidates	$B\ (KK)$
	$N_{\text{pb}}^{\overline{B}^0\ (KK)}$	N. $\overline{B}^0 \to D^*\overline{K}^{*0}$ candidates	$\overline{B}\ (KK)$
	$N_{\text{pb}}^{B^0+\overline{B}^0\ (K\pi SS)}$	N. $B^0 \to D^*K^{*0}$ and $\overline{B}^0 \to D^*\overline{K}^{*0}$ cand.	$B + \overline{B}\ (K\pi SS)$
	$N_{\text{pb}}^{B^0\ (K\pi OS)}$	N. $B^0 \to D^*K^{*0}$ candidates	$B\ (K\pi OS)$
	$N_{\text{pb}}^{\overline{B}^0\ (K\pi OS)}$	N. $\overline{B}^0 \to D^*\overline{K}^{*0}$ candidates	$\overline{B}\ (K\pi OS)$
	$N_{\text{pb}}^{\overline{B}_s^0+B_s^0\ (K\pi OS)}$	N. $\overline{B}_s^0 \to D^*K^{*0}$ and $B_s^0 \to D^*\overline{K}^{*0}$ cand.	$B + \overline{B}\ (K\pi OS)$
Cross-feed	$N_{\text{cross-feed}}^{B^0+\overline{B}^0\ (K\pi SS+OS)}$	N. $B^0 \to D\rho^0$ candidates	$B + \overline{B}\ (K\pi SS + OS)$

Table 5.14: *Free fit parameters of the invariant mass distribution (background).*

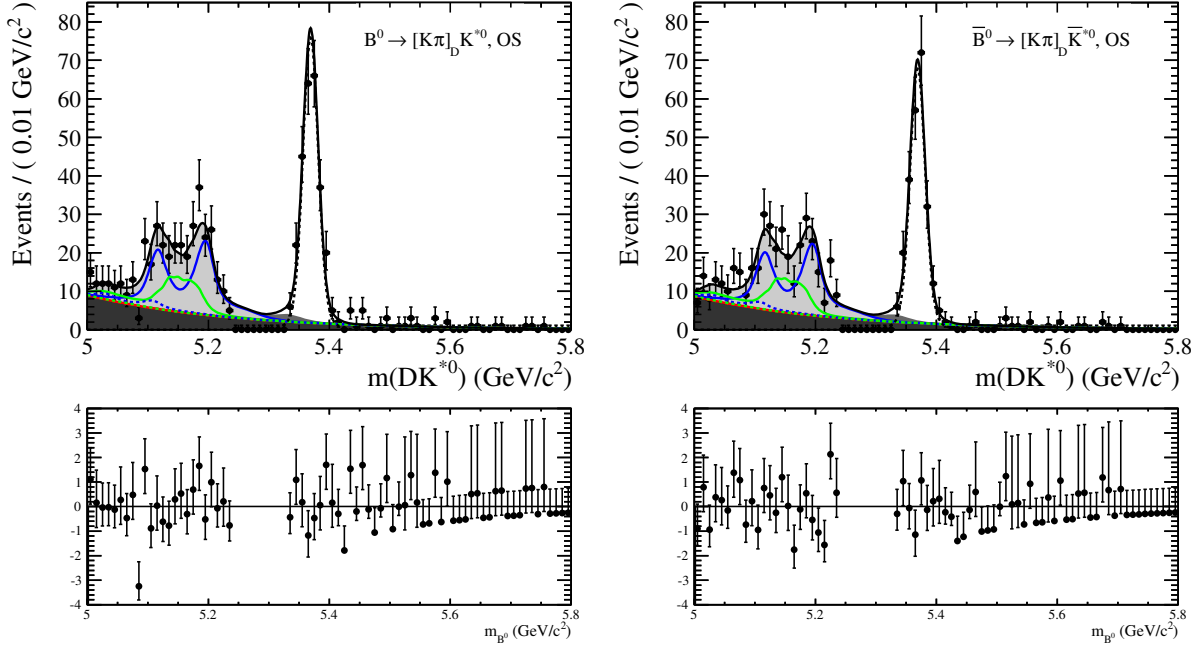| Signal Parameters	Result	Background Par.	Result
μ	$(5282.3 \pm 0.6)\,\text{MeV}/c^2$		
σ	$(12.2 \pm 0.5)\,\text{MeV}/c^2$	c	$(-4.4 \pm 0.3)\,\text{GeV}^{-1}c^2$
$N^{B^0\ (KK)}$	21^{+6}_{-5}	$N_{\text{comb}}^{(KK)}$	170^{+20}_{-18}
$N^{\overline{B}^0\ (KK)}$	8 ± 4	$N_{\text{comb}}^{(K\pi SS)}$	495^{+44}_{-42}
$N^{\overline{B}_s^0\ (KK)}$	24^{+6}_{-5}	$N_{\text{comb}}^{(K\pi OS)}$	396^{+49}_{-47}
$N^{B_s^0\ (KK)}$	23^{+6}_{-5}	$N_{\text{pb}}^{B^0\ (KK)}$	13^{+11}_{-10}
$N^{B^0\ (K\pi SS)}$	108^{+12}_{-11}	$N_{\text{pb}}^{\overline{B}^0\ (KK)}$	-3 ± 10
$N^{\overline{B}^0\ (K\pi SS)}$	94 ± 11	$N_{\text{pb}}^{B^0+\overline{B}^0\ (K\pi SS)}$	308 ± 37
$N^{B^0\ (K\pi OS)}$	$--$	$N_{\text{pb}}^{B^0\ (K\pi OS)}$	18^{+22}_{-21}
$N^{\overline{B}^0\ (K\pi OS)}$	$--$	$N_{\text{pb}}^{\overline{B}^0\ (K\pi OS)}$	17^{+22}_{-23}
$N^{\overline{B}_s^0\ (K\pi OS)}$	245^{+17}_{-16}	$N_{\text{pb}}^{\overline{B}_s^0+B_s^0\ (K\pi OS)}$	527 ± 33
$N^{B_s^0\ (K\pi OS)}$	226 ± 16	$N_{\text{cross-feed}}^{(K\pi)}$	52 ± 1

Table 5.15: *Fit result on the floating parameters.*

Figure 5.12: *Invariant mass distributions of the Opposite Sign $[K^-\pi^+]_D K^{*0}$ category (left), corresponding to B^0 and $\overline{B}^0_s$ candidates, and $[K^+\pi^-]_D \overline{K}^{*0}$ (right), corresponding to $\overline{B}^0$ and B^0_s candidates. The black points are the data, while the solid black line represents the result of the fit. The different contributions are visible: the signal peak is indicated by a dashed black line, while the different grey areas correspond to the different backgrounds which are, from darkest to lightest, combinatorial, cross-feed from $B^0, \overline{B}^0 \to D\rho^0$, and low-mass from partially reconstructed $B^0, \overline{B}^0_s \to D^* K^{*0}$ and $\overline{B}^0, B^0_s \to D^* \overline{K}^{*0}$. The coloured lines represent the different helicities amplitudes contributing to the low-mass background: red is "001", blue is "010" and green is "100"; solid lines correspond to the B^0_s low-mass background, dashed lines to the B^0. The signal region of the suppressed decay $B^0 \to DK^{*0}, \overline{B}^0 \to D\overline{K}^{*0}$ is kept blind. The bottom histograms are the differences between the value of the bin in the data histogram distribution and the value of the fit function in the center of the same bin, divided by the uncertainty on the number of entries in that bin.*

Figure 5.13: *Invariant mass distributions of the Same Sign $[K^+\pi^-]_D K^{*0}$ category (left), corresponding to B^0 and $\overline{B}^0_s$ candidates, and $[K^-\pi^+]_D \overline{K}^{*0}$ (right), corresponding to $\overline{B}^0$ and B^0_s candidates. The different contributions are represented as in Figure 5.12.*
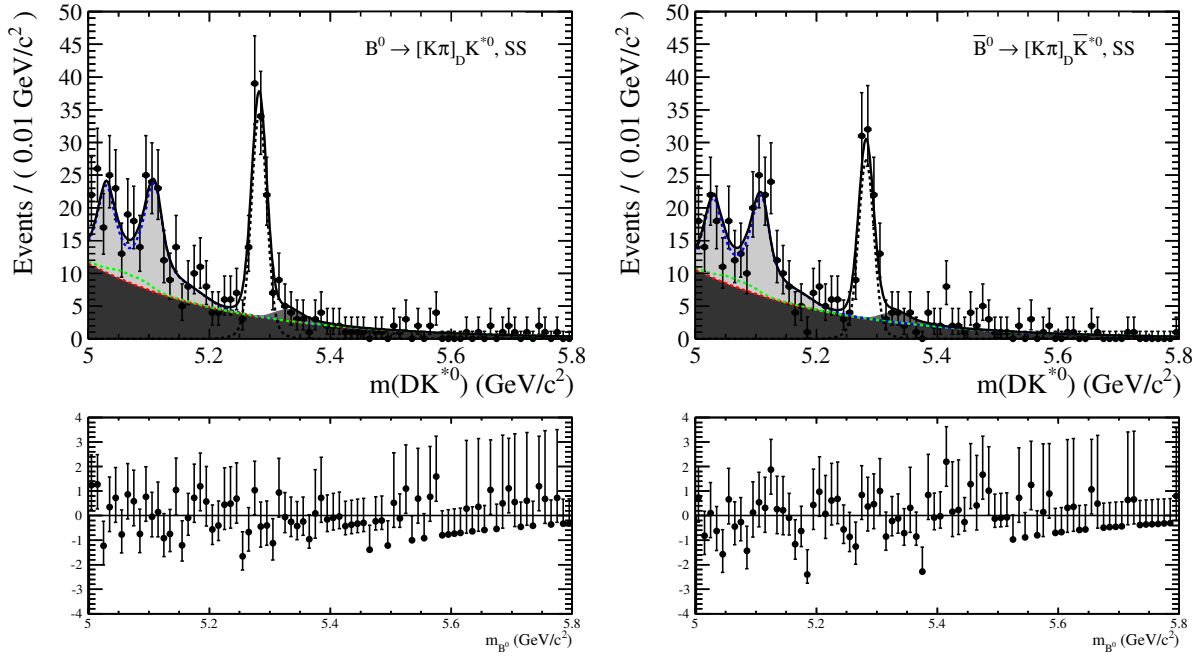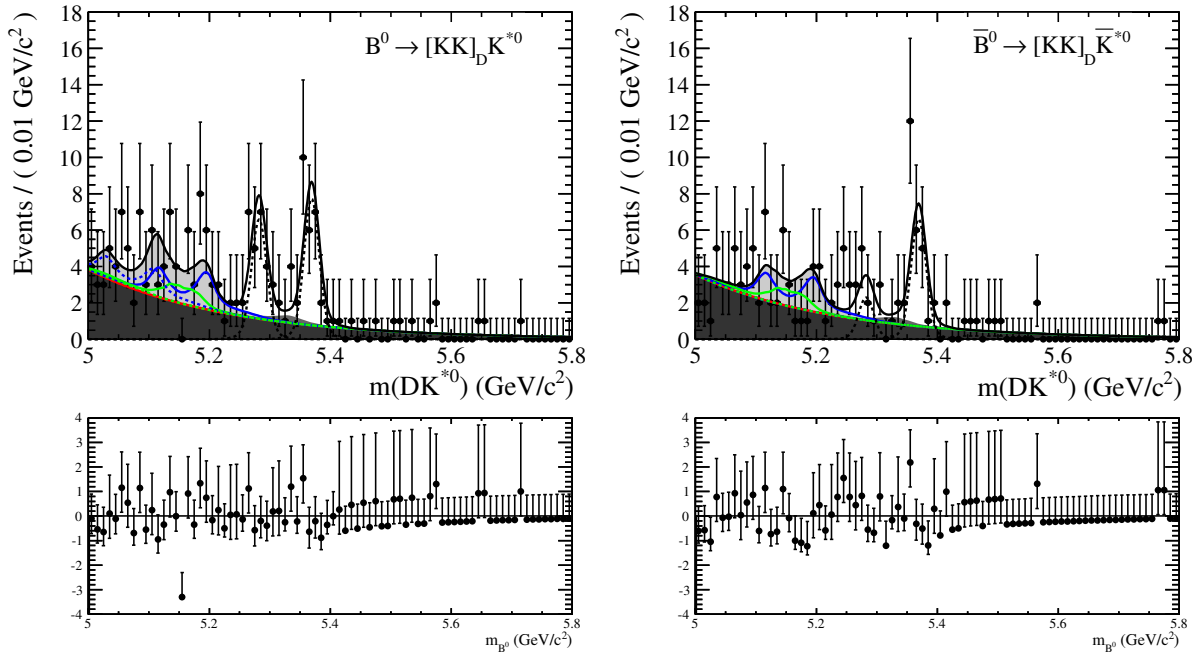

Figure 5.14: *Invariant mass distributions of the $[K^+K^-]_D K^{*0}$ category (left), corresponding to B^0 and $\overline{B}^0_s$ candidates, and $[K^+K^-]_D \overline{K}^{*0}$ (right), corresponding to $\overline{B}^0$ and B^0_s candidates. The different contributions are represented as in Figure 5.12.*

Parameter	Pull bias	Yield correction
$N^{B^0\ (K\pi SS)}$	-0.025 ± 0.013	-0.29 ± 0.15
$N^{\overline{B}^0\ (K\pi SS)}$	-0.033 ± 0.013	-0.36 ± 0.14
$N^{B^0\ KK}$	-0.052 ± 0.013	-0.29 ± 0.07
$N^{\overline{B}^0\ KK}$	-0.076 ± 0.013	-0.30 ± 0.05
$N^{B_s^0\ KK}$	-0.050 ± 0.013	-0.28 ± 0.07
$N^{\overline{B}_s^0\ KK}$	-0.055 ± 0.013	-0.30 ± 0.07

Table 5.16: *Biases on the signal yields observed from the toy Monte Carlo samples. The pull biases, given in the second column, are multiplied by the statistical uncertainty on the corresponding parameter resulting from the fit on data, in order to compute the actual bias on the signal yields in the third column. These are used to correct the central value of the yields obtained from the fit on data.*
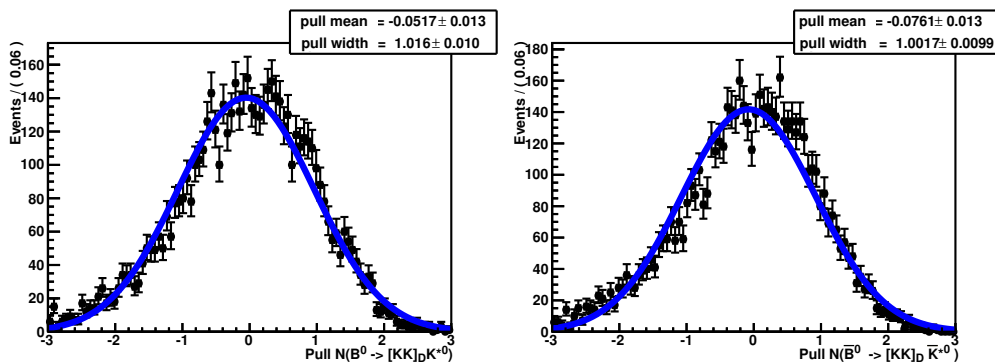

Figure 5.15: *Pull distributions for the B^0 (left) and $\overline{B}^0$ (right) signal yields in the $D \to K^+K^-$ category.*

the fit on data as input for each parameter where possible. For the parameters corresponding to blind yields, sensible estimates have been used as input value for the generation of the toys. These samples are then fitted with the same fit model to check its validity. For each toy Monte Carlo sample, the pull distribution of a given parameter x is defined as the difference between the fitted and the generated value divided by the uncertainty on the parameter fit result,

$$P_x = \frac{x_{\text{Fit}} - x_{\text{Gen}}}{\sigma_x}. \tag{5.25}$$

An example of pull distributions is given in Figure 5.15. Well-behaved pulls must show Gaussian shapes centred in 0 and with width equal to 1. For the signal yields, small but significant biases appear for the $D \to K^+K^-$ modes, see Table 5.16. Studies show that they are due to the low statistics in these modes. The central value obtained from the fit on data for these parameters in Table 5.15 are corrected according to these biases. In addition, for the $D \to K^+K^-$ modes, the pull distributions for the combinatorial and low mass backgrounds are not Gaussian. This is due to correlations between their corresponding parameters. Several tests have been performed showing that this effect does not affect the final results of this analysis.

5.6 Result computation and systematic uncertainties

The five observables outlined in Section 5.1 are computed from the yields resulting from the fit, using the following relations,

$$A_d^{KK} = \frac{a_{\text{prod}}^d \, \hat{\epsilon}_{\text{L0}}^{KK} \, \hat{\epsilon}_{\text{PID}}^{KK} \, N^{\overline{B}^0} \, (KK) - N^{B^0} \, (KK)}{a_{\text{prod}}^d \, \hat{\epsilon}_{\text{L0}}^{KK} \, \hat{\epsilon}_{\text{PID}}^{KK} \, N^{\overline{B}^0} \, (KK) + N^{B^0} \, (KK)}, \tag{5.26}$$

$$A_s^{KK} = \frac{a_{\text{prod}}^s \, \hat{\epsilon}_{\text{L0}}^{KK} \, \hat{\epsilon}_{\text{PID}}^{KK} \, N^{\overline{B}_s^0} \, (KK) - N^{B_s^0} \, (KK)}{a_{\text{prod}}^s \, \hat{\epsilon}_{\text{L0}}^{KK} \, \hat{\epsilon}_{\text{PID}}^{KK} \, N^{\overline{B}_s^0} \, (KK) + N^{B_s^0} \, (KK)}, \tag{5.27}$$

$$A^{\text{fav}} = \frac{a_{\text{prod}}^d \, \hat{\epsilon}_{\text{L0}}^{K\pi} \, \hat{\epsilon}_{\text{PID}}^{K\pi} \, N^{\overline{B}^0} \, (K\pi SS) - N^{B^0} \, (K\pi SS)}{a_{\text{prod}}^d \, \hat{\epsilon}_{\text{L0}}^{K\pi} \, \hat{\epsilon}_{\text{PID}}^{K\pi} \, N^{\overline{B}^0} \, (K\pi SS) + N^{B^0} \, (K\pi SS)}, \tag{5.28}$$

$$R_d^{KK} = \frac{a_{\text{prod}}^d \, \hat{\epsilon}_{\text{L0}}^{KK} \, \hat{\epsilon}_{\text{PID}}^{KK} \, N^{\overline{B}^0} \, (KK) + N^{B^0} \, (KK)}{a_{\text{prod}}^d \, \hat{\epsilon}_{\text{L0}}^{K\pi} \, \hat{\epsilon}_{\text{PID}}^{K\pi} \, N^{\overline{B}^0} \, (K\pi SS) + N^{B^0} \, (K\pi SS)} \times r_{\text{L0}}(\mathcal{R}_d^{KK})$$
$$\times r_{\text{PID}}(\mathcal{R}_d^{KK}) \times r_{\text{sel}}(\mathcal{R}_d^{KK}) \times \frac{\mathcal{B}(D^0 \to K^-\pi^+)}{\mathcal{B}(D^0 \to K^+K^-)}, \tag{5.29}$$

$$R_{ds}^{KK} = \frac{a_{\text{prod}}^d \, \hat{\epsilon}_{\text{L0}}^{KK} \, \hat{\epsilon}_{\text{PID}}^{KK} \, N^{\overline{B}^0} \, (KK) + N^{B^0} \, (KK)}{a_{\text{prod}}^s \, \hat{\epsilon}_{\text{L0}}^{KK} \, \hat{\epsilon}_{\text{PID}}^{KK} \, N^{B_s^0} \, (KK) + N^{\overline{B}_s^0} \, (KK)} \times r_{\text{LT}} \times \frac{f_s}{f_d} \times \frac{\tau_s}{\tau_d}. \tag{5.30}$$

The corrections entering these formulas are:

- $a_{\text{prod}}^d = \frac{1-\kappa^d A_{\text{prod}}}{1+\kappa^d A_{\text{prod}}} = 0.991 \pm 0.012$, the correction for the production asymmetry of B^0 with respect to $\overline{B}^0$, with $\kappa^d = 0.456 \pm 0.011$ and $A_{\text{prod}} = 0.010 \pm 0.013$, see Section 5.6.1;

- $a_{\text{prod}}^s = 1$, the correction for production asymmetry of B_s^0 with respect to $\overline{B}_s^0$, see Section 5.6.1;

- $\hat{\epsilon}_{\text{L0}} = 1$, the ratio of the L0 trigger efficiency for B^0 to the efficiency for $\overline{B}^0$, see Section 5.4.3;

- $r_{\text{L0}}(R_d^{KK}) = 1$, the ratio of L0 trigger efficiency for $D \to K^{\mp}\pi^{\pm}$ with respect to $D \to K^+K^-$, see Section 5.4.3;

- $\hat{\epsilon}_{\text{PID}}$, the ratio of the PID efficiency for B^0 to the efficiency for $\overline{B}^0$, $\hat{\epsilon}_{\text{PID}}^{KK} = 0.99958 \pm 0.00010 \pm 0.00988$ and $\hat{\epsilon}_{\text{PID}}^{K\pi} = 0.98421 \pm 0.00010 \pm 0.01553$, see Section 5.4.2;

- $r_{\text{PID}}(R_d^{KK}) = 1.00964 \pm 0.00010 \pm 0.01553$, the ratio of PID efficiency for $D \to K^{\mp}\pi^{\pm}$ with respect to $D \to K^+K^-$, see Section 5.4.2;

- $r_{\text{sel}}(R_d^{KK}) = 0.94 \pm 0.03$, the ratio of selection efficiency for $D \to K^{\mp}\pi^{\pm}$ with respect to $D \to K^+K^-$, see Section 5.4.1;

- $\frac{\mathcal{B}(D^0 \to K^-\pi^+)}{\mathcal{B}(D^0 \to K^+K^-)} = 9.90 \pm 0.16$, the ratio of branching fractions of the $D^0 \to K^-\pi^+$ with respect to $D^0 \to K^+K^-$, taken from [84];

- $r_{\text{LT}} = 1.07 \pm 0.03$, the lifetime correction factor, see Section 5.6.2;

- $\frac{f_s}{f_d} = 0.267 \pm 0.021$, the ratio of hadronisation fractions [87];

- $\frac{\tau_s}{\tau_d} = 0.965 \pm 0.018$, the ratio of lifetimes [84].

The different corrections are discussed in this Section, together with the evaluation of the systematics uncertainties on the final results.

5.6.1 Production asymmetry

B^0 and $\overline{B}^0$ production rates in proton-proton collisions and in the LHCb acceptance can be different, as well as for $\overline{B}_s^0$ and B_s^0. The CP observables have to be corrected for when computing them from the signal yields. This production asymmetry is investigated using $B^0 \to J/\psi K^{*0}$ decays. It is defined as the difference in the production rate between $\overline{B}^0$ and B^0, and it is measured to be $A_{\text{prod}} = 0.010 \pm 0.013$ [88]. The production asymmetry enters into Equations (5.26) to (5.30) as

$$a_{\text{prod}}^d = \frac{1 - \kappa^d A_{\text{prod}}}{1 + \kappa^d A_{\text{prod}}}, \tag{5.31}$$

where the factor $\kappa^d \left(B^0 \to DK^{*0} \right)$ accounts for dilution effects due to $B^0 - \overline{B}^0$ oscillations. This factor is computed using Monte Carlo simulation as

$$\kappa^d \left(B^0 \to DK^{*0} \right) = \frac{\int_0^{+\infty} e^{-\Gamma_d t} \cos \left(\Delta m_d t \right) \epsilon_{B^0 \to DK^{*0}} \left(t \right) \mathrm{d}t}{\int_0^{+\infty} e^{-\Gamma_d t} \cosh \left(\frac{\Delta \Gamma_d t}{2} \right) \epsilon_{B^0 \to DK^{*0}} \left(t \right) \mathrm{d}t}. \tag{5.32}$$

If we assume $e^{-\Gamma_d t}$ dependence in the number of generated Monte Carlo signal events, where t is the decay time of the B^0, then Equation (5.32) simplifies to

$$\kappa^d \left(B^0 \to DK^{*0} \right) = \frac{1}{N_{\text{offline total}}} \int_0^{+\infty} \cos \left(\Delta m_d t \right) N_{\text{offline selected}} \left(t \right) \mathrm{d}t. \tag{5.33}$$

Here, $N_{\text{offline total}}$ is the total number of selected signal events in Monte Carlo after all offline selections, Δm_d is the difference in masses of B^0 and $\overline{B}^0$ mesons and $N_{\text{offline selected}} \left(t \right)$ is the number of offline selected signal events in Monte Carlo as a function of the B^0 decay time. To compute this, the Monte Carlo events are binned in t and a numerical integration is performed. A value of $\kappa^d = 0.456 \pm 0.011$ is found.

The statistical uncertainties on A_{prod} and κ^d are propagated to the observables in order to estimate the corresponding systematic uncertainty associated to the knowledge of this factor. A similar production asymmetry a_{prod}^s can be defined for B_s^0 and $\overline{B}_s^0$ production rates. However, due to the much faster oscillation in the $B_s^0 - \overline{B}_s^0$ system with respect to $B^0 - \overline{B}^0$, this asymmetry is strongly diluted and we take $a_{\text{prod}}^s = 1$.

The resulting systematic uncertainties on the CP observables are:

	R_{ds}^{KK}	A_{ADS}^{fav}	R_d^{KK}	A_s^{KK}	A_d^{KK}
$\overline{B}^0 - B^0$ production asymmetry	0.0005	0.006	0.003	-	0.005

5.6.2 Lifetime difference

A non uniform lifetime efficiency of our selection and of the LHCb trigger may induce a small uncertainty on the R_{ds} ratio, because of the different B^0 and $\overline{B}_s^0$ lifetimes. Tables 5.5 and 5.6

show a difference in kinematic selection efficiencies between B^0 and $\overline{B}_s^0$ mesons decaying to the same final state.

The difference in selection efficiencies arises from the requirements on the vertex $\chi^2/\text{ndf}\,(B) < 4$, on Min IP$\chi^2\,(B) < 9$ and on $\sum_{\text{tracks}} \sqrt{\text{IP}\chi^2} > 32$, see Table 5.2, which depend on the B decay time. Therefore a correction factor is applied to the R_{ds} ratios of $r_{\text{LT}} = 1.07 \pm 0.03$ to account for the different efficiencies of these cuts on B^0 and $\overline{B}_s^0$ mesons. This factor is computed from the ratio of kinematics selections between $\overline{B}_s^0 \rightarrow [K^\mp\pi^\pm]_D K^{*0}$ and $B^0 \rightarrow [K^\mp\pi^\pm]_D K^{*0}$ obtained from simulation. The statistical uncertainty on this correction is propagated and assigned as the systematic uncertainty from this factor.

The resulting systematic uncertainties on the CP observables are:

	R_{ds}^{KK}	A_{ADS}^{fav}	R_d^{KK}	A_s^{KK}	A_d^{KK}
Lifetime difference	0.004	-	-	-	-

5.6.3 Relative trigger efficiency

The L0 trigger efficiency has been discued in Section 5.4.3. The total efficiencies are equal for B and $\overline{B}$ in all cases, and also for different D modes, as shown in Table 5.10, leading to a correction factor $r_{\text{L0}}\left(R_d^{KK}\right) = 1$. The efficiency of the "OtherB" trigger requirement is assumed to be identical for all categories and thus cancels exactly in the asymmetries and ratios measured here. The largest deviation of these factors would then be observed if all events were "TOS" for the L0 Hadron trigger. This hypothesis is used to estimate the uncertainty due to the trigger efficiency, defined as the difference in the value of the CP observables when using ϵ_{TOS} from Table 5.9 as total efficiencies instead of that on Table 5.10.

The resulting systematic uncertainties on the CP observables are:

	R_{ds}^{KK}	A_{ADS}^{fav}	R_d^{KK}	A_s^{KK}	A_d^{KK}
Trigger efficiency	0.0003	0.0009	0.02	0.004	0.003

5.6.4 Relative PID efficiency

The PID efficiencies for each mode have been shown in Table 5.8. A correction factor $r_{\text{PID}}\left(R_d^{KK}\right)$ for differing PID efficiency between the $D \rightarrow K^\mp\pi^\pm$ and $D \rightarrow K^+K^-$ modes is applied to the R_d^{KK} ratio. Correction factors are also applied for the difference in PID efficiency between B^0 and $\overline{B}^0$ decays, $\hat{\epsilon}_{\text{PID}}^{KK}$ and $\hat{\epsilon}_{\text{PID}}^{K\pi}$. These factors are discussed in Section 5.4.2 and given by Equations (5.10), (5.11) and (5.12). The total uncertainty on these factors is propagated and assigned as systematic uncertainty from the relative PID efficiencies.

The resulting systematic uncertainties on the CP observables are:

	R_{ds}^{KK}	A_{ADS}^{fav}	R_d^{KK}	A_s^{KK}	A_d^{KK}
PID efficiency	0.0003	0.008	0.015	0.005	0.004

5.6.5   Relative selection efficiency

The selection efficiencies shown in Tables 5.5 to 5.7 are assumed to be identical between all modes, with the exception of the stripping efficiency and lifetime related cuts, which have different efficiencies between B^0 and $\overline{B}_s^0$ and have been addressed in Section 5.6.2, and the efficiencies of the kinematic cuts, which have different efficiencies between different D decay modes. To take into account the second effect, a correction factor is applied to the R_d^{KK} ratio only. This correction factor $r_{\text{sel}}\left(R_d^{KK}\right)$ is given by Equation (5.9). The statistical uncertainty on this correction is propagated and assigned as the systematic from the relative selection efficiencies.

The resulting systematic uncertainties on the CP observables are:

	R_{ds}^{KK}	A_{ADS}^{fav}	R_d^{KK}	A_s^{KK}	A_d^{KK}
Selection efficiency	-	-	0.04	-	-

5.6.6   Fit-related systematics

To evaluate the fit-related systematics, toy Monte Carlo samples are generated with variations of the fit model explained in Section 5.5.2, and then fitted with the nominal model. The bias shown by the pull distributions for each signal yield is used to calculate the corresponding systematic uncertainty in the final observables.

Signal shape

To evaluate the systematic uncertainty related to the description of the signal shape, the fit is repeated on data leaving the parameter f_{core} of Equation (5.16) free. The result is $f_{\text{core}} = 0.93$. The fit is then done on toy Monte Carlo samples generated with this value but analyzed with the value $f_{\text{core}} = 0.87$ used for the nominal fit.

Low mass background shape from $\mathbf{B^0 \to D^*K^{*0}}$ and $\mathbf{\overline{B}_s^0 \to D^*K^{*0}}$

The shape of the partially reconstructed low mass background depends strongly on the unknown values of the polarisation parameters in the $B^0 \to D^*K^{*0}$ and $\overline{B}_s^0 \to D^*K^{*0}$ decays, parametrised in the nominal fit by the fixed values of α_{001}, α_{010}, β_{001} and β_{010}, in Equation (5.18). In order to estimate the effect of the low mass background description on the signal yields, toy Monte Carlo samples are generated with different intermediate values of the polarisation parameters, namely $\alpha_{001} = \frac{1}{3}$, $\alpha_{010} = \frac{1}{3}$, $\beta_{001} = \frac{1}{3}$ and $\beta_{010} = \frac{1}{3}$. The fit is performed on these samples fixing the α_{001}, α_{010}, β_{001} and β_{010} to the values used in the nominal fit.

Cross-feed fraction from $\mathbf{B^0 \to D\rho^0}$

The fit is performed on data fitting also for the cross-feed fraction which is fixed in the nominal fit from the value expected from PID calibration samples. The fraction is found to be equal to $\epsilon_{\text{cross-feed}} = 0.007 \pm 0.005$. In order to estimate the effect of the description of the $B^0 \to D\rho^0$ cross-feed on the signal yields, toy Monte Carlo samples have been generated with this value but fitted with the value of the nominal fit, $\epsilon_{\text{cross-feed}} = 0.0126$.

Fit bias correction

In order to take into account the fit bias due to low statistics shown by the toy simulation studies, the central values of the fit result for the $D \to K^+K^-$ signal yields are corrected, as explained in Section 5.5.4. Half of the correction is assigned as systematic uncertainty.

Fit related systematics summary

The resulting systematic uncertainties on the CP observables are:

	R_{ds}^{KK}	A_{ADS}^{fav}	R_d^{KK}	A_s^{KK}	A_d^{KK}
Signal model	0.0014	0.00019	0.014	0.0005	0.006
Low mass background model	0.010	0.002	0.05	0.0018	0.02
$B^0 \to D^0\rho^0$ cross-feed model	0.0007	0.0003	0.0013	0.003	0.0011
Fit bias correction	0.0007	-	0.014	0.00011	0.005

5.6.7   Additional systematics

The systematics from the ratio of hadronisation fractions f_s/f_d, the lifetime ratio τ_s/τ_d and the D^0 branching fraction ratio are computed by propagating the uncertitude on each quantity. For each one of them, the resulting systematic uncertainties on the CP observables are:

	R_{ds}^{KK}	A_{ADS}^{fav}	R_d^{KK}	A_s^{KK}	A_d^{KK}
f_s/f_d	0.006	-	-	-	-
τ_s/τ_d	0.0017	-	-	-	-
D^0 decay BFs	-	-	0.02	-	-

5.6.8   Total systematic uncertainties

Table 5.17 shows the value of each systematic uncertainty, for each source and for each observable. These are added in quadrature to give the total systematic uncertainty in the last row.

Source	Observable				
	R_{ds}^{KK}	A_{ADS}^{fav}	R_d^{KK}	A_s^{KK}	A_d^{KK}
$\overline{B}^0 - B^0$ production asymmetry	0.0005	0.006	0.003	-	0.005
f_s/f_d	0.006	-	-	-	-
τ_s/τ_d	0.0017	-	-	-	-
D^0 decay BFs	-	-	0.02	-	-
Trigger efficiency	0.0003	0.0009	0.02	0.004	0.003
Lifetime difference	0.004	-	-	-	-
PID efficiency	0.0003	0.008	0.015	0.005	0.004
Selection efficiency	-	-	0.04	-	-
Signal model	0.0014	0.00019	0.014	0.0005	0.006
Low mass background model	0.010	0.002	0.05	0.0018	0.02
$B^0 \to D^0\rho^0$ cross-feed model	0.0007	0.0003	0.0013	0.003	0.0011
Fit bias correction	0.0007	-	0.014	0.00011	0.005
Total	0.013	0.010	0.075	0.007	0.025

Table 5.17: *Summary of the systematic uncertainties eveluated from each source, for each measured observable.*

5.7   Results

The CP observables are measured to be equal to

$$A_d^{KK} = -0.452 \,{}^{+0.228}_{-0.230} \pm 0.025, \tag{5.34}$$

$$A^{\text{fav}} = -0.084 \pm 0.079 \pm 0.010, \tag{5.35}$$

$$A_s^{KK} = 0.040 \pm 0.165 \pm 0.007, \tag{5.36}$$

$$R_d^{KK} = 1.360 \,{}^{+0.366}_{-0.319} \pm 0.075, \tag{5.37}$$

$$R_{ds}^{KK} = 0.167 \,{}^{+0.053}_{-0.046} \pm 0.013, \tag{5.38}$$

where the first uncertainty is statistical and the second systematic. The statistical uncertainty takes into accout the correlation between the different fit parameters. The correlation matrix between the CP observables is equal to

$$\rho = \begin{pmatrix} 1 & \rho(A_d^{KK}, R_d^{KK}) & \rho(A_d^{KK}, A^{\text{fav}}) & \rho(A_d^{KK}, A_s^{KK}) \\ \rho(A_d^{KK}, R_d^{KK}) & 1 & \rho(A^{\text{fav}}, R_d^{KK}) & \rho(A_s^{KK}, R_d^{KK}) \\ \rho(A_d^{KK}, A^{\text{fav}}) & \rho(R_d^{KK}, A^{\text{fav}}) & 1 & \rho(A_s^{KK}, A^{\text{fav}}) \\ \rho(A_d^{KK}, A_s^{KK}) & \rho(R_d^{KK}, A_s^{KK}) & \rho(A^{\text{fav}}, A_s^{KK}) & 1 \end{pmatrix} \tag{5.39}$$

$$= \begin{pmatrix} 1.0000 & 0.1604 & -0.0004 & 0.0024 \\ 0.1604 & 1.0000 & 0.0014 & -0.0038 \\ -0.0004 & 0.0014 & 1.0000 & 0.0001 \\ 0.0024 & -0.0038 & 0.0001 & 1.0000 \end{pmatrix}. \tag{5.40}$$

The GLW CP asymmetry A_d^{KK} is measured to be different from zero, showing the CP violation effect in the $B^0 \to [K^+K^-]_D K^{*0}$ decay. On the other hand, the other two measured asymmetries A^{fav} and A_s^{KK} are compatible with zero, as expected. These results, performed with

1 fb^{-1} of 2011 LHCb data, are still limited by the statistics, and more precise results are expected by combining the 2011 and 2012 data samples. These measurements have resulted in a publication in the Journal of High Energy Physics [64]. The first observation of the $B^0 \to [K^+K^-]_D K^{*0}$ decay, shown in Figure 5.14, is performed with a 5.1 σ significance (B^0 and $\overline{B}^0$ combined).

5.8   Appendix: CP observables in $\overline{B}^0 \to D\overline{K}^{*0}$ with $D \to \pi^+\pi^-$

In addition to the $B^0 \to DK^{*0}$ with $D \to K^+K^-$, also the CP-even $D \to \pi^+\pi^-$ mode was studied at the same time, where D again represents either a D^0 or a $\overline{D}^0$ meson. Four CP observables can be defined for this decay in the same way. These are the the two CP asymmetries for the $D \to \pi^+\pi^-$ mode for B^0 and $\overline{B}^0_s$

$$A_d^{\pi\pi} = \frac{\Gamma(\overline{B}^0 \to [\pi^+\pi^-]_D\overline{K}^{*0}) - \Gamma(B^0 \to [\pi^+\pi^-]_D K^{*0})}{\Gamma(\overline{B}^0 \to [\pi^+\pi^-]_D\overline{K}^{*0}) + \Gamma(B^0 \to [\pi^+\pi^-]_D K^{*0})}, \tag{5.41}$$

$$A_s^{\pi\pi} = \frac{\Gamma(\overline{B}^0_s \to [\pi^+\pi^-]_D K^{*0}) - \Gamma(B^0_s \to [\pi^+\pi^-]_D\overline{K}^{*0})}{\Gamma(\overline{B}^0_s \to [\pi^+\pi^-]_D K^{*0}) + \Gamma(B^0_s \to [\pi^+\pi^-]_D\overline{K}^{*0})}, \tag{5.42}$$

the ratio of B^0 widths for the $D \to \pi^+\pi^-$ over $D \to K^{\mp}\pi^{\pm}$ SS favoured modes

$$\begin{aligned} R_d^{\pi\pi} &= \frac{\Gamma(\overline{B}^0 \to [\pi^+\pi^-]_D\overline{K}^{*0}) + \Gamma(B^0 \to [\pi^+\pi^-]_D K^{*0})}{\Gamma(\overline{B}^0 \to [K^-\pi^+]_D\overline{K}^{*0}) + \Gamma(B^0 \to [K^+\pi^-]_D K^{*0})} \\ &= R_{CP+}, \end{aligned} \tag{5.43}$$

and the ratio of B^0 and B^0_s widths for the $D \to \pi^+\pi^-$ modes

$$R_{ds}^{\pi\pi} = \frac{\Gamma(\overline{B}^0 \to [\pi^+\pi^-]_D\overline{K}^{*0}) + \Gamma(B^0 \to [\pi^+\pi^-]_D K^{*0})}{\Gamma(\overline{B}^0_s \to [\pi^+\pi^-]_D K^{*0}) + \Gamma(B^0_s \to [\pi^+\pi^-]_D\overline{K}^{*0})}. \tag{5.44}$$

The branching fraction of this D^0 decay is $\mathcal{B}(D^0 \to \pi^+\pi^-) = (1.401 \pm 0.027) \times 10^{-3}$ [34]. Due to the smaller branching fraction of the $D^0 \to \pi^+\pi^-$ with respect to $D^0 \to K^+K^-$, lower yields are expected in this signal channel. However, the analysis of the $B^0 \to DK^{*0}$ with $D^0 \to \pi^+\pi^-$ on (1.03 ± 0.04) fb^{-1} of 2011 LHCb data has been done simultaneously with $D \to K^+K^-$ and $D \to K^{\mp}\pi^{\pm}$ during this thesis, and a measurement of these GLW observables was extracted together with the ones already presented in this chapter. As sensitivity to CP violation is expected in the $B^0 \to [\pi^+\pi^-]_D K^{*0}$ decay, the B^0 signal region was kept blind throughout this analysis until all the choices were made. The specific features related to the $D^0 \to \pi^+\pi^-$ channel are presented in this section.

5.8.1   Selection, specific background studies and efficiencies

Selection

The data sets, simulation samples, stripping and trigger selection requirements are the same than those presented in Section 5.2.1. Regarding the specific criteria to select events in the $B^0 \to DK^{*0}$ decay channel with $D^0 \to \pi^+\pi^-$, the requirements that are applied are those listed on Table 5.2 and detailed in Section 5.2.

The optimisation of the requirements on the D daughters p_{T} and PID variables is performed on data by maximising the significance of the expected B^0 signal defined as $S/\sqrt{S+B}$, where the blind B^0 signal yield S is estimated from the decay $\overline{B}^0_s \to [\pi^+\pi^-]_D K^{*0}$ as explained in Section 5.2.5 and B is the background in the B^0 mass region. Both the $\overline{B}^0_s$ yield and the
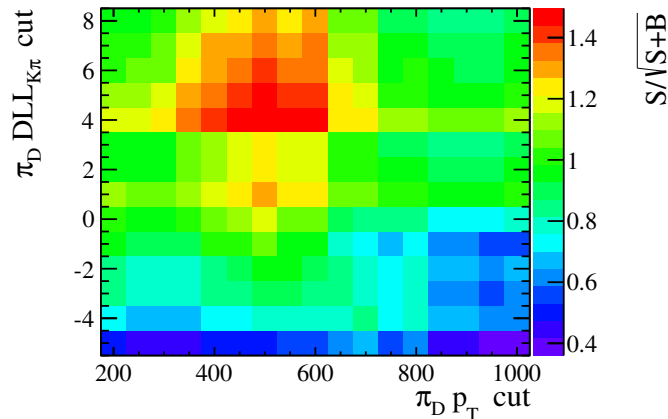
Figure 5.16: *Expected significance $S/\sqrt{S+B}$ of $B^0 \to [\pi^+\pi^-]_D K^{*0}$ as a function of $\mathrm{DLL}_{K\pi}$ and p_T cuts on the D daughter tracks, calculated using the value for the strong phase δ_{B^0} that results in the highest possible signal yield, $\delta_{B^0_{\max}} = 0$.*

background in the B^0 signal region are extracted from a simplified version of the fit presented in Section 5.8.2. The result of the optimisation is shown in Figure 5.16. The selections for the $D \to \pi^+\pi^-$ mode favoured by this procedure are $\mathrm{DLL}_{K\pi}(\pi) < 4$, $p_\mathrm{T}(\pi) > 400\,\mathrm{MeV}/c$. These requirements are again identical to those applied to the K in the $D \to K^{\mp}\pi^{\pm}$ mode.

Specific background studies

Peaking background coming from charmless $B^0 \to \pi^+\pi^- K^{*0}$ decays is studied following the procedure explained in Section 5.3.1. The sidebands of the D invariant mass distribution are used, relaxing the requirement on the D mass window. The D invariant mass is shown on the left pannel of Figure 5.17, after applying all the selection criteria but relaxing the D mass window cut and without any requirement on the D flight distance significance. The D mass sideband is identified from this plot as $M(\pi^+\pi^-) > 1895\,\mathrm{MeV}/c^2$.

The B invariant mass distribution for the events in this sideband is shown in Figure 5.18. A considerable peaking charmless contribution is present, especially at the B^0 mass. This distribution is fitted with a linear combinatorial background and double Gaussian functions for the signal B^0 and $\overline{B}{}^0_s$ peaks. The resulting signal yields, scaled to the D signal mass region, are represented as a function of the D flight distance significance cut in Figure 5.19. A requirement on the flight distance significance of the D meson greater than 2.5 allows to reduce these charmless background contributions to a negligible level.

The right panel of Figure 5.17 shows the invariant mass distribution of the D after all selection cuts, including the requirement on the D flight distance significance. One can see that this cut also helps to reduce the combinatorial background. Cross-feed background from the $D \to K^{\mp}\pi^{\pm}$ mode into $D \to \pi^+\pi^-$ is present at low mass values. However, this contribution is negligeable inside the $\pm 20\,\mathrm{MeV}/c^2$ signal region selected for the analysis.

Other peaking backgrounds are investigated as in Section 5.3.4. Backgrounds from Λ_b^0 decays are found also negligible for $D \to \pi^+\pi^-$. A veto is applied to remove backgrounds from $B^0 \to D^{\mp}_{(s)}(h'h''h''')h$ $(h, h', h'', h''' = \pi^{\pm}, K^{\pm})$, by applying a cut of $\pm 15\,\mathrm{MeV}/c^2$ on the difference between $K^{\mp}\pi^{\pm}\pi^{\pm}$ combinations out of the four particles in the final state and $D^{\pm}$ nominal mass.
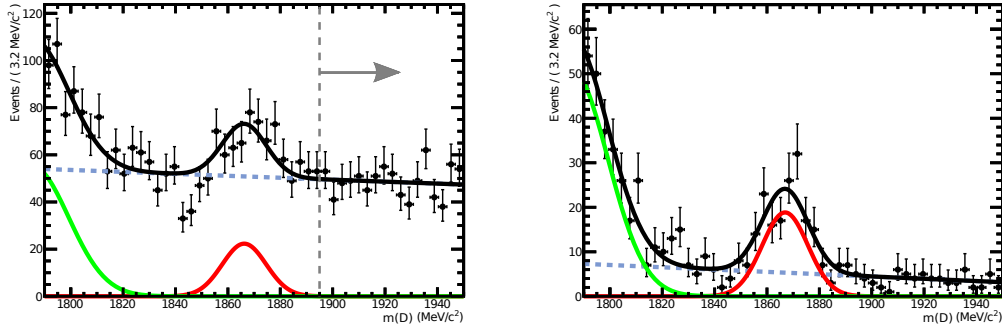
Figure 5.17: *Fit to the D invariant mass distribution for $D \to \pi^+\pi^-$, before applying the D flight distance significance cut (left) and after (right). All the other cuts are applied except the D mass window. The black line superimposed on the distributions is the fit result, sum of a linear combinatorial background (dashed blue line), a Gaussian function for the signal (red line) and a Crystal Ball function for the mis-ID of $D \to K^{\mp}\pi^{\pm}$ into $D \to \pi^+\pi^-$ (green line). The grey arrows indicate the sideband regions defined in the text.*
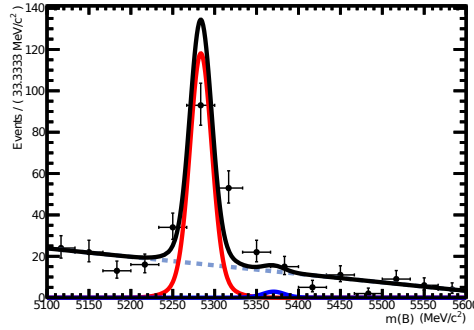

Figure 5.18: *Fit to the B invariant mass of the reconstructed events in the D sidebands as defined in the text, for $D \to \pi^+\pi^-$. The black line superimposed on the distributions is the fit result, sum of a linear combinatorial background (dashed grey line) and two double Gaussian functions, one for the B^0 signal (red line) and the other for $\overline{B}^0_s$ signal (blue line).*
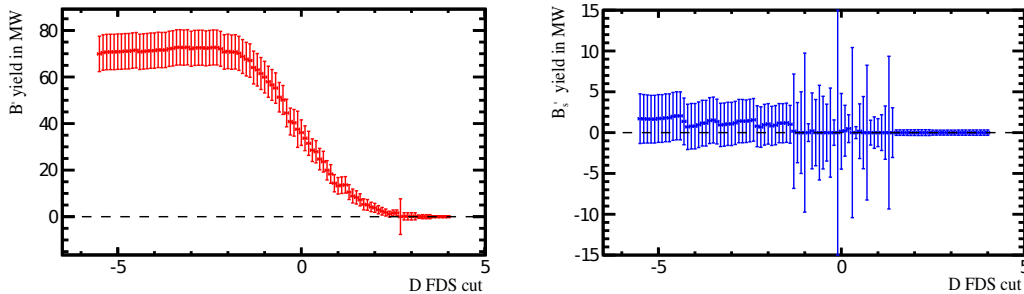

Figure 5.19: *Yields of peaking backgrounds from charmless B^0 decays (left) and $\overline{B}^0_s$ decays (right) scaled to the D signal region as a function of the flight distance significance cut on the D, for $D \to \pi^+\pi^-$. The uncertainties are subject to fluctuations from the fit procedure on Figure 5.18, as when a peak is not found the likelihood curve for the yield is not well-behaved.*

114

Cut	Efficiency		
Acceptance	0.151	$\pm$	0.001
Stripping	0.0285	$\pm$	0.0002
Vertex $\chi^2/\mathrm{ndf}\left(B^0\right) < 4$	0.961	$\pm$	0.0016
Min IP$\chi^2\left(B^0\right) < 9$	0.961	$\pm$	0.0016
$\cos(\theta_{\mathrm{dira}}) > 0.99995$	0.979	$\pm$	0.0012
$|\cos\theta^*| > 0.4$	0.927	$\pm$	0.0023
$\sum_{\mathrm{tracks}} \sqrt{\mathrm{IP}\chi^2} > 32$	0.98	$\pm$	0.0013
$\left|M(K^{\mp}\pi^{\pm}\pi^{\pm}) - M(D^{\pm})\right|(\pi_D^+) > 15\,\mathrm{MeV}/c^2$	0.998	$\pm$	0.0004
$\left|M(K^{\mp}\pi^{\pm}\pi^{\pm}) - M(D^{\pm})\right|(\pi_D^-) > 15\,\mathrm{MeV}/c^2$	0.998	$\pm$	0.0004
Min IP$\chi^2\left(K^{*0}\right) > 25$	0.992	$\pm$	0.0008
$\left|M(K^+\pi^-) - M(K^{*0}_{PDG})\right| < 50\,\mathrm{MeV}/c^2$	0.76	$\pm$	0.0039
$p_{\mathrm{T}}(K_{K^{*0}}) > 300\,\mathrm{MeV}/c$	0.998	$\pm$	0.0005
$p_{\mathrm{T}}(\pi_{K^{*0}}) > 300\,\mathrm{MeV}/c$	0.919	$\pm$	0.0029
Vertex $\chi^2/\mathrm{ndf}\left(D^0\right) < 5$	0.956	$\pm$	0.0022
Flight distance significance$(D^0) > 2.5$	0.739	$\pm$	0.0049
Min IP$\chi^2\left(D^0\right) > 4$	0.997	$\pm$	0.0007
$\left|M(D^0) - M(D^0_{PDG})\right| < 20\,\mathrm{MeV}/c^2$	0.923	$\pm$	0.0035
$p_{\mathrm{T}}(\pi_D^+) > 400\,\mathrm{MeV}/c$	0.971	$\pm$	0.0023
$p_{\mathrm{T}}(\pi_D^-) > 400\,\mathrm{MeV}/c$	0.966	$\pm$	0.0025
Total kinematic efficiency	0.00148	$\pm$	0.00002
PID	0.5921	$\pm$	0.00012
L0Hadron TOS requirement (ϵ_{TOS}), B^0	0.539	$\pm$	0.007
L0Hadron TOS requirement (ϵ_{TOS}), $\overline{B}^0$	0.550	$\pm$	0.007
L0 total requirement (ϵ_{L0}), B^0	0.49	$\pm$	0.03
L0 total requirement (ϵ_{L0}), $\overline{B}^0$	0.50	$\pm$	0.03
Total efficiency	0.00043	$\pm$	0.00003

Table 5.18: *Efficiencies of kinematic selection on* $B^0 \to [\pi^+\pi^-]_D K^{*0}$.

Efficiencies

Kinematic, PID and trigger efficiency are assessed using the same procedures explained in Section 5.4. Table 5.18 shows the summary of these efficiencies for the $D \to \pi^+\pi^-$ mode[14]. Selection and PID efficiencies are equal between B^0 and $\overline{B}^0$ modes.

5.8.2 Fit strategy

The signal yields are extracted from the DK^{*0} invariant mass distribution of the B candidates with an unbinned maximum likelihood fit, performed simultaneously for the $D \to K^{\mp}\pi^{\pm}$, $D \to K^+K^-$ and $D \to \pi^+\pi^-$ modes. The fit model used is similar to the one described in Section 5.5. Two additional categories are introduced:

---

[14]The methods for computation of the PID and L0 trigger efficiencies were improved between the first stage of this analysis, when all the three modes $D \to K^{\mp}\pi^{\pm}$, $D \to K^+K^-$ and $D \to \pi^+\pi^-$ were studied simultaneously for preliminary results, and the second stage, were only $K^{\mp}\pi^{\pm}$ and $D \to K^+K^-$ were kept for publication purposes. This explains the differences between the efficiencies presented in this section with respect to those shown in Section 5.4.

Group	Parameter	Description	Category
Signal	$N^{B^0\ (\pi\pi)}$	Number of B^0 signal candidates	$B\ (\pi\pi)$
	$N^{\overline{B}^0\ (\pi\pi)}$	Number of $\overline{B}^0$ signal candidates	$\overline{B}\ (\pi\pi)$
	$N^{\overline{B}^0_s\ (\pi\pi)}$	Number of $\overline{B}^0_s$ signal candidates	$B\ (\pi\pi)$
	$N^{B^0_s\ (\pi\pi)}$	Number of B^0_s signal candidates	$\overline{B}\ (\pi\pi)$
Combinatorial bkg.	$N^{(\pi\pi)}_{\text{comb}}$	N. combinatorial bkg. candidates	$B + \overline{B}\ (\pi\pi)$

Table 5.19: *Free fit parameters of the invariant mass distribution related to the $D \to \pi^+\pi^-$ categories.*

- $B\ (\pi\pi)$:
  $B^0 \to [\pi^+\pi^-]_D\, K^{*0}(K^+\pi^-)$, and $\overline{B}^0_s \to [\pi^+\pi^-]_D\, K^{*0}(K^+\pi^-)$;

- $\overline{B}\ (\pi\pi)$:
  $\overline{B}^0 \to [\pi^+\pi^-]_D\, \overline{K}^{*0}(K^-\pi^+)$ and $B^0_s \to [\pi^+\pi^-]_D\, \overline{K}^{*0}(K^-\pi^+)$.

Table 5.19 shows the four signal and one background yields that are included corresponding to this new categories, which together with those presented in Tables 5.13 and 5.14 complete the set of free parameters of this simultaneous fit.

The only significant difference between the fit model used here and the one described in Section 5.5 is the description of the combinatorial background. In the first version of the fit, which included simultaneously the three modes $D \to K^\mp\pi^\pm$, $D \to K^+K^-$ and $D \to \pi^+\pi^-$, the combinatorial slope common to all the modes was not free but fixed to a value that was determined from studies on the $B^0 \to D\rho^0$ decay mode. It has also four particles in the final state and a very similar topology, and thus can be used to estimate the shape of the combinatorial background in the $B^0 \to DK^{*0}$ channel. The slope was fixed to $c = (-3.89 \pm 0.12)\ \text{GeV}^{-1}c^2$. An additional systematic uncertainty is assigned to account for this choice using toy Monte Carlo pseudo-experiments varying the values assigned to the slopes. Fixing the slope modeling the combinatorial background allows to reduce correlations between the different background contributions at low mass. The yields of combinatorial background in the B and $\overline{B}$ categories are constrained to be equal. A too wide mass window for the B candidates invariant mass distribution is not necessary here, and it was set to $[5.0; 5.6]\ \text{GeV}/c^2$. This mass window was broadened and the slope left free for the simultaneous fit of the $D \to K^\mp\pi^\pm$ and $D \to K^+K^-$, aiming for journal publication. This modification does not introduce significant variations in the signal yields resulting from the fit.

Low mass background from partially reconstructed $B^0 \to D^*K^{*0}$ and $\overline{B}^0_s \to D^*K^{*0}$ events is also present in this mode, where D^* denotes a D^{*0} or a $\overline{D}^{*0}$ meson which decays as $D^{*0} \to D^0\pi^0$ or $D^{*0} \to D^0\gamma$, where the π^0 or γ are missed by the reconstruction, and $D^0 \to \pi^+\pi^-$. These contributions, taking into account the three different helicity components possible, are modelled using the same shapes detailed in Section 5.5.2.3. However, no additional parameters are added to the fit, as the corresponding background yields are constrained from those assigned to the

Signal Parameters	Result	Background Parameters	Result
$N^{B^0\ (\pi\pi)}$	4^{+3}_{-2}	$N^{(\pi\pi)}_{\mathrm{comb}}$	55 ± 11
$N^{\overline{B}^0\ (\pi\pi)}$	0^{+3}_{-2}		
$N^{\overline{B}^0_s\ (\pi\pi)}$	5^{+3}_{-2}		
$N^{B^0_s\ (\pi\pi)}$	4^{+3}_{-2}		

Table 5.20: *Fit result on the floating parameters related to the* $D \to \pi^+\pi^-$ *categories.*

$D \to K^+K^-$ categories, scaled using the involved D branching fractions and selection efficiencies,

$$N^{\overline{B}^0_s+B^0_s\ (\pi\pi)}_{\mathrm{pb}} \;=\; N^{\overline{B}^0_s+B^0_s\ (KK)}_{\mathrm{pb}} \times \frac{\mathcal{B}(D^0 \to \pi^+\pi^-)}{\mathcal{B}(D^0 \to K^+K^-)} \times \frac{\epsilon_{\mathrm{sel}}(B^0 \to [\pi^+\pi^-]_D K^{*0})}{\epsilon_{\mathrm{sel}}(B^0 \to [K^+K^-]_D K^{*0})}, \quad (5.45)$$

$$N^{B^0\ (\pi\pi)}_{\mathrm{pb}} \;=\; N^{B^0\ (KK)}_{\mathrm{pb}} \times \frac{\mathcal{B}(D^0 \to \pi^+\pi^-)}{\mathcal{B}(D^0 \to K^+K^-)} \times \frac{\epsilon_{\mathrm{sel}}(B^0 \to [\pi^+\pi^-]_D K^{*0})}{\epsilon_{\mathrm{sel}}(B^0 \to [K^+K^-]_D K^{*0})}, \quad (5.46)$$

$$N^{\overline{B}^0\ (\pi\pi)}_{\mathrm{pb}} \;=\; N^{\overline{B}^0\ (KK)}_{\mathrm{pb}} \times \frac{\mathcal{B}(D^0 \to \pi^+\pi^-)}{\mathcal{B}(D^0 \to K^+K^-)} \times \frac{\epsilon_{\mathrm{sel}}(B^0 \to [\pi^+\pi^-]_D K^{*0})}{\epsilon_{\mathrm{sel}}(B^0 \to [K^+K^-]_D K^{*0})}, \quad (5.47)$$

assuming that the efficiencies are equal between the B^0 and the $\overline{B}^0_s$ decay modes. In these equations, $\mathcal{B}(D^0 \to \pi^+\pi^-) = 0.14\ \%$ [34], and $\epsilon_{\mathrm{sel}}(B^0 \to [\pi^+\pi^-]_D K^{*0}) = 0.852\ \%$ is measured from fully Monte Carlo simulated events. The yields for the B^0_s background are constrained to the same value in the B and $\overline{B}$ categories.

Similarly, cross-feed background from $B^0 \to D\rho^0$ decays is considered for the $D \to \pi^+\pi^-$ category, when one of the π from the $\rho^0 \to \pi^+\pi^-$ decay is misidentified as a K. This background is modelled as shown in Section 5.5.2.4, and the corresponding $D \to \pi^+\pi^-$ cross-feed background yields are constrained to those in the $D \to K^+K^-$ categories as

$$N^{(\pi\pi)}_{\mathrm{cross-feed}} = N^{(KK)}_{\mathrm{cross-feed}} \times \frac{\mathcal{B}(D^0 \to \pi^+\pi^-)}{\mathcal{B}(D^0 \to K^+K^-)} \times \frac{\epsilon_{\mathrm{sel}}(B^0 \to [\pi^+\pi^-]_D K^{*0})}{\epsilon_{\mathrm{sel}}(B^0 \to [K^+K^-]_D K^{*0})}. \quad (5.48)$$

The result of the unbinned extended likelihood fit to the invariant mass distribution of the B candidates for the parameters related to the $D \to \pi^+\pi^-$ category are summarised in Table 5.20 and Figure 5.20.
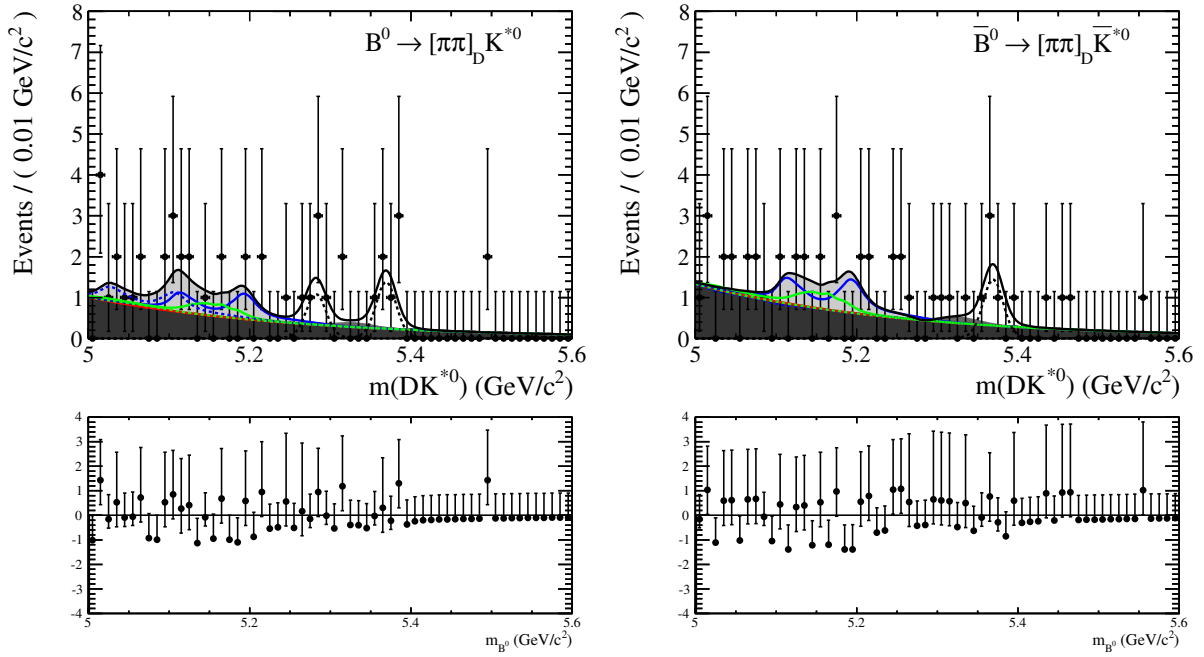
Figure 5.20: *Invariant mass distributions of the $[\pi^+\pi^-]_D K^{*0}$ category (left), corresponding to B^0 and $\overline{B}_s^0$ candidates, and $[\pi^+\pi^-]_D \overline{K}^{*0}$ (right), corresponding to $\overline{B}^0$ and B_s^0 candidates. The black points are the data, while the solid black line represents the result of the fit. The different contributions are visible: the signal peak is indicated by a dashed black line, while the different grey areas correspond to the different backgrounds: from darkest to lightest, combinatorial, cross-feed from $B^0 \to D\rho^0$, and low-mass from partially reconstructed $B^0, \overline{B}_s^0 \to D^*K^{*0}$ and $\overline{B}^0, B_s^0 \to D^*\overline{K}^{*0}$. The coloured lines represent the different helicities amplitudes contributing to the low-mass background: red is "001", blue is "010" and green is "100"; solid lines correspond to the B_s^0 low-mass background, dashed lines to the B^0. The bottom histograms are the differences between the value of the bin in the data histogram distribution and the value of the fit function in the center of the same bin, divided by the uncertainty on the number of entries in that bin.*

5.8.3   Results

The CP observables defined in Equations (5.41) to (5.44) are computed from the signal yields resulting from the fit as

$$A_d^{\pi\pi} = \frac{a_{\text{prod}}^d \, \hat{\epsilon}_{\text{L0}}^{\pi\pi} \, \hat{\epsilon}_{\text{PID}}^{\pi\pi} \, N^{\overline{B}^0 \ (\pi\pi)} - N^{B^0 \ (\pi\pi)}}{a_{\text{prod}}^d \, \hat{\epsilon}_{\text{L0}}^{\pi\pi} \, \hat{\epsilon}_{\text{PID}}^{\pi\pi} \, N^{\overline{B}^0 \ (\pi\pi)} + N^{B^0 \ (\pi\pi)}}, \tag{5.49}$$

$$A_s^{\pi\pi} = \frac{a_{\text{prod}}^s \, \hat{\epsilon}_{\text{L0}}^{\pi\pi} \, \hat{\epsilon}_{\text{PID}}^{\pi\pi} \, N^{\overline{B}^0 \ (\pi\pi)} - N^{B^0 \ (\pi\pi)}}{a_{\text{prod}}^s \, \hat{\epsilon}_{\text{L0}}^{\pi\pi} \, \hat{\epsilon}_{\text{PID}}^{\pi\pi} \, N^{\overline{B}^0 \ (\pi\pi)} + N^{B^0 \ (\pi\pi)}}, \tag{5.50}$$

$$R_d^{\pi\pi} = \frac{a_{\text{prod}}^d \, \hat{\epsilon}_{\text{L0}}^{\pi\pi} \, \hat{\epsilon}_{\text{PID}}^{\pi\pi} \, N^{\overline{B} \ (\pi\pi)} + N^{B^0 \ (\pi\pi)}}{a_{\text{prod}}^d \, \hat{\epsilon}_{\text{L0}}^{K\pi} \, \hat{\epsilon}_{\text{PID}}^{K\pi} \, N^{\overline{B}^0 \ (K\pi SS)} + N^{B^0 \ (K\pi SS)}} \times r_{\text{L0}}(R_d^{\pi\pi})$$
$$\times r_{\text{PID}}(\mathcal{R}_d^{\pi\pi}) \times r_{\text{sel}}(\mathcal{R}_d^{\pi\pi}) \times \frac{\mathcal{B}(D^0 \to K^-\pi^+)}{\mathcal{B}(D^0 \to \pi^+\pi^-)}, \tag{5.51}$$

$$R_{ds}^{\pi\pi} = \frac{a_{\text{prod}}^d \, \hat{\epsilon}_{\text{L0}}^{\pi\pi} \, \hat{\epsilon}_{\text{PID}}^{\pi\pi} \, N^{\overline{B}^0 \ (\pi\pi)} + N^{B^0 \ (\pi\pi)}}{a_{\text{prod}}^s \, \hat{\epsilon}_{\text{L0}}^{\pi\pi} \, \hat{\epsilon}_{\text{PID}}^{\pi\pi} \, N^{\overline{B}_s^0 \ (\pi\pi)} + N^{B_s^0 \ (\pi\pi)}} \times r_{\text{LT}} \times \frac{f_s}{f_d} \times \frac{\tau_s}{\tau_d}, \tag{5.52}$$

where

- $r_{\text{L0}}(\mathcal{R}_d^{\pi\pi}) = 1$, the ratio of L0 trigger efficiency for $D \to K^{\mp}\pi^{\pm}$ with respect to $D \to \pi^+\pi^-$,

- $r_{\text{PID}}(\mathcal{R}_d^{\pi\pi}) = 0.9380 \pm 0.0002 \pm 0.01214$, the ratio of PID efficiency for $D \to K^{\mp}\pi^{\pm}$ with respect to $D \to \pi^+\pi^-$,

- $r_{\text{sel}}(\mathcal{R}_d^{\pi\pi}) = 1.010 \pm 0.007$, the ratio of selection efficiency for $D \to K^{\mp}\pi^{\pm}$ with respect to $D \to \pi^+\pi^-$,

- $\frac{\mathcal{B}(D^0 \to K^-\pi^+)}{\mathcal{B}(D^0 \to \pi^+\pi^-)} = 27.9 \pm 0.5$, the ratio of branching fractions of the $D^0 \to K^-\pi^+$ with respect to $D^0 \to \pi^+\pi^-$, taken from [84],

and all the other factors are as shown in Section 5.6.

The systematic uncertainties on the CP observables corresponding to the $D \to \pi^+\pi^-$ mode are assessed in the same way as detailed in Section 5.6. These are summarised in Table 5.21.

The CP observables in the $D \to \pi^+\pi^-$ mode are measured to be

$$
\begin{align}
A_d^{\pi\pi} &= -1.109 \; ^{+0.843}_{-1.955} \pm 0.247, \tag{5.53}\\
A_s^{\pi\pi} &= 0.117 \; ^{+0.395}_{-0.394} \pm 0.015, \tag{5.54}\\
R_d^{\pi\pi} &= 0.516 \; ^{+0.532}_{-0.398} \pm 0.134, \tag{5.55}\\
R_{ds}^{\pi\pi} &= 0.112 \; ^{+0.127}_{-0.095} \pm 0.013, \tag{5.56}
\end{align}
$$

where the first uncertainty is statistical and the second systematic.

As can be seen from Equations (5.53) to (5.56), all the CP observables are measured to be compatible with 0 within their uncertainties, which are dominated by statistics. Nevertheless, these uncertainties are large, which makes this result barely precise. This is the reason why these results have not been published. The reconstructed yiels in the $\overline{B} \to \pi^+\pi^-$ mode are however compatible with the expectation from the $D \to K^+K^-$ yields, when taking into account the corresponding branching fractions.

Source	Observable			
	$R_d^{\pi\pi}$	$R_{ds}^{\pi\pi}$	$A_s^{\pi\pi}$	$A_d^{\pi\pi}$
$\overline{B}^0 - B^0$ production asymmetry	0.003	0.00010	0.0	0.0013
f_s/f_d	0.0	0.004	0.0	0.0
τ_s/τ_d	0.0	0.0012	0.0	0.0
D^0 decay BFs	0.009	0.0	0.0	0.0
Trigger efficiency	0.006	0.0011	0.010	0.002
Lifetime difference	0.0	0.0011	0.0	0.0
PID efficiency	0.007	0.0	0.0	0.0
Selection efficiency	0.004	0.0	0.0	0.0
Signal model	0.07	0.007	0.006	0.13
Combinatorial model	0.07	0.009	0.005	0.13
Low mass background model	0.07	0.005	0.006	0.12
$B^0 \to D\rho^0$ cross-feed model	0.05	0.003	0.006	0.11
Total	0.134	0.014	0.015	0.247

Table 5.21: *Summary of all the contributing systematic uncertainties on each $D \to \pi^+\pi^-$ observable.*

Chapter 6

Measurement of CP observables in $\overline{B}^0 \to D\overline{K}^{*0}$ with $D \to K^+\pi^-$

In addition to the $1 \, \text{fb}^{-1}$ of 2011 data, LHCb has collected another $2 \, \text{fb}^{-1}$ of LHC proton-proton collision data in 2012. The complete $3 \, \text{fb}^{-1}$ data sample is analysed, in order to extract a measurement of the CP observables in the $B^0 \to DK^{*0}$ channel using the $D \to K^-\pi^+$ mode. Sizeable CP violation effects are expected in this decay, and sensitivity to the CKM γ angle arises through the ADS approach (*c.f.* Section 2.4.2). This analysis is performed in the same way than the GLW one described in Chapter 5. It completes the work done during this thesis, and the preliminary results are detailed in this chapter.

6.1   Analysis introduction

This chapter describes preliminary results on the CP observables for B^0 and $\overline{B}^0_s$ decays to the DK^{*0} final state, where D can be a D^0 or a $\overline{D}^0$. The theoretical motivation is the same as introduced in Section 5.1: sensitivity to the weak phase γ arises from the interference between the $b \to u$ and $b \to c$ tree-level mediated amplitudes (*c.f.* Section 2.4.2), both of which are colour-suppressed. Here, we consider only neutral D decays to the quasi-specific flavour eigenstates $D \to K^\mp\pi^\pm$. The ADS method [47] can be used to extract γ from these modes, as the suppressed $B^0 \to DK^{*0}$ with $D \to K^-\pi^+$ is expected to be sensitive to CP violation effects. This mode is characterised by opposite sign (OS) kaons in the final state $B^0 \to [K^-\pi^+]_D K^{*0}(K^+\pi^-)$. The favoured $B^0 \to DK^{*0}$ with $D \to K^+\pi^-$ decay, characterised by same sign (SS) kaons in the final state $B^0 \to [K^+\pi^-]_D K^{*0}(K^+\pi^-)$, is not expected to have a sizeable sensitivity to γ with the current LHCb data sample, and is used in this analysis as a normalisation channel. Contributions from $\overline{B}^0_s$ decaying to the same final state are also anticipated for $B^0 \to DK^{*0}$ with $D \to K^\mp\pi^\pm$ OS.

CP observables can be built from the partial widths of these decays, which can be experimentally measured from ratios of reconstructed signal yields, relative efficiencies and relative D^0 branching fractions. They are the two CP assymetries for the OS mode for B^0 and $\overline{B}^0_s$

$$
\begin{aligned}
A_d^{\text{sup}} &= \frac{\Gamma(\overline{B}^0 \to [K^+\pi^-]_D \overline{K}^{*0}) - \Gamma(B^0 \to [K^-\pi^+]_D K^{*0})}{\Gamma(\overline{B}^0 \to [K^+\pi^-]_D \overline{K}^{*0}) + \Gamma(B^0 \to [K^-\pi^+]_D K^{*0})} & (6.1)\\
&= A_{ADS}, \\
A_s &= \frac{\Gamma(B^0_s \to [K^-\pi^+]_D \overline{K}^{*0}) - \Gamma(\overline{B}^0_s \to [K^+\pi^-]_D K^{*0})}{\Gamma(B^0_s \to [K^-\pi^+]_D \overline{K}^{*0}) + \Gamma(\overline{B}^0_s \to [K^+\pi^-]_D K^{*0})}, & (6.2)
\end{aligned}
$$

the ratio of B^0 widths for the suppressed OS over the favoured SS modes

$$
\begin{aligned}
R_d &= \frac{\Gamma(\overline{B}^0 \to [K^+\pi^-]_D \overline{K}^{*0}) + \Gamma(B^0 \to [K^-\pi^+]_D K^{*0})}{\Gamma(\overline{B}^0 \to [K^-\pi^+]_D \overline{K}^{*0}) + \Gamma(B^0 \to [K^+\pi^-]_D K^{*0})} \\
&= R_{ADS},
\end{aligned}
\tag{6.3}
$$

and the B^0 CP asymmetry in the favoured SS mode

$$
A_d^{\mathrm{fav}} = \frac{\Gamma(\overline{B}^0 \to [K^-\pi^+]_D \overline{K}^{*0}) - \Gamma(B^0 \to [K^+\pi^-]_D K^{*0})}{\Gamma(\overline{B}^0 \to [K^-\pi^+]_D \overline{K}^{*0}) + \Gamma(B^0 \to [K^+\pi^-]_D K^{*0})}.
\tag{6.4}
$$

A blind analysis is performed for the B^0 and $\overline{B}^0$ signal mass windows of the suppressed OS decay. As both B^0 and $\overline{B}^0_s$ contributions are involved, the candidate events of the analysis are more generally denoted by B.

6.2 Data sets and event selection

6.2.1 Data and simulation samples

This analysis is based on $3.02 \pm 0.14\,\mathrm{fb}^{-1}$ of data recorded at the LHCb experiment (*c.f.* Chapter 3) from the LHC proton-proton collisions at a centre-of-mass energy of $\sqrt{s} = 7\,\mathrm{TeV}$ during the year 2011 and $\sqrt{s} = 8\,\mathrm{TeV}$ during 2012. B candidates are preselected by the stripping software[1] by a line dedicated to select B hadron decays to charmed particles (*c.f.* Section 3.4). The events are required to be triggered at the hardware trigger level L0 by the signal candidate (Trigger On Signal, "TOS") by any line. Concerning the software trigger, events must be triggered at the first level HLT1 by a specific line relying on track information, and at the second level HLT2 by the topological lines, which select b-hadron decays in an inclusive way by requiring at least two charged particles in the final state and a displaced decay vertex (*c.f* Section 3.3). The Monte Carlo simulation samples used to determine efficiencies and to model B invariant mass distribution components were produced with the 2011 configuration of the software, as the 2012 configuration was still being finalised at the time when this analysis was performed.

Further specific criteria are applied in addition to the stripping selection, summarised in Table 6.3. The cut based selection used in the $\overline{B} \to [K^+K^-]_D \overline{K}^{*0}$ analysis described in Chapter 5 (*c.f* Section 5.2) is used as reference, but it is substantially modified. In particular, a multivariate method is implemented by a "Boosted Decision Tree" instead of rectangular cuts for an important number of selection variables. The complete selection criteria is described in the following sections. B and $\overline{B}$ candidates are treated together along all the selection and background studies procedure.

6.2.2 Boosted Decision Tree selection

Boosted Decision Tree: a multivariate method

Particle physics analyses need to apply appropriate selection criteria in order to separate the interesting signal from the undesired background pollution. A certain group of variables is identified that allow to perform this discrimination when suitable cuts are applied on them. Classically, these variables are treated independently, and a sensible cut is chosen for each variable, usually by using Monte Carlo simulation of the signal and expected background contibutions to the

---

[1]This stripping selection is essentially the same as the one detailed in Table 5.1.
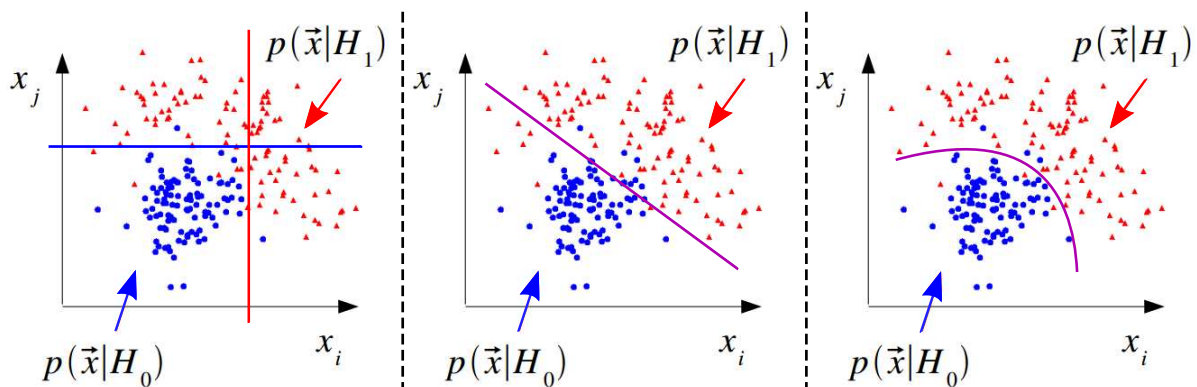
Figure 6.1: *Illustration of multivariate selections, for two variables x_i and x_j, and two data species H_0 and H_1 (for example signal and background). The left plot represents a classic selection using rectangular cuts. The middle and right plots show the optimised discrimination between the two species when taking into account the two variables together (multivariate algorithms): a linear discriminant is used in the middle plot (Fisher discriminants), a non-linear contour in the right plot (Boosted Decision Trees, Neural Networks, etc.).*

channel in study. These individual "rectangular" cuts applied to each one of the variables in the set are determined by demanding to retain as much signal as possible, while rejecting as much background as possible. This is illustrated on the left panel of Figure 6.1.

Modern methods are being developed in order to improve the background rejection while keeping a high efficiency on signal. The basis of multivariate analysis (MVA) is to take into account the discriminant variables in the set together, instead of studying them independently. Instead of applying rectangular cuts, different classifiers built by combining the variables are obtained from the different multivariate methods, and the best individual cut on this combined classifier is chosen. The signal-background separation in data can be optimised through this methods, even when the two species have similar distributions: the selected region is not necessarily a "rectangle", but other linear and non-linear shapes are applied in order to perform the most efficient selection, as exemplified in the middle and right panels of Figure 6.1.

The multivariate method used in the analysis described in this chapter is a Boosted Decision Tree (BDT). A decision tree is a sequence of binary splits performed as cuts on the given set of variables, as illustrated in Figure 6.2 [89]. Two separate signal and background samples are needed to train the decision tree. At each node, starting from the "root" node where all the signal and background events are merged together, the cut on the variable that gives the best separation between signal and background is applied. That is to say, at every split a fixed number of cuts on each one of the variables is tested in order to choose the most discriminant one, according to a certain criterion. The phase space is split in this way into many regions, until the specified minimum number of events is left on the final nodes or "leafs", or until the defined maximum depth of the tree is reached. The leaf nodes are then classified as signal or background according to the species that the majority of the contained events belongs to. Several possibilities are available to define the separation of the signal and background evaluated and maximised in every node. The one we used here is the "Gini index", defined as $p \times (1-p)$, where p is the purity $p = \frac{S}{S+B}$, with S the number of signal events and B the number of background events in the new leaf after the considered splitting.

The "boosted" component arises from the fact that not only one decision tree is used for the final signal-background discrimination in the data, but a collection of them. This forest is built by giving a higher weight to misclassified events in the decision trees. That is to say, a new tree is built by starting from the same signal and background samples, but multiplying the events
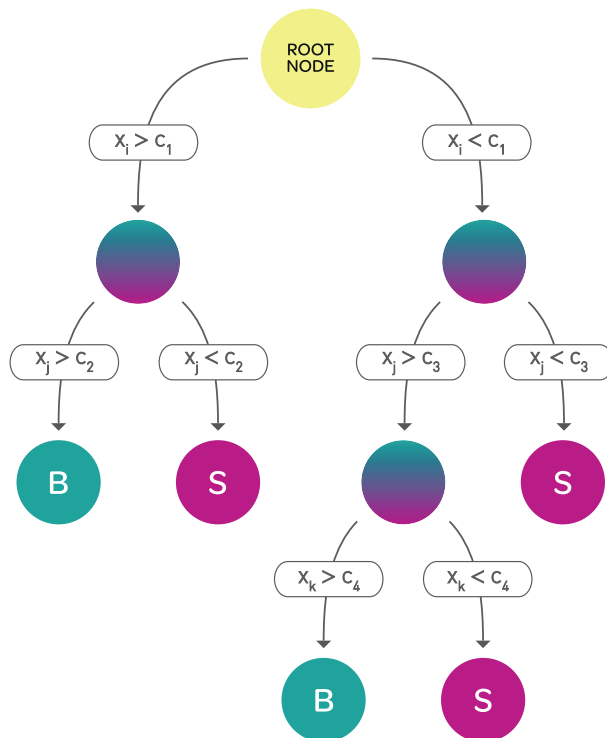
Figure 6.2: *Diagram of a decision tree. At each node, the most discriminant variable to separate the signal events S from the background events B is cut on. A set of discriminant variables $x_i, x_j, x_k, \ldots$ is tested, and the best cut $c_1, \ldots, c_4$ is determined at every split.*

that were misclassified in the previous tree by a common factor, the "boost weight". In this way, the classification peformance is enhanced, as well as the stability against statistical fluctuations.

The boosting method used in this analysis is a Gradient Boost. The forest is identified with a function $F(\mathbf{x})$ built as a weighted sum of boosted decision trees, represented by parametrised base functions $f(\mathbf{x}; a_m)$, also called "weak-learners",

$$F(\mathbf{x}; P) = \sum_{t=0}^{T} \beta_t f(\mathbf{x}; c_t); \qquad P \in \{\beta_t; c_t\}_0^T \,, \tag{6.5}$$

where $\mathbf{x}$ is the set of discriminating variables, the sum on t is performed over the total number of trees T, c_t is the set of parameters defining the trees and β_t are the boosting weights. The boosting procedure consists on adjusting the parameters P so that the deviation between the BDT model response $F(\mathbf{x})$ and the true value y obtained from the training data samples is minimised. To measure the deviation between these two, a loss function is defined as a binomial log-likelihood[2]

$$L(F, y) = \ln\left(1 + e^{-2F(\mathbf{x})y}\right). \tag{6.6}$$

In order to develop an efficient MVA method, two different sets of signal and background events are needed as input: a training sample, to perform the MVA learning, and a testing sample, to validate the learning. An important issue that needs to be taken care of is the risk of overtraining. That is to say, it can happen that a MVA method "learns to much", and while the performance seems to be very good in the training sample, it is not when measured on

---

[2]Other boosting methods appear for different definitions of the loss function $L(F, y)$. For example, in the AdaBoost (adaptative boost) method it is $L(F, y) = e^{-F(\mathbf{x})y}$.

the testing one. For a BDT, this can happen for instance when the number of trees or nodes is too high. The main purpose of the testing sample is to detect this possible problem. The Kolmogorov-Smirnov test is a statistical method that can be used to quantify the overtraining. It compares two distributions, in this case the training and testing classifier outputs (separetely for signal and background) and computes the distance between the two corresponding empirical distributions. The Kolmogorov-Smirnov test can have values between 0 and 1, being 1 the case where the two distributions are exactly the same. As a rule, we consider 0.1 as the critical value under which there is evidence of overtraining.

The BDT training produces a set of weights in order to classify the events as signal or background. The application of these BDT weights on the actual data to be analysed produces, for each each event in the sample, a BDT response taking values between 0 and 1, that can be somehow understood as a probability of an event to be signal. This BDT response or BDT classifier can be used as a new variable to cut on, in order to reject background from the data.

A Boosted Decision Tree using a Gradient Boost is implemented in this analysis by means of the TMVA package[3] [90]. Other MVA methods have been tested in order to choose the one giving the highest performance on the considered data. Roughly tuned versions of a BDT, a Neural Network and a Fisher discriminant were compared at an early stage. A ROC (Receiver Operating Characteristic) diagram is used for this comparison: it represents the background rejection versus the signal efficiency obtained from a MVA method by cutting on the classifier output for the events on the test sample. This is shown in Figure 6.3. The BDT provides a slightly better performance. This together with the fact that the BDT is more transparent and adjustable motivated the choice of this MVA for this analysis. The specific characteristics of the final BDT, as well as the training procedure and optimisation for the $B^0 \to DK^{*0}$ candidates are detailed in the following section.

A Boosted Decision Tree for $B^0 \to DK^{*0}$

A Boosted Decision Tree is developed for $B^0 \to DK^{*0}$, implemented using the TMVA package [90] in ROOT. This BDT is optimised for $D \to K^{\mp}\pi^{\pm}$ Opposite Sign, as this is the signal we are interested in. The following samples are used to train and test the BDT:

- Signal: Monte Carlo simulation of signal $B^0 \to [K^{\mp}\pi^{\pm}]_D K^{*0}$, matched to truly generated signal decays.

- Background: 2011 real data candidates from the upper sideband of the $B^0 \to DK^{*0}$ Opposite Sign mode. This upper sideband is defined as events outside the B candidates mass window that is used for the invariant mass distribution fit in Section 6.4, that is to say $M(B) > 5.8$ GeV/c^2.

A small preselection is applied to these data sets, namely the mass windows of the D and K^{*0} mesons and the cut on the θ^* helicity angle: $\left|M(K^{\mp}\pi^{\pm} - M(D^0)\right| < 20$ MeV/c^2, $\left|M(K^+\pi^-) - M(K^{*0})\right| < 50$ MeV/c^2 and $|\cos\theta^*| > 0.4$. The number of events available after these cuts is shown in Table 6.1 for both the signal and background categories. The signal sample is split randomly in two halves, one to perform the BDT training and the other to test this training in order to control possible overtraining effects. For the background sample, the same number of training events as for the signal is assigned, and the rest is left for training, choosing also the events in a random way.

---

[3]TMVA is a ROOT-integrated toolkit for multivariate classification and regression analysis. It integrates a large variety of multivariate methods, and the appropriate routines for their training, testing and performance evaluation to apply them to the particular problem of the user.
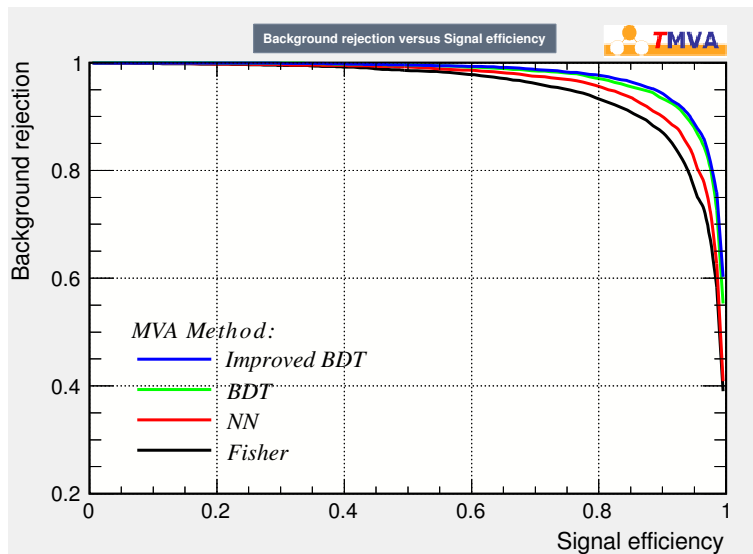
Figure 6.3: *ROC (Receiver Operating Characteristic) diagrams, giving the peformance of different MVA methods applied to the $B^0 \to [K^\mp\pi^\pm]_D K^{*0}$ Opposite Sign channel. The horizontal axis shows the efficiency on signal, while the vertical axis shows the background rejection. A method performs better when the area integrated under the corresponding curve is larger. The four represented tested methods are: a Fisher discriminant (black line), a Neural Network (red line), a Boosted Decision Tree (green line), and a slightly better tuned Boosted Decision Tree (blue line).*

	data sample	
	Signal	Background
training	4664	4663
testing	4664	9154
total	9328	13817

Table 6.1: *Number of events in the signal and background samples for the $B^0 \to [K^\mp\pi^\pm]_D K^{*0}$ Opposite Sign BDT training and testing processes.*

The variables used for the BDT training are chosen among those from the previous cut based analysis which are oriented to remove combinatorial background. These are listed in Table 6.2: the transverse momentum of the particles in the final state, the vertex fit χ^2/ndf of the D and B mesons, the minimal impact parameter significance Min IPχ^2 for the D, the K^{*0} and the B, the pointing angle of the B between its momentum direction and its direction of flight, and the the sum of the square roots of the IPχ^2 of the four charged tracks with respect to the primary vertex[4]. Despite their importance for background rejection, the particle identification variables DLL$_{K\pi}$ are not included, due to the fact that they are not well reproduced by the simulation. The distribution of the variables in the training samples for both signal and background are shown in Figure 6.4.

The linear correlations between these variables are shown in Figure 6.5 for both signal and background. Relatively high correlations exist for impact parameter variables, namely the sum of the square roots of the IPχ^2 of the four charged tracks with the minimum IPχ^2 of the D and K^{*0}

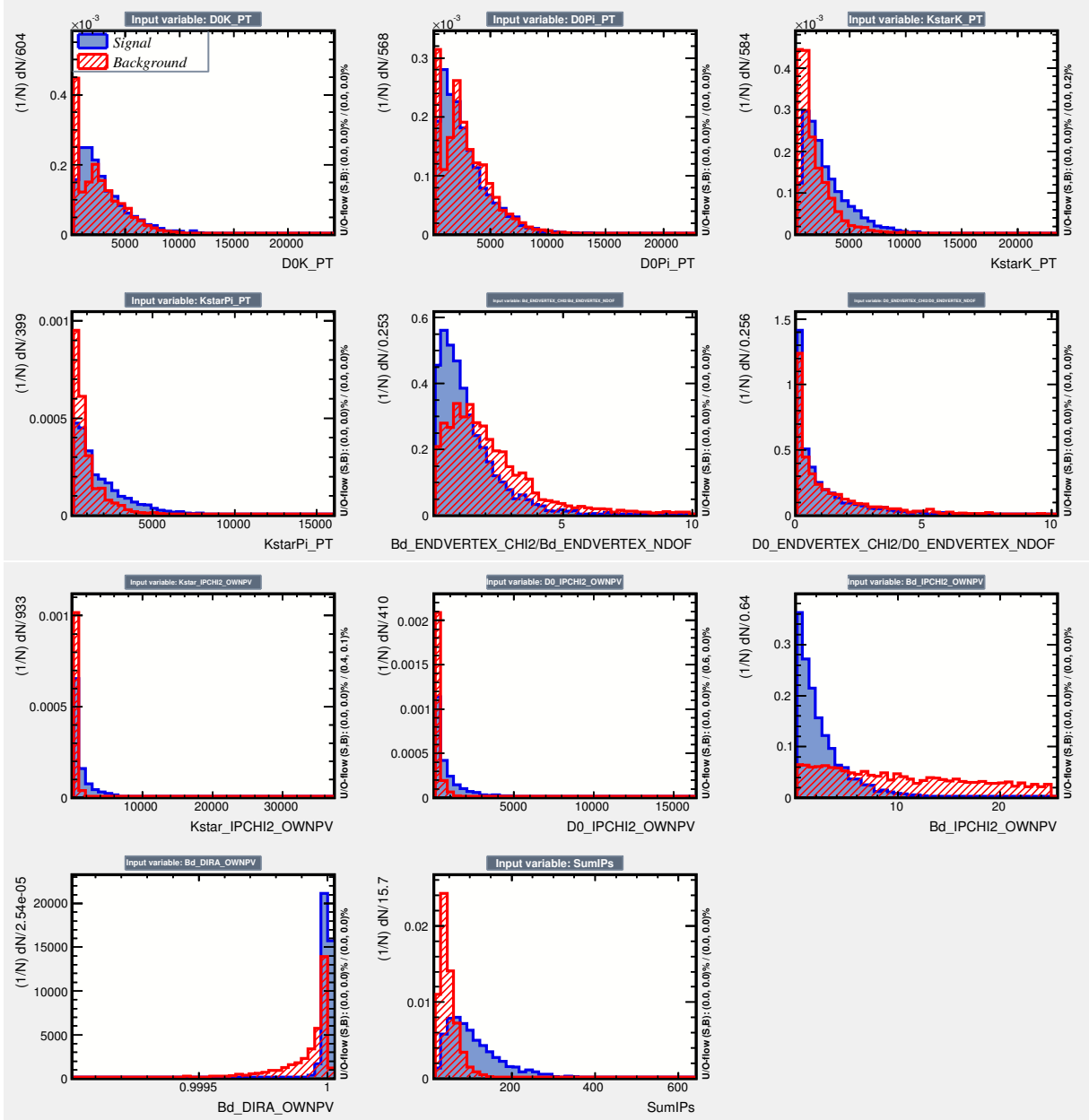[4]For a more precise description of these quantities, see Section 5.2.

Figure 6.4: *Signal and background distributions of the variables used to train the BDT, for the training sample. See Table 6.2 for the explanation of the variables.*

Meson	BDT training variables	code name
Charged track	p_T	X_PT
D^0	Vertex χ^2/ndf	D0_ENDVERTEX_CHI2/
		D0_ENDVERTEX_NDOF
	Min IPχ^2	D0_IPCHI2_OWNPV
K^{*0}	Min IPχ^2	Kstar_IPCHI2_OWNPV
B	Vertex χ^2/ndf	Bd_ENDVERTEX_CHI2/
		Bd_ENDVERTEX_NDOF
	Min IPχ^2	Bd_IPCHI2_OWNPV
	$\cos(\theta_{\mathrm{dira}})$	Bd_DIRA_OWNPV
	$\sum_{\mathrm{tracks}} \sqrt{\mathrm{IP}\chi^2}$	SumIPs

Table 6.2: *Input variables for the training of the BDT. A code is provided to match the name of each variable with the corresponding distribution in Figure 6.4.*

mesons. In order to improve the BDT performance in discriminating signal from background, the input variables distributions are preprocessed before the training. Two transformation operations are applied: a "Gaussianisation", which transforms the distribution of the input variables into Gaussian shapes, plus a linear decorrelation (which works better on Gaussian distributions).

Several studies were performed in order to select the BDT parameters giving the most efficient BDT for these data. The final BDT has the following characteristics:

- Number of trees in the forest: 200.

- Maximum depth allowed in each decision tree: 2.

- Number of cuts or steps during the node cut optimisation: 20.

- Boosting type: Gradient. Shrinkage (learning rate): 0.1.

These parameters were chosen by training the tree with different values for each one of them, and comparing the performance while keeping the overtraining at a safe level. Special attention has been paid to the number of trees and the maximum depth. Higher values for these parameters give better performance, but at the same time the overtraining becomes important (which can be understood as the BDT learning "too fast" the difference between signal and background). The chosen combination is a good compromise between improving the performance while controlling the overtraining.

The ROC or performance curve and the signal and background output distributions of the BDT trained in this way is shown in Figure 6.6. The overtraining Kolmogorov-Smirnov test, quantifying the difference between the training and test sample separately for the signal and background categories, is shown in the right panel of the figure: the agreement is good and the test is > 0.1, thus we consider that the BDT is not overtrained.

The total 3 fb^{-1} of real data are thus processed in order to obtain the BDT classifier distribution, using the weights resulting from the BDT tuned and trained in this way. In order to determine the best cut on this variable, the expected numbers of events of signal S and background B in the $B^0 \to [K^\mp\pi^\pm]_D K^{*0}$ Opposite Sign signal region are computed. The background is extrapolated from the number of events in the B mass window inside [5.5;5.8] GeV/c^2, where
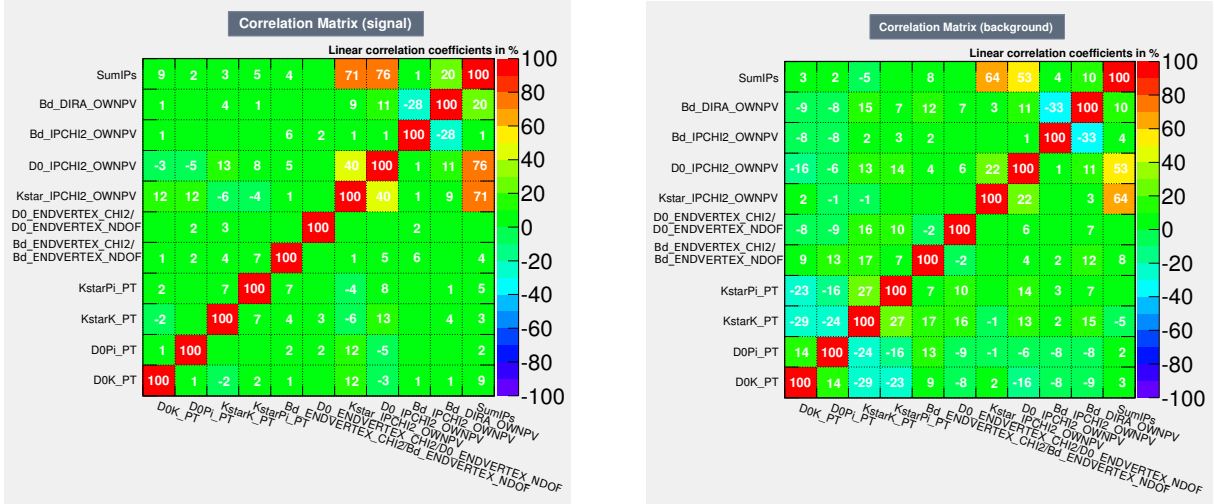
Figure 6.5: *Linear correlations of the input variables for the BDT training, for signal (left) and background (right). See Table 6.2 for the explanation of the variables.*
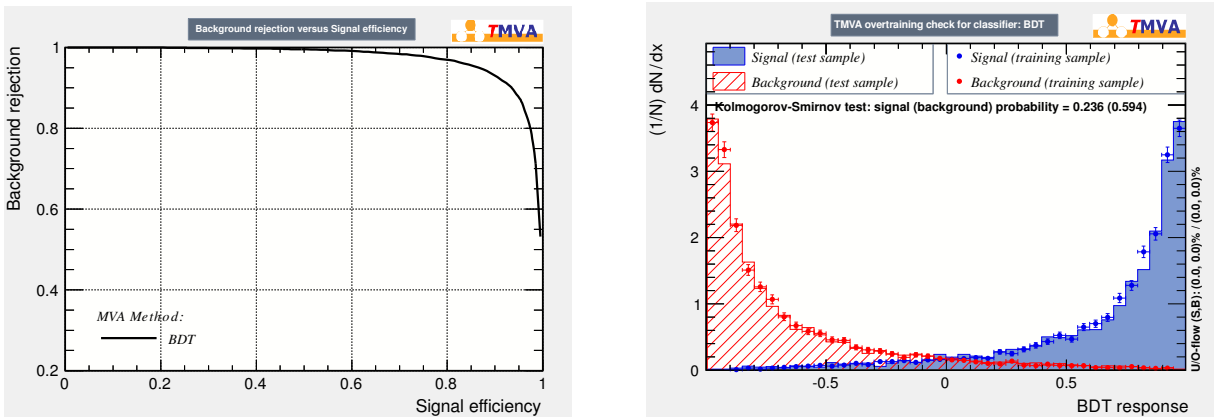

Figure 6.6: *Performance plots for the BDT described in the text, optimised for the $B^0 \rightarrow [K^{\mp}\pi^{\pm}]_D K^{*0}$ Opposite Sign mode. Left: ROC curve (background rejection versus signal efficiency). Right: BDT classifier output for signal and background, for both the training and testing sample. The overtraining can be addressed from this plot, where the value of the Kolmogorov-Smirnov test is provided.*
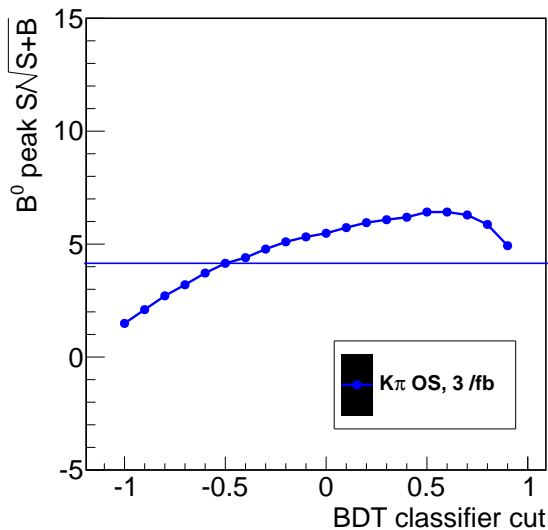
Figure 6.7: *Expected significance $S/\sqrt{S+B}$ of the $B^0 \to [K^\mp \pi^\pm]_D K^{*0}$ Opposite Sign mode as a function of the cut on the BDT classifier variable. S is estimated from the number of $\overline{B}^0_s$ signal events. The horizontal line represents the expected significance when a cut based selection as the one optimised for the $B^0 \to [K^+ K^-]_D K^{*0}$ analysis (c.f. Table 5.2) is applied.*

only combinatorial background contributes, assuming that this background follows a first order polynomial distribution. As the signal region is blind, S is estimated from the number of events in the $\overline{B}^0_s$ mass window $[5.32; 5.42]$ GeV/c^2, sustracting the corresponding extrapolated background, and scaled multiplying it by a factor computed using the CKM matrix elements, and the ratio of hadronisation fractions $f_s/f_d = 0.276 \pm 0.021$ [87]. One should note that no fit to the B invariant mass distribution is used here.

The expected significance in the B^0 signal region, defined as $S/\sqrt{S+B}$ is represented as a function of the cut on the BDT classifier in Figure 6.7. The additional cuts that are described in the next sections are also applied, using those before their optimisation[5]. The expected significance resulting when applying the cut based selection optimised for the $B^0 \to [K^+ K^-]_D K^{*0}$ analysis (*c.f.* Section 5.2.1) to the current data sample is represented by the horizontal line, for comparison. The BDT selection performs better than the cut based one, according to this plot. A cut on the BDT classifier > 0.6 is chosen.

Additional cuts need to be applied on top of the one on the BDT response in order to obtain an optimal selection. These are described in the following sections.

6.2.3 D^0 selection

D^0 or $\overline{D}^0$ mesons are reconstructed in the $D \to K^\mp \pi^\pm$ decay modes. Particle identification (PID) criteria are applied to distinguish π from K, namely the difference between the logarithmic likelihoods of the K and π hypotheses $\mathrm{DLL}_{K\pi}$ must be larger than -2 for K and smaller than 8 for π.

To suppress background from the charmless decays $B^0 \to K^\mp \pi^\pm K^{*0}$, a condition on the D flight distance (FD) significance with respect to the B vertex is applied, requesting that it

---

[5]These additional cuts were optimised after the choice of the BDT, so in this plot the values before optimisation, shown in Table 5.2, are considered, for the variables not used to train the BDT (no cut is applied on the BDT training variables).

is larger than 3, that is to say requiring the D daughters to come from a displaced D vertex with respect to the B vertex (see Section 6.3.1). Finally, only D candidates with an invariant mass within $\pm 20\,\mathrm{MeV}/c^2$ of the D^0 nominal mass ($1864.86\,\mathrm{MeV}/c^2$ [34]) are kept to form B candidates.

6.2.4 K^{*0} selection

K^{*0} mesons are reconstructed in the mode $K^{*0} \to K^+\pi^-$. Concerning particle identification criteria, the $\mathrm{DLL}_{K\pi}$ is required to be larger than 3 for the K and lower than 3 for the π. Possible contamination from protons in the K sample ($\Lambda_b^0 \to \overline{D}^0 p h^-$ decays, see Section 6.3.3) is reduced by keeping only K candidates with a difference between the logarithmic likelihoods of the proton and K hypotheses DLL_{pK} smaller than 10. K^{*0} candidates with an invariant mass within $\pm 50\,\mathrm{MeV}/c^2$ of the nominal mass ($891.66\,\mathrm{MeV}/c^2$ [34]) are selected.

6.2.5 B^0 selection

B hadron candidates are formed combining D and K^{*0} candidates selected with the above requirements. Events are required to be triggered by any particle in the $B^0 \to [K^\mp\pi^\pm]_D K^{*0}(K^+\pi^-)$ final state by the L0 Hadron line ("TOS"), or by any L0 line by the other B hadron decay in the same event ("OtherB"). Using the fact that the signal decay modes are decays of a pseudo-scalar particle (B^0) to a pseudo-scalar particle (D^0) and a vector particle (K^{*0}), the helicity angle θ^* of the K from the K^{*0} is required to have an absolute value of the cosine larger than 0.4.

Specific peaking backgrounds from $B^0 \to D^-_{(s)}\pi^+$ or $B^0 \to D^-_{(s)}K^+$ decays are eliminated by applying a veto on candidates for which the invariant mass of three of the four charged mesons in the final state is compatible with them being produced by a $D^\mp$ or a $D_s^\mp$ decay (see Section 6.3.3). Namely, candidates are rejected when the invariant mass $M(K^\pm\pi^\mp\pi^\mp)$ is within ± 15 MeV/c^2 of the $D^\mp$ nominal mass or when the invariant mass $M(K^\mp K^\pm\pi^\mp)$ is within ± 15 MeV/c^2 of the $D_s^\mp$ or $D^\mp$ nominal mass.

After all selections are applied, 0.9 % of the events contain more than one B candidate. For the final measurement, and in particular for the mass fit described later, only one candidate per event is retained, keeping the one with the largest B flight distance significance with respect to the primary vertex of smallest $\mathrm{IP}\chi^2$.

6.2.6   Selection optimisation

The selection presented before is based on the optimal selection developed for the $\overline{B}^0 \to [K^+K^-]_D \overline{K}^{*0}$ analysis from Chapter 5. The cuts applied on the set of selection variables not used in the BDT training are optimised, to account for the new data and the BDT based selection.

First, the PID on the K and π particles in the final state is optimised. All selection cuts are applied except the one on $\mathrm{DLL}_{K\pi}$ variables of the K and π from the D meson. The same procedure as described in Section 6.2.2 is used to estimate the $B^0 \to [K^\mp\pi^\pm]_D K^{*0}$ Opposite Sign signal significance $S/\sqrt{S+B}$, that is to say extrapolating the background B from the upper sideband of the invariant mass distribution, and estimating the blind signal S by scaling the number of $\overline{B}_s^0$ signal events. The significance is computed as a function of the cut on the $\mathrm{DLL}_{K\pi}$ variables of the D daughters and shown in the left panel of Figure 6.8. The preferred cut for K appears to be $\mathrm{DLL}_{K\pi}(K^\pm) > -2$, while a plateau is reached for the π for cuts larger than $\mathrm{DLL}_{K\pi}(\pi^\pm) < 7$. A value of < 8 is chosen, as for the same significance a tighter cut is preferred in order to reduce the amount of background events. These cuts are looser than the previous ones (*c.f.* Table 5.2), and there is a risk of allowing larger fractions of cross-feed events

Meson	Variable	Cut value
D^0	$\mathrm{DLL}_{K\pi}(K^\pm)$	> -2
	$\mathrm{DLL}_{K\pi}(\pi^\pm)$	< 8
	Flight distance significance	> 3
	$\left\|M(K^\mp\pi^\pm - M(D^0)\right\|$	$< 20\,\mathrm{MeV}/c^2$
K^{*0}	$\mathrm{DLL}_{K\pi}(K^\pm)$	> 3
	$\mathrm{DLL}_{K\pi}(\pi^\pm)$	< 3
	$\mathrm{DLL}_{pK}(K^\pm)$	< 10
	$\left\|M(K^+\pi^-) - M(K^{*0})\right\|$	$< 50\,\mathrm{MeV}/c^2$
B	$\|\cos\theta^*\|$	> 0.4
	$\|M(K^\mp\pi^\pm\pi^\pm) - M(D^\pm)\|$	$> 15\,\mathrm{MeV}/c^2$
	$\|M(K^\pm K^\mp\pi^\pm) - M(D_s^\pm, D^\pm)\|$	$> 15\,\mathrm{MeV}/c^2$
Combined	BDT classifier	> 0.6

Table 6.3: *Selection criteria for $B^0 \to [K^\mp\pi^\pm]_D K^{*0}$ candidates.*

from different D decay modes because of particle misidentification. This effect is checked to be negligible in Section 6.3.2.

The same procedure is applied for the K and π from the K^{*0} meson, using the new PID cuts for the D daughters. The $S/\sqrt{S+B}$ estimated significance for the B^0 signal as a function of the cuts on the $\mathrm{DLL}_{K\pi}$ variables is shown in the left panel of Figure 6.8. Here the potential risk is to allow cross-feed events from $B^0 \to D\rho^0(\pi^+\pi^-)$ events, when one of the π from the ρ^0 is misidentified as a K. Although the favoured cuts seem to be the looser ones, giving a larger significance, it has been noticed that for those pairs the number of background events B in the signal region is larger than the number of expected signal events S, which is not desirable. If we rule out all the combinations giving a significance larger than 7, the next favoured pairs are those with approximately the same cut value on $\mathrm{DLL}_{K\pi}$ for K than for π (with $\mathrm{DLL}_{K\pi} > cut$ for K and $\mathrm{DLL}_{K\pi} < cut$ for π), and the significance is very similar for all of these. It is decided to set the cut on these variables at the same value than used previously, in order to keep the cross-feed from $B^0 \to D\rho^0(\pi^+\pi^-)$ under control, that is to say $\mathrm{DLL}_{K\pi}(K^\pm) > 3$ and $\mathrm{DLL}_{K\pi}(\pi^\pm) < 3$ for the K^{*0} decay products.

6.3 Specific backgrounds studies

6.3.1 Charmless background

Peaking backgrounds from charmless decays, of the type $B^0 \to K^\mp\pi^\pm K^{*0}$ decays, are removed by applying a cut on the D meson flight distance significance[6], as mentioned in Section 6.2.3.

To study this source of background, this requirement on the D flight distance and the D mass window are relaxed. The upper sideband of the D invariant mass distribution is used[7], defined

---

[6]This variable is defined in Section 5.3.1

[7]Only the upper sideband is considered, in order to discard eventual partially reconstructed D events coming from other background sources, populating the D low mass region.
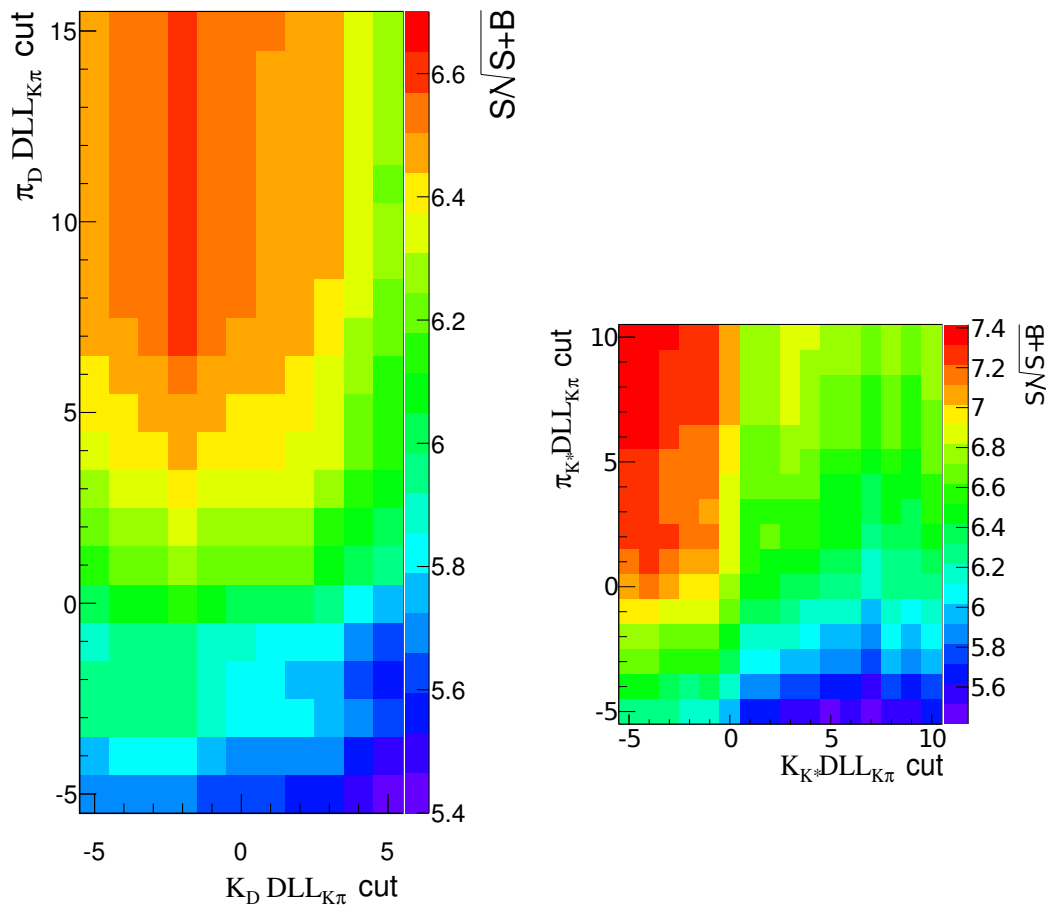
Figure 6.8: *Expected significance $S/\sqrt{S+B}$ of the $B^0 \to [K^{\mp}\pi^{\pm}]_D K^{*0}$ Opposite Sign signal as a function of the PID cuts on the D daughters (left) and the K^{*0} daughters (right). S is estimated from the number of $\overline{B}_s^0$ signal events.*
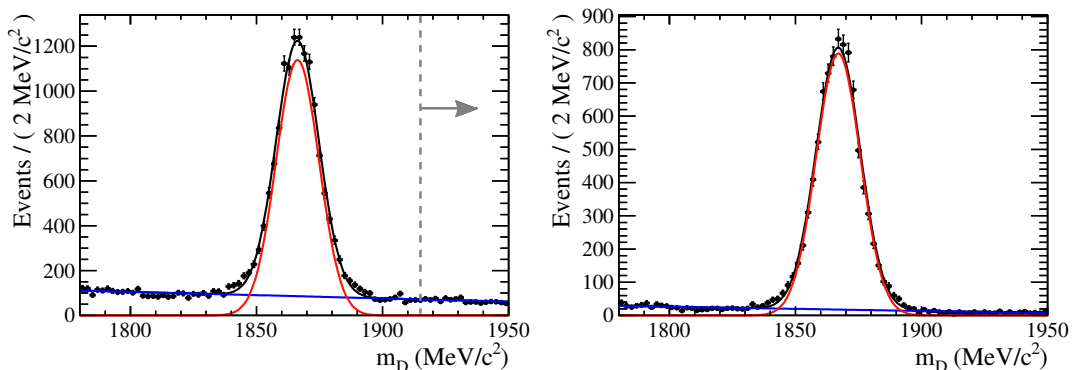
Figure 6.9: *Fit to the D invariant mass distribution after all selection cuts for $D \to K^{\mp}\pi^{\pm}$, relaxing the D mass window and the D flight distance significance requirement (left), or relaxing only the D mass window and requiring the D flight distance significance to be > 3. The black line superimposed on the distributions is the fit result, sum of a linear combinatorial background (blue line) and a Gaussian function for the signal (green line).*

as $M(K^{\mp}\pi^{\pm}) > 1915$ MeV/c^2 as shown in the left panel of Figure 6.9 (where the whole B mass distribution is considered). B and $\overline{B}$ events are treated together along the process.

For the events in this sideband, the B invariant mass distribution is studied and fitted with double Gaussian functions for the B^0 and the $\overline{B}^0_s$ signal peaks, using the same parameters as in the nominal fit of Section 6.4 but additionally fixing the mean value and the signal resolution, and an exponential function for the combinatorial background. The fit is repeated for different cut values on the D flight distance significance requirement. The resulting yields of B^0 and $\overline{B}^0_s$ are scaled to the D signal region selected for the final analysis, and then represented as a function of the D flight distance significance requirement in Figure 6.10 for B^0 and 6.11 for $\overline{B}^0_s$, separately for $D \to K^{\mp}\pi^{\pm}$ Opposite Sign and Same Sign modes.

From these plots it can be seen that the charmless contribution to the B^0 signal is quite reduced in the $D \to K^{\mp}\pi^{\pm}$ Opposite Sign mode, which is the signal channel of this analysis. However, as this B^0 mode is suppressed and the expected final yields are small, we set the D flight distance significance cut at > 3. This cut is also enough to keep the $\overline{B}^0_s$ contribution at a level compatible with zero.

6.3.2 Cross-feed of D modes

From the loose PID cuts for the D products listed in Table 6.3, we anticipate cross-feed background from misidentified events from other $D \to h^+h^-$ decays. The cross-feed background from $D \to K^+K^-$ and $D \to \pi^+\pi^-$ into the $D \to K^{\pm}\pi^{\mp}$ mode under study is assessed from the invariant mass distribution of the D meson in the right panel of Figure 6.9, where D mass window requirement is relaxed. A clear peak appears, centred around the nominal mass of the D^0 meson ($M(D^0) = 1864.86 \pm 0.13$ MeV/c^2 [34]). No other structures are present in this distribution, neither at lower nor at higher masses, which implies that no sizeable cross-feed is present from other D modes.

The double mis-ID contribution of the favoured $D \to K^{\mp}\pi^{\pm}(SS)$ category into the suppressed $D \to K^{\mp}\pi^{\pm}(OS)$ is estimated from simulation to be less than 0.15 %.
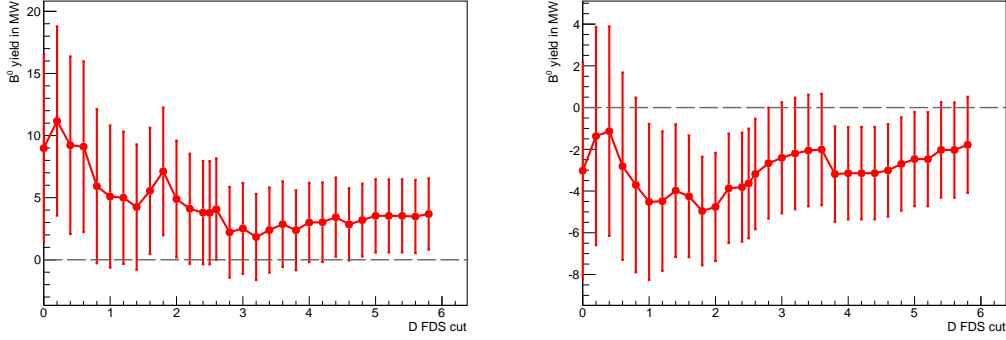
Figure 6.10: *Yields of peaking backgrounds from charmless B^0 decays scaled to the D signal region, as a function of the flight distance significance cut on the D, for the $D \to K^{\mp}\pi^{\pm}$ Opposite Sign (left) and Same Sign (right) categories. The negative values on the right plot are due to fluctuations between signal and background, due to the signal excess being very small or even inexistent.*
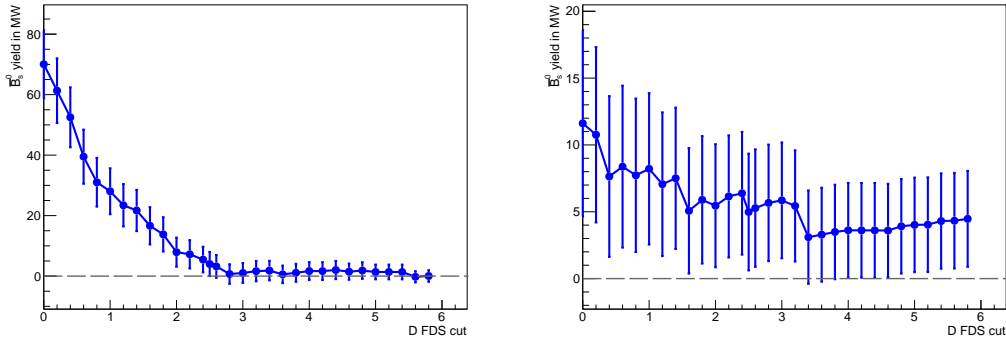

Figure 6.11: *Yields of peaking backgrounds from charmless $\overline{B}_s^0$ decays scaled to the D signal region, as a function of the flight distance significance cut on the D, for the $D \to K^{\mp}\pi^{\pm}$ Opposite Sign (left) and Same Sign (right) categories.*

6.3.3 Other backgrounds

In order to avoid possible backgrounds from $\Lambda_b^0 \to \overline{D}^0 p\pi^-$ and $B^0 \to D^- (h'h''h''') h^+$ or $B^0 \to D_s^+ (h'h''h''') h^-$ decays, the same requirements used for the analysis presented in Chapter 5 (*c.f.* Section 5.3.4) are kept and applied here. These cuts are included in Table 6.3. The requirement on the K PID hypothesis with respect to the proton hypothesis $\mathrm{DLL}_{pK}(K^{\pm}) < 10$ for the K coming from the K^{*0} decay fights against $\Lambda_b^0 \to \overline{D}^0 p\pi^-$ contributions, when the proton is misidentified as a K. The requirement on the mass combination of three of the four particles in the final state, $|M(K^{\mp}\pi^{\pm}\pi^{\pm}) - M(D^{\pm})| > 15\,\mathrm{MeV}/c^2$ and $|M(K^{\pm}K^{\mp}\pi^{\pm}) - M(D_s^{\pm}, D^{\pm})| > 15\,\mathrm{MeV}/c^2$, removes the event when this combination is compatible with a $B^0 \to D^- h^+$ or a $B^0 \to D_s^+ h^-$ decay. The double mis-ID contribution from $K^{*0} \to \pi^+ K^-$ into $K^{*0} \to K^+\pi^-$ is estimated from simulation to be 0.03 % and thus neglected. Other possible background contributions are either considered also negligible, or modelled in the final fit to the B invariant mass.

6.4 Fit strategy

The event yields necessary to compute the ratios and asymetries presented in Section 6.1 are extracted from an extended unbinned maximum likelihood fit to the mass distributions of the reconstructed and selected events. The DK^{*0} invariant mass of the B candidates is computed from the combination of the four final state particles, with a constraint applied on the D meson mass to be equal to D^0 nominal mass (1864.86 ± 0.13) MeV/c^2 [34]. The B candidates invariant mass window considered is defined as $[5.0; 5.8]$ GeV/c^2.

6.4.1 Categories

$B \to DK^{*0}$ events are grouped into categories, according to the D decay mode in which they are reconstructed and the flavour of the B-hadron at its decay time. The following categories are defined:

- B ($K\pi$) Opposite Sign (OS):
  $B^0 \to [K^-\pi^+]_D K^{*0}(K^+\pi^-)$ and $\overline{B}_s^0 \to [K^-\pi^+]_D K^{*0}(K^+\pi^-)$;

- $\overline{B}$ ($K\pi$) Opposite Sign (OS):
  $\overline{B}^0 \to [K^+\pi^-]_D \overline{K}^{*0}(K^-\pi^+)$ and $B_s^0 \to [K^+\pi^-]_D \overline{K}^{*0}(K^-\pi^+)$;

- B ($K\pi$) Same Sign (SS):
  $B^0 \to [K^+\pi^-]_D K^{*0}(K^+\pi^-)$;

- $\overline{B}$ ($K\pi$) Same Sign (SS):
  $\overline{B}^0 \to [K^-\pi^+]_D \overline{K}^{*0}(K^-\pi^+)$.

6.4.2 Fit probability density function components

For each category of events, the mass distribution is fit with a model which is the sum of probability density functions (PDF) describing the different types of contributions. The model is essentially the same as the one used in the analysis for the measurement of the CP observables in the $\overline{B}^0 \to [K^+K^-]_D\overline{K}^{*0}$ channel described in Chapter 5 (c.f. Section 5.5). The modifications introduced due to the large amount of data used here and a better background description from simulation are described in this section. In the following, the B invariant mass variable on which the fit is performed is denoted as M.

6.4.2.1 Signal

The PDF describing the signal is, for each category, a sum of two double Gaussian functions, one for the B^0 signal peak and one for the $\overline{B}_s^0$ signal peak. Except for the signal yields, all the other parameters are common to all categories. The model is exactly the same as the one described in Section 5.5.2.1, namely:

$$f_{\text{signal}}(M; N^{B^0}, N^{\overline{B}_s^0}, \mu, \sigma) = N^{B^0}\left[\frac{f_{\text{core}}}{\sigma\sqrt{2\pi}}e^{-\frac{(M-\mu)^2}{2\sigma^2}} + \frac{1-f_{\text{core}}}{\sigma\kappa\sqrt{2\pi}}e^{-\frac{(M-\mu)^2}{2\sigma^2\kappa^2}}\right] +$$
$$N^{\overline{B}_s^0}\left[\frac{f_{\text{core}}}{\sigma\sqrt{2\pi}}e^{-\frac{(M-\mu-\Delta M)^2}{2\sigma^2}} + \frac{1-f_{\text{core}}}{\sigma\kappa\sqrt{2\pi}}e^{-\frac{(M-\mu-\Delta M)^2}{2\sigma^2\kappa^2}}\right], \quad (6.7)$$

where

- N^{B^0} is the number of signal B^0 events.

- $N^{\overline{B}_s^0}$ is the number of signal $\overline{B}_s^0$ events[8].

- μ is the central value of the Gaussian function for the B^0 peak.

- σ is the resolution of the Gaussian function out of the doublet which has the smallest one, or "core" resolution. The same value is used for the B^0 and the $\overline{B}_s^0$ peaks[9].

- κ is the ratio of the largest resolution to the smallest resolution of the double Gaussian function. It is fixed to the value obtained from Monte Carlo simulation, $\kappa = 2.1$, and the same value is used for B^0 and $\overline{B}_s^0$.

- f_{core} is the fraction of signal events in the Gaussian with the smallest resolution. It is fixed to the value obtained from Monte Carlo simulation, $f_{\text{core}} = 0.87$, and the same value is used for B^0 and $\overline{B}_s^0$.

- ΔM is the mass difference between the mean values of the $\overline{B}_s^0$ peak and B^0 peak. It is fixed to the nominal value $\Delta M = 87.19 \, \text{MeV}/c^2$ [34].

6.4.2.2 Combinatorial background

The combinatorial background is parameterised by a decreasing exponential function with slope parameter c,

$$f_{\text{comb}}(M; N_{comb}, c) = N_{\text{comb}} e^{Mc} \times |c|, \qquad (6.8)$$

where N_{comb} is the number of combinatorial background events. The value of the slope c is the same for all event categories, and the numbers of combinatorial background candidates are constrained to be equal between B and $\overline{B}$. This model is exactly the same as the one used in Section 5.5.2.2.

6.4.2.3 Low mass background from partially reconstructed $B^0 \to D^* K^{*0}$ decays

This category of background is due to $B_{(s)}^0$ decaying to $B^0 \to D^* K^{*0}$ or $\overline{B}_s^0 \to D^* K^{*0}$, where D^* denotes either a D^{*0} or a $\overline{D}^{*0}$, with $D^{*0} \to D^0 \gamma$ or $D^{*0} \to D^0 \pi^0$, and reconstructed as $B^0 \to D K^{*0}$ or $\overline{B}_s^0 \to D K^{*0}$. Because of the missing soft γ or π^0 momentum, the invariant mass of such candidates peaks at values below the nominal B^0 and B_s^0 masses. This component is significantly better modelled in this analysis with respect to that described in Section 5.5.2.3.

Total angular momentum conservation in $B^0 \to D^* K^{*0}$ or $\overline{B}_s^0 \to D^* K^{*0}$, which are decays of a pseudo-scalar particle into two vector particles, implies three non zero (but unknown) helicity amplitudes:

- $\mathcal{A}_{001}$, the amplitude for the decay where the D^{*0} is produced in helicity state -1 and the K^{*0} in helicity state $+1$ (configuration "001", $\lambda(D^{*0}) = -1$, $\lambda(K^{*0}) = +1$).

- $\mathcal{A}_{010}$, the amplitude for the decay where the D^{*0} is produced in helicity state 0 and the K^{*0} in helicity state 0 (configuration "010", $\lambda(D^{*0}) = 0$, $\lambda(K^{*0}) = 0$).

- $\mathcal{A}_{100}$, the amplitude for the decay where the D^{*0} is produced in helicity state $+1$ and the K^{*0} in helicity state -1 (configuration "100", $\lambda(D^{*0}) = +1$, $\lambda(K^{*0}) = -1$).

---

[8]This term is only present in the Opposite Sign categories.

[9]It was checked that this is justified on Monte Carlo simulation samples: the core resolution for both signal $B^0 \to [K^\mp \pi^\pm]_D K^{*0}$ and signal $\overline{B}_s^0 \to [K^\mp \pi^\pm]_D K^{*0}$ is $(10.8 \pm 0.2) \, \text{MeV}/c^2$.

6. MEASUREMENT OF CP OBSERVABLES IN $\overline{B}^0 \to D\overline{K}^{*0}$ WITH $D \to K^+\pi^-$

The DK^{*0} invariant mass depends on only one angle θ', which is the angle between the D momentum direction in the D^* rest frame, and the D^* momentum direction in the B rest frame. The distribution of this angle is given for $D^{*0} \to D^0\pi^0$ decays by [91,92]

$$I(\theta') \propto \frac{1}{2}\left|\mathcal{A}_{001}\right|^2 \sin^2\theta' + \left|\mathcal{A}_{010}\right|^2 \cos^2\theta' + \frac{1}{2}\left|\mathcal{A}_{100}\right|^2 \sin^2\theta' \tag{6.9}$$

and for $D^{*0} \to D^0\gamma$ decays

$$I(\theta') \propto \frac{1}{2}\left|\mathcal{A}_{001}\right|^2\left(1 + \cos^2\theta'\right) + \left|\mathcal{A}_{010}\right|^2 \sin^2\theta' + \frac{1}{2}\left|\mathcal{A}_{100}\right|^2\left(1 + \cos^2\theta'\right). \tag{6.10}$$

Each helicity configuration results in different shapes of the reconstructed $B^0 \to DK^{*0}$ or $\overline{B}_s^0 \to DK^{*0}$ mass, and the shape for the $D^{*0} \to D^0\gamma$ decay is also different from the shape for the $D^{*0} \to D^0\pi^0$ decay. However, these equations state in the two cases that the "001" component should be indistinguishable from the "100" component, as they both follow the same distribution. Figure 6.12 shows the invariant mass distributions obtained with fully simulated events generated in the configurations "001" and "010", and selected by the analysis selection, for the $D^{*0} \to D^0\gamma$ decay in the left panels and $D^{*0} \to D^0\pi^0$ in the right panels.

A comment should be made at this point for the reader comparing these results to those described in Chapter 5 (*c.f.* Section 5.5.2.3). One should note that Figure 5.10 shows different shapes for the "001" and "100" configurations of the $D^{*0} \to D^0\gamma$ decay, which is not compatible with what is displayed in Equation (6.10). This was found to be due to a bug in the EvtGen package [76] used in the LHCb simulation (*c.f.* Section 3.4), where some total angular momentum possibilities for the particles were missing. This bug was discovered late in the publication procedure of this analysis. It was corrected in subsequent simulation productions, but at the moment of the publication of the results in [64] it was not possible to check the real impact of this bug in the results. Nevertheless, simpler tests have been performed, for example forcing the model to fit the same yields in the "001" and the "100" configurations, that gave compatible results with the one published.

The function describing this background category is thus chosen, without interference between the different helicity configurations, as

$$f_{\rm pb}(M; N_{\rm pb}^{\overline{B}_s^0}, N_{\rm pb}^{B^0}) = N_{\rm pb}^{\overline{B}_s^0}\left\{\alpha_{010}\left[\frac{G_{010}}{G_{010} + P_{010}}f_{010}^{\gamma}(M) + \frac{P_{010}}{G_{010} + P_{010}}f_{010}^{\pi^0}(M)\right] + \right.$$

$$\left. (1 - \alpha_{010})\left[\frac{G_{001}}{G_{001} + P_{001}}f_{001}^{\gamma}(M) + \frac{P_{001}}{G_{001} + P_{001}}f_{001}^{\pi^0}(M)\right]\right\} + $$

$$N_{\rm pb}^{B^0}\left\{\beta_{010}\left[\frac{G_{010}}{G_{010} + P_{010}}f_{010}^{\gamma}(M - \Delta M) + \frac{P_{010}}{G_{010} + P_{010}}f_{010}^{\pi^0}(M - \Delta M)\right] + \right.$$

$$\left. (1 - \beta_{010})\left[\frac{G_{001}}{G_{001} + P_{001}}f_{001}^{\gamma}(M - \Delta M) + \frac{P_{001}}{G_{001} + P_{001}}f_{001}^{\pi^0}(M - \Delta M)\right]\right\}. \tag{6.11}$$

$N_{\rm pb}^{B^0}$ and $N_{\rm pb}^{\overline{B}_s^0}$ are the numbers of partially reconstructed background events from the $B^0 \to D^*K^{*0}$ and $\overline{B}_s^0 \to D^*K^{*0}$ contributions respectively. In this function, f_X^{γ} and $f_X^{\pi^0}$ are non-parametric functions reproducing the mass distribution of fully simulated $\overline{B}_s^0 \to D^*K^{*0}$ events[10],

---

[10]These non-parametric functions are implemented using the "RooKeysPdf" class from the RooFit package in ROOT. It provides a one-dimensional estimation which models the distribution of an arbitrary input data set, by superposing Gaussian functions.
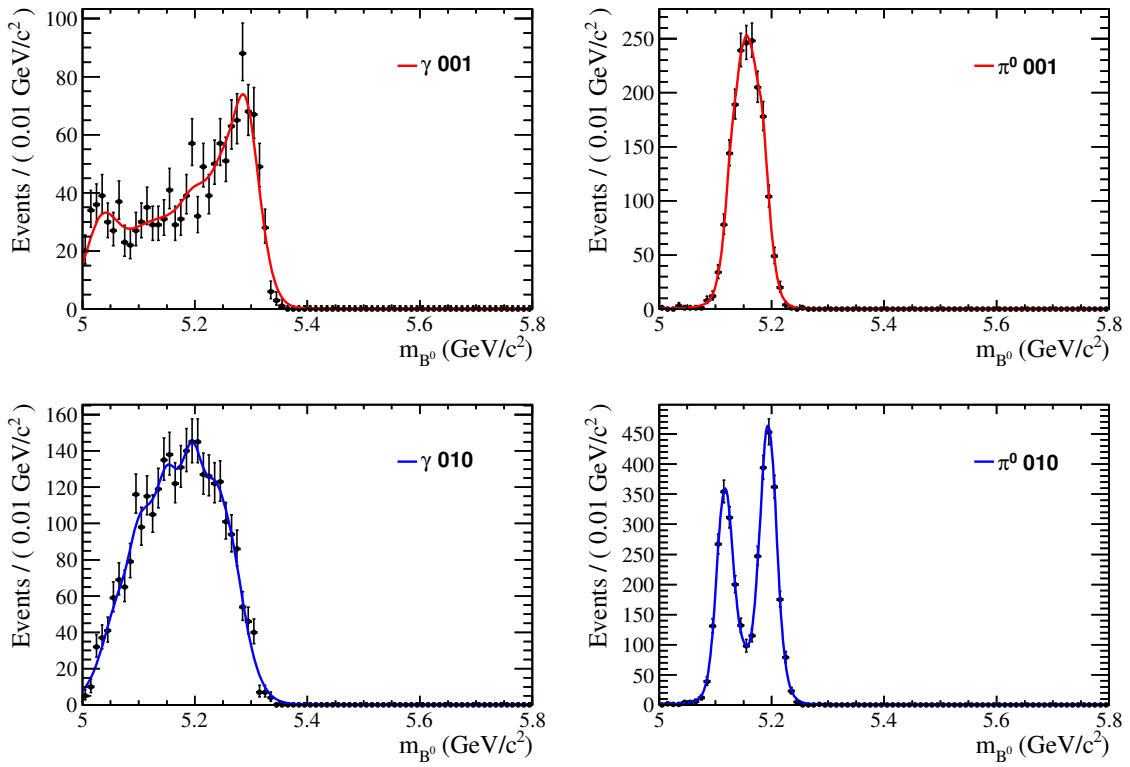
Figure 6.12: $\overline{B}_s^0 \to DK^{*0}$ invariant mass distributions for fully simulated $\overline{B}_s^0 \to D^*K^{*0}$ decays selected by the analysis selection with $D^{*0} \to D^0\gamma$ (left) and $D^{*0} \to D^0\pi^0$ (right) and $D \to K^-\pi^+$ in the "001" configuration (top) and "010" configuration (bottom). The superimposed curves are non-parametric PDFs describing the distributions.

Quantity	$D^{*0} \to D^0\pi^0$	$D^{*0} \to D^0\gamma$
Branching fraction	62 %	38 %
ϵ_acc	16 %	16 %
$\epsilon_\mathrm{sel}^{001}$	0.337 %	0.268 %
$\epsilon_\mathrm{sel}^{010}$	0.643 %	0.532 %

Table 6.4: *Branching fractions and efficiencies of the $B_s^0 \to D^*K^{*0}$ modes, with $D \to K^\mp\pi^\pm$.*

with $D^{*0} \to D^0\gamma$ and $D^{*0} \to D^0\pi^0$ respectively and D^0 decaying to $K^\mp\pi^\pm$ Opposite Sign mode, and generated in the configuration "X" ("001" or "010"), reconstructed as $\overline{B}_s^0 \to DK^{*0}$. These functions are the ones superimposed on the invariant mass distributions shown in Figure 6.12. The mass distributions obtained from the Monte Carlo simulation are smeared and shifted to take into account the different mass resolutions of the data[11], $\sigma = 12.9\,\mathrm{MeV}/c^2$ and of the simulation $\sigma = 10.8\,\mathrm{MeV}/c^2$, and the different mean values of the B^0 peaks, $M = 5\,282.1\,\mathrm{MeV}/c^2$ for the data and $M = 5\,279.3\,\mathrm{MeV}/c^2$ for the simulation.

The G_X and P_X factors in Equation (6.11) are the products of the branching fraction of $D^{*0} \to D^0\gamma$ or $D^{*0} \to D^0\pi^0$ decays respectively and of the corresponding efficiency factors in order to correctly normalise the different helicity amplitudes contributions,

$$G_X = \mathcal{B}(D^{*0} \to D^0\gamma)\,\epsilon_\mathrm{acc}(D^0\gamma)\,\epsilon_\mathrm{sel}^X(D^0\gamma) \text{ and} \tag{6.12}$$

$$P_X = \mathcal{B}(D^{*0} \to D^0\pi^0)\,\epsilon_\mathrm{acc}(D^0\pi^0)\,\epsilon_\mathrm{sel}^X(D^0\pi^0), \tag{6.13}$$

where ϵ_acc and ϵ_sel are the geometrical acceptance and the selection efficiency, respectively, both computed from fully simulated events for each configuration. Table 6.4 shows the value of each one of the factors entering this computation. The geometrical acceptance is computed as the number of events with all the final tracks inside the detector acceptance, over the total number of simulated events. The selection efficiency is computed as the number of events remaining after all selection cuts, over the number of simulated events with all the tracks inside the acceptance.

The same functions $f_X^{\pi^0}$ and f_X^γ are used to fit all categories, as well as the values of the parameters α_{010} and β_{010}, that give the relative normalisation between the different helicity configurations, are common to all of them. These parameters are left free in the fit.

The yields of partially reconstructed candidates for the $\overline{B}_s^0$ background are constrained to the same value for the B and $\overline{B}$ categories. The same constraint is applied to the yields of partially reconstructed candidates for the B^0 background in the $D \to K^\mp\pi^\pm$ Same Sign category, where the CP violation effects are expected to be negligible. However, this can not be done in the $D \to K^\mp\pi^\pm$ Opposite Sign category, because of the expected sizeable CP violation effects to which they are sensitive. Indeed, the $B^0 \to D^*K^{*0}$ decays happen through the interference between the $b \to u$ and $b \to c$ amplitudes, which follows the same pattern as that in $B^0 \to DK^{*0}$. The following yields of partially reconstructed background are left free in the fit: $N_\mathrm{pb}^{\overline{B}_s^0 + B_s^0\ (K\pi OS)}$, $N_\mathrm{pb}^{B^0 + \overline{B}^0\ (K\pi SS)}$, $N_\mathrm{pb}^{B^0\ (K\pi OS)}$, $N_\mathrm{pb}^{\overline{B}^0\ (K\pi OS)}$.

---

[11]This value of the mass resolution is found with a modified version of the fit, where B and $\overline{B}$ are not separated, and therefore is slightly different from the final value presented in Table 6.7.
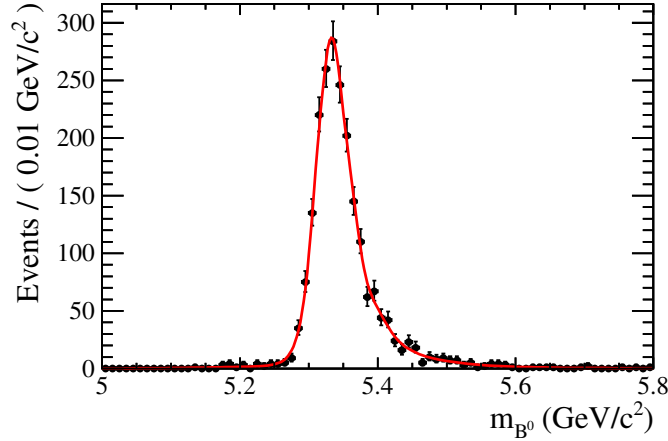
Figure 6.13: $B^0 \to DK^{*0}$ *invariant mass distribution for fully simulated* $B^0 \to D\rho^0$ *decays with* $D \to K^{\mp}\pi^{\pm}$, *selected by the analysis selection. The red line is the non-parametric function describing the distribution, used in the mass fit to model the cross-feed background component.*

6.4.2.4 Cross-feed background from $B^0 \to D\rho^0$

The last source of background considered is that due to $B^0 \to D\rho^0$ decays with $\rho^0 \to \pi^+\pi^-$, when one π from the ρ^0 is misidentified as a K and used to reconstruct the K^{*0} in the $B^0 \to DK^{*0}$ decay. The same procedure than the one in Section 5.5.2.4 is used here, updated to account for the larger data set and the new selection. The invariant mass shape of these events is modelled with a non-parametric PDF $f_\rho^{\text{cross-feed}}(M)$ extracted from $B^0 \to D\rho^0$ Monte Carlo simulated events, with a K mass hypothesis assigned to one of the π from the ρ^0, applying a selection as close as possible to the one used for $B^0 \to DK^{*0}$ events. The resulting distribution for the selection described in Section 6.2 is shown in Figure 6.13. It has also been smeared and shifted to account for the differences between data and simulation, using the same factors as in Section 6.4.2.3.

The function used to model this background category is

$$f_{\text{cross-feed}}(M; N_{\text{cross-feed}}) = N_{\text{cross-feed}} f_\rho^{\text{cross-feed}}(M). \tag{6.14}$$

The numbers of cross-feed candidates are constrained to be equal in the B and $\overline{B}$ candidates in the $D \to K^{\mp}\pi^{\pm}$ Opposite Sign and Same Sign categories,

$$N_{\text{cross-feed}}^{B\ (K\pi OS)} = N_{\text{cross-feed}}^{\overline{B}\ (K\pi OS)} = N_{\text{cross-feed}}^{B\ (K\pi SS)} = N_{\text{cross-feed}}^{\overline{B}\ (K\pi SS)}. \tag{6.15}$$

The expected value $N_{\text{cross-feed}}^{(K\pi)} = 187 \pm 3$ is constrained in the fit by means of a Gaussian, and is computed from:

- The number of signal $B^0 \to D\rho^0$, $D^0 \to K^-\pi^+$ candidates reconstructed in the same data sample. This number is extracted from a maximum likelihood fit to the $D\rho^0$ invariant mass distribution with a probability distribution function which is the sum of a double Gaussian representing the signal and an exponential function describing the background. The number of signal $D\rho^0$ candidates is equal to $N^{D\rho^0} = 10\,108 \pm 129$.

- The efficiency to reconstruct a $B^0 \to D\rho^0$, $D^0 \to K^-\pi^+$ signal candidate as a $B^0 \to DK^{*0}$, $D \to K^{\mp}\pi^{\pm}$ with the selection described above. This efficiency is computed from fully Monte Carlo simulation samples, using PID calibration tables for the PID efficiencies and mis-ID fractions, and is found to be equal to $\epsilon_{cross-feed} = (1.85 \pm 0.02)$ %.

6.4.3 Fit results

The total fit function is the sum of the individual PDFs described above, and all categories are fit simultaneously. The 18 free parameters are summarized in Tables 6.5 and 6.6. The result of the unbinned extended likelihood fit to the DK^{*0} invariant mass distributions of the B candidates in data is shown in Table 6.7 and Figures 6.14 and 6.15.

Group	Parameter	Description	Category
Signal	μ	Central value of the B^0 mass	Common to all
	σ	Core resolution for B^0 and $\overline{B}^0_s$	Common to all
	$N^{B^0\ (K\pi SS)}$	Number of B^0 signal candidates	$B\ (K\pi SS)$
	$N^{\overline{B}^0\ (K\pi SS)}$	Number of $\overline{B}^0$ signal candidates	$\overline{B}\ (K\pi SS)$
	$N^{B^0\ (K\pi OS)}$	Number of B^0 signal candidates	$B\ (K\pi OS)$
	$N^{\overline{B}^0\ (K\pi OS)}$	Number of $\overline{B}^0$ signal candidates	$\overline{B}\ (K\pi OS)$
	$N^{\overline{B}^0_s\ (K\pi OS)}$	Number of $\overline{B}^0_s$ signal candidates	$B\ (K\pi OS)$
	$N^{B^0_s\ (K\pi OS)}$	Number of B^0_s signal candidates	$\overline{B}\ (K\pi OS)$

Table 6.5: *Free fit parameters of the invariant mass distribution (signal).*

Group	Parameter	Description	Category
Combinatorial background	c	Exponential slope	Common to all
	$N_{\text{comb}}^{(K\pi SS)}$	N. combinatorial background candidates	$B + \overline{B}\ (K\pi SS)$
	$N_{\text{comb}}^{(K\pi OS)}$	N. combinatorial bkg. cand.	$B + \overline{B}\ (K\pi OS)$
Low mass background	α_{010}	Relative normalisation of the "010" helicity component in $\overline{B}_s^0 \to D^* K^{*0}$ and $B_s^0 \to D^* \overline{K}^{*0}$	Common to all
	β_{010}	Relative normalisation of the "010" helicity component in $B^0 \to D^* K^{*0}$ and $\overline{B}^0 \to D^* \overline{K}^{*0}$	Common to all
	$N_{\text{pb}}^{B^0 + \overline{B}^0\ (K\pi SS)}$	N. $B^0 \to D^* K^{*0}$ and $\overline{B}^0 \to D^* \overline{K}^{*0}$ cand.	$B + \overline{B}\ (K\pi SS)$
	$N_{\text{pb}}^{B^0\ (K\pi OS)}$	N. $B^0 \to D^* K^{*0}$ candidates	$B\ (K\pi OS)$
	$N_{\text{pb}}^{\overline{B}^0\ (K\pi OS)}$	N. $\overline{B}^0 \to D^* \overline{K}^{*0}$ candidates	$\overline{B}\ (K\pi OS)$
	$N_{\text{pb}}^{\overline{B}_s^0 + B_s^0\ (K\pi OS)}$	N. $\overline{B}_s^0 \to D^* K^{*0}$ and $B_s^0 \to D^* \overline{K}^{*0}$ cand.	$B + \overline{B}\ (K\pi OS)$
Cross-feed	$N_{\text{cross}-\text{feed}}^{B^0 + \overline{B}^0\ (K\pi SS + OS)}$	N. $B^0 \to D\rho^0$ candidates	$B + \overline{B}\ (K\pi SS + OS)$

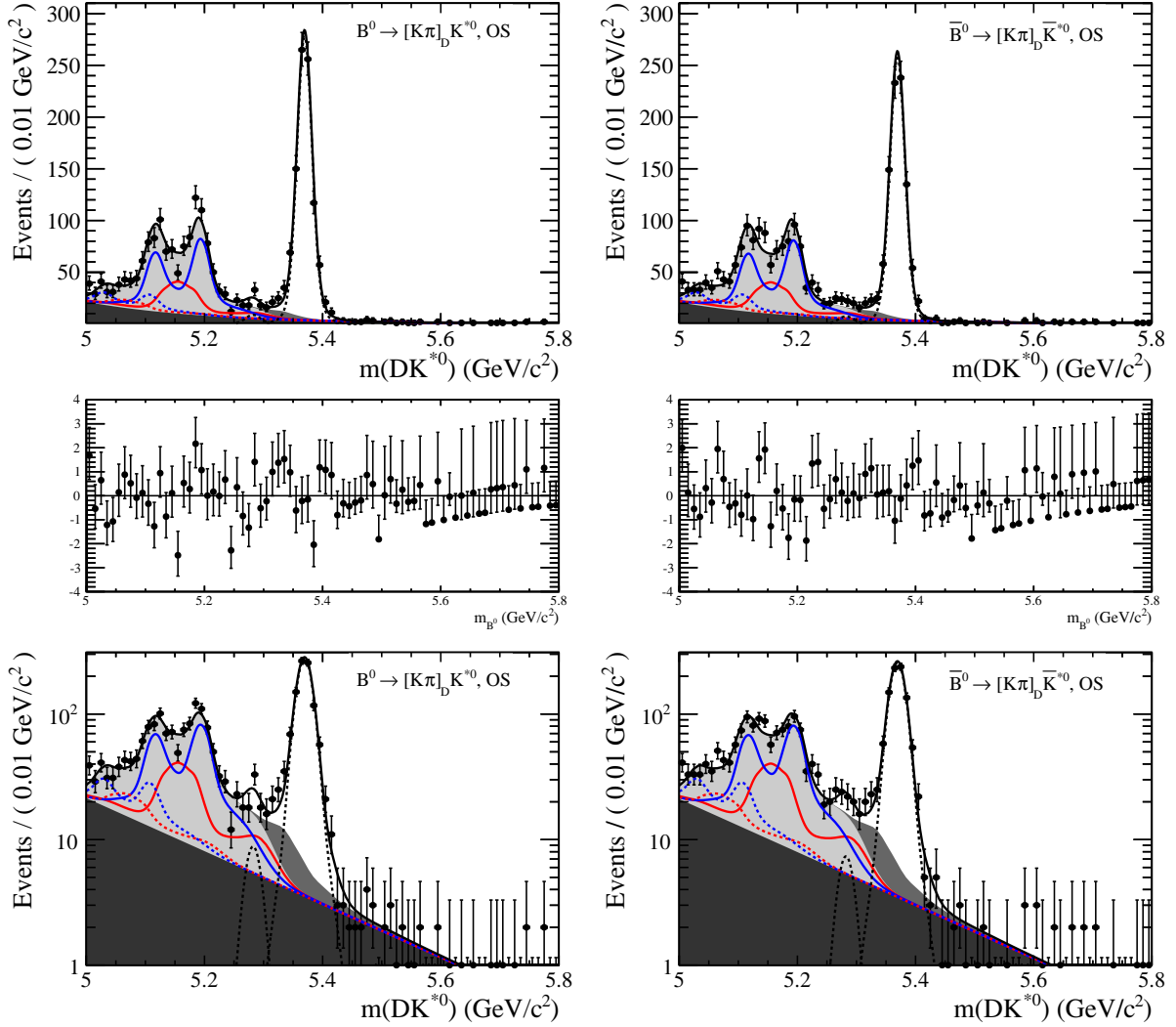Table 6.6: *Free fit parameters of the invariant mass distribution (background).*

Figure 6.14: *Invariant mass distributions of the Opposite Sign $[K^-\pi^+]_D K^{*0}$ category (left), corresponding to B^0 and $\overline{B}^0_s$ candidates, and $[K^+\pi^-]_D \overline{K}^{*0}$ (right), corresponding to $\overline{B}^0$ and B^0_s candidates. The bottom plots are as the top ones, but using a logarithmic scale instead of a linear one. The black points are the data, while the solid black line represents the result of the fit. The different contributions are visible: the signal peak is indicated by a dashed black line, while the different grey areas correspond to the different backgrounds which are, from darkest to lightest, combinatorial, cross-feed from $B^0, \overline{B}^0 \to D\rho^0$, and low-mass from partially reconstructed $B^0, \overline{B}^0_s \to D^*K^{*0}$ and $\overline{B}^0, B^0_s \to D^*\overline{K}^{*0}$. The coloured lines represent the different helicities amplitudes contributing to the low-mass background: red is "001" and blue is "010"; solid lines correspond to the B^0_s low-mass background, dashed lines to the B^0. The middle histograms are the differences between the value of the bin in the data histogram distribution and the value of the fit function in the center of the same bin, divided by the uncertainty on the number of entries in that bin. The bottom histograms provide a logarithmic scale for the vertical axis.*
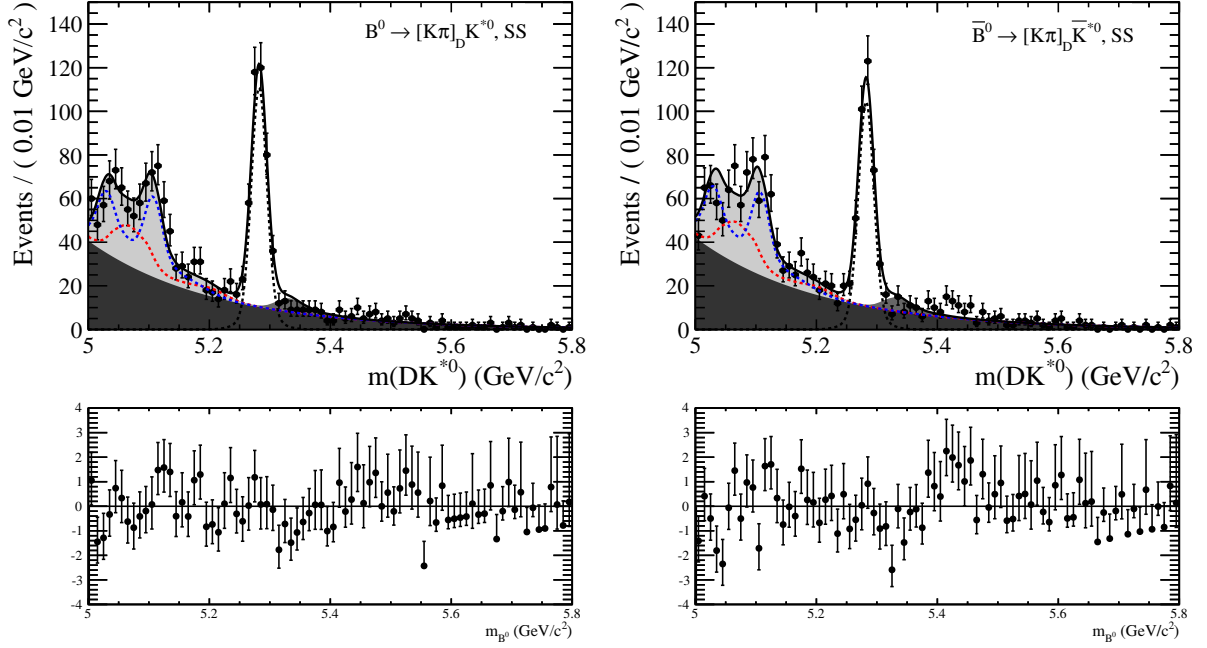
Figure 6.15: *Invariant mass distributions of the Same Sign $[K^+\pi^-]_D K^{*0}$ category (left), corresponding to B^0 and $\overline{B}^0_s$ candidates, and $[K^-\pi^+]_D \overline{K}^{*0}$ (right), corresponding to $\overline{B}^0$ and B^0_s candidates. The different contributions are represented as in Figure 5.12.*

Signal Parameters	Result	Background Par.	Result
μ	$(5282.2 \pm 0.3)\,\mathrm{MeV}/c^2$	c	$(-4.9 \pm 0.2)\,\mathrm{GeV}^{-1}c^2$
σ	$(12.5 \pm 0.3)\,\mathrm{MeV}/c^2$	$N^{(K\pi SS)}_{\mathrm{comb}}$	1669^{+92}_{-90}
$N^{B^0\ (K\pi SS)}$	381^{+22}_{-21}	$N^{(K\pi OS)}_{\mathrm{comb}}$	854^{+91}_{-87}
$N^{\overline{B}^0\ (K\pi SS)}$	346^{+21}_{-20}	α_{010}	0.70 ± 0.04
$N^{B^0\ (K\pi OS)}$	29 ± 11	β_{010}	0.66 ± 0.06
$N^{\overline{B}^0\ (K\pi OS)}$	25 ± 11	$N^{B^0+\overline{B}^0\ (K\pi SS)}_{\mathrm{pb}}$	1024 ± 80
$N^{\overline{B}^0_s\ (K\pi OS)}$	925^{+32}_{-31}	$N^{B^0\ (K\pi OS)}_{\mathrm{pb}}$	212 ± 42
$N^{B^0_s\ (K\pi OS)}$	873^{+31}_{-30}	$N^{\overline{B}^0\ (K\pi OS)}_{\mathrm{pb}}$	220 ± 43
		$N^{\overline{B}^0_s+B^0_s\ (K\pi OS)}_{\mathrm{pb}}$	1953 ± 61
		$N^{(K\pi)}_{\mathrm{cross-feed}}$	187 ± 2

Table 6.7: *Fit result on the floating parameters.*

6.5 Results

The four observables outlined in Section 6.1 are computed from the yields resulting from the fit, using the following relations,

$$A_d^{sup} = \frac{a_{\mathrm{prod}}^d \, \hat{\epsilon}_{\mathrm{L0}}^{K\pi} \, \hat{\epsilon}_{\mathrm{PID}}^{K\pi} \, N^{\overline{B}^0 \ (K\pi OS)} - N^{B^0 \ (K\pi OS)}}{a_{\mathrm{prod}}^d \, \hat{\epsilon}_{\mathrm{L0}}^{K\pi} \, \hat{\epsilon}_{\mathrm{PID}}^{K\pi} \, N^{\overline{B}^0 \ (K\pi OS)} + N^{B^0 \ (K\pi OS)}}, \tag{6.16}$$

$$A_s = \frac{a_{\mathrm{prod}}^s \, \hat{\epsilon}_{\mathrm{L0}}^{K\pi} \, \hat{\epsilon}_{\mathrm{PID}}^{K\pi} \, N^{B_s^0 \ (K\pi OS)} - N^{\overline{B}_s^0 \ (K\pi OS)}}{a_{\mathrm{prod}}^s \, \hat{\epsilon}_{\mathrm{L0}}^{KK} \, \hat{\epsilon}_{\mathrm{PID}}^{K\pi} \, N^{B_s^0 \ (K\pi OS)} + N^{\overline{B}_s^0 \ (K\pi OS)}}, \tag{6.17}$$

$$A_d^{\mathrm{fav}} = \frac{a_{\mathrm{prod}}^d \, \hat{\epsilon}_{\mathrm{L0}}^{K\pi} \, \hat{\epsilon}_{\mathrm{PID}}^{K\pi} \, N^{\overline{B}^0 \ (K\pi SS)} - N^{B^0 \ (K\pi SS)}}{a_{\mathrm{prod}}^d \, \hat{\epsilon}_{\mathrm{L0}}^{K\pi} \, \hat{\epsilon}_{\mathrm{PID}}^{K\pi} \, N^{\overline{B}^0 \ (K\pi SS)} + N^{B^0 \ (K\pi SS)}}, \tag{6.18}$$

$$R_d^{K\pi} = \frac{a_{\mathrm{prod}}^d \, \hat{\epsilon}_{\mathrm{L0}}^{K\pi} \, \hat{\epsilon}_{\mathrm{PID}}^{K\pi} \, N^{\overline{B}^0 \ (K\pi OS)} + N^{B^0 \ (K\pi OS)}}{a_{\mathrm{prod}}^d \, \hat{\epsilon}_{\mathrm{L0}}^{K\pi} \, \hat{\epsilon}_{\mathrm{PID}}^{K\pi} \, N^{\overline{B}^0 \ (K\pi SS)} + N^{B^0 \ (K\pi SS)}} . \tag{6.19}$$

The correction factors appearing in these equations are:

- $a_{\mathrm{prod}}^d = \frac{1-\kappa A_{\mathrm{prod}}}{1+\kappa A_{\mathrm{prod}}} = 0.991 \pm 0.012$, the correction for production asymmetry of B^0 with respect to $\overline{B}^0$, with $\kappa = 0.456 \pm 0.011$ and $A_{\mathrm{prod}} = 0.010 \pm 0.013$;

- $a_{\mathrm{prod}}^s = 1$, the correction for production asymmetry of B_s^0 with respect to $\overline{B}_s^0$;

- $\hat{\epsilon}_{\mathrm{L0}}^{K\pi} = 1$, the ratio of the L0 trigger efficiency for B^0 to the efficiency for $\overline{B}^0$;

- $\hat{\epsilon}_{\mathrm{PID}}^{K\pi} = 0.98421 \pm 0.00010 \pm 0.01553$, the ratio of the PID efficiency for B^0 to the efficiency for $\overline{B}^0$,

where the same values as those used for the $D \to K^{\mp}\pi^{\pm}$ in the analysis for the measurement of the GLW observables presented in Chapter 5 are used (*c.f.* Section 5.6). The results presented here are thus only preliminary, as a rigorous result requires an update of the efficiencies by applying the corresponding efficiency computation methods to the 2012 data set and the 2012 simulation[12].

The preliminary measurement of the CP observables give

$$A_d^{sup} = -0.094 \, {}^{+0.303}_{-0.318}, \tag{6.20}$$

$$A_s = -0.037 \pm 0.025, \tag{6.21}$$

$$A_d^{\mathrm{fav}} = -0.060 \pm 0.042, \tag{6.22}$$

$$R_d = 0.075 \, {}^{+0.023}_{-0.022}, \tag{6.23}$$

where the only quoted uncertainty is statistical and takes into accout the correlation between the different fit parameters. This uncertitude is still large, and the CP violation effects are still difficult to observe.

---

[12]Not available yet at the time when this results were obtained.

Conclusion

The γ angle of the Unitary Triangle of the CKM mechanism is one of the parameters of the Standard Model of particles physics which is still known with a large uncertainty. The study of the Unitary Triangle involves b-physics, and in particular the γ measurements are performed by looking at B hadron decays. Precision measurements in this sector need to be made, in order to further constrain the γ angle and the CKM Unitary Triangle, which allows to test the consistency of the Standard Model. Efficient and reliable detectors are needed, and LHCb is especially designed for heavy flavour physics. A precise measurement of γ is one of its main purposes. LHCb has collected over 3 fb^{-1} of proton-proton collision data at 7 TeV and 8 TeV between 2011 and 2012. With this first data set, and among many other achievements, the CP observables for different B decay modes are already measured.

This thesis has presented the analysis of the $\overline{B}^0 \to D\overline{K}^{*0}$ decay channel, which is sensitive to the γ angle through the interference of $b \to u$ and $b \to c$ amplitudes, where only tree diagrams are involved. Both transitions are colour-suppressed, which enhances the interference by a factor of 3 with respect to $B^- \to DK^-$, although on the other hand the branching ratios are smaller. First, 1 fb^{-1} of LHCb data collected in 2011 are analysed using the CP-even final state $D \to K^+K^-$, that is to say the GLW approach is considered. The CP observables in the $\overline{B}^0 \to [K^+K^-]_D\overline{K}^{*0}(K^-\pi^+)$ channel are measured to be

$$A_d^{KK} = -0.452 \ ^{+0.228}_{-0.230} \pm 0.025 = A_{CP+},$$
$$R_d^{KK} = \ \ 1.360 \ ^{+0.366}_{-0.319} \pm 0.075 = R_{CP+},$$

where the favoured $\overline{B}^0 \to [K^-\pi^+]_D\overline{K}^{*0}(K^-\pi^+)$ mode is used as normalisation channel, which is not sensitive to sizeable CP violation effects.

The complete 3 fb^{-1} data set is analysed using the quasi-specific final state $D \to K^\mp\pi^\pm$, corresponding to the ADS approach. A preliminary measurement of the CP observables of the suppressed $\overline{B}^0 \to [K^+\pi^-]_D\overline{K}^{*0}(K^-\pi^+)$ decay mode with respect to the favoured $\overline{B}^0 \to [K^-\pi^+]_D\overline{K}^{*0}(K^-\pi^+)$ is performed,

$$A_d^{sup} = -0.094 \ ^{+0.303}_{-0.318} = A_{ADS},$$
$$R_d = \ \ 0.075 \ ^{+0.023}_{-0.022} = R_{ADS}.$$

These are the first measurements of the ADS and GLW CP asymmetries on the $\overline{B}^0 \to D\overline{K}^{*0}$ decay channel. The uncertainty on these results is still large, and a precise measurement of these quantities needs a larger data set. With the approximately 50 fb^{-1} of data that the LHCb experiment expects to collect, at the nominal LHC collision energy and during the upgrade phase of the experiment, these CP observables will be measured accurately, and the results will introduce new constrains for a precise direct measurement of the γ angle.

Appendix A

Calorimeter simulation calibration

The calibration of the calorimeter response in the LHCb simulation is an additional task performed as part of this thesis. This work is summarised in this Appendix.

LHCb follows the common practise in particle physics experiments of using Monte Carlo simulation, as a tool for physics analysis on real data. The simulation reproduces the physics processes and the detector response, making use of the current knowledge in particle physics and the interactions of particles with matter. Specific software exist in LHCb for simulation production (*c.f.* Section 3.4).

Regarding the calorimeters, the key quantity needed in the simulation to reproduce their performance is the so-called "Active/Total" ratio. It is defined as the quotient between the total energy actually carried by the particles and the active energy in the calorimeters, which is the visible energy that they see in the scintillators,

$$r = \frac{E^{total}}{E^{active}}. \tag{A.1}$$

This ratio, which is calculated from simulation, allows to make the conversion between simulated energy and visible energy from the calorimeters response. Assuming that the simulation is accurate, the Active/Total ratio is the same in simulation than in real data. This ratio is then used as a calibration factor in real data, with the particularity that an additional cell-by-cell calibration factor needs to be included. The total energy is then reconstructed as

$$E_{data}^{total} = E_{data}^{active} \times r \times r^{fine}, \tag{A.2}$$

where r is the Active/Total ratio from simulation, r^{fine} is the additional cell-by-cell calibration factor, and we assume that the calorimeter photomultiplier gains are set in such a way that $E_{data}^{active} = E_{simulation}^{active}$. The cell-by-cell calibration factor r^{fine} is computed using radioactive sources, namely a ^{137}Cs gamma source for the HCAL, and a LED calibration system for both the ECAL and HCAL.

New simulation productions are done every year to provide the Collaboration with simulation samples that reproduce as accurately as possible the real data, considering the detector operation conditions of each period of data taking. The simulation calibration factors need to be updated with each new software version.

To compute the Active/Total ratio r, special simulation data sets are produced. They are called "particle guns", and contain charged pions (as hadronic particles) or photons (as electromagnetic particles) generated with a fixed energy and which are sent to a predefined point on the calorimeter, in order to study its response. Nothing else is generated in the event. Only the calorimeter geometry is taken into account in the simulation, but not the magnetic field (so
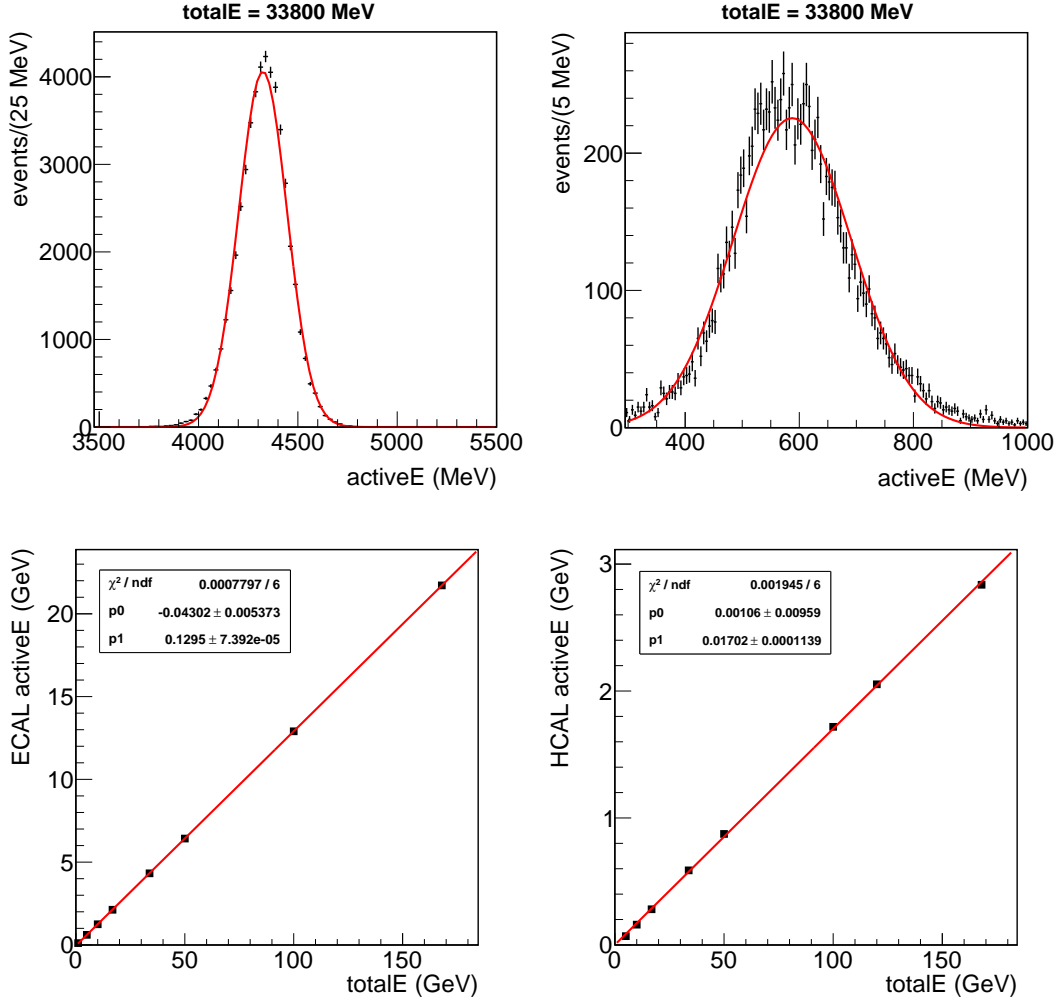
Figure A.1: *Top: distribution of the active energy E^{active} seen by the calorimeters for particles generated with a total energy of 33.8 GeV, for photons on the left and for charged pions on the right. Bottom: linear fit to the pairs (E^{total}, E^{active}) for all the generated values of total energy E^{total}, for the ECAL (photons) on the left and HCAL (pions) on the right. The inverse of the fitted slope is the Active/Total calibration ratio. All these plots correspond to the 2010 simulation configuration.*

year / configuration	r^{ECAL}	r^{HCAL}
2010	7.75	58.8
2011 / "no cuts"	7.73	59.2
2011 / "LHCb"	9.03	63.17

Table A.1: *Active/Total calibration ratios for 2010 and two different 2011 simulation configurations.*
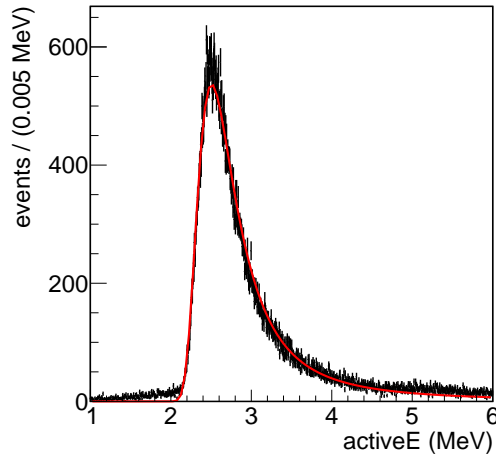
Figure A.2: *Distribution of the active energy deposited by simulated pions on the PreShower detector, showing the Minimum Ionisation Particle peak, corresponding to the 2010 simulation configuration.*

the tracks are not bent). The fixed energy with which these particles are generated is the total energy E^{total}. The values used for the energy of the particle guns are 1 GeV, 5 GeV, 10 GeV, 16.8 GeV, 33.8 GeV, 50 GeV, 100 GeV, 120 GeV and 168 GeV.

For each particle gun, the visible or active energy seen by the calorimeters is retrieved. In the case of pions, which are used to study the hadronic calorimeter HCAL, it is required that very little energy is deposited in the electromagnetic calorimeter ECAL, more precisely less than 100 MeV; in the case of photons, which are used to study the ECAL, it is required that they deposit less than 100 MeV in the HCAL. This is done in order to be able to assume, with a very small error, that all of the energy of the particles is deposited in the calorimeter under study.

For each value of total energy of the particle guns, a fit to the active energy distribution in the concerned calorimeter is performed, using a Gaussian function. Pairs of values are extracted by taking each total energy value and the fitted mean value of the active energy distribution. The curve defined by these pairs is again fitted with a first order polynomial: the y-intercept should be compatible with 0, and the slope is the inverse of the Active/Total ratio r.

The results corresponding to 2010 Monte Carlo simulation are shown in Figure A.1. The E^{active} distributions and the Gaussian fit for the particle guns corresponding to 33.8 GeV are shown in the top panels of the figure, for photons on the left and pions on the right. The linear fits to the pairs (E^{total}, E^{active}) are shown in the bottom panels.

The Active/Total ratios for ECAL and HCAL for 2010 simulation, which correspond to the inverse of the fitted slope in the bottom plots of Figure A.1, are shown in the first row of Table A.1. These results represent a 28 % variation for the ECAL and 58 % for the HCAL with respect to 2008 simulation, that used the previous version of the Geant4 package; the 2010 results are compatible with 2004 and 2006 simulation. Changes in the Geant4 package translate into a different detector response in simulation, which is the reason why the Active/Total ratio needs to be recomputed when new versions of the software are released.

Concerning the PreShower detector (*c.f.* Section 3.2.4), the quantity that is needed in the simulation is the Minimun Ionising Particle (MIP) energy. Electromagnetic particles crossing the calorimeters start developing their shower in the PreShower, while hadrons do it later. That is to say, a hadron only leaves a MIP deposit in this subdetector.

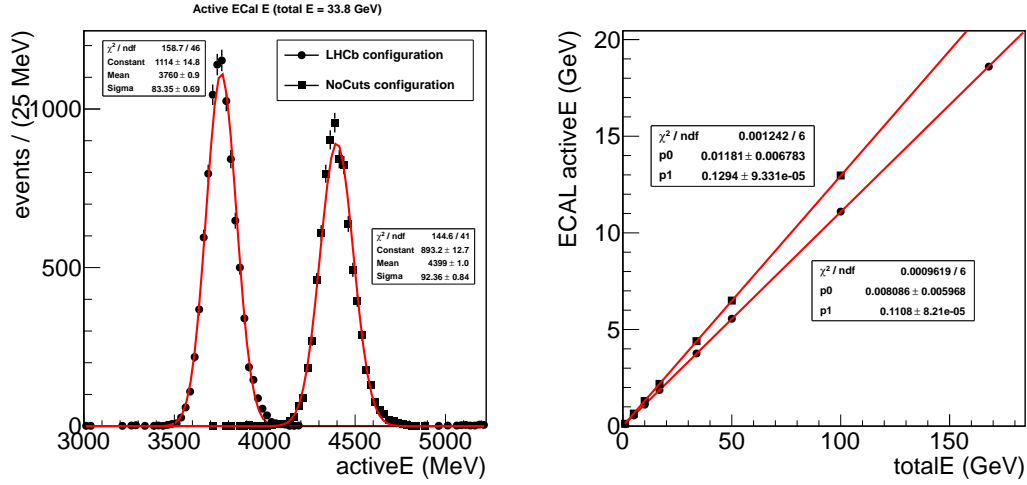The same pion particle guns used to study the HCAL response are taken to measure the

Figure A.3: *Left: distribution of the active energy E^{active} seen by the ECAL for photons generated with a total energy of 33.8 GeV. Bottom: linear fit to the pairs (E^{total}, E^{active}) for the generated values of total energy E^{total}. The circles correspond to the "LHCb" 2011 configuration, while the squares correspond to the "no cuts" 2011 configuration.*

MIP energy. The requirement on the energy deposit on the ECAL to be smaller than 100 MeV is kept. The distribution of the active energy seen by the PreShower for all the pion guns is shown in Figure A.2. A fit is performed using a Landau function, and a value of 2.54 MeV/MIP is found, to be used for the simulation calibration.

In 2011 simulation two configurations were tested: the "no cuts" configuration, aiming at reproducing the 2010 one, and the "LHCb" configuration, that was suggested for a better description of multiple scattering processes. In order to choose between one or the other, or even a combination of the two, the Active/Total ratios and the MIP peak were studied for both cases. The ECAL results are shown in Figure A.3, for photon guns of both configurations.

The second and third rows of Table A.1 show the Active/Total ratios for the two 2011 configurations. While the "no cuts" configuration reproduces well the Active/Total ratios of 2010 simulation, the "LHCb" configuration introduces a 17 % variation for the ECAL and 7 % for the HCAL. The position of the MIP peak does not change with respect to 2010 simulation.

The "LHCb" configuration was chosen in the end, as it performed faster than the "no cuts" one[1]. The impact of the variation of the Active/Total ratio when used in real data is small, and can be corrected by an additional factor to be absorbed by the cell-by-cell calibration.

---

[1]The "LHCb" configuration had some preselection to remove low energy tracks that was not present in the "no cuts" configuration. This preselection reduces the number of events to run on, resulting in a faster execution, which is an important issue in simulation production.

Acknowledgements

Tout d'abord, j'aimerais remercier Achille Stocchi, directeur du Laboratoire de l'Accélérateur Linéaire, et Guy Wormser, ancien directeur, pour m'avoir permis de faire cette thèse au LAL. Ce n'est pas la seule raison que j'ai pour remercier Achille. Merci de m'avoir accepté au Master NPAC à mon arrivée en France, et de m'avoir donné l'opportunité de faire mon premier stage dans le groupe LHCb en 2009. Merci pour tes bons conseils en fin de thèse, merci de m'avoir écouté et d'avoir accepté faire partie de mon jury. Merci aussi à toi et à Fabien Cavalier de m'avoir fait confiance comme représentante des étudiants au Conseil du Laboratoire.

Thanks to Jonas Rademacker and merci to Jean-Pierre Lees for having accepted the task of being my referees. I appreciate your effort of reading my thesis in such detail and giving me such interesting and useful comments. Merci also to Jean Orloff and gracias to Fernando Martínez Vidal for accepting being a part of the jury. I hope you did enjoy this thesis.

Un grand merci à Patrick Robbe, mon directeur de thèse. Tu as toujours été là pour moi pour m'encadrer comme il faut depuis mon stage jusqu'à la fin de ma thèse, tu as toujours été disponible au labo ou par mail, toujours été là pour répondre à mes questions, résoudre mes problèmes de code et corriger mes typos dans toutes les langues possibles ! Merci de m'avoir encouragé à faire de présentations devant la collaboration et à participer à des conférences. Tu as vraiment été un directeur de thèse excellent, j'ai beaucoup apprécié travailler avec toi, et j'espère avoir été à la hauteur de tes attentes. Encore un grand merci à Marie-Hélène Schune, pour m'avoir accueillie au sein de ce groupe trop bien qui est LHCb. J'admire vraiment ton travail comme directrice du groupe, ainsi que ta capacité à faire tout ce que tu fais et malgré tout d'avoir le temps de t'assurer que tout se passe bien pour tout le monde. C'était aussi un plaisir de travailler avec toi sur cette analyse. Vous deux, Marie-Hélène et Patrick, avez été formidables. Je vous remercie aussi tous les deux pour vos conseils sur le plan personnel et sur mon futur. Sachez que mon choix n'a rien à voir avec la qualité de votre encadrement et de mon sujet : ils auraient très difficilement pu être mieux !

Merci à tous les autres membres du groupe, présents et passés. Danke schön Claire, little bunny, for bearing my angry talking against my computer in the office, for tea time, for laughing at my jokes on your healthy diet, and for being so lovely indeed. Thanks (sorry, I don't know how to write it in Russian) to Olga, you also lovely girl, for all the existential conversations. We did a lot of talking in these two years and I really appreciate you. Thanks to Michelle, you M, now that you are gone my English level has gone much worse and you know it. It was great to have you around and very sad to see you go, but it is so wonderful that you come for my defence! Long life to the party lamps, parties at R1, and "quiero un menúuu" ;) Merci à Aurélien pour me donner les bases pour l'analyse $B^0 \to DK^{*0}$, et d'avoir si bien écrit ta thèse, qui m'a été d'une grande aide ! Merci Alexis, pour occuper si bien le poste de "l'étudiant français" du groupe après Aurélien. Sans vos ragots, ce serait beaucoup moins drôle ! Grazie Martino, mangiare !, de m'avoir fait découvrir de Inkscape. Thanks (same problem of lack of Ukrainian knowledge) to Maksym for your peaceful presence around. Merci à Yasmine ! J'ai vu la fin de ta thèse, maintenant tu vois la fin de la mienne, je trouve ça super. Merci pour ton réel soutien pendant

ces derniers mois. Thanks to Jibo, I would have never been able to use the Grid without your help! J'aimerais remercier aussi tous les permanents du groupe LHCb au LAL, Jacques qui a toujours des questions pertinentes, Bernard et ses noix du Périgord, Olivier, Guy, Frédéric, Benoit et Sergey avec lesquels j'ai énormément de souvenirs de conversations agréables. C'était un vrai plaisir de faire partie de ce groupe et de partager des pique-niques (au soleil ou pas) avec vous tous. I have also very nice memories with people from the LHCb Collaboration, that I would like to quote here : Stéphane Monteil, Olivier Deschamps, Elie Aslanides, Eli Ben-Haim, Mathieu, Cosme, Marc, Denis, Wenbin, Jordi, and many others. Finally, thanks to Edmund Smith and Stefania Ricciardi, it was nice doing analysis with you.

Sophie, hola chica, je suis très contente d'avoir partagé ce dur moment de fin de thèse au LAL avec toi : sorties (et oui, on peut faire des soirées en fin de thèse !), anecdotes, procédures administratives, rédaction et même vérification des slides dans l'amphi. Et pas que ça, tu m'apprends des mots français pointus, des blagues pour les enfants de 3 ans, les meilleurs endroits parisiens. Je suis ravie d'avoir eu la chance de trouver une copine comme toi ici. Je te souhaite le meilleur pour la suite, ainsi que plein de chance et de bonheur. Merci aussi à Marine, tu as aussi été adorable même si j'ai mis du temps à m'adapter à ta vitesse quand tu parlais français au NPAC. Merci à Laurent et à Stéphane pour les repas du vendredi midi ! Et merci à ma promo du NPAC 2009-2010, c'était une année exceptionnelle et j'ai fait beaucoup de très bonnes rencontres parmi vous : Joany, Loïc (mon binôme de TL !), Simon, Alexandre, Nadir, Nicolas et tous les autres. Bon courage à tous pour la fin de la thèse et pour la suite !

Encore au LAL, Espinelliii ! Marta, grazie pour ta bonne humeur constante et ton soutien aussi. Merci pour avoir accepté de prendre le relais au Conseil du Labo, présidente ! Tu es un peu folle et j'ai bien eu besoin de ça ces derniers temps ;) Ne t'en fais pas, je ne t'abandonne pas, on va continuer à se voir, hein ? Merci aux autres étudiants du LAL pour les pauses café (sur l'herbe ou pas), Samah, Driss, Lan, etc. Un grand merci à Nicolas Leroy, mon parrain de thèse ! J'ai vraiment apprécié tous tes conseils autour d'un café et ton engagement pour t'assurer que ma thèse se passait bien, c'était très rassurant d'avoir quelqu'un d'autre en plus avec qui discuter de temps en temps, et tu l'as très bien fait. J'aimerais aussi remercier François le Diberder, pour avoir toujours le temps pour discuter avec moi dans ton bureau tellement bien rangé, un jour il faudra que tu me donnes ton secret ! Tu es vraiment quelqu'un de remarquable. Et merci pour ton soutien pour ma présentation à ICHEP, c'était vraiment gentil de ta part. Enfin merci à tout le personnel administratif du laboratoire : Chloé, Catherine Bourge, Catherine Zomer, Geneviève, Jocelyne, Annick, Dominique Longieras, le service du personnel, le service mission et le service informatique.

Gracias a los profesores del instituto o la carrera que me hicieron apasionarme por estos estudios y seguir este camino. Gracias a José Antonio Rosón, que me hizo interesarme por la física por primera vez. Cómo olvidar aquel "tú que eres alta y hermosa como dice la canción". Gracias a Rosa, que el día que me explicó el efecto fotoeléctrico me decidió a hacer la carrera de Física. Y gracias a Alfredo Valcarce, por las asignaturas maravillosas de Simetrías y Física de Partículas, por haberme hablado de DESY y por tu gran ayuda con becas y múltiples cartas de recomendación.

Merci à Michaël et Fabien ! Désolée de vous avoir pris Vincent et de m'être immiscée dans votre trio magique, avec défis sportifs inclus ! Vous avez toujours été tellement gentils avec moi, et m'avez toujours encouragée pour mes stages, le NPAC et ma thèse (mais bon, vous avez toujours un peu d'avance sur moi, hein !). Bonne chance à Michaël pour tes entretiens à venir, et à Fabien, tu es notre héro dans la recherche, ne l'oublie pas ! Merci également à Sylvain, quelle colloc magique était la nôtre ! Merci aussi pour ton apport à ma thèse avec tes schémas trop bien faits. Et donc je ne peux que remercier aussi Céline et David ! Merci aux "doctoriants" des Doctoriales du PRES Sorbonne Paris Cité 2012. Ça a aussi été une rencontre exceptionnelle.

Rosa, on ne peut plus concevoir une semaine sans tes apéros. Comme on s'est déjà dit, on aurait dû se rencontrer avant toi et moi, on se serait trop éclaté il y a quelques années ! Bon écoute, on va faire en sorte de s'éclater maintenant alors, malgré les fins de thèse ! Et aussi merci à Valentine, Diana, Sébastien, Laura et tous les autres, vous êtes des gens vraiment très sympas.

Gracias a todos los amigos que dejé en España (o españoles por el mundo), a los que echo de menos (venid a vermeee). Os agradezco el esfuerzo de seguir en contacto conmigo aunque no sea fácil y aunque vaya poco a España. Sois mis vecis, Lucía y Marta, Marta Cortefi super triatleta, Bea Flores ("hola chata, como estás"), Cristina, Carlitos, María (esas amigas que se recuperan años más tarde en el momento oportuno).

Maintenant, je ne sais pas comment vous remercier vous, ma famille française. Martine et Thierry, je n'ai pas les mots qu'il faut ni en français ni en espagnol pour vous dire merci pour tout ce que vous faites pour moi. De mon arrivée en France à la fin de ma thèse vous m'avez accueillie chez vous et avez tout fait pour que je me sente comme chez moi (et vous avez réussi !). Vous m'avez toujours aidé quand j'en ai eu besoin, et avec vous je passe toujours des bons moments. Vous êtes vraiment adorables. Un grand merci à Cécile, tu sais que je te considère comme ma soeur ! Et tu sais que je t'admire, sur une scène ou pas, c'est génial ce que tu fais. Je te souhaite beaucoup de chance pour tous tes projets, et sache que je serai toujours là quand tu en auras besoin. Olé ! Merci aussi aux grands-parents, tantes, oncles et cousins, qui font aussi partie de cet accueil d'exception.

GRACIAS a mis padres, Manoli y Chago. Por estar siempre orgullosos de mí. Por apoyarme aunque estudie unas cosas "tan raras, con tanto número" y por darme todo lo necesario para llegar hasta aquí. ¡Me encanta mi familia! Siempre habeis estado ahí animándome a hacer lo que yo quiero. Siento haberme marchado tan lejos (eh, tanto no, que podeis venir en coche), gracias por no haberme puesto trabas en ningún momento para nada. Gracias por permitirme ser feliz. Sois los mejores y os quiero. Dani, no sabes cuánto siento no estar en casa durante estos años en los que tú estás haciendo la carrera. ¡Menos mal que existe el teléfono para que me lo cuentes todo! Me acuerdo de cuando estudiaba yo para mis exámenes y venías y me decías, "¿pero entiendes algo en esos apuntes?" XD Ánimo, porque suerte no te hace falta, estás hecho un champion, y estoy muy orgullosa de mi bro! Sabes que el sofá de París te acoge siempre que quieras :) Os echo un montón de menos a los tres. Y a mis abuelos, tíos y primos, por supuesto.

And last but not least, merci Vincent. Merci Zeuthen et Berlin, param param bitte, here we go again! Tu m'as changé la vie, les deux mois de Summer School étaient exceptionnels, mais ça n'a rien à voir avec les presque 5 ans d'après. Avec toi j'ai une vie géniale et je suis heureuse. Tu ne te rends pas compte de tout ce que tu m'as donné : tu m'apprends la culture et la langue françaises, tu m'aides avec la physique, tu m'aides avec tout ce qu'il faut, tu me montres Paris et la France ; avec toi j'ai un chez moi. Merci pour tout ce que tu fais pour moi tous les jours. Merci pour ton énorme soutien de ces derniers mois, d'avoir supporté mes moments de stress et même de craquage. J'ai certainement été pénible, mais toi, tu as été super. J'ai hâte de vivre ensemble la vie que nous avons devant nous.

"Bientôt" est enfin arrivé !

Bibliography

[1] E. Fermi, *Tentativo di una teoria dei raggi β*, Ricerca Scientifica (1933).

[2] E. Noether, *Invariant Variation Problems*, Gott. Nachr. **1918** (1918) 235, `arXiv:physics/0503066`.

[3] T. Lee and C.-N. Yang, *Question of Parity Conservation in Weak Interactions*, Phys. Rev. **104** (1956) 254.

[4] C. Wu *et al.*, *Experimental Test of Parity Conservation in Beta Decay*, Phys. Rev. **105** (1957) 1413.

[5] M. Goldhaber, L. Grodzins, and A. Sunyar, *Helicity of Neutrinos*, Phys. Rev. **109** (1958) 1015.

[6] S. Glashow, *Partial Symmetries of Weak Interactions*, Nucl. Phys. **22** (1961) 579.

[7] S. Weinberg, *A Model of Leptons*, Phys. Rev. Lett. **19** (1967) 1264.

[8] A. Salam, *Weak and Electromagnetic Interactions*, Conf. Proc. **C680519** (1968) 367.

[9] F. Englert and R. Brout, *Broken Symmetry and the Mass of Gauge Vector Mesons*, Phys. Rev. Lett. **13** (1964) 321.

[10] P. W. Higgs, *Broken Symmetries, Massless Particles and Gauge Fields*, Phys. Lett. **12** (1964) 132.

[11] P. W. Higgs, *Broken Symmetries and the Masses of Gauge Bosons*, Phys. Rev. Lett. **13** (1964) 508.

[12] G. Guralnik, C. Hagen, and T. Kibble, *Global Conservation Laws and Massless Particles*, Phys. Rev. Lett. **13** (1964) 585.

[13] ATLAS Collaboration, G. Aad *et al.*, *Observation of a new particle in the search for the Standard Model Higgs boson with the ATLAS detector at the LHC*, Phys. Lett. **B716** (2012) 1, `arXiv:1207.7214`.

[14] CMS Collaboration, S. Chatrchyan *et al.*, *Observation of a new boson at a mass of 125 GeV with the CMS experiment at the LHC*, Phys. Lett. **B716** (2012) 30, `arXiv:1207.7235`.

[15] J. Thomson, *Cathode Rays*, Phil. Mag. **44** (1897) 293.

[16] J. Chadwick, *Possible Existence of a Neutron*, Nature **129** (1932) 312.

[17] C. Anderson, *The Positive Electron*, Phys. Rev. **43** (1933) 491.

[18] S. Neddermeyer and C. Anderson, *Note on the Nature of Cosmic Ray Particles*, Phys. Rev. **51** (1937) 884.

[19] H. Yukawa, *On the Interaction of Elementary Particles*, Proc. Phys. Math. Soc. Jap. **17** (1935) 48.

[20] M. Gell-Mann, *A Schematic Model of Baryons and Mesons*, Phys. Lett. **8** (1964) 214.

[21] G. Zweig, *An SU(3) Model for Strong Interaction Symmetry and its Breaking*, CERN-TH-401 (1964).

[22] N. Cabibbo, *Unitary Symmetry and Leptonic Decays*, Phys. Rev. Lett. **10** (1963) 531.

[23] S. Glashow, J. Iliopoulos, and L. Maiani, *Weak Interactions with Lepton-Hadron Symmetry*, Phys. Rev. **D2** (1970) 1285.

[24] E598 Collaboration, J. Aubert *et al.*, *Experimental Observation of a Heavy Particle J*, Phys. Rev. Lett. **33** (1974) 1404.

[25] SLAC-SP-017 Collaboration, J. Augustin *et al.*, *Discovery of a Narrow Resonance in e^+e^- Annihilation*, Phys. Rev. Lett. **33** (1974) 1406.

[26] J. Christenson, J. Cronin, V. Fitch, and R. Turlay, *Evidence for the 2π Decay of the $K_{(2)}^0$ Meson*, Phys. Rev. Lett. **13** (1964) 138.

[27] M. Kobayashi and T. Maskawa, *CP Violation in the Renormalizable Theory of Weak Interaction*, Prog. Theor. Phys. **49** (1973) 652.

[28] S. Herb *et al.*, *Observation of a Dimuon Resonance at 9.5-GeV in 400-GeV Proton-Nucleus Collisions*, Phys. Rev. Lett. **39** (1977) 252.

[29] CDF Collaboration, F. Abe *et al.*, *Evidence for top quark production in $\bar{p}p$ collisions at $\sqrt{s} = 1.8$ TeV*, Phys. Rev. Lett. **73** (1994) 225, `arXiv:hep-ex/9405005`.

[30] B. Pontecorvo, *Mesonium and Anti-mesonium*, Sov. Phys. JETP **6** (1957) 429.

[31] B. Pontecorvo, *Inverse Beta Processes and Nonconservation of Lepton Charge*, Sov. Phys. JETP **7** (1958) 172.

[32] Z. Maki, M. Nakagawa, and S. Sakata, *Remarks on the Unified Model of Elementary Particles*, Prog. Theor. Phys. **28** (1962) 870.

[33] L. Wolfenstein, *Parametrization of the Kobayashi-Maskawa Matrix*, Phys. Rev. Lett. **51** (1983) 1945.

[34] Particle Data Group, J. Beringer *et al.*, *Review of Particle Physics (RPP)*, Phys. Rev. **D86** (2012) 010001.

[35] UTfit, www.utfit.org.

[36] CKMfitter, www.ckmfitter.in2p3.fr.

[37] HFAG, http://www.slac.stanford.edu/xorg/hfag.

[38] BABAR Collaboration, J. P. Lees *et al.*, *Observation of direct CP violation in the measurement of the Cabibbo-Kobayashi-Maskawa angle γ with $B^\pm \to D^{(*)}K^{(*)\pm}$ decays*, BABAR-PUB-12-025, SLAC-PUB-15328 (2013), `arXiv:1301.1029`.

[39] Belle collaboration, K. Trabelsi, *Study of direct CP in charmed B decays and measurement of the CKM angle γ at Belle* (2013), `arXiv:1301.2033`.

[40] LHCb Collaboration, *Improved constraints on γ from $B^{\pm} \to DK^{\pm}$ decays including first results on 2012 data*, LHCb-CONF-2013-006 (2012).

[41] LHCb Collaboration, B. Adeva *et al.*, *Roadmap for selected key measurements of LHCb*, LHCB-PUB-2009-029 (2009), `arXiv:0912.4179`.

[42] R. Fleischer, *Exploring CP violation and penguin effects through $B_d^0 \to D^+D^-$ and $B_s^0 \to D_s^+D_s^-$*, Eur. Phys. J. **C51** (2007) 849, `arXiv:0705.4421`.

[43] LHCb Collaboration, R. Aaij *et al.*, *Implications of LHCb measurements and future prospects*, LHCB-PUB-2012-006, LHCB-PAPER-2012-031, CERN-PH-EP-2012-334 (2012), `arXiv:1208.3355`.

[44] LHCb collaboration, R. Aaij *et al.*, *Measurement of CP violation and the B_s^0 meson decay width difference with $B_s^0 \to J/\psi K^+K^-$ and $B_s^0 \to J/\psi \pi^+\pi^-$ decays*, CERN-PH-EP-2013-055, LHCB-PAPER-2013-002 (2013), `arXiv:1304.2600`.

[45] M. Gronau and D. Wyler, *On determining a weak phase from CP asymmetries in charged B decays*, Phys. Lett. **B265** (1991) 172.

[46] M. Gronau and D. London, *How to determine all the angles of the unitarity triangle from $B_d^0 \to DK_S$ and $B_s^0 \to D\phi$*, Phys. Lett. **B253** (1991) 483.

[47] D. Atwood, I. Dunietz, and A. Soni, *Improved methods for observing CP violation in $B^{\pm} \to KD$ and measuring the CKM phase γ*, Phys. Rev. **D63** (2001) 036005, `arXiv:hep-ph/0008090`.

[48] A. Giri, Y. Grossman, A. Soffer, and J. Zupan, *Determining γ using $B^{\pm} \to DK^{\pm}$ with multibody D decays*, Phys. Rev. **D68** (2003) 054018, `arXiv:hep-ph/0303187`.

[49] BABAR Collaboration, P. del Amo Sanchez *et al.*, *Evidence for direct CP violation in the measurement of the Cabibbo-Kobayashi-Maskawa angle γ with $B^{\pm} \to D^{(*)}K^{(*)\pm}$ decays*, Phys. Rev. Lett. **105** (2010) 121801, `arXiv:1005.1096`.

[50] BABAR Collaboration, B. Aubert *et al.*, *Search for CP violation in the decays $D^0 \to K^-K^+$ and $D^0 \to \pi^-\pi^+$*, Phys. Rev. Lett. **100** (2008) 061803, `arXiv:0709.2715`.

[51] CDF Collaboration, T. Aaltonen *et al.*, *Measurement of the difference of CP-violating asymmetries in $D^0 \to K^+K^-$ and $D^0 \to \pi^+\pi^-$ decays at CDF*, Phys. Rev. Lett. **109** (2012) 111801, `arXiv:1207.2158`.

[52] Belle Collaboration, M. Staric *et al.*, *Measurement of CP asymmetry in Cabibbo suppressed D^0 decays*, Phys. Lett. **B670** (2008) 190, `arXiv:0807.0148`.

[53] LHCb Collaboration, R. Aaij *et al.*, *Evidence for CP violation in time-integrated $D^0 \to h^-h^+$ decay rates*, Phys. Rev. Lett. **108** (2012) 111602, `arXiv:1112.0938`.

[54] CLEO Collaboration, D. M. Asner *et al.*, *Determination of the $D^0 \to K^+\pi^-$ Relative Strong Phase Using Quantum-Correlated Measurements in $e^+e^- \to D^0\bar{D^0}$ bar at CLEO*, Phys. Rev. **D78** (2008) 012001, `arXiv:0802.2268`.

[55] CLEO Collaboration, N. Lowrey *et al.*, *Determination of the $D^0 \to K^-\pi^+\pi^0$ and $D^0 \to K^-\pi^+\pi^+\pi^-$ Coherence Factors and Average Strong-Phase Differences Using Quantum-Correlated Measurements*, Phys. Rev. **D80** (2009) 031105, `arXiv:0903.4853`.

[56] M. Gronau, *Improving bounds on γ in $B^{\pm} \to DK^{\pm}$ and $B^{\pm,0} \to DX_{(s)}^{\pm,0}$*, Phys. Lett. **B557** (2003) 198, `arXiv:hep-ph/0211282`.

[57] S. Pruvot, M. Schune, V. Sordini, and A. Stocchi, *Measuring γ with $B^0 \to D^0 K^{*0}$ decays at Babar*, SLAC-PUB-12495 (2007), `arXiv:hep-ph/0703292`.

[58] BABAR Collaboration, B. Aubert *et al.*, *Search for $b \to u$ transitions in $B^0 \to D^0 K^{*0}$ decays*, Phys. Rev. **D80** (2009) 031102, `arXiv:0904.2112`.

[59] BABAR Collaboration, B. Aubert *et al.*, *Constraints on the CKM angle γ in $B^0 \to \overline{D}^0 (D^0) K^{*0}$ with a Dalitz analysis of $D^0 \to K_{(S)} \pi^+ \pi^-$*, Phys. Rev. **D79** (2009) 072003, `arXiv:0805.2001`.

[60] BABAR Collaboration, P. del Amo Sanchez *et al.*, *Measurement of CP observables in $B^{\pm} \to D_{CP} K^{\pm}$ decays and constraints on the CKM angle γ*, Phys. Rev. **D82** (2010) 072004, `arXiv:1007.0504`.

[61] CDF Collaboration, T. Aaltonen *et al.*, *Measurements of branching fraction ratios and CP asymmetries in $B^{\pm} \to D(CP)K^{\pm}$ decays in hadron collisions*, Phys. Rev. **D81** (2010) 031105, `arXiv:0911.0425`.

[62] LHCb Collaboration, R. Aaij *et al.*, *Observation of CP violation in $B^+ \to DK^+$ decays*, Phys. Lett. **B712** (2012) 203, `arXiv:1203.3662`.

[63] Heavy Flavor Averaging Group, Y. Amhis *et al.*, *Averages of b-hadron, c-hadron, and tau-lepton properties as of early 2012*, SLAC-R-1002 (2012), `arXiv:1207.1158`.

[64] LHCb collaboration, R. Aaij *et al.*, *Measurement of CP observables in $B^0 \to DK^{*0}$ with $D \to K^+ K^-$*, JHEP **1303** (2013) 067, `arXiv:1212.5205`.

[65] BABAR Collaboration, P. del Amo Sanchez *et al.*, *Search for $b \to u$ transitions in $B^- \to DK^-$ and $D^* K^-$ decays*, Phys. Rev. **D82** (2010) 072006, `arXiv:1006.4241`.

[66] Belle Collaboration, Y. Horii *et al.*, *Evidence for the Suppressed Decay $B^- \to DK^-$, $D \to K^+ \pi^-$*, Phys. Rev. Lett. **106** (2011) 231803, `arXiv:1103.5951`.

[67] CDF Collaboration, T. Aaltonen *et al.*, *Measurements of branching fraction ratios and CP-asymmetries in suppressed $B^- \to D(\to K^+ \pi^-)K^-$ and $B^- \to D(\to K^+ \pi^-)\pi^-$ decays*, Phys. Rev. **D84** (2011) 091504, `arXiv:1108.5765`.

[68] Belle Collaboration, K. Negishi *et al.*, *Search for the decay $B^0 \to DK^{*0}$ followed by $D \to K^- \pi^+$*, Phys. Rev. **D86** (2012) 011101, `arXiv:1205.0422`.

[69] LHCb Collaboration, J. Alves, A. Augusto *et al.*, *The LHCb Detector at the LHC*, JINST **3** (2008) S08005.

[70] LHCb Collaboration, R. Aaij *et al.*, *Measurement of $\sigma(pp \to b\bar{b}X)$ at $\sqrt{s} = 7$ TeV in the forward region*, Phys. Lett. **B694** (2010) 209, `arXiv:1009.2731`.

[71] LHCb Collaboration, R. Aaij *et al.*, *Absolute luminosity measurements with the LHCb detector at the LHC*, JINST **7** (2012) P01010, `arXiv:1110.2866`.

[72] The Gaudi project, http://proj-gaudi.web.cern.ch/proj-gaudi.

[73] ROOT, http://root.cern.ch.

[74] M. Clemencic *et al.*, *The LHCb simulation application,* Gauss*: design, evolution and experience*, J. of Phys: Conf. Ser. **331** (2011) 032023.

[75] T. Sjöstrand, S. Mrenna, and P. Skands, *PYTHIA 6.4 physics and manual*, JHEP **05** (2006) 026, `arXiv:hep-ph/0603175`.

[76] D. J. Lange, *The EvtGen particle decay simulation package*, Nucl. Instrum. Meth. **A462** (2001) 152.

[77] GEANT4 collaboration, S. Agostinelli *et al.*, *GEANT4: a simulation toolkit*, Nucl. Instrum. Meth. **A506** (2003) 250.

[78] GEANT4 collaboration, J. Allison *et al.*, *Geant4 developments and applications*, IEEE Trans. Nucl. Sci. **53** (2006) 270.

[79] R. Aaij *et al.*, *The LHCb Trigger and its Performance in 2011*, JINST **8** (2013) P04022, `arXiv:1211.3055`.

[80] A. Martín Sánchez, P. Robbe, and M.-H. Schune, *Performance of the LHCb L0 Calorimeter Trigger*, LHCb-PUB-2011-026 (2011).

[81] LHCb Collaboration, R. Aaij *et al.*, *First observation of the decay $\bar{B}_s^0 \to D^0 K^{*0}$ and a measurement of the ratio of branching fractions $\frac{\mathcal{B}(\bar{B}_s^0 \to D^0 K^{*0})}{\mathcal{B}(\bar{B}^0 \to D^0 \rho^0)}$*, Phys. Lett. **B706** (2011) 32, `arXiv:1110.3676`.

[82] A. Martens, *Towards a measurement of the angle γ of the Unitarity Triangle with the LHCb detector at the LHC (CERN): calibration of the calorimeters using an energy flow technique and first observation of the $B_s^0 \to \overline{D}^0 \overline{K}^{*0}$ decay*, PhD thesis, CERN-THESIS-2011-128, LAL-11-172 (2011).

[83] M. Adinolfi *et al.*, *Performance of the LHCb RICH detector at the LHC*, CERN-LHCB-DP-2012-003, LHCB-DP-2012-003 (2012), `arXiv:1211.6759`.

[84] Particle Data Group, K. Nakamura *et al.*, *Review of particle physics*, J. Phys. **G37** (2010) 075021.

[85] M. Pivk and F. R. Le Diberder, *SPlot: A Statistical tool to unfold data distributions*, Nucl. Instrum. Meth. **A555** (2005) 356, `arXiv:physics/0402083`.

[86] LHCb Collaboration, *Studies of beauty baryons decaying to $D^0 p\pi^-$ and $D^0 pK^+$*, LHCb-CONF-2011-036 (2011).

[87] LHCb Collaboration, R. Aaij *et al.*, *Measurement of b-hadron production fractions in 7 TeV pp collisions*, Phys. Rev. **D85** (2012) 032008, `arXiv:1111.2357`.

[88] LHCb Collaboration, *Charmless charged two body B-decays at LHCb with 2011 data*, LHCb-CONF-2011-042 (2011).

[89] A. Hoecker *et al.*, *TMVA 4: Toolkit for Multivariate Data Analysis with ROOT, Users Guide*, CERN-OPEN-2007-007 (2009), `arXiv:physics/0703039`.

[90] TMVA: Toolkit for Multivariate Data Analysis with ROOT, http://tmva.sourceforge.net.

[91] M. Jacob and G. Wick, *On the general theory of collisions for particles with spin*, Annals Phys. **7** (1959) 404.

[92] J. D. Richman, *An Experimenter's Guide to the Helicity Formalism*, CALT-68-1148 (1984).